Synthesis, applications and phenomena of anisotropic inorganic colloids

By

Adam R. Morgan

A thesis submitted in fulfilment of the requirements for the degree Doctor of Philosophy in Chemistry.

University of Warwick, Department of Chemistry

October 2013

Table of Contents

Table of Figures

Table of Tables

Acknowledgements

I would like to thank the entire Bon group both past (Roberto, Catheline, Nick, Gabit, Andy E., Nicole, Brooke, Nyle, Nadia, Attyah, Patrik, Tom 2, Ashton, Rhys, Chris, Bruno, Tom R., and all other masters/project students) and present (Alan, Rob Y., Yunhua, Tom S., Holly, Rong, Saif, Rob B., Joe, Sang, and Andy R.) for making my time during my Ph.D. both enjoyable and rewarding.

In particular I would like to thank Thomas Skelhon, Holly McKenzie, Alan Dawson, Gabit Nurumbetov and Nicholas Ballard for the collaborative work that we engaged in. Special thanks to Assoc. Prof. Stefan Bon for his continued enthusiasm and input into the projects that we have worked on, and for the fun times we have had over a Grolsch (or 6).

Also, I would like to thank all of the academic staff, support staff, and other Ph.D. students/Post-Docs whom I have worked with/been taught by at the University of Warwick over the last 8 years.

Thanks go to AkzoNobel and the EPSRC for funding the project. In particular I would like to thank Nikki Strickland, Martin Murray, Ron Schmidt, Daragh McLoughlin, Fraser Robertson, Abdessamad Arbaoui, Krisztina Erdelyi-Brooks, and Neal Williams for the discussions had in relation to the investigations conducted on hollow SiO_2 particles as opacity modifiers in waterborne coatings (**Chapter 1** and **2**).

Furthermore, I would like to thank Chemistry Innovation and the CASE awards for organizing the funding for the project. Thanks goes to the Birmingham

Science City AM2 initiative (uses for advanced materials in the modern world – West Midlands centre for advanced materials project 2), with support from Advantage West Midlands (AWM) and the European Regional Development Fund (ERDF) for providing funding for some of the equipment which I have used.

Thanks goes to Steve York, Richard Beanland (both Department of Physics), and Ian Hands-Portman (Department of Life Sciences) for their help with some of the electron microscopy. Thanks to Dave Hammond for advice over TGA and DSC measurements and Ben Douglas for advice over porosimetry. Thanks go to Peter Dunne, Luke Rochford, and David Burnett for assistance with XRD and AFM.

I would like to thank my housemates and other friends from Warwick and Aylesbury over the years, particularly at HFD's, for their friendship and the good times we had. A further acknowledgement must go to my best friend Henry Franks (Department of Computer Science) for his collaboration over the analysis of the particle tracking data in the chemotaxis work of **Chapter 4**.

Finally, a most special thank you goes to my family whose support and love I am eternally grateful for. All my love to Mumzo, Lizzie, Fred, Joyce & Co., Jo & Co., Joe & Co., Margaret & Gerald, Laura & Co., Alan, Sam, Abi, Paul, Di & Andy, Val & Co., John & Co., Giz, Dibs, Pudsy, Yogi, Ambie and Amie and most of all Bobo, whom I miss dearly every day.

Declaration

I hereby declare that this thesis consists of my own work and that it has not previously been submitted for any previous degree at any institution.

Film reflectance and density measurements in **Chapter 1** and **2** were performed by Krisztina Erdelyi-Brooks (AkzoNobel, Slough). Cryo-TEM imaging in **Chapter 2** was performed by Ian Hands-Portman (University of Warwick, School of Life Sciences).

Dr. Nicholas Ballard collaborated with me in **Chapter 3** on the simulation work performed in MATLAB. Luke Rochford assisted with the AFM measurements.

Alan Dawson assisted with some of the synthesis behind the work in **Chapter 4**. In the same chapter Thomas Skelhon provided the latex particles to be used as trackers in the chemotaxis experiment. Henry Franks wrote the custom .jar file to help process the raw data. Luke Rochford, Peter Dunne, and David Burnett assisted with the collection of the XRD data.

Any work previously published is referenced on the opening page of each chapter. Where other sources of information have been used, they have been acknowledged and referenced.

Signed _____ **Date** _____

Adam R. Morgan

Abstract

We investigate the synthesis and application of anisotropic hollow silica colloids as air voided opacity modifiers in dry polymer films in **Chapter 1**, with the aim of improving upon the light scattering efficacy of the commercially used isotropic hollow latex particles, ROPAQUE™.

In order to generate anisotropic hollow silica particles we utilized a sacrificial templating method, ultimately leading us to investigate the opacifying power of hollow silica particles derived from a calcium carbonate template known as SOCAL P3.

Initial investigations indicated that shell fragmentation and collapse of our "1st generation" hollow silica particles (with thin shells) led to a loss of opacity, as few air voids remained intact.

Tuning the reaction parameters afforded hollow silica particles with thicker shells that displayed enhanced light scattering over the 1st generation hollow SiO_2 particles and to SOCAL P3 when film thickness was accounted for.

Chapter 2 is an extension of the work done in **Chapter 1**, wherein we aim to improve pigment dispersion (and consequently opacity) by grafting negatively charged, hydrophilic, polymer brushes to $CaCO_3$@SiO_2 particles. This confers enhanced colloidal stability to the particles through electrosteric stabilization.

For this we first functionalize the surface with a tertiary alkyl bromide atom transfer radical polymerization (ATRP) initiator to furnish a surface capable of growing polymer brushes from. The initiator is anchored to the surface through siloxane bonds and an amide group, the latter to enhance hydrolytic stability over a

wide pH range. We then used a SI-ATRP (where SI = surface initiated) in order to grow the polymer brushes, which we found to generate highly colloidally stable hollow SiO_2 particles that demonstrate an enhanced contrast ratio to the sterically stabilized hollow SiO_2-PVP particles used in **Chapter 1**.

In **Chapter 3** we investigate the multiple orientations of hematite superellipsoids (pseudocubes stabilized with PVP) trapped at an oil-water interface, through a combination of experiments and simulations.

We find three orientations in all; two of which are thermodynamic minima and one which corresponds to a kinetically-trapped orientation. The latter results from some particles going through a negligible free energy gradient upon re-orientation. Experimental and computational results for the relative balance of particle populations are found to be in excellent agreement with one another.

We show that the final position of the particle is both a function of the free energy landscape and the precise orientation of the particle at the point of contact with the interface.

A modified silica rod synthesis from an oil-in-water emulsion is demonstrated in **Chapter 4**, whereby we manage to asymmetrically include a manganese oxide head at one end of the rod to generate a colloidal "matchstick" morphology.

Placing these particles into a solution of hydrogen peroxide as fuel facilitates their propulsion as they form an asymmetrical gradient of the breakdown products of hydrogen peroxide; water and oxygen. Adjusting fuel concentration alters the effective diffusion coefficient with a 1^{st} order relationship.

Furthermore, we demonstrate that these particles can undergo chemotaxis towards a higher concentration of fuel when placed into a fuel gradient. We rule out convection and other external forces as the reason for directional motion by simultaneously imaging catalytically inert microspheres which travel under convection in the opposite direction to that of the rods.

Abbreviations

AA	Acrylic acid
AFM	Atomic force microscopy
APTES	(3-aminopropyl)triethoxysilane
ATRP	Atom transfer radical polymerization
BA	Butyl acrylate
BET	Brauner, Emmett, and Teller (method to determine surface area)
BiBB	α-bromoisobutyryl bromide
DMCPS	Decamethylcyclopentasiloxane
DVB	Divinylbenzene
EDAX	Energy dispersive X-ray spectroscopy
FTIR	Fourier transform infrared spectroscopy
HDTMOS	Hexadecyltrimethoxysilane
HMDS	Hexamethyldisilazane
KPS	Potassium persulfate
MSD	Mean squared displacement
NaSS	Sodium 4-styrene sulfonate
PDMS	Polydimethylsiloxane
PMDETA	N,N,N′,N″,N″-pentamethyldiethylenetriamine
PVC	Pigment volume concentration
PVP	Poly(N-vinyl-2-pyrrolidone)
S	Styrene
SDS	Sodium dodecyl sulfate
SI	Surface initiated

SEM	Scanning electron microscopy
TEM	Transmission electron microscopy
TEOS	Tetraethylorthosilicate
TGA	Thermogravimetric analysis

List of Publications

1). "Quiescent water-in-oil Pickering emulsions as a route toward healthier fruit juice infused chocolate confectionary" Thomas S. Skelhon, Nadia Grossiord, **Adam R. Morgan**, and Stefan A. F. Bon, *J. Mater. Chem.*, **2012**, *22*, 19289-19295.

2). "Understanding the Multiple Orientations of Isolated Superellipsoidal Hematite Particles at the Oil-Water Interface" **Adam R. Morgan**, Nicholas Ballard, Luke A. Rochford, Gabit Nurumbetov, Thomas S. Skelhon, and Stefan A. F. Bon, *Soft Matter*, **2013**, *9*, 487-491.

3). "High internal phase Agar hydrogel dispersions in cocoa butter and chocolate as a route towards reducing fat content" Thomas S. Skelhon, Patrik K. A. Olsson, **Adam R. Morgan**, and Stefan A. F. Bon, *Food and Function*, **2013,** *4* (9), 1314-1321. (Front cover).

4). "Chemotaxis of Catalytic Silica-Manganese Oxide “Matchstick” Particles" **Adam R. Morgan**, Alan B. Dawson, Holly S. McKenzie, Thomas S. Skelhon, Richard Beanland, Henry P. W. Franks, and Stefan A. F. Bon, *Mater. Horiz.*, **2014**, *1* (1), 65-68. (Inside cover).

Chapter 1

"Hollow SiO_2 Particles as Opacity Modifiers in Dry Polymer Films as Decorative Coatings"

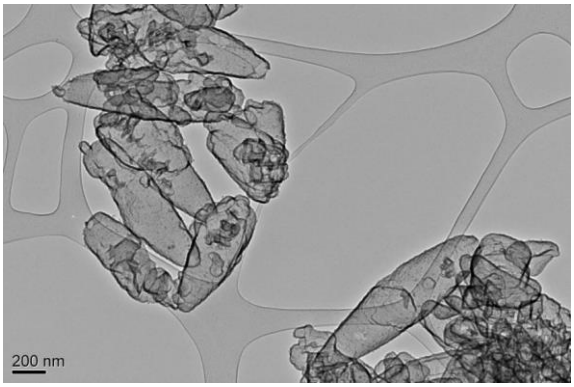

TiO_2 is the most widely used pigment in white decorative coatings due to its excellent hiding power and brilliant whiteness. However, its use comes at both an economic and environmental cost.

Air voided particles, such as the spherical hollow polymer latex ROPAQUE™, can be added to decorative coatings to act as light scattering centers. This allows for reductions in the amount of TiO_2 required to achieve the desired optical properties of the film.

In this work we investigate the use of anisotropic air-voided particles in an attempt to improve on the hiding power of ROPAQUE, which would allow further reductions in the amount of TiO_2 required in the coating formulation.

Initially we looked at using monodisperse Cu_2O and Fe_2O_3 colloids as a template in a sacrificial templating route to hollow SiO_2 particles, following growth

of a SiO_2 shell. This proved to be unfeasible in terms of generating enough material for pigment testing.

This led us to develop hollow SiO_2 particles templated upon a commercially available grade of precipitated $CaCO_3$, known as SOCAL P3. This is a commonly used extender comprising a mixture of ellipsoidal and polyhedral particle morphologies with an equivalent spherical diameter in the submicron size range. It is used in the coatings industry primarily to spatially separate TiO_2 pigment particles in the dry film in order to reduce an effect known as optical crowding.

$CaCO_3$ itself is not an effective material at light scattering in styrene-acrylic polymer films as the refractive index difference between the two materials is very small (dn ~ 0.04-0.19). Introducing an air void into the particle by means of sacrificial templating would increase this difference in refractive index to around 0.48-0.60, whilst maintaining particulate morphology to still serve as an extender.

We found the shells of the hollow SiO_2 particles to fragment upon acid etch of the calcite core/collapse upon film formation, destroying the air voids inside the particles, thus making them ineffective at scattering light. Through tuning of the reaction parameters we increased the thickness of the shell and found these to be much more effective light scattering centers.

1.1 Introduction

A waterborne coating used as a decorative paint typically consists of a low T_g latex binder, rheology modifiers, organic/inorganic pigments, performance enhancing inorganic "fillers" and other additives such as anti-foaming agents and biocides.[1,2] Typically a slurry of some of the components is made up first and well dispersed under extreme shear in what is known as the "grind" stage (**Table 1.1**). Then, a secondary "mixing" stage is used to finish the paint formulation (**Table 1.2**).

Table 1.1. A typical formulation for the pigment slurry (TiO_2), extender slurry (SOCAL P3) and the low-shear rheology slurry (Optigel CK). Formulations were obtained from AkzoNobel. [a] SOCAL P3 is a registered trademark, however the use of ® will be omitted throughout the rest of the document.

Component	**TiO_2 Slurry Component Mass (g)**	**SOCAL® P3[a] Slurry Component Mass (g)**	**Optigel CK Slurry Component Mass (g)**
Water	50.40	34.40	20.69
Orotan N-4045	4.20	1.40	-
Rocima V189	1.80	0.60	0.15
Dispelair CF823	3.60	1.20	-
Disponil A1580	3.00	1.00	-
SOCAL P3	-	59.80	-
Coapur 830W	-	1.00	-
Optigel CK	-	0.60	4.16
Tioxide R-TC90	237.00	-	-
TOTAL MASS	**300.00**	**100.00**	**25.00**

Table 1.2. A typical formulation for a white decorative waterborne coating consisting of a pigment slurry, extender slurry, rheology modifiers, stabilizers and the film forming binder.

Component	Mass (g)
Water	60.51
TiO_2 slurry	75.88
SOCAL P3 slurry	41.43
Optigel CK slurry	5.51
Coapur 830W	5.42
Disponil A1580	1.44
Latex binder	109.81
TOTAL MASS	**300.00**

Orotan N-4045 is a polycarboxylic acid pigment dispersant, Rocima V189 is a biocide and Dispelair CF823 is an emulsion of mineral oil, SiO_2 and surfactants that is used to prevent the formation of foam. Disponil A1580 is a modified ethoxylated fatty alcohol surfactant, used to help disperse the more hydrophobic components of the formulation. SOCAL P3 is a precipitated grade of calcium carbonate, which is used as an extender to space apart TiO_2 pigment particles. Coapur 830W is a mid-range polyurethane associative thickening agent. Optigel CK consists of bentonite particles and is used as a low shear thickener/thixotropic agent. Finally, Tioxide R-TC90 is a grade of rutile TiO_2 that is used as a white pigment with excellent hiding power.

The solid components of the coating are left behind in a dry film after the water has evaporated from the applied wet film, which causes the soft latex particles to deform and then coalesce, trapping the remaining solids in the dry film. A schematic of the film formation process for a waterborne latex is outlined in **Figure 1.1**. An excellent review on the subject of latex film formation is given by Keddie.[3]

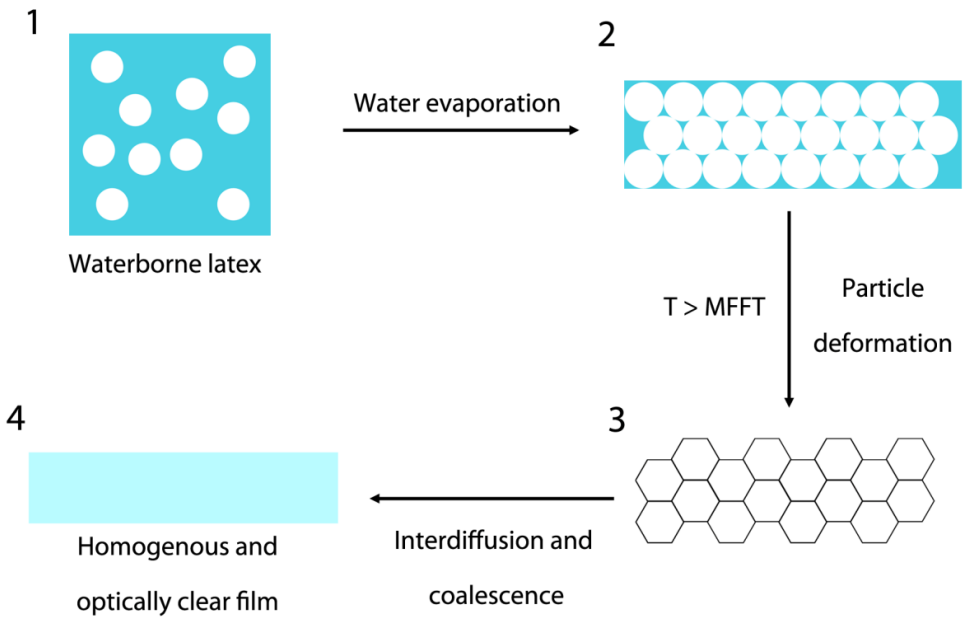

Figure 1.1. Schematic of the film formation process for a soft waterborne latex. (**1**) Aqueous coating is applied to a substrate, (**2**) Evaporation of water brings latex particles closer together, (**3**) Depending on both the T_g of the latex and the ambient temperature, the particles can deform into a honeycomb type of array, (**4**) Interdiffusion and coalescence of the polymer chains yields a homogenous film.

A critical property of a film forming latex is the minimum film formation temperature (MFFT), which is defined as the minimum temperature that a latex will coalesce at when applied to a substrate.[4] It is important that the temperature of film formation is above the MFFT to ensure that a continuous film with good adhesion to

the substrate is obtained. This is why a low T_g polymeric latex is used in paint formulation, to ensure that film drying after application occurs above the MFFT.

However, it is undesirable to use a latex with a very low MFFT as it can lead to increased tack and loss of workability upon application. Coalescing agents, which are plasticizers (glycol ethers for example), can be added to a formulation if necessary to lower the film formation temperature of the binder.[5]

The dry film thickness, DFT (µm), can be calculated by knowing the volume solids, VS (%), and wet film thickness, WFT (µm), of the coating that has been applied to a substrate, assuming 1D drying (**Equation 1.1**).

$$\boldsymbol{DFT = \frac{VS \times WFT}{100}} \quad \textbf{(1.1)}$$

An important factor in determining the WFT is the spreading rate, SR ($m^2 \cdot L^{-1}$), which can be defined as follows (**Equation 1.2**).

$$\boldsymbol{SR = \frac{VS \times 10}{DFT\ required}} \quad \textbf{(1.2)}$$

Coatings formulations need to have the correct rheological profile in response to shear stress.[6] At low shear (i.e. after application to a surface) the coating needs to be viscous enough to resist sagging and drip. Having a higher viscosity in storage and transportation (low shear) also prevents sedimentation and separation in the high solids coating formulations.

It is important that the non-Newtonian fluid is shear thinning at higher shear rates (i.e. application with a paint brush) to enable easy application, prevent bubble trapping and promote spreading in order to prevent track marks from the brush.

Pigments are included in the film to selectively reflect certain portions of the visible spectrum from the film to give the paint a certain color. The efficiency with which they scatter light will also determine the extent to which they visually hide the surface they are coating, known as "hiding power". Of course other factors extrinsic to the particles themselves such as the degree of dispersion, thickness of the film and total pigment volume will also play a role in this.

The pigment volume concentration (PVC) of a coating is the ratio of the pigment volume to the total volume of solids, including that of the pigment (**Equation 1.3**).

$$\boldsymbol{PVC = \frac{V_{Pigment}}{(V_{pigment} + V_{Solids})}} \quad \textbf{(1.3)}$$

White pigments are ubiquitous in modern life – primarily used in the paper, coating, cosmetic and textile industries. High refractive index materials such as TiO_2 are ideal white opacifying pigments[7] for latex-based coatings due to the large difference in light refraction between the pigment (n ~ 2.50-2.70)[8] and the acrylic-styrene binder (n ~ 1.48-1.60),[9] as well as the pigments' broadband reflectance properties in the visible spectrum.

As the concentration of pigment increases it approaches the critical pigment volume concentration (CPVC), where the amount of binder is insufficient to cover

the solids in the coating upon film formation i.e. the pigment particles are no longer fully wetted by the binder. This results in a dramatic deterioration of film properties including increased permeability and loss of gloss, stability and mechanical strength.[10] Sometimes extender particles are used above the CPVC to achieve "dry hiding", where the hiding power of the film is increased due to the inclusion of air voids in the dry film. This allows for the same level of hiding power, but with less TiO_2.[11,12]

It is highly desirable to reduce the amount of TiO_2 in coatings formulations as its use is problematic from both an economic and environmental standpoint. It is generally the most expensive component of a white coating, in part due to mine closures and tightening environmental regulations involved in its production.[13] From an environmental perspective, the production of rutile and anatase TiO_2 (largely in South America and Africa) leads to destruction and loss of habitat,[14] creation of hazardous waste products such as sulfuric acid (which are now more heavily regulated than a few decades ago),[8] and has a substantial carbon footprint, with 5.2 t of CO_2 produced for every 1 t of TiO_2.[15]

By incorporating air voids into dry polymer films, it is also possible to attain light scattering (although nowhere near as strong as that of TiO_2). Nevertheless, it allows for a reduction in the amount of TiO_2 required in a white coating. Coatings containing air-voided particles may also find uses in thermally and acoustically insulating films,[16,17] as well as reduced transportation costs due to the lower density of the hollow particles. Low density coatings may also be desirable for aviation

purposes, where the weight of the paint can contribute a considerable amount towards the amount of fuel required.

Several hollow particulate/pore forming technologies exist to mitigate the use of TiO_2 in coatings by acting as light scattering centers. The most commercially successful hollow polymer opacifiers are the ROPAQUE brand, which comprise hollow polymer spheres containing an air void usually between 0.2 - 1.0+ µm in diameter (**Figure 1.2**).

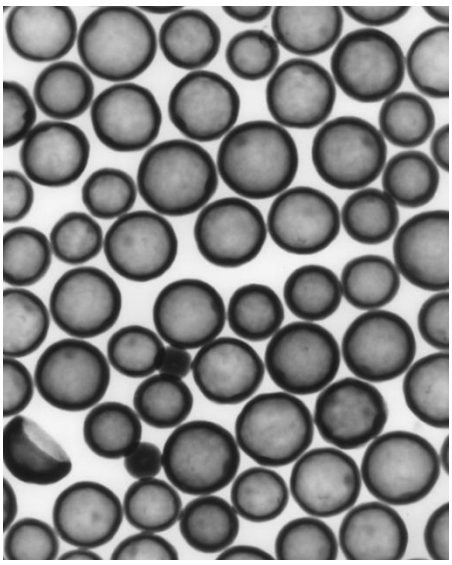

Figure 1.2. Hollow polymer latex particles of around 1 µm in diameter, with a 50% air void by volume, are used as opacity modifiers in white decorative coatings. Image from reference.[18]

ROPAQUE is typically made by the dynamic swelling of a soft-hard core-shell (alternative notation is core@shell) latex particle. An example synthesis of a hollow polymer particle would entail emulsion polymerization of a seed comprised of butyl acrylate (BA):methyl methacrylate (MMA):methacrylic acid (MAA) in a

weight ratio of 0.52:0.47:0.01. This seed is then used in a sequential emulsion polymerization which forms a shell around the core, comprising MMA:MAA:ethylene glycol diacrylate (EGDA) in a weight ratio of 0.7:0.29:0.01. The core-shell latex is then heated to above the glass transition temperature, T_g, of the outer shell and a base such as ammonia is added.

The latter can freely travel through the outer shell into the core by means of hydrophilic MAA channels across the shell. This neutralizes the charge on the acid groups in the core and causes the particles to swell with water. These swollen particles are then cooled below the T_g of the outer polymer shell, preventing volume contraction, which traps the particle with a water filled void that evaporates upon film drying to give an air void.[19] It is this air void that can then act as a light scattering center.

It has been noted that following evaporation of the water from inside the hollow polymer particles, collapse of the particle structure is possible due to the formation of a vacuum, which renders the pigment less effective at scattering light.[20] An example of this phenomenon can be seen in the bottom left of the TEM image above (**Figure 1.2**). A potential solution to this issue could be to use particles with porous shells, such as silicon dioxide or phase separated polymers for example. This should lower the pressure differential experienced across the shell upon drying.

Another synthetic route for obtaining hollow polymer particles was outlined by Kasai and co-workers. The synthetic procedure is similar to that used in the production of ROPAQUE but it does have a few salient differences. Essentially they start with an emulsion polymerization of styrene latex in the presence of a chain transfer agent to shorten the length of the polymer chains. A mixture of

MMA/divinylbenzene (DVB) is then fed into the reaction, which causes the styrene seed to swell with monomer. Polymerization yields a hollow particle so long as the DVB ratio is kept < 40% wt. with respect to MMA. DVB cross-links the outer shell of the swollen particle, which prevents it from contracting. Following polymerization one is then left with a hollow inside the particle.[21]

Galembeck *et al.* observed that non-crystalline aluminium phosphate particles undergo a morphological transformation (aggregation) upon film formation, whereby closed pores are formed within the particles. This results in opacification of the film.[22,23] Whilst being very effective opacity modifiers, this method leads to large fractures in the film on the order of tens of microns, reminiscent of a film above the CPVC wherein film integrity is compromised.

If we look to nature for inspiration on generating opacity then the *Cyphochilus* beetle is one of the best examples (**Figure 1.3 A**).[24,25] What is most striking about the structure of the beetle's shell is its exceptional brilliant whiteness at only 5 µm thickness. This is much thinner than a decorative coating used to the same end (40-70 µm). A network of randomly orientated aperiodic air voids with an average diameter of 250 nm is responsible for this dramatic opacity (**Figure 1.3 B** and **C**).

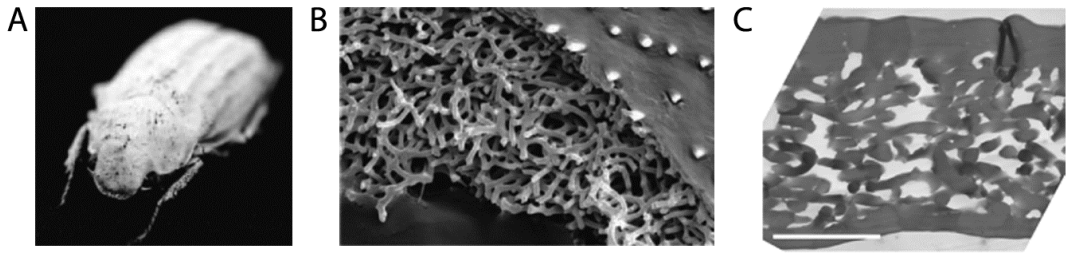

Figure 1.3. (**A**) Digital photograph of the *Cyphochilus* beetle (**B**) Scanning electron microscope (SEM) image of the *Cyphochilus*' white shell, showing a random network of cuticular filaments (**C**) TEM image of a transverse section of the 5 µm thick shell, scale bar = 3 µm. Image **A** and **B** adapted from reference,[26] image **C** adapted from reference.[24]

From this we can deduce that neither monodisperse nor symmetric structures are necessarily prerequisites for efficient hiding power. Indeed, disordered structures are actually preferable for the scattering of light.[26]

A popular method for synthesizing hollow particles in the literature is a process known as sacrificial templating.[27] Essentially one starts with a colloidal template that is then coated with a "shell" of another material, to give a core-shell particle. We shall refer to this as a nanocomposite throughout the remainder of this chapter and use the notation core@shell. The core is then selectively removed through either physical or chemical means to yield a hollow particle (**Figure 1.4**).

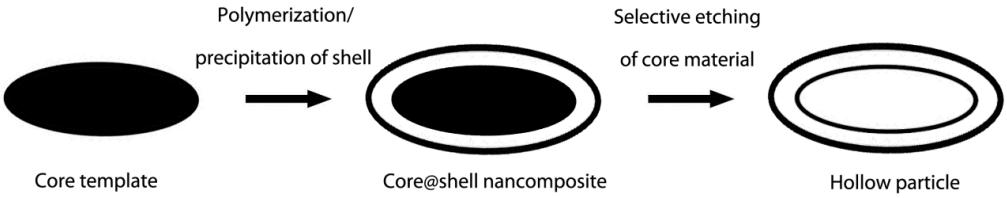

Figure 1.4. Schematic of the synthetic procedure known as "sacrificial templating". Coating of a colloidal core with a shell via polymerization of an organic or inorganic monomer forms a core-shell structure. Selective removal of the core via physical or chemical means furnishes a hollow particle.

This method is very powerful as it allows one to precisely tune the geometry of the air void from the beginning. Advances in colloidal synthesis have opened up a diverse range of colloidal materials with a plethora of geometries.[28,29] Furthermore, it is possible to use a variety of materials to form the shell. Commonly used materials include SiO_2,[30] metal oxides[31] and polymers.[32]

It is possible to scale the reaction up to generate large quantities of material for testing as opacity modifiers, assuming one has enough of the template material available. For these reasons we decided to use sacrificial templating to form hollow particles that could potentially be used as opacity modifiers.

Some colloidal templates might require prior surface modification to either disperse them in the reaction medium used in the coating step, or to facilitate interactions between the condensing shell material and the colloids surface. One of the best examples of this is the work of van Blaaderen and co-workers who adsorb poly(vinyl pyrrolidone) (PVP) onto the surface of various colloids including gibbsite, gold and polystyrene, in order to disperse them in a basic alcohol/water

medium for subsequent coating with a SiO_2 shell by the hydrolysis and condensation of TEOS.[33]

It has been shown before that acicular, or needle-like, pigment morphologies can confer enhanced opacity to paint films over spherical pigments.[34] Despite numerous theoretical simulations of light scattering by uniform non-spherical air voids,[35] there are very few (if any) experimental studies of monodisperse non-spherical air voids as light scattering entities in coatings.

We decided to investigate the use of non-spherical hollow particles as opacity modifiers in decorative coatings to see if they displayed an improvement over hollow spherical ROPAQUE particles.

We started by using Cu_2O particles as a template because of the excellent control one can achieve over particle shape and dispersity.[36] This could allow for a structure-activity relationship investigation with regards to the influence of air void geometry on the scattering coefficient of the particle. Lou and co-workers utilized Cu_2O nanocubes to generate hollow iron oxide nanoboxes by a redox etching method with $FeCl_3$.[37]

For the same reasons we also looked at using Fe_2O_3 colloids for sacrificial templating. One of the advantages of this system over Cu_2O is that the synthesis can be conducted to give a much larger quantity of template particles.[38] Many groups have prepared hollow polymer[39] and SiO_2 particles[40] based around Fe_2O_3 templates. The solids content is often kept low during the coating step however due to the orthokinetic flocculation of particles, caused by their large Hamaker constants. This means that there is a very large van der Waals attractive force between particles, leading to the formation of aggregates during the coating stage.[41]

Finally, we use $CaCO_3$ as a template to generate hollow SiO_2 particles. Investigations with these hollow particles form the bulk of the work in this chapter for the reason that $CaCO_3$ can be coated under concentrated conditions, it is cheap, widely available and is already used in the coatings industry extensively as extenders.[42] The latter minimize potential reductions in the opacity of TiO_2 particles at high loading, caused by an effect known as optical crowding.[43] There are several theories on why this phenomenon occurs. Some believe the reduction in opacity is due to the fact that pigments interface is decreased, leading to a reduction in multiple scattering events of photons. Others believe that there is an overlap in the scattering cross-section of multiple particles in close proximity, leading to a deviation away from the optimum particle size for light scattering. Extenders also serve to enhance hiding power and brightness, as well as scrub resistance.

The refractive index of $CaCO_3$ (n ~ 1.64-1.67)[44] is only slightly different to that of the binder (n ~ 1.48-1.60), giving it a refractive index difference of ~ dn = 0.04-0.19. This small difference in refractive index makes it quite ineffective at scattering light. By introducing an air void in its place one obtains a refractive index difference of between 0.48-0.60, which would substantially improve the light scattering per unit volume, reduce coating density (and hence transport costs) and still perform the same morphological role as SOCAL P3 i.e. as extender for TiO_2 particles.

Wen *et al.* make hollow SiO_2 particles templated around $CaCO_3$ by a sodium silicate (water-glass) method, although they do not demonstrate any control over the shell morphology or show any applications of the material.[45]

Wang and co-workers use a similar method to generate core-shell particles and their hollow analogues, although there appears to be significant secondary

nucleation, and not all of the $CaCO_3$ appears to have been removed following an acid etch.[46]

Note that all template materials used (Cu_2O, Fe_2O_3, $CaCO_3$) can be removed by acid etch, after coating with an acid-resistant shell, to give hollow particles.

We decided to use SiO_2 as our shell material (in order to generate hollow SiO_2 particles) for several reasons.

First, SiO_2 has larger pores than ROPAQUE, and so this might mitigate the problem experienced by ROPAQUE wherein a vacuum is pulled inside the particle upon drying; leading to air void collapse.

Second, SiO_2 is resistant to most acids (not HF!) and so will remain behind following an acid etch of the core template.

Third, SiO_2 is negatively charged at the coating pH~9, and so it is electrostatically stabilized.

Finally, the refractive index of SiO_2 is 1.45, meaning that it has a similar refractive index to the film-forming latex binder. Therefore, if there is any improvement in light scattering over the $CaCO_3$ template, we can reasonably attribute this improvement to the inclusion of air voids and not just the presence of the SiO_2 shells themselves. This will allow us to conclude whether SOCAL P3 as a template has a suitable morphology for the equivalent air void to scatter light.

If we wanted to generate opacity from the shell as well then we could use TiO_2 which, although we are trying to remove from the coating, would be present in a much smaller mass fraction than a non-voided TiO_2 particle.

A seeded Stöber synthesis[47] was used to coat the template particles with a SiO_2 shell. In this synthesis one typically uses a reaction medium of alcohol/water and a basic or acidic catalyst to facilitate the hydrolysis and condensation of an organic SiO_2 precursor e.g. tetraethylorthosilicate (TEOS). This species forms dimers, oligomers and then polymers. These precipitate out of solution and onto the surface of the seed particle. The mechanism by which this occurs is outlined in **Figure 1.5**.

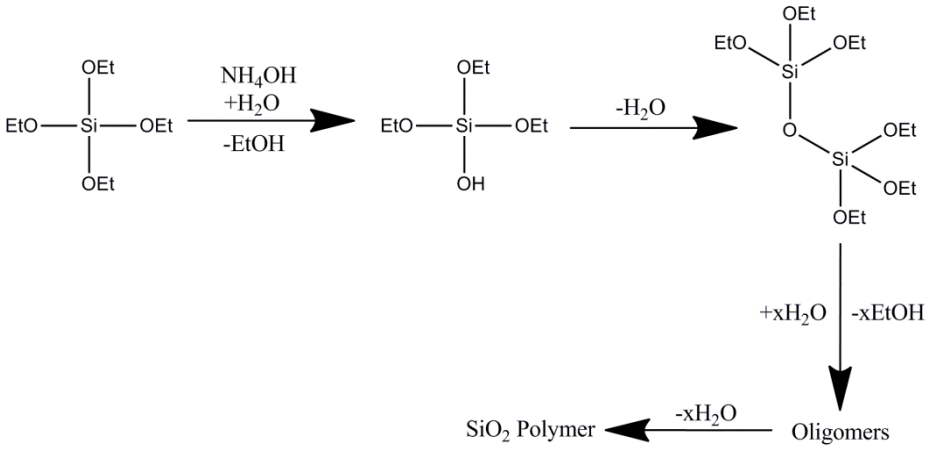

Figure 1.5. Hydrolysis of TEOS in the presence of water, catalyzed by a base (NH_4OH). This is followed by condensation reactions to form oligomers and eventually a polymeric SiO_2 network.

Shell formation will only occur if there are favorable interactions between the SiO_2 species and the template surface.

Secondary nucleation of the SiO_2 particles also needs to be suppressed by keeping the concentration of the SiO_2 precursor in the reaction medium low enough to prevent homogenous nucleation and growth. Furthermore, the surface area of template needs to be sufficiently high to capture the condensing SiO_2 species before they can homonucleate.

It is also plausible to make this synthesis of hollow SiO_2 particles into an environmentally friendly process as TEOS (the precursor which is used to make the shell) can be made from $SiCl_4$. The latter being a waste product of the photovoltaic industry, the disposal of which is currently an environmental concern.[48]

Herein, we investigate hollow SiO_2 particles with non-spherical geometries as opacity modifiers in dry polymer films. Our aim is to improve upon the light scattering efficiency of the commercially available opacity modifier, ROPAQUE (a hollow spherical polymer latex). Ultimately, the goal is to mitigate the amount of TiO_2 required to achieve a desired level of opacity in the film. The desire to reduce the amount of TiO_2 stems from adverse economic and environmental implications associated with its use.

1.2 Results and Discussion

1.2.1 Synthesis of Cu_2O and Fe_2O_3 colloidal templates, coating with SiO_2 and generation of hollow SiO_2 particles by acid etching of the core template

Initially we looked at using Cu_2O and Fe_2O_3 as templates in the synthesis of anisotropic hollow SiO_2 particles. That is, following coating with SiO_2 and acid etch of the template. We chose these templates as they would give us a synthetic route to non-spherical hollow SiO_2 particles with good control over size/shape dispersity. Inclusion of these particles into a dry film should provide visible opacity due to light scattering from air voids inside the particle following the evaporation of water.

1.2.1.1 Synthesis of cubic, octahedral, and multi-faceted Cu_2O particles. Coating of Cu_2O cubes with SiO_2 and acid etch to form hollow SiO_2 cubes

Cuprous oxide particles with tunable geometries were synthesized by the procedure outlined by Kuo and Huang.[49] The best way to describe the synthesis conditions is with the aid of a diagram from their paper (**Figure 1.6**).

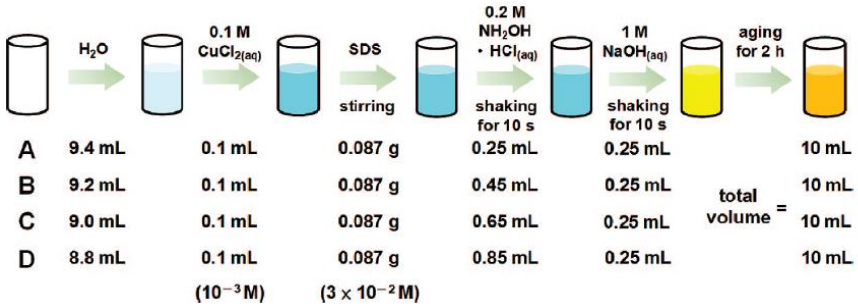

Figure 1.6. Schematic of the synthetic procedure outlined by Kuo and Huang to generate polyhedral Cu_2O particles. Image from reference[49]

Where **A** forms cubic particles, **B** - cuboctahedral, **C** - truncated octahedral, **D** - octahedral. For more detailed synthesis conditions please refer to experimental **Section 1.4.3**.

The reason that the particles are monodisperse is that there is a very rapid nucleation time, followed by a separated growth stage. These conditions are a prerequisite for the formation of monodisperse particles as rapid nucleation ensures that all the particles are growing at a similar rate.[50]

Different morphologies are obtained by adding varying concentrations of hydroxylamine. This can be rationalized from a thermodynamic point of view in that

certain molecules adsorb with different energies on different crystal faces. This causes retarded growth in some directions and comparatively rapid growth in others, which alters the shape of the particles. In this case hydroxylamine regulates growth along the [100] and [111] crystal faces.

We decided to synthesize cubic and octahedral Cu_2O particles, with the aim of coating them with a shell of SiO_2 via a seeded Stöber process. Following this, HCl would be used to remove the solid template - reforming the starting compound, $CuCl_2$, and water. A hollow SiO_2 cube or octahedron would remain that could be investigated as an opacity modifier in dry polymer films.

SEM images of the Cu_2O particles synthesized are shown in **Figure 1.7**. It is clear that the synthetic procedure yields monodisperse and well-defined templates.

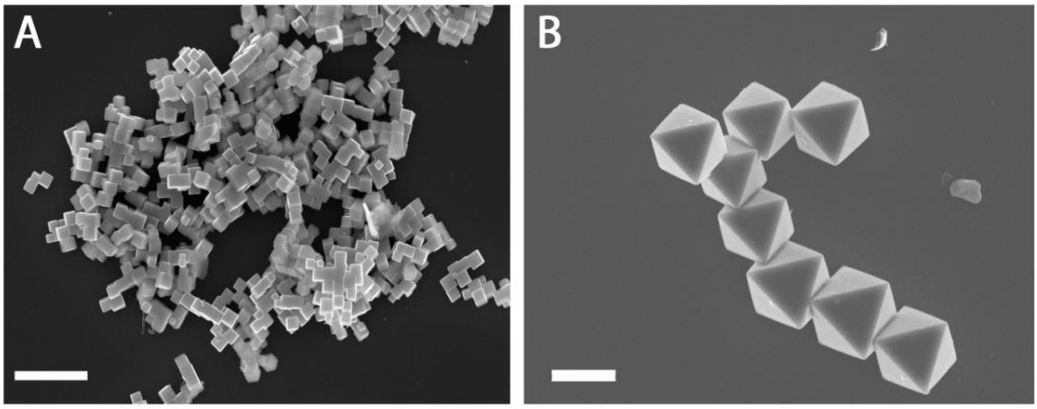

Figure 1.7. SEM image of Cu_2O particles with (**A**) cubic morphology and (**B**) octahedral morphology. Scale bar = 2 µm.

We also found that complex multifaceted Cu_2O particles could be formed by incorporating negatively charged PS-DVB-AA copolymer latex as directing agent, in combination with $NH_2OH.HCl$ (**Figure 1.8**). For more information please refer to

experimental **Section 1.4.4**. Further characterization of the latex particles is also given in **Appendix II.1**. Interesting morphologies of other metal oxides have been noted after the addition of latex particles during precipitation.[51]

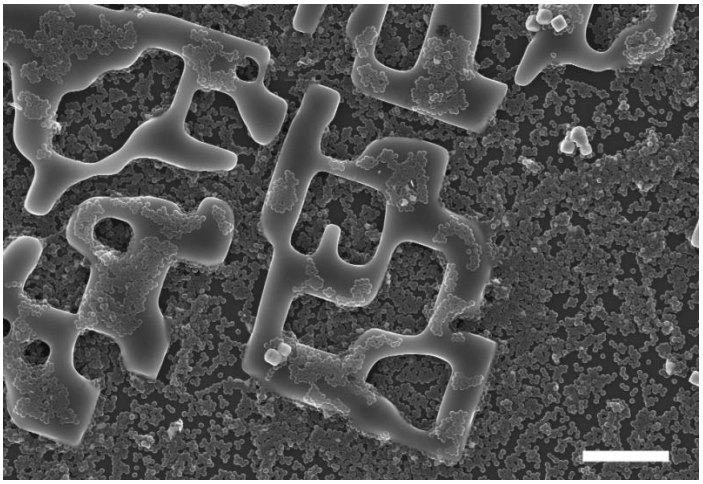

Figure 1.8. Growth of Cu_2O particles in the presence of PS-DVB-AA latex particles leads to the formation of complex multifaceted particle morphologies. Scale bar = 4 μm.

Whilst this colloid-directed crystal growth is interesting in its own right, these particles would be too large to act as a pigment in a waterborne coating. We therefore decided to focus on the feasibility of forming hollow SiO_2 cubes from the template shown in **Figure 1.7 A** as these particles have dimensions approximating that of the optimal spherical air void for light scattering (~280 nm).[52]

As mentioned before, people have used Cu_2O particles as a template in sacrificial templating or redox etching but to the best of our knowledge, no-one has generated hollow SiO_2 particles from them as shown in the TEM image (**Figure 1.9**).

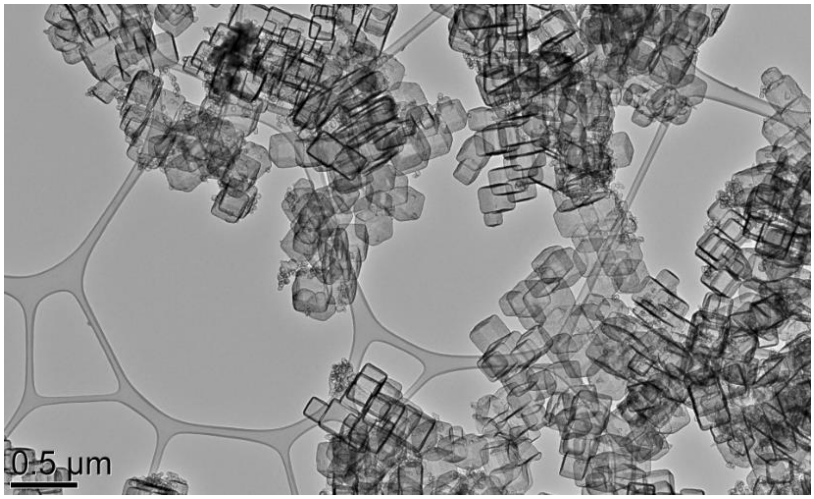

Figure 1.9. TEM image of hollow SiO_2 cubes formed by coating Cu_2O cubes with SiO_2 and then removing the core with HCl. Scale bar = 500 nm.

For more details on the synthesis conditions used in the formation of these hollow SiO_2 particles please refer to experimental **Section 1.4.3**.

In order to assess the effectiveness of the particles as opacifying pigment by the in-house test method used at our sponsors (AkzoNobel), 50 mL of waterborne coating is required at the very least. 100 mL is ideal - to allow for possible user error in the drawdown process of the films.

Thus in order to produce a coating of 30% PVC with a low volume solids content of 20%, one would require at least 3 cm^3 of particles. Given that Cu_2O has a density of ~ 6.32 $g \cdot cm^{-3}$ (0.16 $cm^3 \cdot g^{-1}$) then one would need to coat and hollow 18.8 g of template material. Despite efforts to concentrate the reaction, which were successful based upon exact increases of scale based upon the original synthesis, this was realistically unattainable (1L reaction medium yielded <1 g). Note that it may be possible to achieve higher yields with a continuous flow reactor.

1.2.2.2 Synthesis of Fe_2O_3 pseudocubes, prolate spheroids and ellipsoids. Coating of Fe_2O_3 ellipsoids with SiO_2 and acid etch to form hollow SiO_2 ellipsoids

Due to limitations in the amount of Cu_2O template we could produce, we were forced to pick another template that could be synthesized in larger quantities.

Hydrothermal synthesis of Fe_2O_3 seemed to be the perfect alternative as we could synthesize large quantities of colloidal template (> 10 g), whilst tuning the size and shape of the template by adding different amounts of Na_2SO_4 that acts as a crystal face directing agent (**Figure 1.10**). By increasing the concentration of sodium sulphate present in the reaction it was possible to tune the particle morphology from pseudocubic, through spheroidal, to ellipsoidal. In all syntheses control was maintained over particle size dispersity. Image analysis of 100 particles provided us with a statistical description of particle dimensions, which are reported in **Table 1.3**.

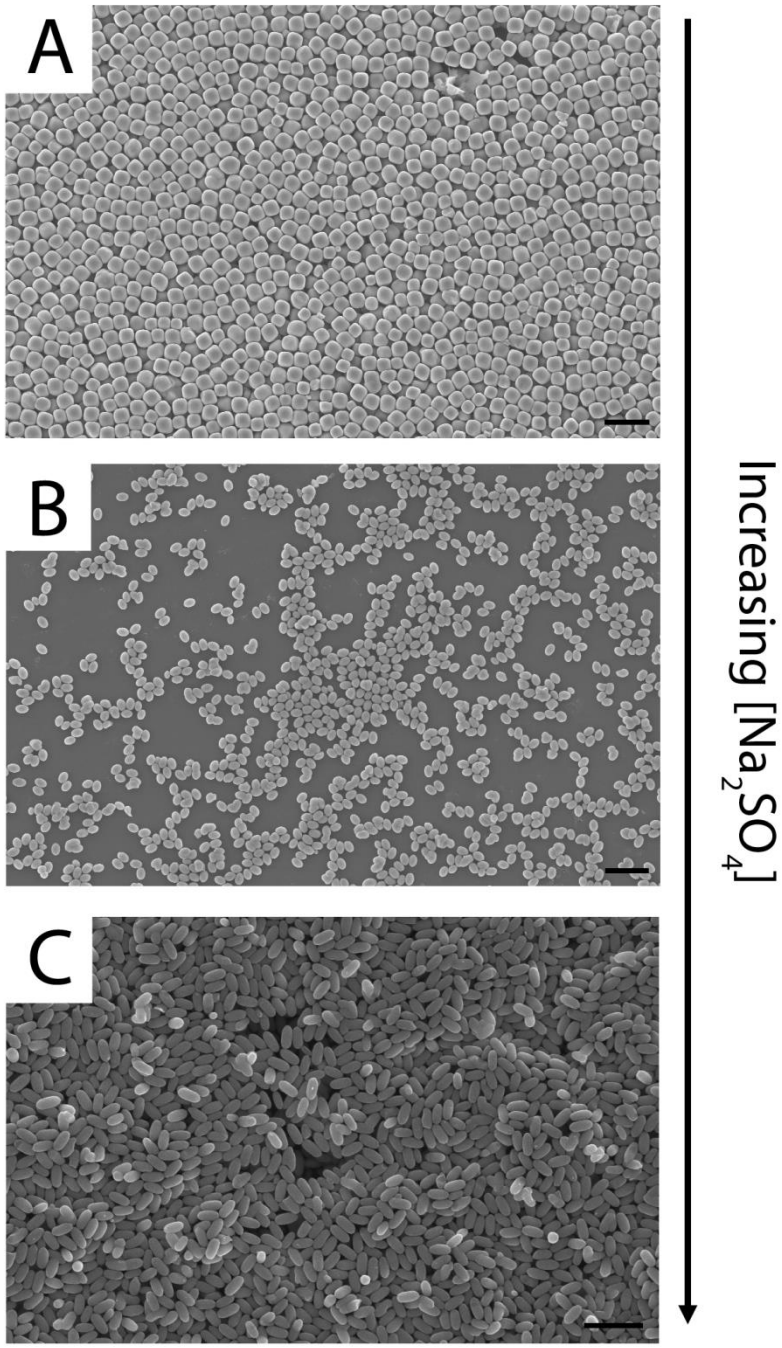

Figure 1.10. SEM images of Fe_2O_3 particles with (**A**) pseudocubic, (**B**) prolate spheroidal and (**C**) ellipsoidal morphologies. Scale bar = 4 μm.

Table 1.3. Dimensions of particles shown in **Figure 1.10** as a function of [Na_2SO_4]. Results were obtained by image analysis of 100 particles.

[Na_2SO_4] (M)	**Morphology**	**Long axis (nm)**	**Short axis (nm)**	**Aspect ratio**
0	Pseudocubic	1361 ± 124	n/a	1
1×10^{-2}	Prolate spheroid	1043 ± 67	743 ± 39	1.41 ± 0.06
3×10^{-2}	Ellipsoid	686 ± 94	318 ± 40	2.16 ± 0.17

Laser diffraction measurements (Mie scattering) were used to determine volume average equivalent spherical particle diameters for the three Fe_2O_3 templates in order to corroborate the image analysis measurements in **Table 1.3**. The volume-weighted size distribution for the three particles is shown in **Figure 1.11**. What this shows is the frequency of particles that produce a light scattering pattern generated by a sphere of equivalent volume. We decided to quote the volume-weighted average for this sample as the particles appear monodisperse from image analysis (**Figure 1.10**), and so all particles will be given an equally weighted intensity. Tabulated statistical descriptors for the data are also given in **Table 1.4**. Briefly, d(0.1) refers to the equivalent spherical particle diameter that 10% of the population is smaller than, d(0.5) 50% of the population etc. Optical properties used in the experiment are given in experimental **Table 1.22**. Uniformity is also defined in **Appendix I.3**, **Equation I.2**.

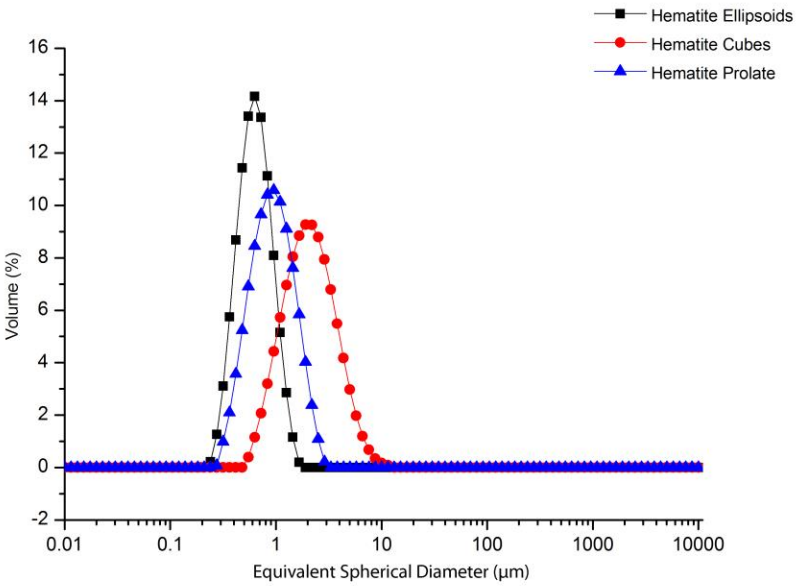

Figure 1.11. Laser diffraction size frequency plot for Fe_2O_3 ellipsoids, pseudocubes and prolate spheroidal particles shown in **Figure 1.10**. The plot shows the frequency of particles that produce a light scattering pattern which is the same as the diameter of a sphere with equivalent volume.

Table 1.4. Tabulated statistics describing the size distribution plots shown in **Figure 1.11** for the three Fe_2O_3 templates.

Material	Vol. weighted mean (µm)	d(0.1) (µm)	d(0.5) (µm)	d(0.9) (µm)	Uniformity	Weighted residual (%)
Fe_2O_3 ellipsoids	0.62	0.36	0.58	0.94	0.31	2.71
Fe_2O_3 pseduocubic	1.60	0.74	1.42	2.70	0.43	2.83
Fe_2O_3 prolate spheroid	1.08	0.46	0.85	1.58	0.57	1.72

The volume weighted mean of each template is in good agreement with the size measured by image analysis except for the cubes, which are slightly larger in the light scattering measurements than the image analysis. It must be borne in mind that the numbers quoted in **Table 1.3** are characteristic lengths of the particles i.e. more accurate descriptors than those measured by light scattering in **Table 1.4**, which is the diameter of a sphere with equivalent volume to the particle.

Coating of the Fe_2O_3 particles with SiO_2 and removal of the core with HCl will generate hollow SiO_2 particles. We decided to investigate coating PVP-stabilized Fe_2O_3 ellipsoids first as these were the more appropriate size of the three templates in terms of light scattering in the visible part of the spectrum. Also, these particles had the highest aspect ratio, and so represented the largest deviation from the well-studied case of the hollow sphere.

Whilst it was easy to make these particles on > 10 g scale, it is a recognized problem that coating of primary hematite particles in solution with SiO_2 is difficult.

This is due to the large attractive van der Waals forces between the Fe_2O_3 particles in solution, which causes the particles to form aggregates that are themselves coated.[53]

Usually to avoid this problem people coat the particles in very dilute suspensions.[41,54] However, it has been shown that ultrasound can be effective at coating slightly more concentrated dispersions.[55]

We decided to investigate the SiO_2 coating of concentrated Fe_2O_3-PVP dispersions in ethanol/water/NH_4OH media both with and without the aid of ultrasound during the coating step.

Before coating the hematite particles it is important to determine their surface area so that one can deduce a suitable volume and feed rate of SiO_2 precursor. If the feed rate is too high then secondary nucleation of SiO_2 particles will occur. If it is too low then there is a risk of SiO_2 bridging, whereby SiO_2 shells condense with another over time, fusing particles together. This would have a detrimental effect on the dispersion of the pigment and, ultimately, the opacity. It must be borne in mind however that one needs to add enough TEOS to ensure that a sufficiently thick shell is grown.

Analysis of the BET surface area was carried out by nitrogen porosimetry. The transform plot and linear fit of which can be seen in **Figure 1.12**. For an in-depth discussion of the theory behind the BET model please refer to **Appendix I.4.2**.

One can see that the C value is within the range of $0 < C < 300$ accepted by the model, which indicates that the material is suitable for analysis by BET. Furthermore, the correlation coefficient is suitably close to unity. The surface area of the particles was determined to be 65.40 ± 0.13 $m^2 \cdot g^{-1}$.

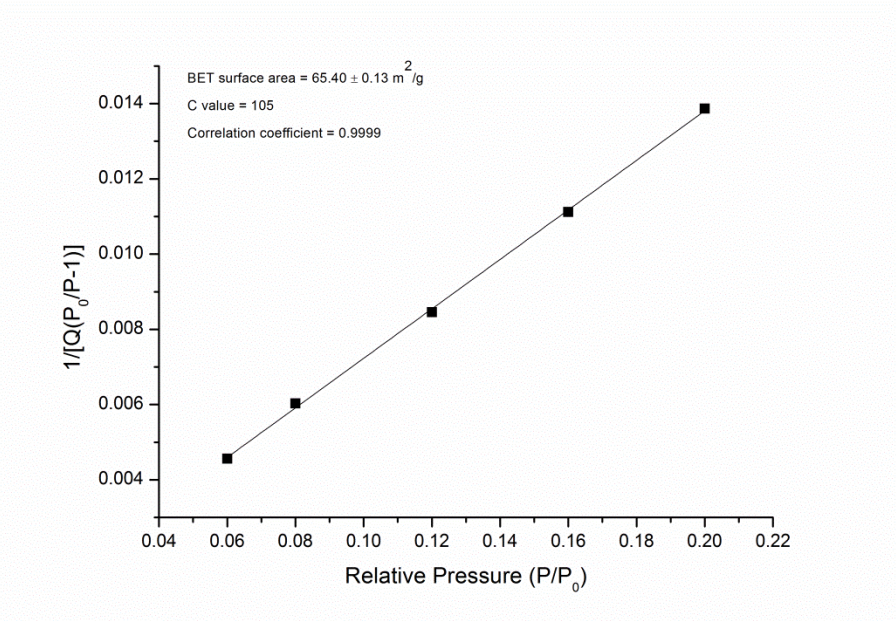

Figure 1.12. BET transform plot of Fe_2O_3 ellipsoids obtained by nitrogen porosimetry measurements of the quantity of gas adsorbed as a function of relative pressure.

Our sol-gel reaction parameters consisted of Fe_2O_3-PVP ellipsoids (2 g, 13.8 m^2) dispersed in ethanol (100 mL), water (3 mL), and NH_4OH (2 mL). A solution of TEOS in ethanol (2 mL/2 mL) was added to the solution in 0.5 mL batches every 30 minutes over 4 hours, at which time the reaction was quenched by centrifugation and redispersal into deionized water over three cycles. Addition of TEOS/ethanol to the solution was either conducted under stirring or under ultrasonic dispersion. For more details the reader is referred to experimental **Section 1.4.6**.

Laser diffraction measurements were conducted on the Fe_2O_3@SiO_2 nanocomposite particles in order to deduce whether any aggregates had formed (as one would expect if the particles had undergone orthokinetic flocculation during the coating process).

It was clear from laser diffraction measurements that when stirring alone was the dispersion force during coating, aggregates were formed (**Figure 1.13 A**). The increase in particle size to several microns (from under a micron) indicates that coated aggregates have been formed.

However, when ultrasonic agitation was applied during the coating procedure perfectly dispersed Fe_2O_3@SiO_2 particles were formed (**Figure 1.13 B**); as evidenced by retention of particle size distribution. Note that the shell is very thin, hence there is no appreciable increase in size. Proof of silica coating is given later via EDAX and TEM measurements.

Statistical descriptors from the analysis are given in **Appendix II.2**, **Table II.2**. Optical properties used in the experiment are given in the experimental section, **Table 1.22**.

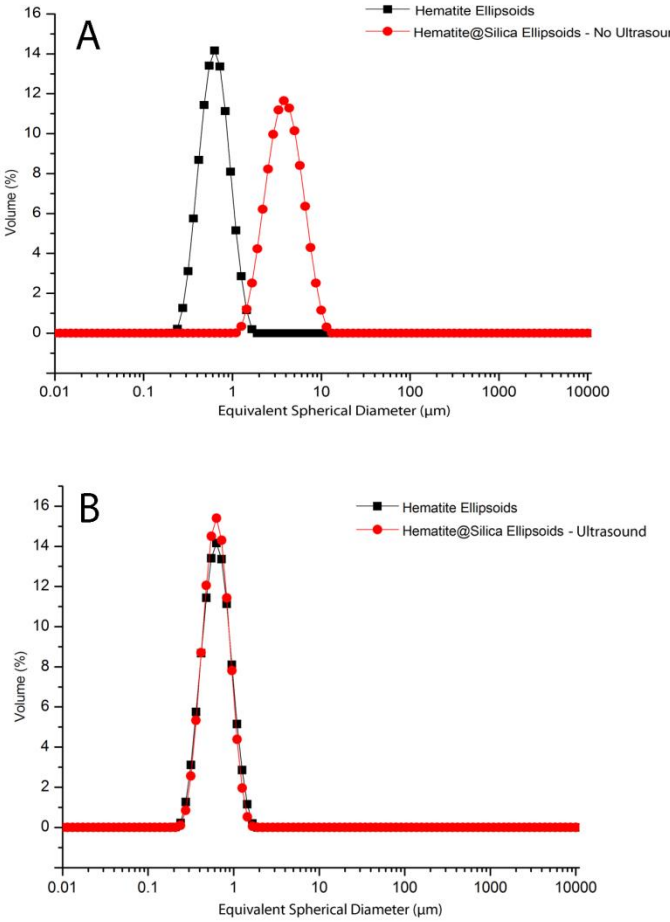

Figure 1.13. Particle size distributions obtained by light scattering measurements comparing the Fe_2O_3 ellipsoid template and the nanocomposite following sol-gel coating with SiO_2. Reaction conditions were (**A**) without ultrasound - stirring only during coating and (**B**) with ultrasound agitation during coating.

SEM imaging of the two samples also indicates that in the absence of ultrasound the nanocomposite particles tend to cluster together during coating (**Figure 1.14 A**), whereas the particles that had been coated under ultrasound maintain monomodal size distribution, packing individually into colloidal crystals (**Figure 1.14 B**) that display opalescence (see **Appendix II.2**, **Figure II.2**).

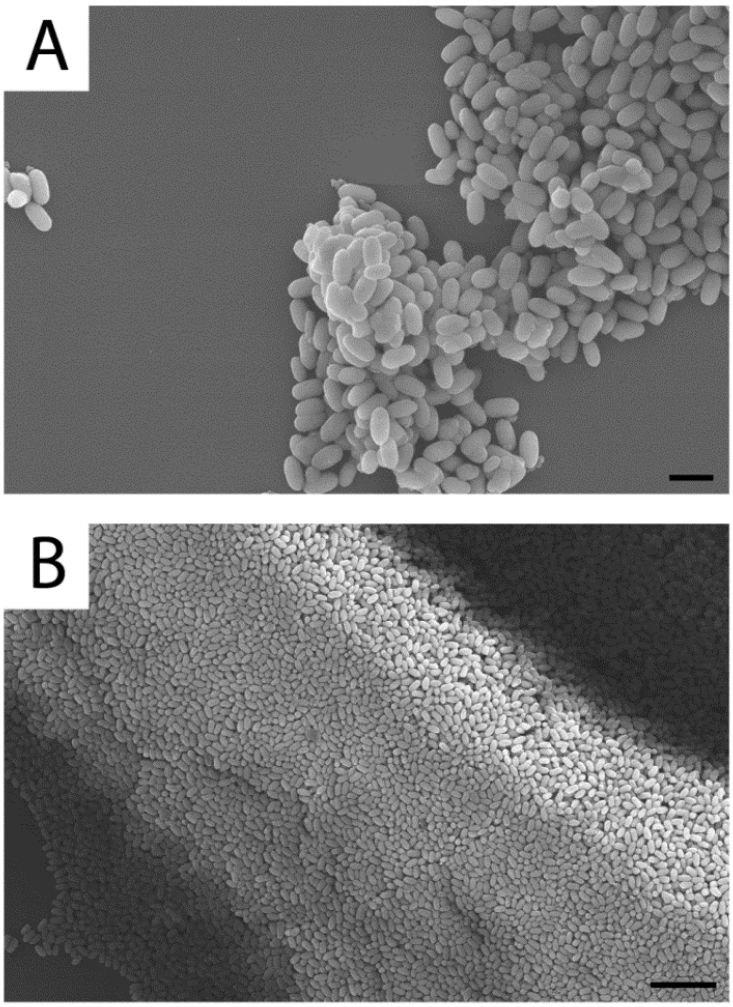

Figure 1.14. SEM images of the two Fe_2O_3@SiO_2 samples prepared under (**A**) stirring during TEOS feed, scale bar = 1 µm. (**B**) Ultrasonication during TEOS feed, scale bar = 4 µm.

EDAX analysis was used to confirm that both of the Fe_2O_3 samples had in fact been coated with SiO_2. **Figure 1.15 A** shows the EDAX spectra for the nanocomposite that had been coated under stirring and **Figure 1.15 B** shows the particles that had been coated under ultrasound conditions. In both cases we can see that SiO_2 is present.

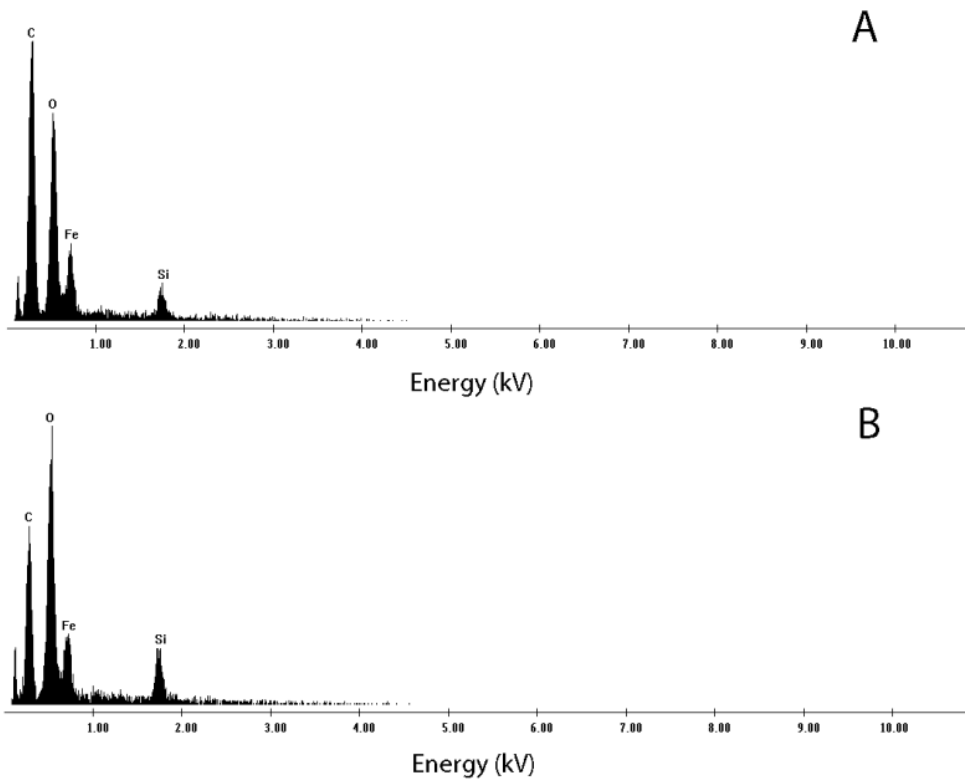

Figure 1.15. EDAX spectra of the Fe_2O_3@SiO_2 nanocomposites at the end of the reaction (**A**) with stirring and (**B**) with ultrasound.

Following coating of the particles with SiO_2, HCl was used to remove the Fe_2O_3 core to reform the starting salt ($2FeCl_3$) and water. Analysis of the particles with TEM showed the core to be fully removed and no SiO_2 bridging between particles (**Figure 1.16**). We believe that this is the most concentrated example of Fe_2O_3 coating with SiO_2 that has been conducted (20 $g \cdot L^{-1}$, 1300 $m^2 \cdot L^{-1}$) to successfully yield exclusively primary particles with intact SiO_2 shells.

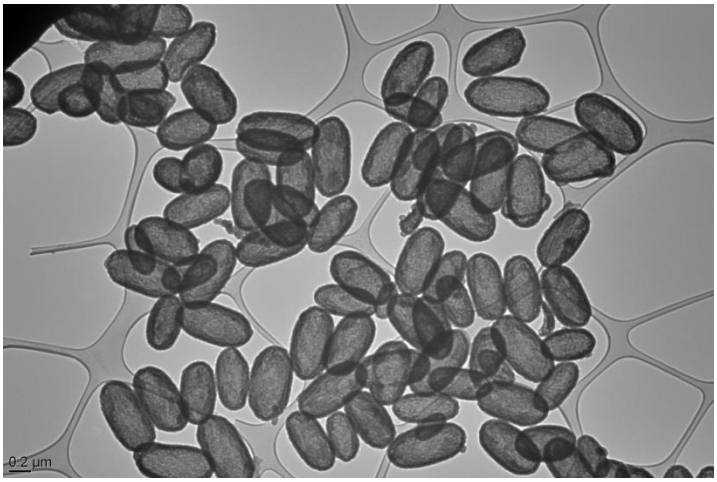

Figure 1.16. TEM image of hollow SiO_2 ellipsoids synthesize by a sacrificial templating of Fe_2O_3 particles. Scale bar = 200 nm.

The density of the Fe_2O_3 ellipsoids was measured via helium pycnometry, which gave a value of 4.37 $g \cdot cm^{-3}$ (0.23 $cm^3 \cdot g^{-1}$). Thus in order to generate our desired minimum of $3cm^3$ hollow air void for the coating we would need to coat 13.04 g of hematite template. Despite our advances in the synthesis of large quantities of monodisperse hollow SiO_2 ellipsoids from Fe_2O_3 we found that maintaining monomodal particle size distribution of the core-shell particles at larger reaction volumes was not possible with ultrasonic agitation as some portions of the dispersion medium were not being subjected to intense ultrasonic waves. For this reason it was unfeasible to generate hollow SiO_2 pigments for testing by this method as well. Note that it may be possible to enhance colloidal stability further with the use of sterically bulky, highly charged, polymeric surfactants that can also favourably interact with the condensing SiO_2.

1.2.2 Synthesis and characterization of hollow SiO_2 particles templated on SOCAL P3

1.2.2.1 Characterization of the SOCAL P3 template

It became apparent that it was not possible to generate a large enough volume of hollow SiO_2 particles for pigment testing by using either Cu_2O or Fe_2O_3 as the template. Thus we decided to investigate the plausibility of introducing air voids into some of the components already present in decorative coatings.

We chose the inorganic filler SOCAL P3[42] as a template (a grade of precipitated calcium carbonate, scalenohedral) as it is cheap, widely available and its morphology confers a number of benefits to the coating that should be possible to retain with the hollow analogues, particularly the minimization of optical crowding and improved scrub resistance.

SOCAL P3 has a mixture of particulate morphologies, as can be seen from the SEM and TEM images of the material (**Figure 1.17**). Two predominant categories can be defined however; "cigar-shaped" spheroids of around 1μm in length and a few hundred nanometers in width and smaller polyhedral particles of a few hundred nanometers in characteristic length. This means that as a template it is also of a suitable size to scatter light in the visible part of the spectrum.

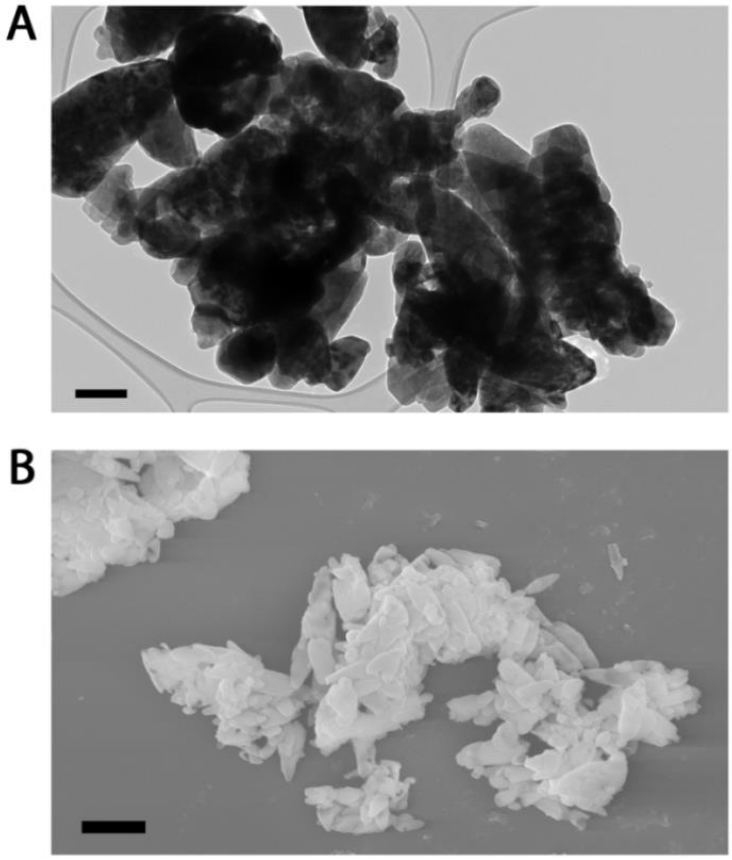

Figure 1.17. (**A**) TEM image of SOCAL P3, scale bar = 200 nm. (**B**) SEM image of SOCAL P3, scale bar = 1 µm.

If we look at the nitrogen adsorption isotherm of volume of gas adsorbed ($cm^3 \cdot g^{-1}$) as a function of the relative pressure, P/P_0, it is clear that SOCAL P3 displays a type II isotherm, which indicates that the material is essentially non-porous (**Figure 1.18**). The flat region at low-mid relative pressure corresponds to monolayer gas formation, whereas the sharp increase at higher pressure shows the gas condensing into a liquid on the surface. There is hardly any increase in the gradient of the curve between the relative pressure range of 0-0.2, which indicates that there are hardly any observable micropores (1-2 nm). A small degree of hysteresis in the high relative pressure range (0.7-1.0) indicates that there are some

macropores. For a more detailed discussion on the theory behind nitrogen porosimetry please refer to **Appendix I.4**.

The lack of pores is also reflected in the total pore volume measurements, with SOCAL P3 having a very low pore volume of only 0.03 $cm^3 \cdot g^{-1}$.

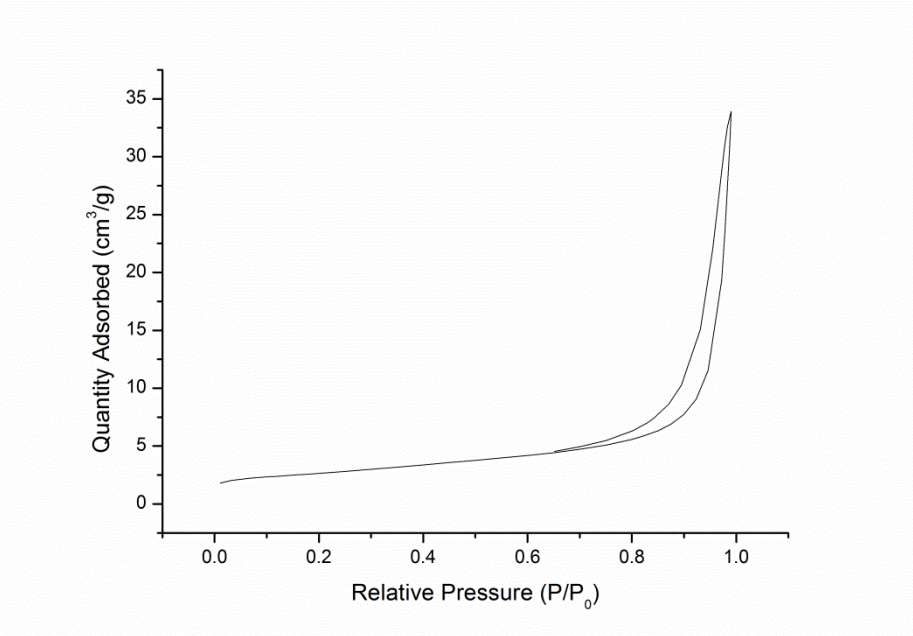

Figure 1.18. Nitrogen adsorption isotherm of SOCAL P3 shows that it has a type II isotherm, meaning that it is essentially non-porous.

SOCAL P3 has a relatively low BET surface area of only 8.92 ± 0.05 $m^2 \cdot g^{-1}$ (**Figure 1.19**) and so a relatively slow feed rate of shell precursor will be required to prevent secondary nucleation.

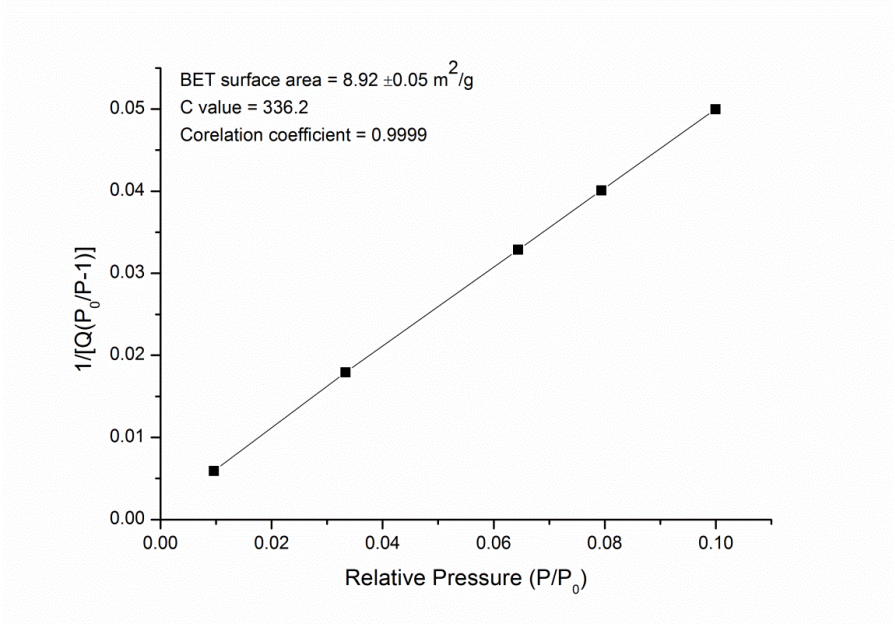

Figure 1.19. BET transform plot of SOCAL P3 with linear regression fit.

1.2.2.2 Synthesis and characterization of the SOCAL P3@SiO_2 nanocomposite and its hollow analogue

Now that we have characterized the $CaCO_3$ template we will be using, we are ready to coat the particles with a shell of SiO_2. As mentioned earlier we will be using a seeded Stöber synthesis where the $CaCO_3$ is the seed.

A general synthesis would involve SOCAL P3 (stabilized with physisorbed PVP-K30 at 10% wt.) dispersed in an ethanol:water medium of between 90:10 and 40:60 by vol. (higher ethanol content = faster reaction). Into this is added concentrated NH_4OH (18.10 M) at around 2-18% wt. depending on the rate of reaction/shell thickness required (higher catalyst = faster reaction). TEOS (either 1:1 or 2:1 wt. ratio with respect to $CaCO_3$) is then fed in by syringe pump at RT over the course of between 5-24 hours depending on the extent of reaction that one desires (although longer reactions may lead to aggregation of particles by interparticle cross-

linking). Particles are purified by centrifugation and redispersal into water several times (see experimental **Section 1.4.7**/**1.4.8** for more details). A drip feed of acid (either hydrochloric or acetic) at a concentration of between 0.5-2.0 M and purification by further centrifugation then yields hollow SiO_2 particles.

Following coating of the SOCAL P3 particles with SiO_2 and removal of the core with a drip feed of hydrochloric acid, laser diffraction experiments (Mie scattering) were performed to measure particle size and more importantly, check for the presence of aggregates following the SiO_2 coating and acid etch steps.

The result of the analysis on the SOCAL P3 core, nanocomposite and hollow SiO_2 particles can be seen in the size distribution plotted in **Figure 1.20**, with some of the pertinent statistics given in the **Table 1.5**.

As our sample is highly polydisperse we did not want to heavily weight the larger particles within the sample and so we opted for a number average weighting where each particle is given an equal intensity irrespective of its size.

Information regarding the optical properties used in the analysis can be found in the experimental **Table 1.22**.

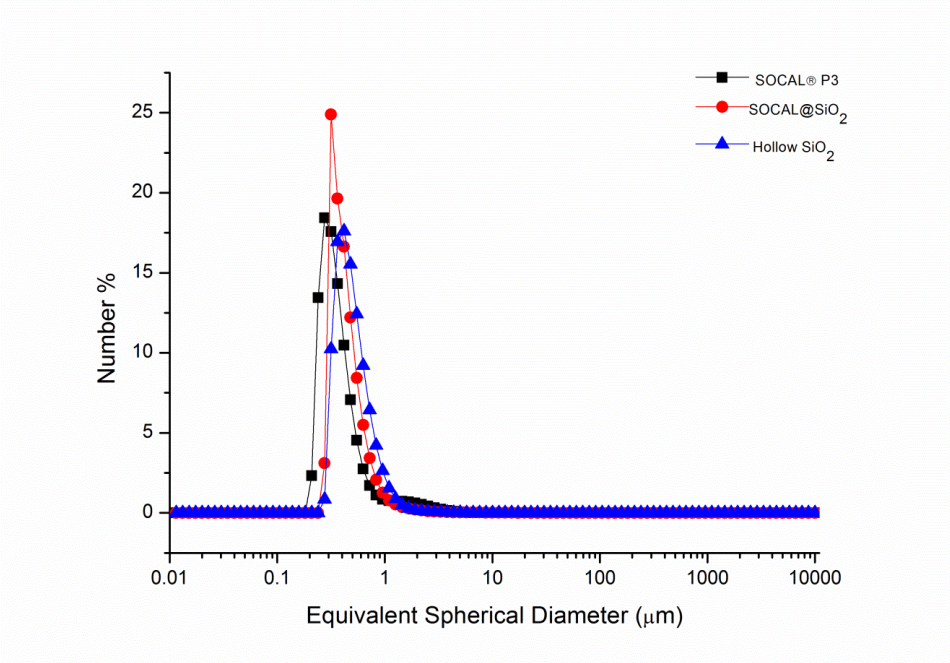

Figure 1.20. Particle size frequency distribution as determined by laser diffraction measurements for SOCAL P3 template, nanocomposite and hollow SiO_2. Size is given as equivalent spherical diameter (number average).

Table 1.5. Tabulated statistical descriptors of the laser diffraction data plotted in **Figure 1.20**.

Material	**d(0.1) (µm)**	**d(0.5) (µm)**	**d(0.9) (µm)**	**Uniformity**
SOCAL P3	0.23	0.31	0.60	0.53
SOCAL P3@SiO_2	0.29	0.37	0.62	0.37
Hollow SiO_2	0.31	0.43	0.74	0.34

It can be seen that the d(0.5) of SOCAL P3 is about 300 nm, which is near the optimal 280 nm often quoted as being the optimal diameter of a spherical air void for scattering white light.[52]

Slowly dropping in 2 M hydrochloric acid to the nanocomposite particles (**Figure 1.21 A/B**) dissolved the $CaCO_3$ template away, leaving behind the hollow SiO_2 particles to be used as pigment - as evidenced by TEM (**Figure 1.21 C/D**).

Secondary nucleation of SiO_2 particles was not evident from SEM image analysis, indicating that the feed rate was not so fast as to cause homonucleation of SiO_2 species in solution (**Figure 1.21 B**). The resulting SiO_2 shell thickness was calculated from 100 measurements of TEM micrographs to be 23.9 ± 2.2 nm.

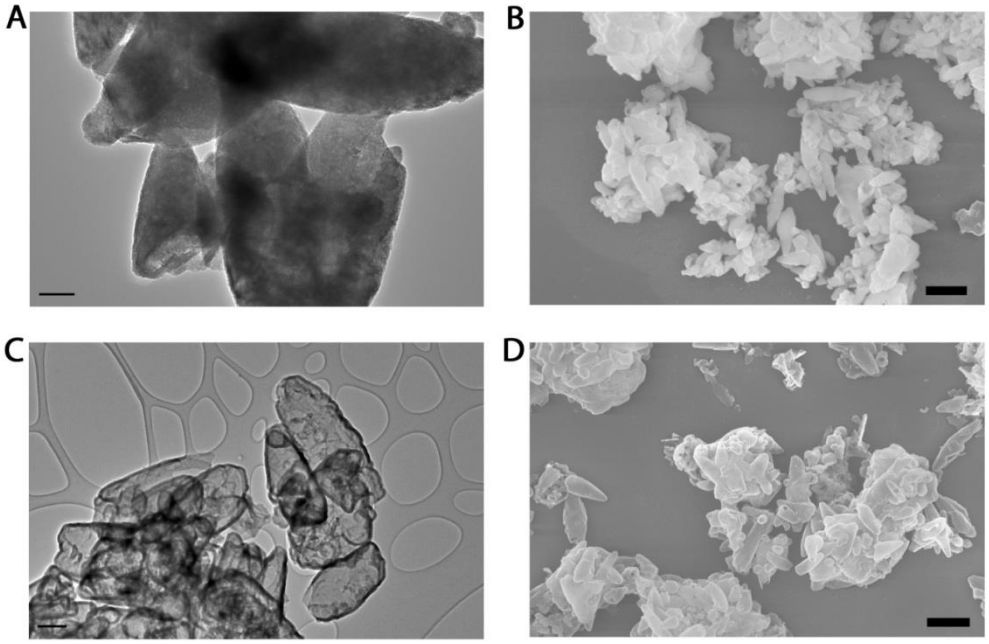

Figure 1.21. (**A**) TEM image of $CaCO_3$@SiO_2 nanocomposite, scale bar = 100 nm. (**B**) SEM image of $CaCO_3$@SiO_2 nanocomposite, scale bar = 1 µm. (**C**) TEM image of hollow SiO_2 particles following acid etch of the $CaCO_3$@SiO_2 nanocomposite, scale bar = 2 µm. (**D**) SEM image of hollow SiO_2 particles, scale bar = 1 µm.

EDAX measurements were taken for each sample at an accelerating voltage of 5 kV to give an appropriate depth of scattering, with a sample to detector

scattering angle of 35°. It can be seen that the $CaCO_3$ template (**Figure 1.22 A**) has been coated with a layer of SiO_2 (**Figure 1.22 B**). Following treatment of the particles with HCl, which dissolves the $CaCO_3$ template, the particles were cleaned and analyzed via EDAX to ensure all of the core had been dissolved (**Figure 1.22 C**). Tabulated results of the exact proportions of the elements are not given as these would be semi-quantitative at best due to the rough nature of the surface and the complexities involved with electron scattering of randomly oriented core-shell particles. Nevertheless, the qualitative assessment of the presence of each element is valid.

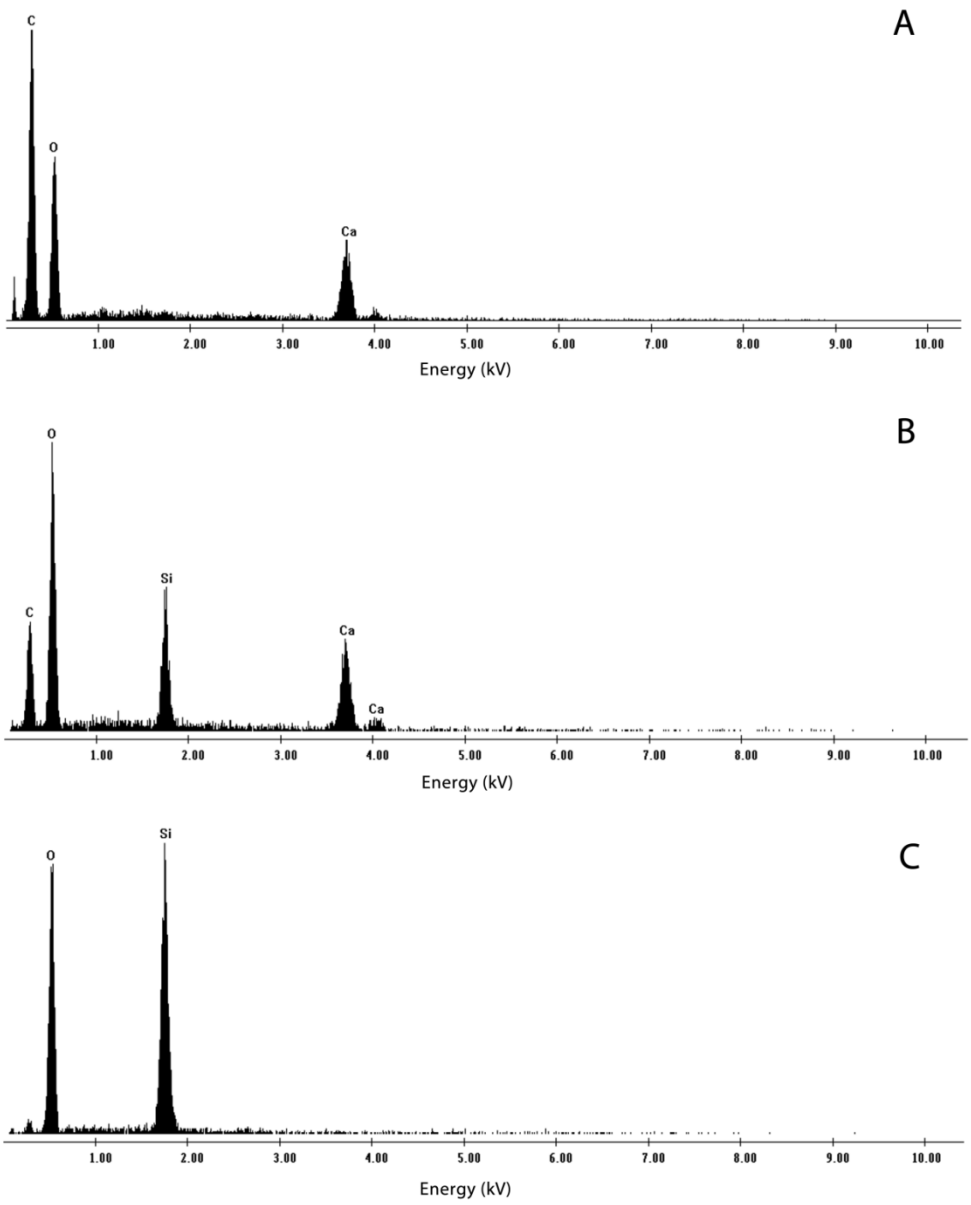

Figure 1.22. Comparison of the EDAX patterns for (**A**) $CaCO_3$ (SOCAL P3), (**B**) $CaCO_3$@SiO_2 nanocomposite and (**C**) hollow SiO_2 obtained through acid etch of **B**.

High resolution transmission electron microscopy (HR-TEM) was used to image the pore structure of the hollow SiO_2 particles obtained (**Figure 1.23**). It is clear from these images that there are only micropores present (< 2 nm), with no observable mesopores (2-50 nm). The material also appears to have quite a low pore

volume as well, something we shall investigate in more detail later via nitrogen porosimetry.

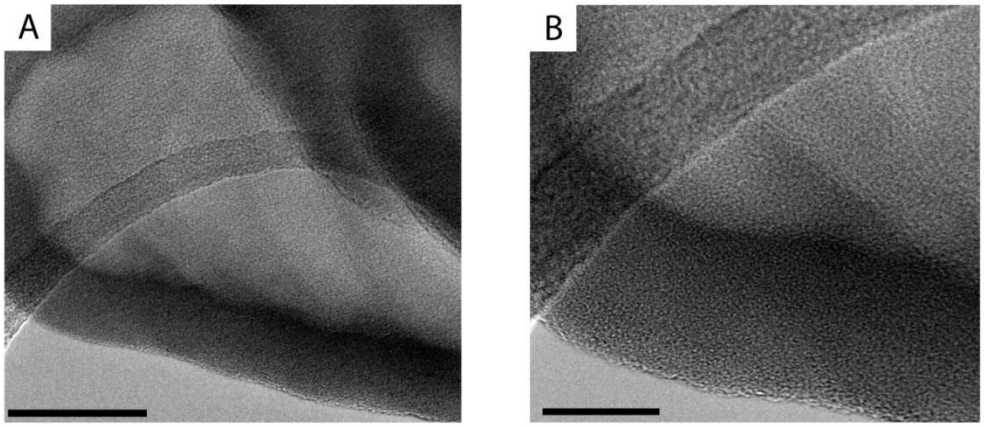

Figure 1.23. HR-TEM images at two different magnifications of the hollow SiO_2 particles shown in **Figure 1.21 C**. Scale bar (**A**) = 50 nm, (**B**) = 20 nm.

The nitrogen adsorption isotherm of the hollow SiO_2 particles is given in **Figure 1.24**.

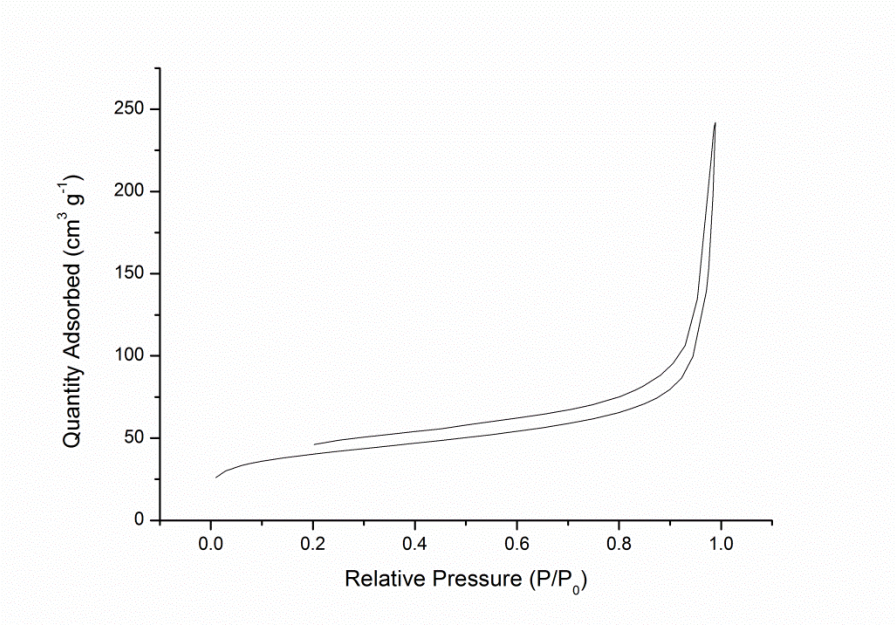

Figure 1.24. Nitrogen adsorption isotherm of 1st generation hollow SiO_2 particles. The lower curve represents the adsorption part of the isotherm, whereas the higher curve represents the desorption branch.

The small initial increase in the gradient of the adsorption branch is due to capillary condensation of nitrogen in the small population of micropores, reinforcing the results from HR-TEM in **Figure 1.23**. The hysteresis present between the adsorption and desorption branch is likely due to the presence of macropores inside the particles as there are clearly no mesopores present. Hysteresis in this region is due to a difference in the rate of condensation and evaporation from the interior cavity. Deviations in pore size cause differential rates of condenstation and evaportation. Similar results have been obtained by others who have conducted nitrogen porosimetry on hollow SiO_2 nanoparticles.[56] It must be mentioned that the isotherm on the desorption branch should close at a relative pressure of 0.6-0.8, as the only pores still filled will be the micropores that are relatively monomodal in characteristic dimension i.e. 1-5 nm. The fact that it does not is indicative of the

equilibration time not being long enough (see **Appendix I.4**). Several runs were conducted with increasing equilibration times however no improvement was noted. There is a trade off as well because increasing the equilibration time also increases the analysis time dramatically, which leads to a fall in the level of cryogen that also affects the analysis (note that it is not possible to top the level up during analysis).

Figure 1.25 shows the low pressure region of the adsorption branch for the hollow SiO_2 particles, with a linear fit of the points following micropore filling as required by the t-plot method. The salient data from the analysis is given in **Table 1.6**. For a full discussion on the theory the reader is referred to **Appendix I.4.3**.

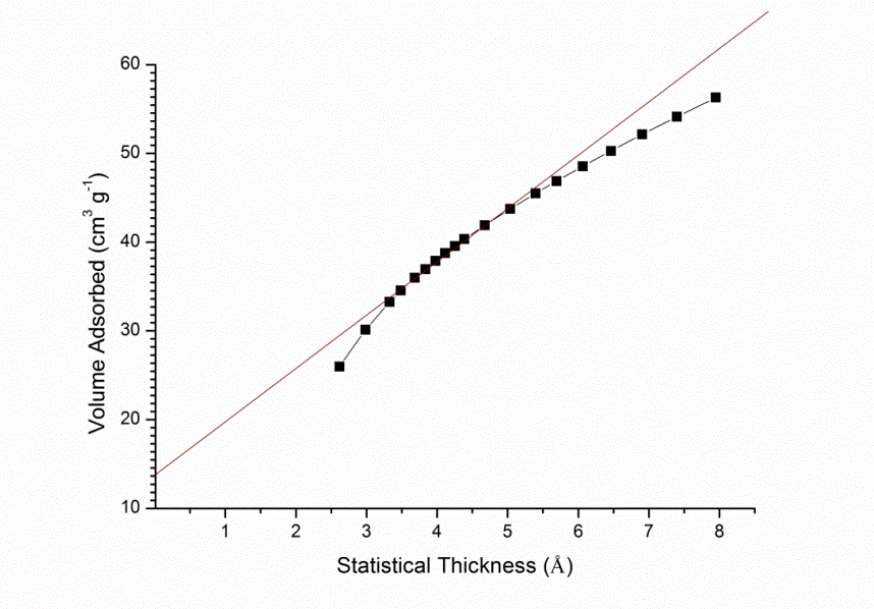

Figure 1.25. V_A-t plot with fit for the hollow SiO_2 particles required for the calculation of micropore volume, micropore area, and external surface area.

Table 1.6. Tabulated data obtained from the V_A-t plot shown in **Figure 1.25** for the hollow SiO_2 particles.

Micropore Volume ($cm^3 \cdot g^{-1}$)	**Micropore Area ($m^2 \cdot g^{-1}$)**	**External Surface Area ($m^2 \cdot g^{-1}$)**	**Correlation Coefficient**
21.73×10^{-3}	49.22	92.57	0.999

The results presented in **Table 1.6** confirm the notion that the pore volume in the shell is very low.

1.2.2.3 Calculating the effective particle density of the hollow SiO_2 particles (1^{ST} generation)

The quantity of pigment in a coating is usually expressed on a volume basis as the pigment volume concentration (PVC), see **Equation 1.3**. Thus in order to be able to compare the light scattering power of our hollow SiO_2 particles with the original SOCAL P3 template and ROPAQUE we need to know the effective particle density of each sample i.e. taking into account the hollow nature of the SiO_2 and ROPAQUE particles.

First though it might be useful to define some of the relevant types of density that can be reported:

- Bulk density is the measure of dry sample mass over the total volume occupied by the powder i.e. interstitial spaces, open/closed pore volume and

solid volume. Of course this will depend on how the particles pack and is usually reported as poured or tapped densities.

- Skeletal density is the mass of the particle divided by the volume occupied by the solid material i.e. it takes the pore and interstitial volumes to be freespace.
- Effective particle density is the mass of the particles divided by its volume, including open and closed pores. This is the density we will use for converting pigment mass into pigment volume for our hollow particles.

Skeletal density was measured by helium pycnometry for the SOCAL P3 ($CaCO_3$) template, SOCAL P3@SiO_2 nanocomposite, and hollow SiO_2 particles (1st generation) (**Table 1.7**). Note that the hollow particles are termed "1st generation" as we later investigated a "2nd generation" of hollow particles with thicker silica shells.

Table 1.7. Skeletal density as determined by helium pycnometry for the SOCAL P3 template, SOCAL P3@SiO_2 nanocomposite, and hollow SiO_2 particles (1st generation).

Material	**Mass (g)**	**Volume Displaced (cm^3)**	**Skeletal Density ($g \cdot cm^{-3}$)**
SOCAL P3	0.8750	0.3133	2.7929
SOCAL P3@SiO_2	0.7841	0.3104	2.5265
Hollow SiO_2 (1st generation)	0.1342	0.0628	2.1381

It can be seen from **Table 1.7** that the skeletal density of SOCAL P3 is 2.7929 $g \cdot cm^{-3}$ and so there is (1/2.7929) = 0.358 $cm^3 \cdot g^{-1}$ of solid material. We could

quote the effective particle density by incorporating the pore volume in this calculation but we will omit this for three reasons. First of all we do not know how many pores are surface pores that are filled in by binder upon film formation. Second, the pore volume is negligible ~ 0.03 $cm^3 \cdot g^{-1}$. Third, industrial formulations do not account for this in their density values. Therefore if we wish to compare results later on, it is best to keep the pigment density as that of the skeletal density quoted above, which is also close to that of the manufacturer specification (2.71 $g \cdot cm^{-3}$).

It is very important to get the value of the effective particle density for the hollow particles correct. A small error in effective particle density can lead to quite a large variation in the number of particles and hence the total volume of air voids.

In order to calculate the effective particle density of the hollow particles we used **Equation 1.4**.

$$d_{eff\ SiO_2} = \left(\frac{m_{SiO_2}}{\left(\frac{m_{SOCAL\ P3}}{d_{SOCAL\ P3}}\right) + \left(\frac{m_{SiO_2}}{d_{SiO_2}}\right)} \right) \qquad \textbf{(1.4)}$$

Where m_{SiO_2} = mass of SiO_2/g nanocomposite, $m_{SOCAL\ P3}$ = mass of SOCAL P3/g nanocomposite, $d_{SOCAL\ P3}$ = skeletal density of SOCAL P3, d_{SiO_2} = skeletal density of SiO_2.

Essentially we take the mass of SiO_2 shell per gram of nanocomposite and divide it by the total volume occupied by both the core and the shell, making the assumption that there is negligible volume contraction upon removal of the core.

In order to deduce the amount of SiO_2 per gram of nanocomposite we can use TGA. When $CaCO_3$ is heated to around 600-750°C under N_2 it loses CO_2, leaving behind CaO (**Equation 1.5**).

$$CaCO_3 \rightarrow CaO + CO_2 \quad (\mathbf{1.5})$$

With Ca = 40.08 amu, C = 12.01 amu, and O = 16.00 amu. Therefore there should be 56.1% of the sample mass retained as CaO after heating to remove CO_2.

If we compare the final mass of the nanocomposite particles with SOCAL P3 then any difference will give us the percentage mass of SiO_2 shell in the nanocomposite.

The TGA plot of SOCAL P3 and the nanocomposite can be seen in **Figure 1.26**. The mass of SOCAL P3 following heating to 1000°C is 55.97%, which is in good agreement with the theoretical mass outlined above. The resulting mass of the SOCAL P3@SiO_2 particles was 63.38%, giving a percentage mass of SiO_2 shell equivalent to 7.41%.

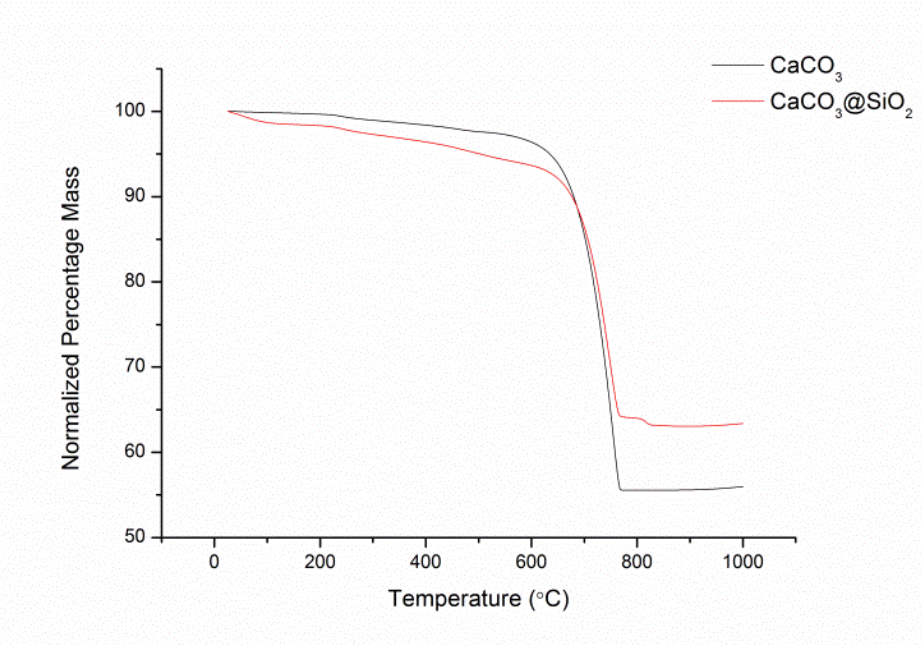

Figure 1.26. TGA plot of $CaCO_3$ and $CaCO_3@SiO_2$ from 25-1000°C. A heating rate of 10°C min^{-1} was used under a N_2 atmosphere.

Note that there is a difference in water content between the two samples although it is difficult to distinguish when the onset of CO_2 begins and water evaporation ends. Therefore we have avoided correcting for water content as it would most likely introduce more errors than it would correct for.

The difference in mass between the two samples is 7.41%, or in other words, for every gram of nanocomposite material there is 0.9258g SOCAL P3 and 0.0741g of SiO_2. We can now work out the volume of these two components from their skeletal densities given in **Table 1.7** (ignoring the pore contribution which as we have deduced is negligible for the $CaCO_3$ template and, as we shall see from subsequent analyses, is also negligible for the SiO_2 shell).

SOCAL P3 = 0.9258 g / 2.7929 g·cm^{-3} = 0.3315 cm^3

SiO_2 shell = 0.0741 g / 2.1381 g·cm^{-3} = 0.0347 cm^3

This gives a total volume of nancomposite per gram = 0.3662 cm^3. Now we can divide the mass of SiO_2 per gram by the total volume of the particle per gram to give an effective particle density of 0.2026 g·cm^{-3}.

1.2.3 Opacity testing of SOCAL P3 and hollow SiO_2 templated around SOCAL P3 (1st generation, thin shell SiO_2)

Waterborne coatings containing SOCAL P3 and hollow SiO_2 particles (1st generation, thin shell) as pigments were formulated to have a PVC of 30% and total volume solids ~ 17%. It must be noted that both PVC and volume solids for the hollow particles are highly dependent on the air voids within the particles remaining intact. Should any particles collapse then both the PVC and volume solids will decrease.

The formulation details for the two coatings can be found in experimental **Section 1.4.9**, in **Table 1.27** and

Table 1.28 respectively. Some of the key formulation parameters are given in

Table 1.8 and

Table 1.9.

.

Table 1.8. Key formulation parameters for waterborne coating with SOCAL P3 particles as pigment.

	Mass solids (%)	**Mass fraction pigment (%)**	**Vol. solids (%)**	**PVC (%)**
Theoretical	26.6	13.7	18.2	29.4
Experimental (TGA)	26.6	14.7	16.1	32.7

Table 1.9. Key formulation parameters for waterborne coating with hollow SiO_2 particles (1st generation, thin shell) as pigment. [a] Note that these values only hold true when all of the particles are intact, which as we shall is not the case. Corrected values are given later.

	Mass solids (%)	**Mass fraction pigment (%)**	**Vol. solids (%)[a]**	**PVC (%)[a]**
Theoretical	15.8	1.2	18.2	29.3
Experimental (TGA)	14.7	1.3	20.1	32.2

TGA was performed on the coatings (**Figure 1.27**) to experimentally verify the total mass of solids and mass fraction of pigment with respect to solid content. From these values, one can calculate an experimental PVC (**Equation 1.6**) and volume solids (**Equation 1.7**). These values are reported in

Table 1.8 and **Table 1.9**

Table 1.9for the respective coatings. Note that water evaporation from the pan was corrected for by taking the initial sample mass as being 100%.

$$PVC = \frac{\frac{m_{pigment}}{d_{pigment}}}{\left[\left(\frac{m_{pigment}}{d_{pigment}}\right) + \left(\frac{\left(m_{solids} - m_{pigment}\right)}{d_{binder}}\right)\right]} \quad \textbf{(1.6)}$$

Where $m_{pigment}$ = mass of pigment per gram of coating, $d_{pigment}$ = effective particle density of pigment, m_{solids} = total mass of solids per gram of coating, d_{binder} = skeletal density of dry polymer film.

$$VS = \left(\frac{\left(m_{solids} - m_{pigment}\right)}{d_{binder}}\right) + \left(\frac{m_{pigment}}{d_{pigment}}\right) \quad \textbf{(1.7)}$$

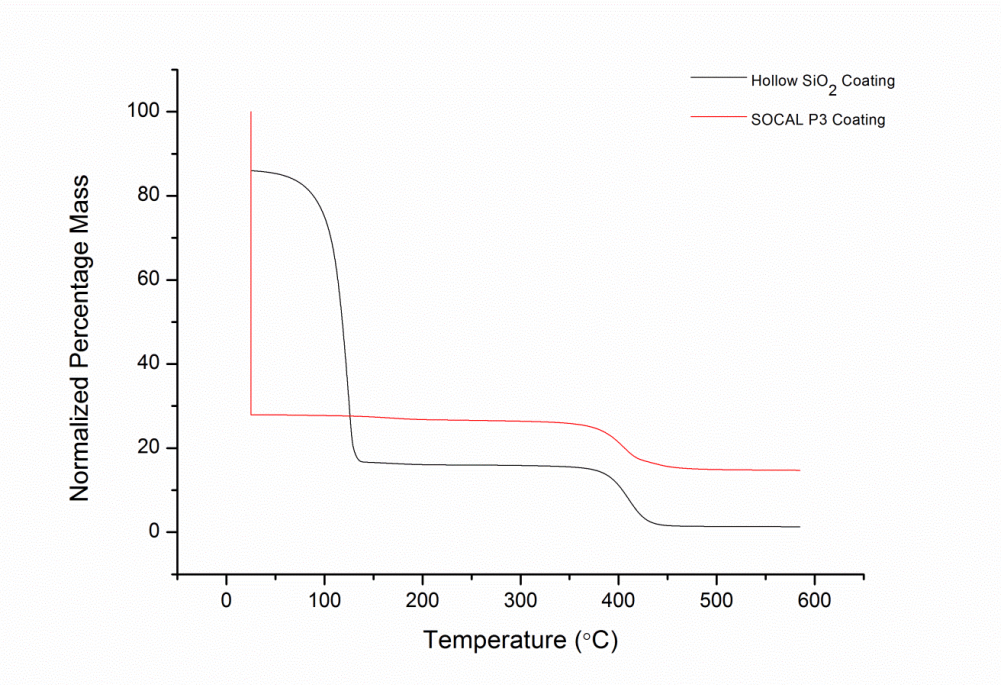

Figure 1.27. TGA plots of the two formulations with SOCAL P3 and hollow SiO_2 (1^{st} generation) as pigments. Sample mass was normalized and recorded between 25-580°C. Heating was at a rate of 10°C $min^{-1}$and the atmosphere was air.

Optical microscopy was conducted on the coatings to confirm that the pigment dispersants used were effective. **Figure 1.28 A** is an optical microscope image of the SOCAL P3 coating whilst it is drying. It can be seen that there are no aggregates larger than a few microns in diameter, which would indicate that the particles are reasonably well dispersed. Similarly the hollow SiO_2 particles (**Figure 1.28 B)** seem reasonably well dispersed, with no aggregates larger than a few microns present. Note that the line running across the image is the drying front of the coating.

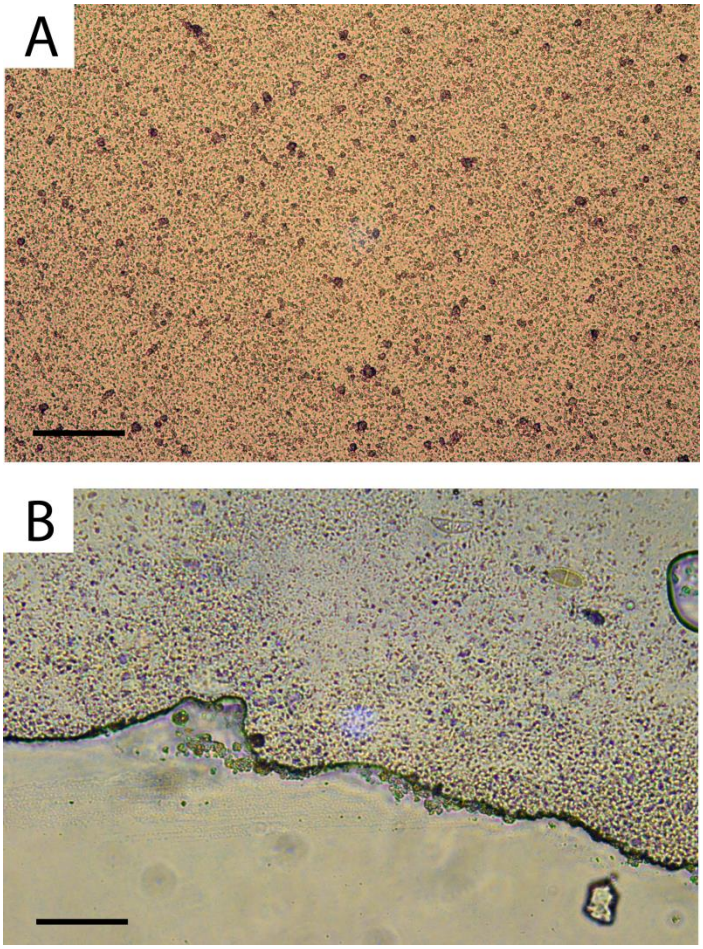

Figure 1.28. Optical microscope images of coating formulations with pigments of (**A**) SOCAL P3 stabilized with Orotan N-4045, (**B**) hollow SiO_2 particles stabilized with PVP-K30 (1^{st} generation). Scale bar = 20 µm.

The coatings were then applied to a black and white cardboard Lenetta panel with a multifilm applicator. A digital photograph of the dry films can be seen in **Figure 1.29**. The numbers above each film correspond to a wet and dry film thickness given in **Appendix II.3, Table II.3**. Note that the dry film thickness is theoretical, being calculated with **Equation 1.1** and data obtained from TGA in

Table 1.8 and

Table 1.9. As we shall see, many of the hollow SiO_2 particles have collapsed in the dry film, which means that the effective particle density (and hence the volume) is markedly different from the case where all would be intact i.e. density is higher and volume is much less. Subsequent film density measurements that we shall look at allow us to estimate the effective particle density of the particles dispersed in the film, and so correct for volume solids (and hence dry film thickness).

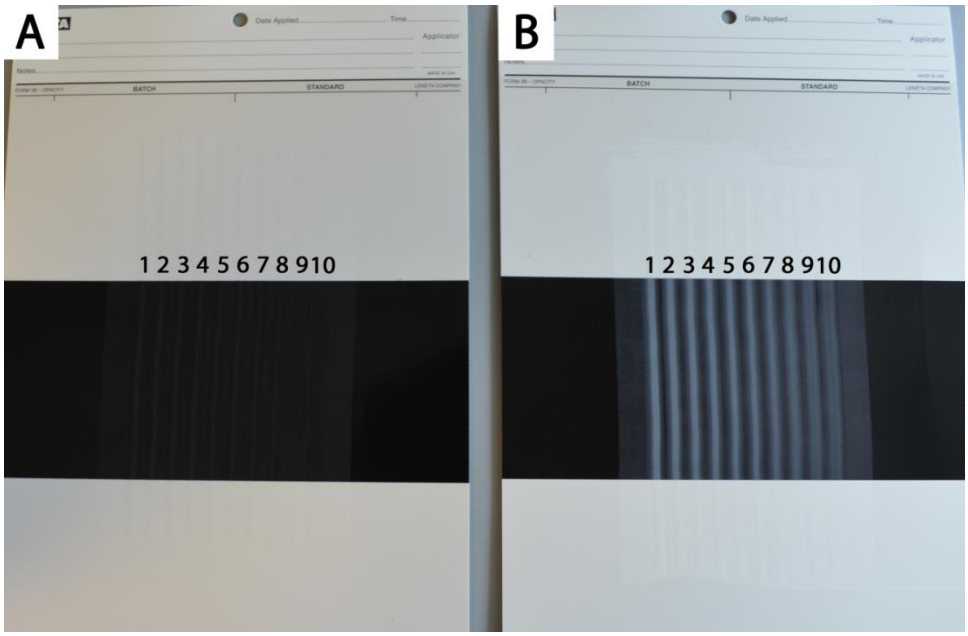

Figure 1.29. Digital photograph showing dry films after application of the coatings with a multifilm applicator for (**A**) 1st generation hollow SiO_2 particles @ 32.2% PVC[a], 20.1% vol. solids[a] and (**B**) SOCAL P3 @ 32.7% PVC, 16.1% vol. solids. Wet and film thickness for each label can be found in **Appendix II.3**, **Table II.3**. [a] These values are assuming that all of the air voids are intact. Following corrections a more accurate representation would be @ 5.3% PVC, 13.1% vol. solids.

It can be seen that there is no almost opacity for the hollow SiO_2 particles (**Figure 1.29 A**), a marked reduction from the original SOCAL P3 particles (**Figure 1.29 B**).

We decided to investigate the reason for this lack of opacity as conceptually the hollow SiO_2 particles should impart greater opacity to the film, due to the fact that the air voids inside have a larger refractive index with the film than the calcium carbonate. Furthermore, the air voids in the hollow particles should be of an appropriate size to effectively scatter visible light. Clearly some, or all, of the air voids must have collapsed or been filled by binder.

We can work out the percentage of air voided particles that remain in the dry films by finding where the experimental film density lies in relation to the theoretical film density. One can define a theoretical range of film density between when the effective particle density of the pigment = 0.2026 $g \cdot cm^{-3}$ (i.e. all air voids are intact) and when all of the particles are broken and completely wetted by binder (and pigment density is simply that of the skeletal density of the SiO_2 = 2.1381$g \cdot cm^{-3}$). The relationship we use to calculate the theoretical film density, $d_{theoretical}$, is given in **Equation 1.8**.

$$d_{theoretical} = \frac{m_{solids}}{\left[\left(\frac{m_{pigment}}{d_{pigment}}\right) + \left(\frac{\left(m_{solids} - m_{pigment}\right)}{d_{binder}}\right)\right]} \quad \textbf{(1.8)}$$

Where m_{solids} = mass solids per gram of waterborne coating as determined by TGA, $m_{pigment}$ = mass pigment per gram of waterborne coating as determined by TGA, $d_{pigment}$ = effective particle density of pigment and d_{binder} = skeletal density of the dry polymer film.

Film density can be measured by the hydrostatic weighing. A film is drawn down onto release film (Melinex® polyester film), which allows for it to be peeled off. The mass of the film is then recorded in air and in decamethylcyclopentasiloxane (DMCPS). The specific gravity of the film can then be worked out by the following relationship (**Equation 1.9**).

$$S.G._{film} = \frac{(mass\ of\ film\ in\ air) \times (d_{DMCPS})}{(mass\ in\ air) - (mass\ in\ DMCPS)} \quad \textbf{(1.9)}$$

Table 1.10 gives the theoretical film densities at the two extreme cases for the transparent hollow silica particles, and the experimentally obtained value. Raw measurement data for all film density calculations can be found in **Appendix II.4**, **Table II.4**.

Table 1.10. Comparison of the experimental film density for the hollow SiO_2 coating (1st generation) with the theoretical film density in the case where all particles are intact voided structures, and when none of the particles are intact voided structures.

Experimental average film	Theoretical film density with	Theoretical film density with

specific gravity ($g \cdot cm^{-3}$)	**all hollow particles** ($g \cdot cm^{-3}$)	**no hollow particles** ($g \cdot cm^{-3}$)
1.08	0.78	1.13

We find that only 14.3% of air voids remain in the dry polymer film, which explains why there is little opacity in the film. From this value we can recalculate the PVC and volume solids of the film, whereby pigment is considered air voided particles (we ignore the broken ones as they are effectively transparent). From our value of 14.3% of particles still containing an air void, we can estimate an average effective particle density (that is averaged over intact voided particles and collapsed) of 1.8613 $g \cdot cm^{-3}$. This would give a corrected PVC of only 5.3% and volume solids of 13.1%.

Film density measurements were also conducted for SOCAL P3. **Table 1.11** gives the theoretical film density and experimentally obtained density.

Table 1.11. Experimental and theoretical film density for the SOCAL P3 coating based on experimentally obtained data in

Table 1.8.

Experimental average film specific gravity ($g \cdot cm^{-3}$)	**Theoretical film density** ($g \cdot cm^{-3}$)
1.58	1.63

The results are found to be in reasonable agreement with one another. The deviation is likely due to the assumption that the skeletal density of the SOCAL P3 is equivalent to its effective particle density, which would be less due to the inclusion of some pores in the structure.

1.2.4 Tuning reaction parameters to obtain hollow SiO_2 particles without cracked shells

From the results of the film density measurements in the previous section it is apparent that most of the voids (~86%) in the 1st generation of hollow SiO_2 particles had collapsed or been filled in by binder. This would explain the lack of opacity as the refractive index of SiO_2 is very close to that of the binder. Upon closer inspection of the hollow SiO_2 particles under the SEM it became apparent that many of the particles were cracked (**Figure 1.30**) and so it is possible that the binder either fills in these voids, or the hollow particles collapse upon film formation.

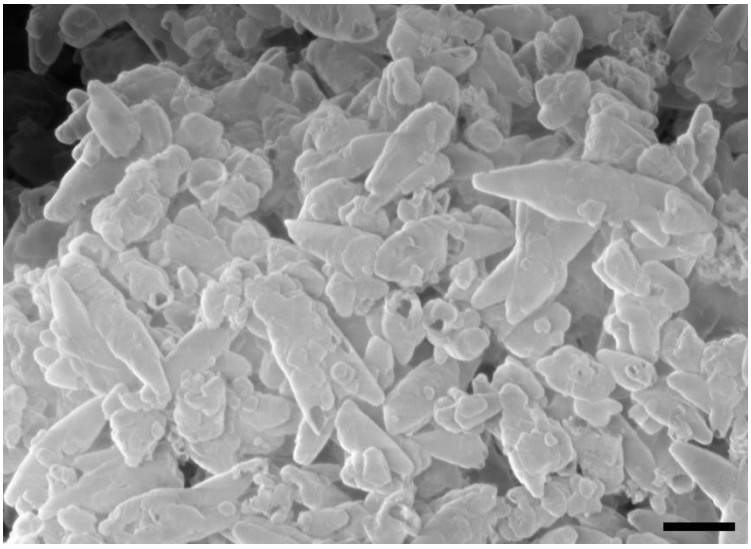

Figure 1.30. SEM image of hollow SiO_2 particles following aggressive acid etch with 2 M HCl. Scale bar = 1 µm.

Fragmentation of hollow SiO_2 structures is a recognized problem in the literature.[57,58] There are many factors that might be behind the fracture of the shells and in the following discussion we shall outline what we deemed to be the prominent reasons, and how these could be potentially resolved. Following this we will outline an investigation into the effect that the reaction parameters have on shell structure and demonstrate an improved hollow opacifying pigment particle.

It is rational to think that the strength of the hydrochloric acid used in the acid etch (pK_a = -8.0) is too high, causing too large an osmotic shock for the shell to withstand fracture. Therefore it is reasonable to think that etching with an organic acid with a lower pK_a, such as acetic acid (pK_a = 4.6) might mitigate the osmotic shock experienced due to the slower reaction acetic acid has with $CaCO_3$, and hence slower generation of CO_2 which causes the pressure differential across the shell.

By-products of this reaction would be calcium acetate and carbon dioxide so on an industrial scale one would get a useful by-product (calcium acetate) and a gas that needs to scrubbed before removal into the atmosphere.

Another parameter we could tune to both slow the dissolution of the calcium carbonate and increase the solubility of the carbon dioxide would be to decrease the temperature of the solution with an ice bath.[59,60] We will therefore etch all particles synthesized in the remainder of this section in an ice bath with a drip feed of acetic acid at a lower concentration than that used before (0.5 M instead of 2 M).

Preventing the formation of carbon dioxide might also limit the osmotic shock experienced. One way to etch the calcium carbonate out, without the formation of carbon dioxide bubbles, is to form calcium bicarbonate through reaction with carbonic acid, generated by dissolving carbon dioxide in water.

Our source of carbonic acid came from dialysis against soda water. Although the etch worked to some extent, it was not complete after 2 weeks, due to both the low solubility of carbon dioxide in water and the low dissociation constant of carbon dioxide into carbonic acid.[61]

However, if this could be made to work effectively by increasing the pressure used in the etch then one would have a very environmentally friendly closed-loop process as calcium bicarbonate breaks down upon evaporation of solvent into calcium carbonate, water and CO_2. Therefore, following generation of the hollow particles one obtains by-products that are the original templating material and the species used to etch (**Equation 1.10**).

$$Ca(HCO_3)_2 \rightarrow CO_2 + H_2O + CaCO_3 \qquad (\mathbf{1.10})$$

We also rationalized that particles may be collapsing during film formation due to the high lateral drying forces upon latex coalescence.[62] In order to increase the mechanical strength of the SiO_2 shell then it might be beneficial to make it thicker.[63]

Small pores and low pore volume in the SiO_2 shell may also lead to large capillary pressures upon drying which could cause the shell to fragment. [64] This is due to the high differential in capillary pressure formed across the porous structure, caused by the existence of a meniscus at the liquid-vapor interface. The Young-Laplace equation for a cylindrical pore illustrates that the smaller the pore radius, r_p, the higher the maximum capillary tension, P_{max} (**Equation 1.11**).

$$P_{max} = \frac{2\sigma_{\mathrm{lv}} cos\theta}{r_p} \qquad \textbf{(1.11)}$$

Where σ_{lv} = interfacial tension of the liquid-vapor interface, and θ = the contact angle at the liquid-pore wall.

Note that it is the pressure differential which causes the nonuniform stresses in the network ultimately leading to structural failure. If the permeability were uniform then the whole network would compress equally at a given pressure, reducing the stresses inside the shell. Increasing the total permeability of the SiO_2 shell, or uniformity thereof, may have the desired effect of reducing the pressure gradient across the shell.

There are several ways that we could tune pore size and distribution. An increase in the pore size and total pore volume can be attained during the synthesis of the SiO_2 shell by adding pore forming agents such as SDS or CTAB.[65,66] Another approach would be to etch the pores after synthesis by a surfactant-protected etch with sodium hydroxide,[67] or surfactant-directed etch with sodium carbonate.[68] The extent of this etching process is simply controlled by the amount of time that the particles are exposed to the etching solution.

Tuning the reaction parameters used in the sol-gel process can also affect the pore structure and shell thickness. For instance it was reported by Garrido and co-workers that the average pore size in amorphous SiO_2 decreases with increasing ethanol:TEOS molar ratio and pH. On the other hand increasing the water:TEOS molar ratio increases the average pore width. Furthermore, water:TEOS molar ratios of above 6 are required for complete hydrolysis, condensation and cross-linking between the primary particles. Primary SiO_2 particle size increases with increasing water content as well, due to the increase in solubility before precipitation leading to larger pore volumes upon gelation.[69] Increasing water content would also allow us to dope the reaction with water soluble inorganic salts that could act as porogens if necessary,[70] which could potentially lower stresses from osmotic shock and capillary drying.

We decided to investigate the effect of increasing SiO_2 shell thickness on the ability of the particles to retain the voided interior, and hence be effective opacifying pigments. Shell thickness was tuned by increasing the ammonia content (to increase the rate of reaction) and increasing the amount of TEOS per unit surface area of the template.

To this end we changed the reaction parameters by doubling the amount of TEOS from the initial synthesis and we increased the rate of addition from 3 x 10^{-5} to 9 x 10^{-4} ml $_{TEOS}/m^2_{SOCAL\ P3}/mL_{SOLVENT}$/hr. This may seem like an odd expression but we believe it is a necessary way of expressing a feed process of a precursor onto a template, especially if one wants to achieve consistent results when moving between reaction scale.

In the following investigation the surface area of template, amount of TEOS, feed rate and reaction time were all kept constant. Acid etch was conducted in an ice bath with a drip feed of acetic acid (0.5 M) over about 2 hours. For more specific details on the reaction parameters used please refer to experimental **Section 1.4.8**. The salient variations in reaction parameters are given in **Table 1.12**.

Table 1.12. Sample identities and the variations in reaction parameters investigated to tune shell thickness in a bid to improve opacity of the pigment.

Sample identifier	Ammonia concentration (M)	Molar ratio of water:ethanol	Molar ratio of ammonia:TEOS
A1	0.36	0.22	0.2
A2	0.36	6.47	0.2
A3	1.8	6.47	0.97
A4	3.6	6.47	1.94

Briefly, A1 is representative of the hollow particles made previously that failed to generate opacity but with a milder acid etch used to generate the hollow particles. Note that it is slightly different from the original synthesis in that there is a

faster feed rate of TEOS and there is twice as much TEOS fed, but the reaction time is much shorter. It is worth noting that we find the shell thickness, density and pore composition to be very similar to the original highly fractured hollow SiO_2 particles, so this will give an indication as to the effect that using a milder acid etch has on the structure of the hollow particles.

A2 has the same catalyst concentration as A1 but has a much higher ratio of water:ethanol as solvent, which allows us to directly compare the effect of increasing the water content. A3 and A4 have the same solvent composition as A2 but with increasing catalyst content.

First we need to check that the changes in reaction parameters don't lead to formation of aggregates. Laser diffraction was performed to analyze the as generated nanocomposite $CaCO_3$@SiO_2 samples A1-A4 (**Figure 1.31** and **Appendix II.5**, **Table II.5**). It must be noted that the same optical constraints were applied to each sample even though, as we shall see later, the SiO_2 shell fraction is different between the samples (and hence the refractive index/absorption index will be slightly different too). Although this means that the absolute size values for each sample will not be completely accurate, the results do show us that no aggregates are formed in the coating of any of the samples, which is very important for when we come to put the particles into a coatings formulation.

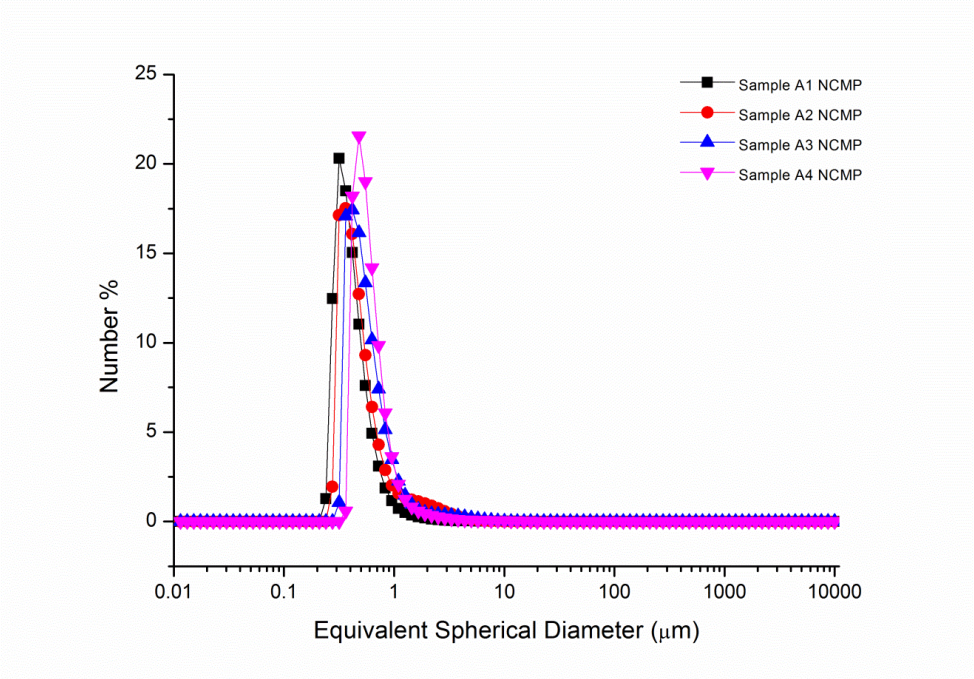

Figure 1.31. Particle size frequency distribution as determined by laser diffraction measurements for $CaCO_3$@SiO_2 nanocomposite samples A1-A4. Size is given as equivalent spherical diameter (number average).

TGA measurements were then conducted on the nanocomposites A1-A4 in order to deduce the conversion of TEOS to SiO_2 (**Figure 1.32**).

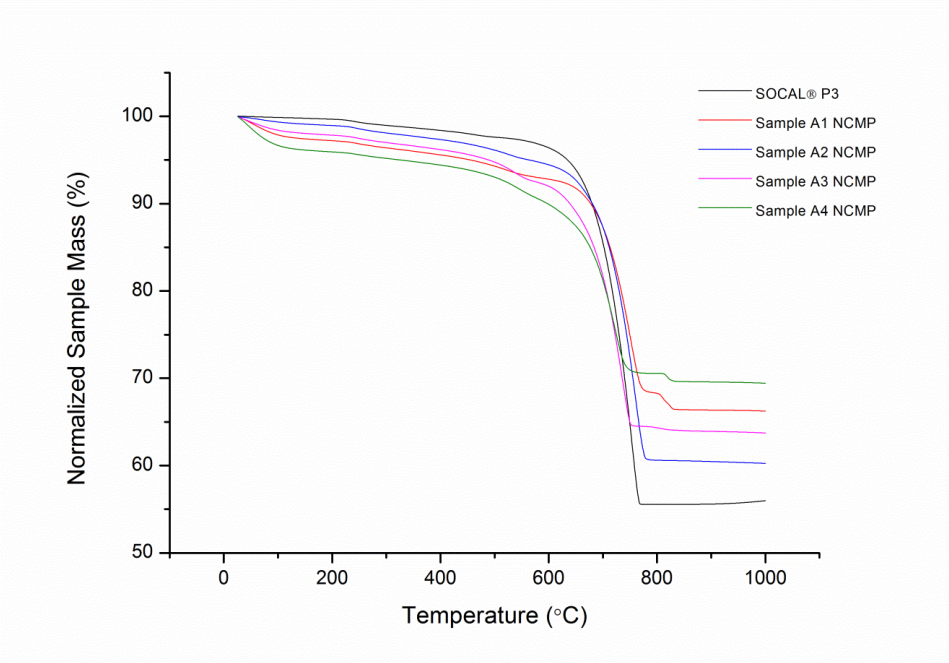

Figure 1.32. TGA curves of the $CaCO_3$@SiO_2 nanocompsite samples A1-A4.

Conversion measurements (**Table 1.13**) calculated from TGA measurements show that the rate of reaction in A1 is over twice as fast as that in A2, even though they both have the same concentration of catalyst. We can deduce from this that a higher ethanol content facilitates a faster reaction, most likely due to the fact that TEOS is more soluble in ethanol than in water. It is also clear that as we increase the ammonia content in A3 and A4 the rate of reaction increases with roughly first order kinetics. The TEOS conversion is quite low, which is likely due to the fact that the reaction is only conducted for only 5 hours. If a higher conversion is desired then the reaction could be left for 24-48 hours, as is often the case in the literature.[71] The drawback with longer reaction times is that silica bridging between particles is more likely to occur, forming unwanted aggregates. Another factor behind the low conversion might be that the NH_4OH is quite volatile, which would slow the reaction as time progresses. If one desired higher conversions then tetramethylammonium

hydroxide (TMAH) might be a more suitable base.[72] Nevertheless, we have achieved our aim, which was to tune the thickness of the SiO_2 shell without the formation of aggregates.

Table 1.13. Tabulated conversions of TEOS in the reactions A1-A4 calculated from **Figure 1.32**.

Sample	**Molar conversion of TEOS to SiO_2**
A1	21.2%
A2	8.3%
A3	15.6%
A4	28.8%

TEM image analysis was used deduce the thickness of the SiO_2 shell grown in the four samples (**Figure 1.33**), the results of which are provided in **Table 1.14**.

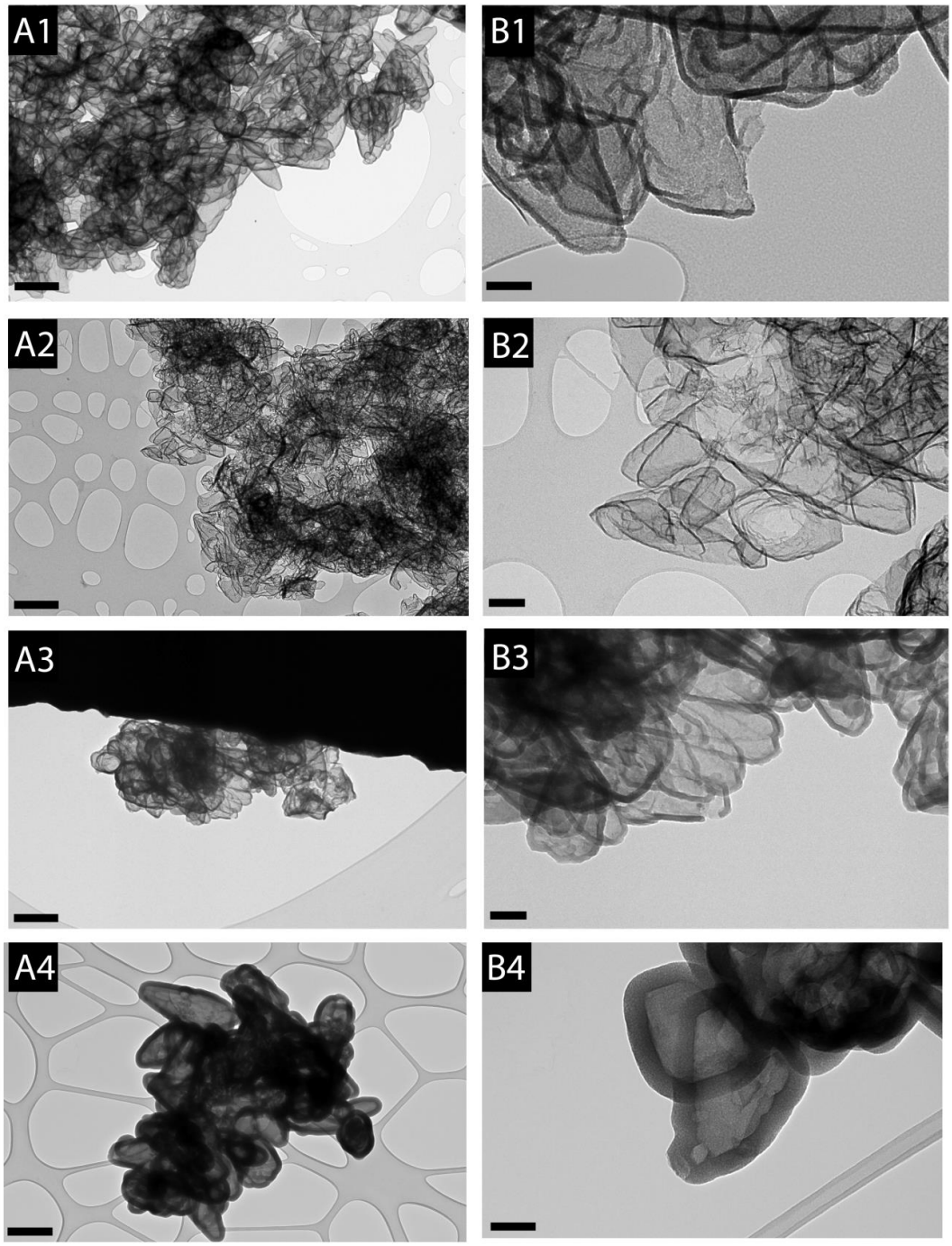

Figure 1.33. TEM images of hollow SiO_2 particles generated from acid etch of samples A1-A4. Figure labels correspond to sample identifiers. BX is the sample AX but at a higher magnification. Scale bar AX = 500 nm, scale bar BX = 100 nm.

Table 1.14. Tabulated mean average SiO_2 shell thicknesses of the samples A1-A4 with standard deviations as determined from 50 measurements from TEM images.

Sample	**Mean SiO_2 shell thickness (nm) with standard deviation**
A1	15.7 ± 2.1
A2	6.7 ± 0.7
A3	17.2 ± 1.7
A4	55.6 ± 6.1

It can be seen that A4 has the thickest shell of 55.6 nm. A2 has the thinnest shell of only 6.7 nm. The trend in shell thickness measurements are in agreement with TGA conversion data reported in **Table 1.13** except for A1 and A3. This is due to A1 having a higher shell density then A3, as deduced by helium pycnometry (**Table 1.15**).

Table 1.15. Tabulated skeletal densities obtained via helium pycnometry for samples A1-A4.

Sample	Mass (g)	Volume displaced (cm^3)	Skeletal density ($g\ cm^{-3}$)
A1	0.0790	0.0358	2.2088
A2	0.1119	0.0525	2.1307
A3	0.0840	0.0397	2.1154
A4	0.3317	0.1526	2.1741

Qualitative assessments of shell fragmentation via SEM are not very reliable as particles often aggregate upon drying, making it difficult to see cracked shells. In all samples there at least a few broken shells towards the periphery of the imaging stub (**Figure 1.34 B**). However, it can be seen that the majority of particles for sample A4 in **Figure 1.34** are crack free (**Figure 1.34 A**), a marked improvement over the particles used previously (the SEM of which is shown in **Figure 1.30**).

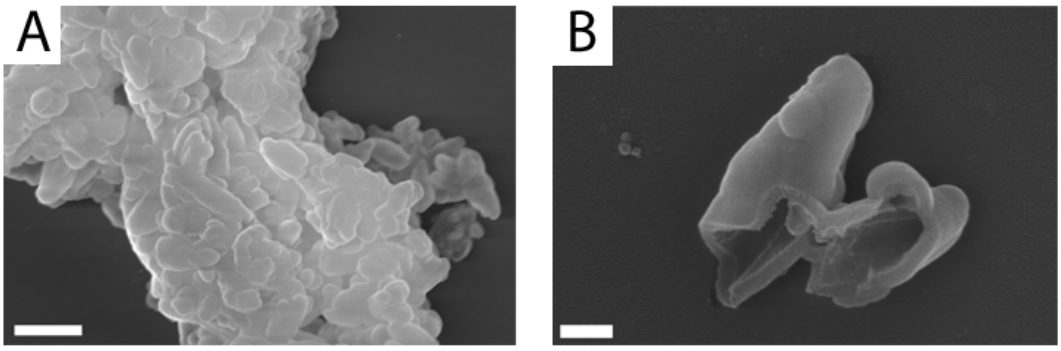

Figure 1.34. SEM morphology of hollow SiO_2 particles generated from acid etch of sample A4 showing the difficulty in assessing the degree of broken particles. (**A**) A cluster in the middle of the stub with no apparent breakages, scale bar = 1 µm. (**B**) Some broken particles are always observed towards the periphery of the imaging stub, scale bar = 200 nm.

SEM image analysis of sample A2 clearly shows that very thin shells (6.7 nm) are highly elastic and lead to buckling of the shell structure (**Figure 1.35**).

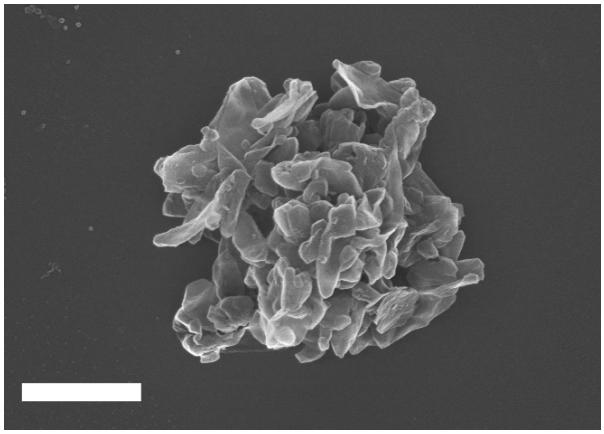

Figure 1.35. SEM morphology of sample A2 shows that the shell is too thin to withstand core removal and buckles when dried. Scale bar = 1 µm.

Prior to analysis of the samples with nitrogen porosimetry, HR-TEM was used to image the pore structure to ensure that the t-plot method was suitable for each sample i.e. that there are only micropores present (**Figure 1.36**).

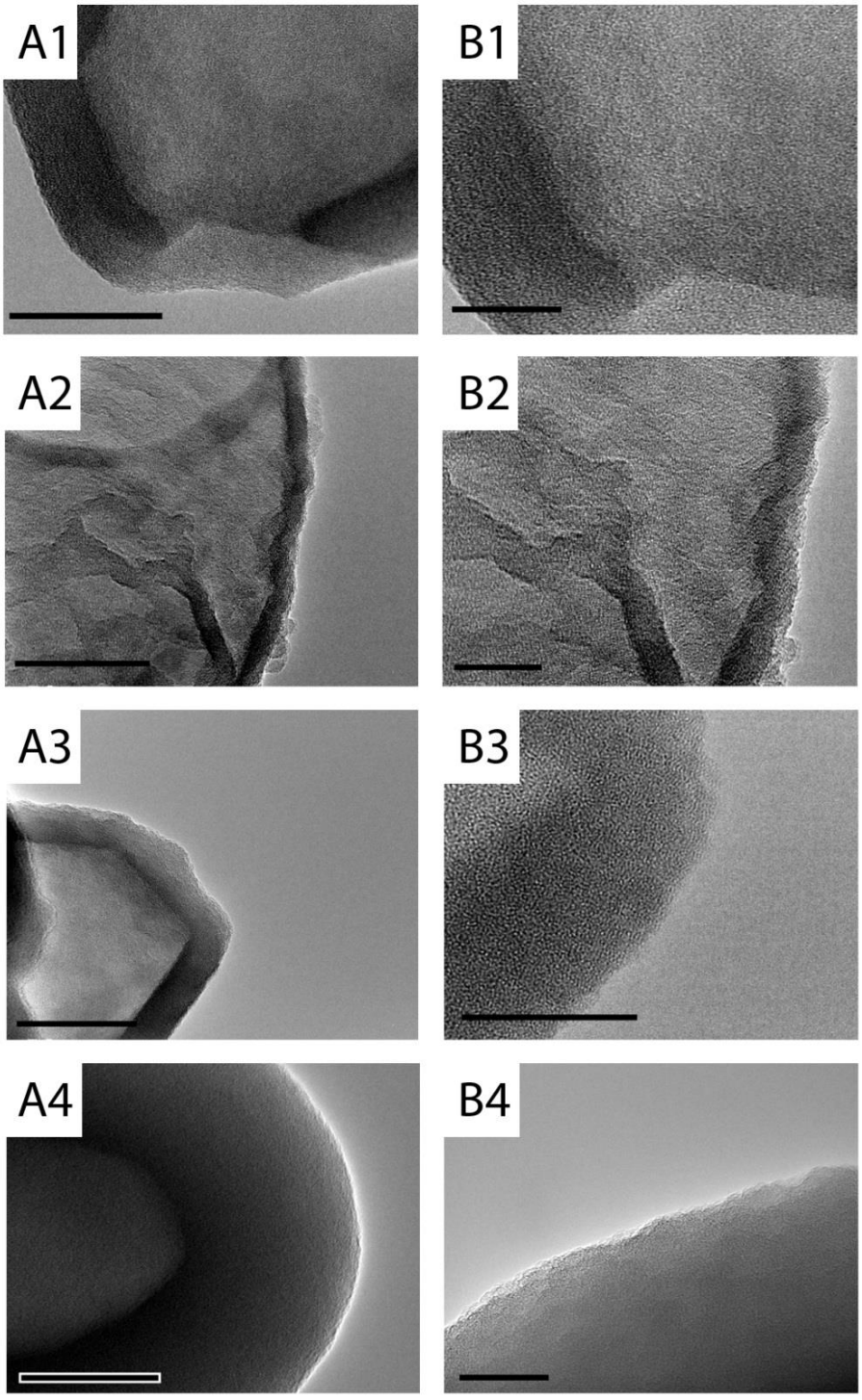

Figure 1.36. HR-TEM images of hollow SiO_2 particles generated from acid etch of samples A1-A4. Sample numbers are as labelled in figure. BX is the sample AX but at a higher magnification. Scale bar AX = 50 nm, scale bar BX = 20 nm.

It can be seen from **Figure 1.36** that the only pores present in all samples are < 2 nm, and those that are present are either cylindrical or slit shaped pores.

Nitrogen adsorption isotherms of each sample are given in **Figure 1.37**. Again it can be seen that each sample presents a small population of micropores and an observable hysteresis at the higher range of relative pressure due to the presence of the closed off macropores inside some of the particles.

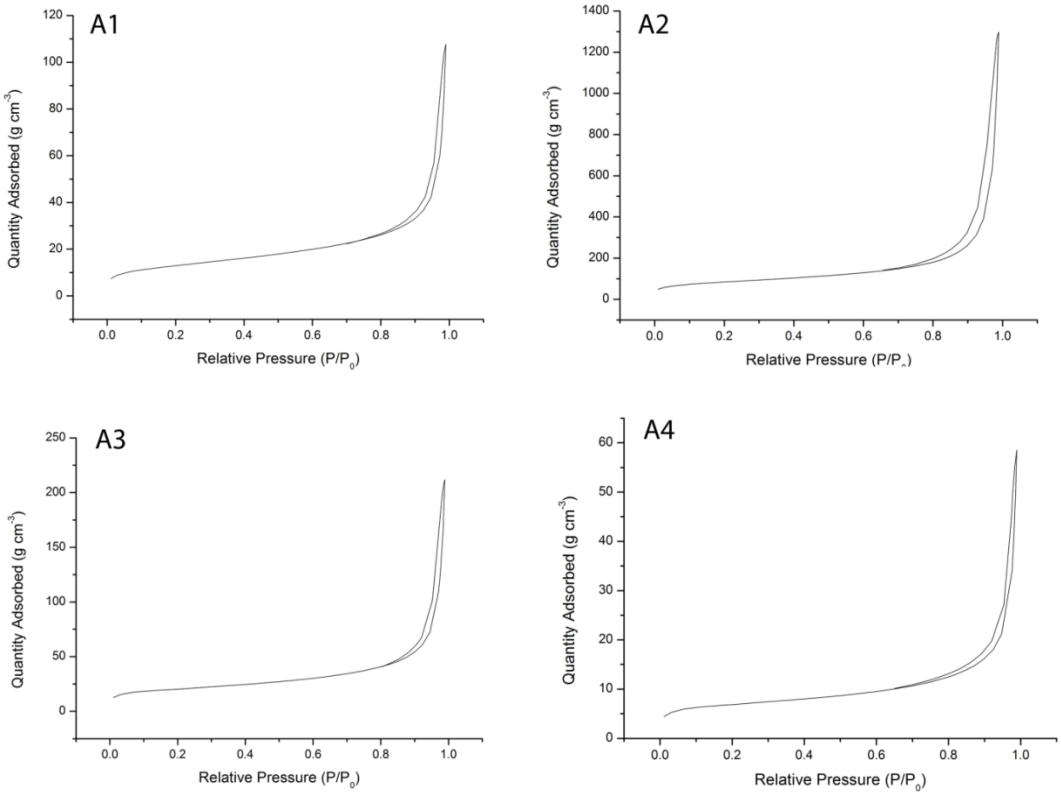

Figure 1.37. Nitrogen adsorption isotherms of quantity of nitrogen adsorbed as a function of relative pressure for the hollow SiO_2 particles. Figure labels correspond to sample ID.

V_A-t plots of the samples are shown in **Figure 1.38** with the linear regression fitted. This allows us to extract information about the micropore surface area and volume (**Table 1.16**).

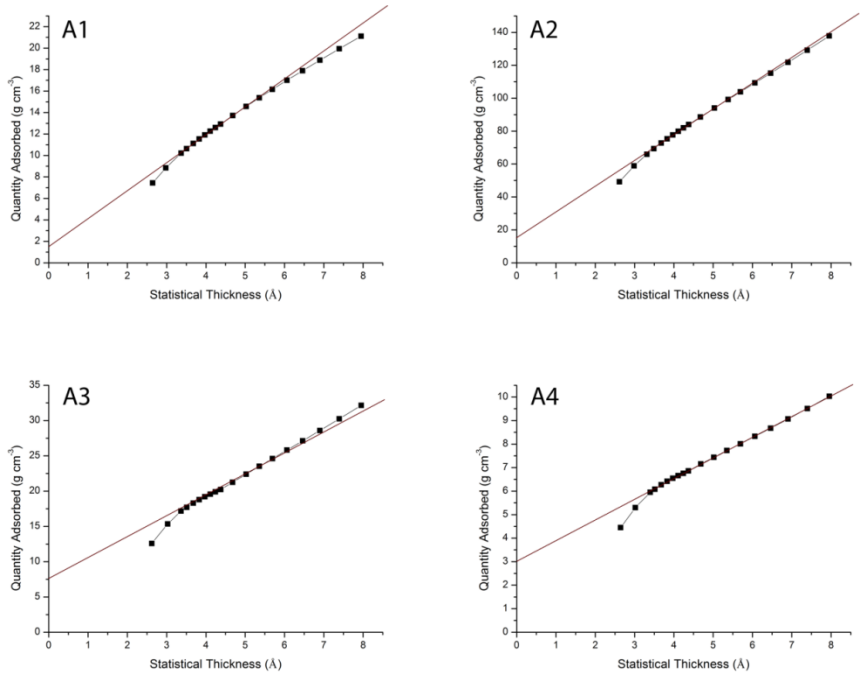

Figure 1.38. V_A-t plots of quantity of nitrogen adsorbed as a function of statistical thickness based on the Harkins-Jura thickness equation on nonporous siliceous oxide for the hollow SiO_2 particles. Figure labels correspond to sample ID.

Table 1.16. Tabulated t-plot surface area data for samples A1-A4.

Sample	Micropore Volume ($cm^3 \cdot g^{-1}$)	Micropore Area ($m^2 \cdot g^{-1}$)	External Surface Area ($m^2 \cdot g^{-1}$)	Correlation Coefficient
A1	2.40×10^{-3}	6.17	40.29	1.000
A2	22.80×10^{-3}	55.77	244.86	1.000
A3	11.62×10^{-3}	25.44	45.27	0.998
A4	4.61×10^{-3}	8.92	12.40	0.998

It is clear that all samples are similar in that they have very low pore volumes and diameters (as evidenced with HR-TEM in **Figure 1.36**). Clearly some of the particles still fragment in the thicker shell sample (**Figure 1.34A**), although there is a clear improvement over the initial attempt (**Figure 1.30**). Therefore we decided to investigate these particles with thicker shells as opacifying pigment.

1.2.5 Opacity testing of hollow SiO_2 templated around SOCAL P3 (2^{nd} generation, thicker shell of SiO_2)

A scale-up synthesis was conducted utilizing the parameters of sample A4 (experimental **Section 1.4.8**, **Table 1.26**).

A coating was formulated to have the same parameters as those investigated before i.e. 30% PVC and ~17% vol. solids (assuming all particles remain intact). For more specific details on the exact formulation parameters please see experimental **Section 1.4.9, Table 1.29**.

Table 1.17. Key formulation parameters for waterborne coating with 2nd generation hollow SiO_2 particles (thicker shell) as pigment. [a] Note that these values only hold true when all of the particles are intact, which as we shall see is not the case. Corrected values are given later based on film density measurements.

	Mass solids (%)	**Mass fraction pigment (%)**	**Vol. solids (%)[a]**	**PVC (%)[a]**
Theoretical	16.3	1.8	18.5	29.3
Experimental (TGA)	16.0	1.9	19.0	31.2

TGA was performed on the improved hollow SiO_2 coating formulation (**Figure 1.39**) to gain a more accurate value for PVC and % vol. solids, which are reported in **Table 1.17**. Note that water evaporation from the pan was corrected for by taking the initial sample mass as being 100%.

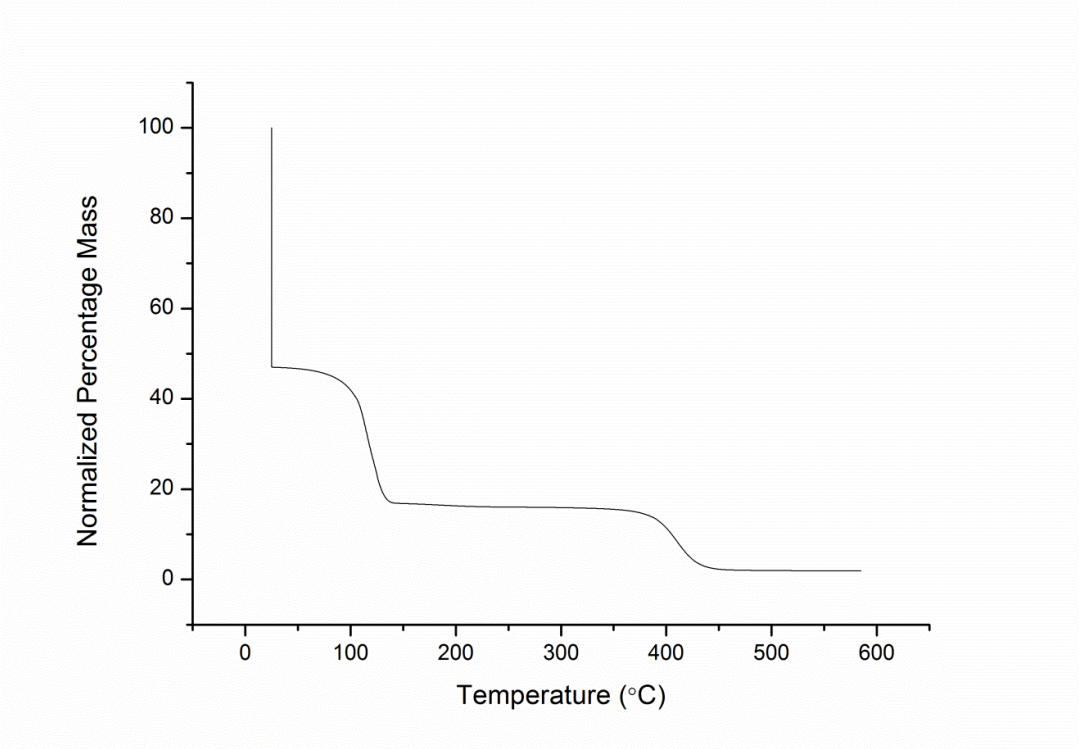

Figure 1.39. TGA plot of the coating containing 2nd generation hollow SiO_2 particles as pigment. Sample mass was normalized and recorded between 25-580°C. Heating was at a rate of 10°C·min^{-1}and the atmosphere was air at a flow rate of 50 mL·min^{-1}.

Optical microscopy was conducted on the coating to ensure that the hollow pigments were well dispersed throughout (**Figure 1.40**). It can be seen that the waterborne coating on the left side of the drying front (running down the center of the image) contains particles that are very finely dispersed with no large aggregates.

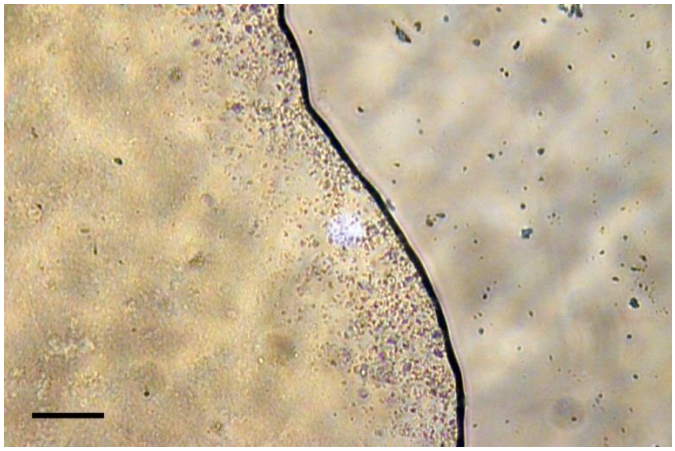

Figure 1.40. Optical microscope image of coating containing 2nd generation hollow SiO_2 particles as pigment. Stabilizer used was PVP-K30. Scale bar = 10 µm.

The coating was then applied to a Lenetta panel with a multifilm applicator. A digital photograph of the dry films is shown in **Figure 1.41.** The improved hollow SiO_2 formulation drawdown can be seen in **Figure 1.41 B**, with the numbers above each film corresponding to the wet and dry film thickness that are given in **Appendix II.6**, **Table II.6**. For comparison, the broken hollow SiO_2 formulation and the SOCAL P3 formulation drawdowns from **Figure 1.29** are also given in **Figure 1.41 A** and **C** respectively.

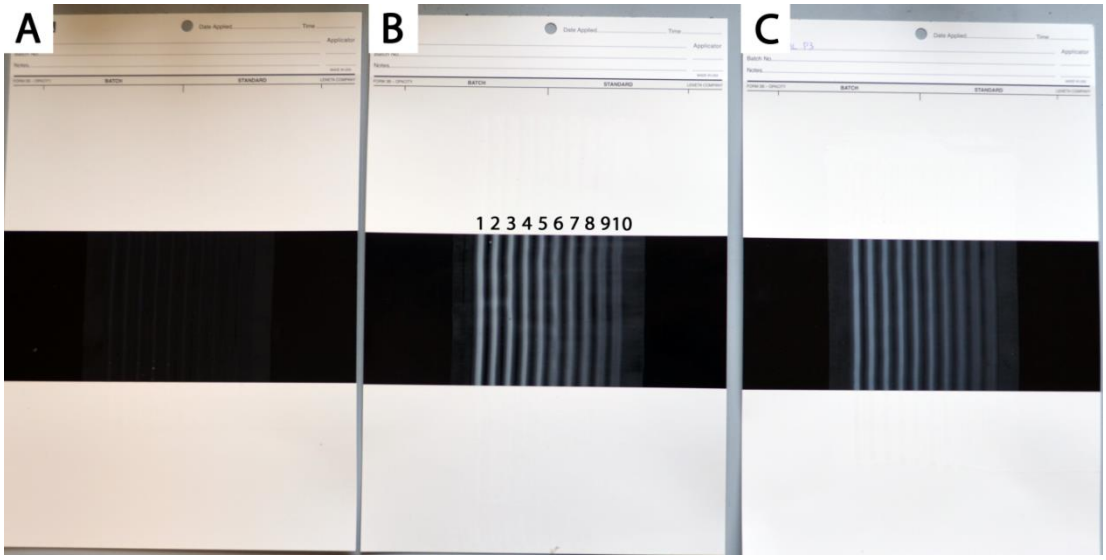

Figure 1.41. Digital photograph comparing dry films after application of the coatings with a multifilm applicator for (**A**) 1st generation hollow SiO_2 particles @ 32.2% PVC,[a] 20.1% vol. solids.[a] (**B**) 2nd generation hollow SiO_2 particles @ 31.2% PVC,[b] 19.0% vol. solids.[b] (Wet and dry film thickness for each label can be found in **Appendix II.6, Table II.6**) and (**C**) SOCAL P3 @ 32.7% PVC, 16.1% vol. solids. [a//b] These values are assuming that all of the air voids are intact. Following corrections for the amount of broken particles from film density measurements (see following section), a more accurate representation for [a] would be PVC = 5.3% and vol. solids = 13.1% and for [b] PVC = 7.4% and vol. solids = 14.1%.

In order to quantify the proportion of intact air voids in the film we again check the experimental film density and compare this to the theoretical film density in the case where there are no voids and when there are 100% voids (**Error! eference source not found.**), as outlined in **Section 1.2.3**.

Table 1.18. Theoretical and experimental volume of air voids in the dry films as determined by the DMCPS hydrostatic weighing analysis.

Experimental average film specific gravity ($g \cdot cm^{-3}$)	**Theoretical film density with all hollow particles ($g \cdot cm^{-3}$)**	**Theoretical film density with no hollow particles ($g \cdot cm^{-3}$)**
1.09	0.84	1.15

From these results it would appear that 19.4% of the particles remain voided, giving an effective particle density for the particles in the dry film of 1.81 $g \cdot cm^{-3}$. This means that a more accurate value for PVC would be 7.4% and volume solids as 14.1%.

Therefore we can say that through a combination of thicker shell and milder acid etch that we have increased the percentage of intact voids by a marginal 5.1%. Nevertheless this increase has caused a dramatic change in opacity of the coating from the case in **Figure 1.41 A** to that shown in **Figure 1.41 B** (note that both have similar film thicknesses due to the similar volume solids). We could attribute this increase in opacity to the thicker silica shell i.e. going from 23.9 to 55.6 nm, although the refractive index difference between the shell and binder is negligible. Furthermore, if we consider the silica fraction by weight in comparison to the weight fraction of calcium carbonate shown in **Figure 1.41 C**, then there is only 1.9% by mass of silica and 14.7% by mass of calcium carbonate in the respective coatings. Clearly these two coatings have similar opacity even though the calcium carbonate coatings are thicker as well. This would indicate that it is predominantly the air voids that are responsible for the scattering of light.

In order to assess the hiding power of the coatings we measured their contrast ratio, which is defined as the reflectance of the coating over a black substrate, R_B,

divided by the reflectance of the coating over a white substrate, R_W. We normalize contrast ratio with respect to film thickness to account for the different film thicknesses. The results are presented for the coatings pigmented with SOCAL P3 (**Table 1.19**), 1st generation hollow SiO_2 (**Table 1.20**), and 2nd generation hollow SiO_2 (**Table 1.21**).

Table 1.19. Tabulated reflectance data showing contrast ratio per micron film thickness for coating with SOCAL P3 as pigment.

Dry film thickness (µm)	**R_B/R_W**	**R_B/R_W micron^{-1}**
11.03	18.57	1.68
10.77	18.26	1.69
10.72	18.10	1.69
10.62	18.07	1.70
10.15	17.43	1.72

Table 1.20. Tabulated reflectance data showing contrast ratio per micron film thickness for coating with hollow SiO_2 (1st generation, thinner shell) as pigment.

Dry film thickness (µm)	**R_B/R_W**	**R_B/R_W micron^{-1}**
4.54	7.39	1.63
4.42	7.40	1.67
4.33	7.34	1.69
4.32	7.33	1.70
4.17	7.32	1.76

Table 1.21. Tabulated reflectance data showing contrast ratio per micron film thickness for coating with hollow SiO_2 (2^{nd} generation, thicker shell) as pigment.

Dry film thickness (µm)	R_B/R_W	R_B/R_W micron^{-1}
5.19	16.21	3.12
5.20	15.87	3.05
4.94	15.42	3.12
4.76	15.40	3.23
4.61	15.22	3.30

Wet film thickness was determined by measuring the mass of the coating, wet density, and keeping the film area constant by the following relationship (**Equation 1.12**). Dry film thickness was then calculated as shown before in **Equation 1.1**.

$$WFT = \frac{m_{wet\ coating}}{\rho_{wet\ coating} \times Area} \quad \textbf{(1.12)}$$

To truly compare the coatings in terms of light scattering coefficient/micron, independent of PVC, one would need to measure contrast ratio at various film thicknesses for coatings with different PVC. Application of the Kubelka-Munk model would then allow one to derive scattering and absorption coefficients.[73]

Unfortunately we didn't have enough material to run these tests. Nevertheless we can see that the 2^{nd} generation hollow silica particles appear to be a promising candidate for light scattering pigment, when one considers that the contrast ratio per

micron is over twice as high as SOCAL P3, and the PVC is less than a quarter of that used in the SOCAL P3 coating.

1.3 Conclusions

The aim of this work was to synthesize hollow colloidal particles with suitable dimensions and composition to rival/improve upon the hollow latex opacity modifier ROPAQUE™. The reason for the existence of such opacity modifiers is to mitigate the amount of TiO_2 required in white decorative coatings, the use of which has detrimental economic and environmental implications.

It has long been theorized that non-spherical air voids (in comparison to ROPAQUE™) could provide enhanced light scattering per unit volume. Sacrificial templating was used as a route to generate hollow silica particles from a variety of colloids. Unfortunately, due to limitations in the quantity we were able to produce, both copper oxide and hematite templates were unsuitable.

By using SOCAL P3 (a commonly used $CaCO_3$ filler) as a sacrificial template after growth of a SiO_2 shell, we proposed that we could generate large quantities of anisotropic hollow particles with an appropriate size for light scattering in the visible portion of the electromagnetic spectrum.

Our 1st generation of hollow silica particles with a shell thickness of 23.9 nm were ineffective at light scattering, which we reasoned as being due to the fact that only about 14% of particles remained voided following film formation.

Whilst many factors were potentially responsible for the collapse of the particles including pore size/volume, strength of acid etch and shell thickness, we decided to focus on tuning the reaction parameters to give a thicker shell while using

a weaker acid to etch the core with. This afforded us our 2nd generation hollow silica particles.

These were investigated as opacity modifiers and were found to be effective even though there was only a marginal improvement upon the number of intact voided particles to 19%. Contrast ratio per micron for the 2nd generation hollow particles was over twice that of SOCAL P3, even though the PVC of the hollow particles was only at a quarter of that used in the SOCAL P3 coating. We attribute the light scattering due to air voids as the mass fraction of silica is so low in the coatings, and the refractive index difference of the shell with the binder is negligible.

Note that since the initial submission of this thesis we have found that shell breakage can be prevented by co-condensing TEOS with cross-linking silane agents with flexible organic groups in between the two reactive siloxane ends.

1.4 Experimental

1.4.1 Materials

SOCAL P3, Orotan N-4045, Acysol SCT-275, and S/BA/AA latex binder were kindly donated by AkzoNobel. Solvay also kindly provided us with SOCAL P3.

Copper(II) chloride (powder, 99%), SDS (ACS reagent, ≥ 99%), $NH_2OH.HCl$ (ACS reagent, 98.0%), $FeCl_3.6H_2O$ (reagent grade, ≥ 98%, purified lumps), styrene (≥ 99%), DVB (technical, 80%), AA (anhydrous, 99%, 180-200 ppm MEHQ inhibitor), tetraethylorthosilicate (TEOS, Reagent grade 98%), and PVP-K30 (40,000 $g \cdot mol^{-1}$) were used as received from Sigma Aldrich.

Ethanol (Absolute, 99.9%) was used as received. Acetic acid (17.4 M) and hydrochloric acid (35%) were diluted down to make the appropriate strength solution. All three were obtained from VWR international.

Ammonium hydroxide (35%), sodium sulfate (anhydrous), potassium persulfate (99+ %), and sodium hydroxide (analytical) was used as received from Fisher Scientific. Deionized water was produced by a Milli-Q purification unit with a conductivity of 18MΩ.

1.4.2 Analytical techniques

1.4.2.1 Mie scattering

In all experiments the dispersant was water (n = 1.33). See **Table 1.22** below for the optical parameters chosen for each material.

Table 1.22. Optical properties used in the light diffraction (Mie scattering) experiments.

Material	Refractive Index	Absorption Index
Fe_2O_3	3.22	1
Fe_2O_3@SiO_2	3.22	1
$CaCO_3$ (SOCAL P3)	1.66	0.5
$CaCO_3$@SiO_2	1.66	0.5
Hollow SiO_2	1.45	0.1

1.4.2.2 Helium pycnometry

Skeletal density measurements were taken with a Micromeritics AccuPyc 1330 helium pycnometer. First, a calibration run was performed with a reference standard of known volume. Then, a fused SiO_2 glass standard rod was run before a sample to ensure the calibration factor is correct (d = 2.20 $g \cdot cm^{-3}$). The mass of the sample chamber and sample added was recorded with a 4 d.p. balance before the sample was inserted into the analysis chamber. A steady purge of helium through the chamber was carried out for 10-15 minutes in order to remove moisture from the sample. Displaced volume in the sample chamber was then measured over a maximum of 50 runs until the values were within 0.02%. Skeletal density was then calculated based on the sample mass, displaced volume, and calibration factor.

1.4.2.3 Nitrogen sorption porosimetry

A blank tube with filler rod was degassed and backfilled with nitrogen. The tube is weighed and the warm and cold freespace recorded; to be used in future measurements as per the recommended procedure outlined by Micromeritics.

Powdered samples were dried in an oven overnight at 140°C before being carefully added into a 25 cm^3 sample tube (10 cm^3 bulb and 1/4" stem diameter). A filler rod was then inserted to minimize freespace error (recommended for samples with total surface area < 100 m^2). Then, the rubber sealed frit was added and the sample degassed to a vacuum setpoint of 10 μm·Hg. The sample was then heated to 180°C at a temperature ramp rate of 10°C min^{-1}, where it was held for 180 minutes. Following the degas phase it was then heated to 300°C for 240 minutes before being backfilled with nitrogen. Note that these are quite harsh conditions, but are necessary

to remove strongly chemisorbed water from the pores of the silica. Following the backfill with nitrogen, the sample was degassed a second time to 10 µm·Hg and heated to 180°C. This step is necessary as purging with inert gas aids in the removal of water (sample is backfilled with nitrogen again). The sample tube was then weighed with a 4 d.p. balance and the sample mass calculated from the difference with the blank tube. Using the skeletal density values obtained from pycnometry, sample mass, and the blank tube freespaces, entered values for the warm (**Equation 1.13**) and cold (**Equation 1.14**) freespace could then be calculated as follows.

$$WFS_{Entered} = WFS_{Measured} - \left[\left(\frac{m_{sample}}{d_{sample}}\right) \times \left(\frac{T_{standard}}{T_{ambient}}\right)\right] \quad \textbf{(1.13)}$$

$$CFS_{Entered} = CFS_{Measured} - \left[\left(\frac{m_{sample}}{d_{sample}}\right) \times \left(\frac{T_{standard}}{T_{bath}}\right)\right] \quad \textbf{(1.14)}$$

Where m_{sample} = mass of sample (g), d_{sample}= density of sample (g·cm^{-3}), $T_{standard}$ = Standard room temperature = 273.15 K, $T_{ambient}$ = Ambient temperature of room (K), T_{bath} = Temperature of liquid nitrogen bath = 77 K.

Isotherms were recorded with 20 points for both the adsorption and desorption branches. For a more detailed discussion on the theory behind the models applied to the isotherm please refer to **Appendix I.4**.

1.4.2.4 SEM/TEM

SEM samples were prepared by diluting the particle solutions to around 0.01% wt. in DIW, and allowing them to dry on silicon wafers supported by an aluminium stub. Sputtering was performed with a platinum target at 1.5 kV for 40 seconds, to give a calculated layer thickness of 5 nm. SEM imaging was performed on a Zeiss Supra 55VP FIB-SEM at 10 kV. For TEM image analysis, samples were mounted on a lacey carbon copper grid, and imaged with a JEOL 2000FX.

1.4.2.5 TGA measurements

All TGA measurements were preceded by running a blank pan beforehand as a calibration, which was then subtracted from the final curve in order to account for buoyancy effects.

TGA measurements of the SOCAL P3@SiO_2 nanocomposite particles were carried out in a 70 µL platinum pan. Sample mass was kept around 20 mg and weighed out with a 5 d.p. balance. The temperature was ramped from 25-1000°C at a rate of 10°C min^{-1} under a flow of N_2 at a rate of 50 $mL \cdot min^{-1}$.

All thermogravimetric measurements of the waterborne coatings were carried out in 40 µL aluminium pans with pierced lids sealed in place. Sample mass was kept at around 15 mg and weighed out with a 5 d.p. balance. The temperature was ramped from 25-580°C at a rate of 10°C min^{-1} under a flow of air at a rate of 50$mL \cdot min^{-1}$.

1.4.2.6 Optical microscopy

Imaging was performed with a Leica DM2500M optical microscope, using a 20-40x ph2 objective.

1.4.2.7 Reflectance measurements

Reflectance measurements were conducted on films that had been drawndown onto a black and white Lenetta panel, as exemplified by the substrate shown in **Figure 1.29**. These films were allowed to dry in an oven at 40°C for 4 days. Film reflectance was measured with a Spectroflash SFX600-CT with specular reflectance over λ = 400-700 nm.

1.4.3 Synthesis of cubic and octahedral Cu_2O particles, SiO_2 coating of the cubic particles, and formation of hollow SiO_2 cubes

SDS (87 mg) was dissolved in deionized water (DIW) in a 20 mL vial (9.4 mL [cube], 8.8 mL [octahedral]). To this was added a solution of $CuCl_2$ (0.1 mL, 0.1 M) under stirring, followed by $NH_2OH.HCl$ (0.25 mL [cube], 0.85 mL [octahedral]). A solution of NaOH (0.25 mL, 1 M) was then added and the solution shaken gently to facilitate a colour change from translucent blue to opaque yellow. The reaction was left to age for 2 hours at room temperature (RT), over which course it turned orange in colour. The particles were purified by three rounds of centrifugation/redispersal into deionized water at 4,000 g.

Hollow SiO_2 cubes were prepared by adding as formed Cu_2O cubes (9 mg) from above into a solution of ethanol (20 mL) and deionized water (2 mL). PVP-K30 was added to the solution (5 mg) and the solution was left to stir for 24 hours to facilitate PVP adsorption onto the cuprous oxide particles. NH_4OH (0.2 mL, 18.1 M) was added to the solution followed by TEOS (0.05 mL) under stirring. The reaction was left stirring at RT for 5 hours before the particles were collected by centrifugation/redisperison into deionized water 3 times at 4,000 g. Hollow particles were formed by dropping in HCl (10 mL, 2 M) over a few hours. The particles were cleaned by a further three rounds of centrifugation/redispersal into deionized water at 7,000 g.

1.4.4 Synthesis of PS-DVB-AA copolymer latex and preparation of multifaceted Cu_2O particles by using latex as directing agent

PS-DVB-AA latex was prepared as follows. A mixture of styrene (50 g) and DVB (0.5 g) were degassed with N_2 for 30 minutes, as was water (200 g) in a jacketed reactor equipped with overhead stirrer. Styrene/DVB (22 mL) was then transferred by syringe to the aqueous phase under stirring at 300 rpm, before the temperature was increased to 70°C. A degassed solution of KPS (0.2 g in 5 mL) was added to the reaction and it was allowed to continue for 3 hours, after which time it had reached 67.8% conversion, as determined by gravimetry. Acrylic acid (15 g) was degassed separately with N_2 for 30 minutes after the reaction had been running for 2.5 hours. At the 3 hour mark AA (1.9 mL) was transferred via syringe, and the reaction allowed to continue for a further 3 hours - at which point it had reached

77.6% conversion as determined by gravimetry. Characterization of the PS-DVB-AA copolymer latex can be found in **Appendix II.1**.

To create the multifaceted cuprous oxide particles seen in **Figure 1.8**, a similar reaction to that for the cubes in **Section 1.4.3** was carried out, but with 1 mL of the 9.4 mL water containing PS-DVB-AA particles at 1% wt.

1.4.5. Synthesis of Fe_2O_3 pseudocubes, prolate spheroids, and ellipsoids.

Iron(III) chloride hexahydrate (2.0 M, 100 mL) was added to a 200 mL pyrex jar along with an aqueous solution (10 mL) containing various concentrations of sodium sulfate (0 M, 1 x 10^{-2} M, 3 x 10^{-2} M). Sodium hydroxide solution (6.0 M, 90 mL) was slowly fed into the solution under vigorous stirring over a period of 5 minutes. The bottle was sealed with a lid and Teflon tape, before being transferred to an oven preheated to 100°C, where it was left for 8 days.

The product was cleaned by three rounds of centrifugation into DIW before PVP-K30 (10.0 g) was added and the solution was allowed to stir for 24 hours to ensure complete adsorption. The particles were then cleaned via a further 3 rounds of centrifugation/dispersion in water.

1.4.6 Synthesis of Fe_2O_3@SiO_2 ellipsoids and the corresponding hollow SiO_2 ellipsoids

In all of the following reactions, the particles had been previously stabilized by an excess of PVP-K30, which was removed from solution by centrifugation and redispersal of the particles-PVP into water.

Both reactions were identical except for the fact that one had TEOS added whilst in an ultrasound bath and the other whilst stirring on a hotplate. The reaction conditions were as follows. Fe_2O_3 particles stabilized with physisorbed PVP-K30 (2 g, 130.8 m^2) were dispersed in ethanol (100 mL) and water (3 mL). To this was added NH_4OH (2 mL, 18.1 M), followed by TEOS (2 mL) in equiponderant ethanol in 0.5 mL batches every 30 minutes i.e. over 4 hours. The reaction was allowed to proceed for a further 1 hour before the particles were collected by centrifugation and purified with three rounds of centrifugation and redispersal into DIW at 1,000 g.

1.4.7 Initial synthesis of hollow SiO_2 particles templated on SOCAL P3 (1st generation)

SOCAL P3 (20 g) was stabilized through physisorption of PVP-K30 in water (2% wt.). Excess PVP was removed through centrifugation and redispersal into the reaction mixture, which consisted of ethanol (190 mL) and deionized water (10 mL). Stirring was allowed to continue for 20 minutes before the addition of ammonium hydroxide (4 mL). TEOS (20 mL) was added via syringe pump at a rate of 1 $mL \cdot hr^{-1}$ i.e. over 20 hours. The reaction was stopped after 24 hours, and the particles cleaned, by three rounds of centrifugation at 4,200 g for 2 minutes into DIW. As generated $CaCO_3@SiO_2$ particles were then redispersed in DIW (200 mL) and more PVP-K30 (1 g) was added to the dispersion in order to prevent any particle sintering/destabilization during the acid treatment step. Physisorption was allowed to proceed for 24 hours before the particles were cleaned via two rounds of centrifugation, redispersing into DIW to remove excess PVP in the aqueous phase. A solution of HCl (600 mL, 2.0 M) was then drip fed into the dispersion under stirring

over the course of about three hours to ensure removal of the $CaCO_3$ template. Particles were cleaned via three rounds of centrifugation at 4,200 g for 2 minutes, redispersing into deionized water.

1.4.8 Investigating the effect of reaction parameters on the thickness of SiO_2 shell as a means to reduce particle fragmentation

The effect of the reaction parameters on SiO_2 shell thickness and pore volume/area was investigated, namely the ethanol:water ratio and the concentration of ammonia. **Table 1.23- Table 1.26** give the exact synthesis conditions used. All reactions were carried out with TEOS feed rates of 2 $mL \cdot hr^{-1}$ i.e. over 5 hours. The reactions were stopped and cleaned via centrifugation three times into DIW at the end of the feed. Total volume of all systems = 50 mL. Surface area of all systems is ~ 50 m^2.

Acid etch was carried out by drip feeding a 2 molar excess (w.r.t. $CaCO_3$) of acetic acid (0.5 M) over the course of about 2 hours. Particles were then cleaned by three rounds of centrifugation into DIW before analysis.

Table 1.23. Synthesis conditions used in the sample A1.

Reagent	Volume (mL)	Mass (g)	Mols
SOCAL P3-PVP	1.79(cm^3)	5	-
Ethanol	46.5	36.7	0.796
Water (TOTAL)	2.5 (3.15)	3.15	0.175
NH_4OH (35% - 18.1M)	1 (0.35)	0.88 (0.31)	(0.01)
TEOS	10	9.4	0.045

Table 1.24. Synthesis conditions used in the sample A2.

Reagent	Volume (mL)	Mass (g)	Mols
SOCAL P3-PVP	-	5	-
Ethanol	16.6	13.1	0.284
Water (TOTAL)	32.4 (33.05)	33.05	1.836
NH_4OH (35% - 18.1M)	1 (0.35)	0.88 (0.31)	(0.01)
TEOS	10	9.4	0.045

Table 1.25. Synthesis conditions used in the sample A3.

Reagent	Volume (mL)	Mass (g)	Mols
SOCAL P3-PVP	-	5	-
Ethanol	16.6	13.1	0.284
Water (TOTAL)	29.8 (33.05)	33.05	1.836
NH_4OH (35% - 18.1M)	5 (1.75)	4.4 (1.54)	(0.044)
TEOS	10	9.4	0.045

Table 1.26. Synthesis conditions used in the sample A4.

Reagent	Volume (mL)	Mass (g)	Mols
SOCAL P3-PVP	-	5	-
Ethanol	16.6	13.1	0.284
Water (TOTAL)	26.55 (33.05)	33.05	1.836
NH_4OH (35% - 18.1M)	10 (3.5)	8.8 (3.08)	(0.088)
TEOS	10	9.4	0.045

1.4.9 Formulation of waterborne coatings containing SOCAL P3 and 1st/2nd generation hollow SiO_2 particles

Formulation details are given in **Table 1.27-Table 1.29** for the waterborne coatings with pigment consisting of SOCAL P3, hollow SiO_2 thin shell (1st generation), and hollow SiO_2 thick shell (2nd generation). Binder pH was adjusted to 8.85 with concentrated NH_4OH. All formulations were dispersed with a Dispermat at 600 rpm for 2 hours, followed by stirring with a spatula, and a further round of dispersion for 2 hours at 800 rpm. They were then left to settle overnight.

Table 1.27. Formulation of 30% PVC waterborne coating with SOCAL P3 as pigment.

Reagent	**Mass (g)**	**Weight % Solids**	**Density Solids ($g \cdot cm^{-3}$)**	**Volume Solids (cm^3)**	**Density aqueous ($g \cdot cm^{-3}$)**	**Volume aqueous (cm^3)**
SOCAL P3	14.14	100	2.79	5.07	-	-
Water	58.92	0	0	0	1	59.82
S/BA/AA Binder	23.60	50	1.08	10.93	-	12.67
Orotan N-4045	1.44	45	2.05	0.32	1.30	0.79
Acrysol SCT-275	5.16	17.5	0.90	1.00	1	4.16

Table 1.28. Formulation of waterborne coating with hollow SiO_2 (thin shell, 1st generation) as pigment. [a] This is assuming that the particles are not fractured and that they still have the internal void volume.

Reagent	Mass (g)	Weight % Solids	Density Solids ($g \cdot cm^{-3}$)	Volume Solids (cm^3)	Density aqueous ($g \cdot cm^{-3}$)	Volume aqueous (cm^3)
Hollow SiO_2	1.03	100	0.20[a]	5.07	-	-
Water	58.92	0	0	0	1	58.92
S/BA/AA Binder	24.29	50	1.08	11.25	-	13.04
Acrysol SCT-275	5.04	17.5	0.90	0.98	1	4.16

Table 1.29. Formulation of waterborne coating with hollow SiO_2 (thick shell, 2nd generation) as pigment. [a] This is assuming that the particles are not fractured and that they still have the internal void volume.

Reagent	Mass (g)	Weight % Solids	Density Solids ($g \cdot cm^{-3}$)	Volume Solids (cm^3)	Density aqueous ($g \cdot cm^{-3}$)	Volume aqueous (cm^3)
Hollow SiO_2	1.63	100	0.32[a]	5.07	-	-
Water	58.92	0	0	0	1	58.92
S/BA/AA Binder	24.37	50	1.08	11.28	-	13.09
Acrysol SCT-275	5.04	17.5	0.90	0.98	1	4.16

Films were applied to black and white Lenetta panels with a multifilm thickness applicator bar (**Appendix II.7**, **Figure II.3**). They were then left to dry

overnight at room temperature before acquisition of the digital photographs seen in **Figure 1.29** and **Figure 1.41**.

1.5 References

(1) Lambourne, R. *Paint and Surface Coatings*; Ellis Horwood Limited, 1993.

(2) Stoye, D.; Freitag, W. *Paints, Coatings and Solvents*; 2nd ed.; Wiley-VCH, 1998.

(3) Keddie, J. L. *Mater. Sci. Eng.* **1997**.

(4) Protzman, T. F.; Brown, G. L. *J. Appl. Polym. Sci* **1960**, *IV*, 81–85.

(5) Zohrehvand, S.; Te Nijenhuis, K. *J. Colloid Interface Sci.* **2005**, *288*, 75–82.

(6) Emélie, B.; Schuster, U.; Eckersley, S. *Prog. Org. Coat.* **1998**, *34*, 49–56.

(7) Nelson, K.; Deng, Y. *J. Colloid Interface Sci.* **2008**, *319*, 130–139.

(8) Braun, J. H.; Baidins, A.; Marganski, R. E. *Prog. Org. Coat.* **1992**, *20*, 105–138.

(9) Keddie, J. L.; Meredith, P.; Jones, R. A. L.; Donald, A. M. *Langmuir* **1996**, *12*, 3793–3801.

(10) Asbeck, W. K.; van Loo, M. *Ind. Eng. Chem.* **1949**, *41*, 1470–1475.

(11) Adkins, A. S. US Pat., 5,171,631 **1992**.

(12) Anwari, F. *J. Coat. Technol.* **1991**, *63*, 35–46.

(13) www2.dupont.com/Titanium_Technologies/en_US/news_events/article20130530.html, Accessed on 01/08/13.

(14) Akiwumi, F. A.; Butler, D. R. *Environ. Monit. Assess.* **2008**, *142*, 309–318.

(15) Http://www.tdma.info/fileadmin/pdf/substainability/TiO2%20Carbon%20footprint%20number%20presentation_June%202012.pdf, Accessed on 01/08/13.

(16) Sun, Z.; Luo, Y. *Soft Matter* **2011**, *7*, 871.

(17) Field, J. R.; Scheidemantel, B. WIPO Patent, WO2003097227 A1 **2003**.

(18) Mcdonald, C. J.; Devon, M. J. *Adv. Colloid Interface Sci.* **2002**, *99*, 181–213.

(19) Kowalski, A.; Vogel, M.; Blankenship, R. M. U.S. Pat., 4,427,836 **1984**.

(20) Cardinal, C. M.; Francis, L. F.; Scriven, L. E. *J. Coat. Technol. Res.* **2009**, *6*, 457–469.

(21) Itou, N.; Masukawa, T.; Ozaki, I.; Hattori, M.; Kasai, K. *Coll. Surf. A* **1999**, *153*, 311–316.

(22) Beppu, M. M.; de Oliveira Lima, E. C.; Sassaki, R. M.; Galembeck, F. *J. Coat. Technol.* **1997**, *69*, 81–88.

(23) Silva, C. A.; Galembeck, F. *Coll. Surf. A* **2010**, *363*, 146–154.

(24) Vukusic, P.; Hallam, B.; Noyes, J. *Science* **2007**, *315*, 348.

(25) Hallam, B. T.; Hiorns, A. G.; Vukusic, P. *Applied optics* **2009**, *48*, 3243–3249.

(26) Wiersma, D. S. *Nature Photonics* **2013**, *7*, 188–196.

(27) Lou, X. W.; Archer, L. A.; Yang, Z. *Adv. Mater.* **2008**, *20*, 3987–4019.

(28) Sacanna, S.; Pine, D. J. *Curr. Opin. Colloid In.* **2011**, *16*, 96–105.

(29) Zhang, J.; Liu, H.; Wang, Z.; Ming, N.; Li, Z.; Biris, A. S. *Adv. Func. Mater.* **2007**, *17*, 3897–3905.

(30) Botterhuis, N. E.; Sun, Q.; Magusin, P. C. M. M.; Van Santen, R. A.; Sommerdijk, N. A. J. M. *Chem. Eur. J.* **2006**, *12*, 1448–1456.

(31) Qian, H.; Lin, G.; Zhang, Y.; Gunawan, P.; Xu, R. *Nanotechnology* **2007**, *18*, 355602 (1–6).

(32) Donath, E.; Sukhorukov, G. B.; Caruso, F.; Davis, S. A.; Möhwald, H. *Angew. Chem.* **1998**, *37*, 2201–2205.

(33) Graf, C.; Vossen, D. L. J.; Imhof, A.; Van Blaaderen, A. *Langmuir* **2003**, *19*, 6693–6700.

(34) Depew, H. A.; Eide, A. C. *Ind. Eng. Chem.* **1940**, *32*, 537–540.

(35) Wriedt, T. *Part. Part. Syst. Charact.* **2002**, *19*, 256–268.

(36) Sui, Y.; Fu, W.; Yang, H.; Zeng, Y.; Zhang, Y.; Zhao, Q.; Li, Y.; Zhou, X.; Leng, Y.; Li, M.; Zou, G. *Cryst. Growth Des.* **2010**, *10*, 99–108.

(37) Wang, Z.; Luan, D.; Li, C. M.; Su, F.; Madhavi, S.; Yin, F.; Boey, C.; Lou, X. W. *J. Am. Chem. Soc.* **2010**, *132*, 16271–16277.

(38) Sugimoto, T.; Muramatsu, A.; Sakata, K.; Shindo, D. *J. Colloid Interface Sci.* **1993**, *158*, 420–428.

(39) Liu, G.; Li, L.; Yang, X. *Polymer* **2008**, *49*, 4776–4783.

(40) Liu, G.; Yang, X.; Wang, Y. *Langmuir* **2008**, *24*, 5485–5491.

(41) Iijima, M.; Yonemochi, Y.; Kimata, M.; Hasegawa, M.; Tsukada, M.; Kamiya, H. *J. Colloid Interface Sci.* **2005**, *287*, 526–533.

(42) Wheeler, S. A.; Barcock, R.; Pearce, C.; Jefferson, G.; Woods, D.; Emmett, S. N.; Perez-Amoros, J. U.S. Pat., 8,362,132 B2, **2013**.

(43) Auger, J-C.; Martinez, V. A.; Stout, B. *J. Coat. Technol. Res.* **2009**, *6*, 89–97.

(44) Ghosh, G. *Opt. Commun.* **1999**, *163*, 95–102.

(45) Chen, J-F.; Wang, J-X.; Liu, R-J.; Shao, L.; Wen, L-X. *Inorg. Chem. Comm.* **2004**, *7*, 447–449.

(46) Bala, H.; Zhang, Y.; Ynag, H.; Wang, C.; Li, M.; Lv, X.; Wang, Z. *Colloids Surf A.* **2007**, *294*, 8–13.

(47) Lu, Y.; McLellan, J.; Xia, Y. *Langmuir* **2004**, *20*, 3464–3470.

(48) http://www.washingtonpost.com/wp-dyn/content/article/2008/03/08/AR2008030802595.html Accessed on 06/08/13.

(49) Kuo, C.-H.; Huang, M. H. *J. Phys. Chem. C* **2008**, *112*, 18355–18360.

(50) Takiyama, K. *Japan J. Chem.* **1958**, *31*, 950 – 953.

(51) Muñoz-Espí, R.; Qi, Y.; Lieberwirth, I.; Gómez, C. M.; Wegner, G. *Chem. Eur. J.* **2005**, *12*, 118–129.

(52) Park, J. M.; Hong, S. M. *J. Ind. Eng. Chem.* **2001**, *7*, 23–29.

(53) Thies-Weesie, D. M. E.; Philipse, A. P.; Kluijtmans, G. J. M. *J. Colloid Interface Sci.* **1995**, *174*, 211–223.

(54) Ohmori, M.; Matijević, E. *J. Colloid Interface Sci.* **1992**, *150*, 594–598.

(55) Rossi, L.; Sacanna, S.; Irvine, W. T. M.; Chaikin, P. M.; Pine, D. J.; Philipse, A. P. *Soft Matter* **2011**, *7*, 4139–4142.

(56) Zhou, J.; Wu, W.; Caruntu, D.; Yu, M. H.; Martin, A.; Chen, J. F.; O'Connor, C. J.; Zhou, W. L. *J. Phys. Chem. C* **2007**, *111*, 17473–17477.

(57) Liu, S.; Wei, M.; Sui, X.; Cheng, X.; Cool, P.; Van Tendeloo, G. *J. Sol-Gel Sci. Technol.* **2009**, *49*, 373–379.

(58) Amiche, F. US. Pat., 6,221,326 B1 **1997**.

(59) Sjöberg, E. L.; Rickard, D. T. *Geochim. Cosmochim. Ac.* **1984**, *48*, 485–493.

(60) Dodds, W. S.; Stutzman, L. F.; Sollami, B. J. *Ind. Eng. Chem. Chem. Eng. Data Series* **1956**, *1*, 92–95.

(61) Hawley, J.; Pytkowicz, R. M. *Geochim. Cosmochim. Ac.* **1969**, *33*, 1557–1561.

(62) Tirumkudulu, M. S.; Russel, W. B. *Langmuir* **2004**, *20*, 2947–2961.

(63) Zhang, L.; D'Acunzi, M.; Kappl, M.; Auernhammer, G. K.; Vollmer, D.; Van Kats, C. M.; Van Blaaderen, A. *Langmuir* **2009**, *25*, 2711–2717.

(64) Mosquera, M. J.; Bejarano, M.; De la Rosa-Fox, N.; Esquivias, L. *Langmuir* **2003**, *19*, 951–957.

(65) Sato, S.; Murakata, T.; Suzuki, T.; Ohgawara, T. *J. Mater. Sci.* **1990**, *25*, 4880–4885.

(66) Kim, J. H.; Yoon, S. B.; Kim, J-Y.; Chae, Y. B.; Yu, J-S. *Colloids Surf. A* **2008**, *313-314*, 77–81.

(67) Zhang, Q.; Zhang, T.; Ge, J.; Yin, Y. *Nano lett.* **2008**, *8*, 2867–71.

(68) Chen, Y.; Chu, C.; Zhou, Y.; Ru, Y.; Chen, H.; Chen, F.; He, Q.; Zhang, Y.; Zhang, L.; Shi, J. *Small* **2011**, *7*, 2935–44.

(69) Musgo, J.; Echeverría, J. C.; Estella, J.; Laguna, M.; Garrido, J. J. *Micropor. Mesopor. Mat.* **2009**, *118*, 280–287.

(70) Murakata, T.; Sato, S.; Ohgawara, T.; Watanabe, T.; Suzuki, T. *J. Mater. Sci.* **1992**, *27*, 1567–1574.

(71) Taniguchi, T.; Kashiwakura, T.; Inada, T.; Kunisada, Y.; Kasuya, M.; Kohri, M.; Nakahira, T. *J. Colloid Interface Sci.* **2010**, *347*, 62–68.

(72) Sacanna, S.; Rossi, L.; Kuipers, B. W. M.; Philipse, A. P. *Langmuir* **2006**, *22*, 1822–1827.

(73) Völz, H. G. *Prog. Org. Coat.* **1985**, *13*, 153 – 169.

Chapter 2

"Improving the Dispersion of Hollow SiO_2 Pigments by Electrosteric Stabilization"

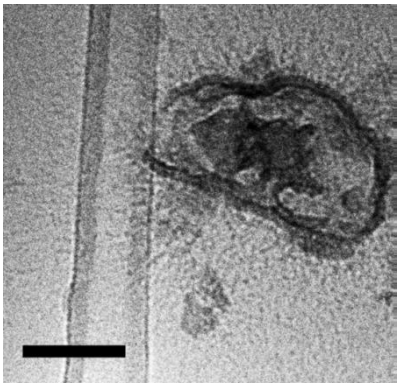

Pigment light scattering efficiency is dramatically affected by the degree of pigment dispersion in the dry film. In **Chapter 1** we synthesized hollow silica particles that were stabilized with poly(vinyl pyrrolidone) (PVP) in the coating.

We reasoned that we could impart electrosteric stabilization to the pigment particles by grafting hydrophilic, negatively charged, polyelectrolyte brushes from the surface. If we could grow long brushes (> 100 nm into solution) at reasonably high density then we could prevent particles from approaching each other within a distance that van der Waals attractive forces operate (typically at inter-particle distances < 10 nm). This would serve to reduce the number of pigment aggregates in the dry film and consequently improve upon the optical properties of the film.

To this end we functionalized the SiO_2 surface with a tertiary alkyl bromide atom transfer radical polymerization (ATRP) initiator that was stable to hydrolysis, achieved by linking to the surface through an amide bond. We then proceeded to

grow poly(styrene sulfonate) brushes from the surface via surface-initiated ATRP (SI-ATRP), producing polymer brushes that extended between 100-200 nm into solution. These conferred enhanced colloidal stability over the hollow SiO_2-PVP particles used as pigment previously in **Chapter 1**, as evidenced by freeze-thaw testing combined with laser diffraction measurements.

These hairy hollow silica particles were then dispersed into a waterborne coating as before and the contrast ratio determined by film reflectance measurements to deduce whether we had improved hiding power through enhanced pigment dispersion.

2.1 Introduction

In **Chapter 1** we demonstrated that a calcium carbonate filler used in paint formulations, SOCAL P3, could be used to fabricate hollow silica particles with the calcium carbonate used as the core in a sacrificial templating method following silica coating via a Stöber type synthesis.

One of the drawbacks of using these hollow particles in waterborne coating formulations was that they tend to cluster upon film formation, leading to derogative effects in the physical properties of the film, such as reduced hiding power.

Factors which affect the efficiency of a pigment in scattering photons can be thought of as being intrinsic and extrinsic to the material itself. Intrinsic properties include the particles' size,[1] shape,[2] and chemical make-up e.g. crystallinity.[3] Extrinsic factors on the other hand account for properties such as pigment volume concentration and dispersion of the particles in the coating (which is also partially dependent on the PVC as well as interparticle forces).[4,5]

Dry pigments often consist of aggregates of pigment particles which, upon paint formulation, need to be dispersed and broken up into their primary particle analogues using high shear.[6] Mechanical breakage of these agglomerates, by outplaying interparticle attractive interactions, often involves using a high shear blender such as a Dispermat, or using a dual asymmetric centrifugal mixer (DAC).

Dispersion agents are used in coatings formulations to adsorb onto the pigment surface in order to confer steric,[7] electrostatic,[8] or electrosteric stabilization,[9] which increase the barrier to agglomeration/aggregation once dispersed.

In addition, the thixotropic nature of the coating formulation slows the process of pigment collision, and thus lowers the probability for aggregation. Commonly, a loose network of aggregates will rebuild over a time frame of minutes to days.[10] Moderate shear conditions (such as the application of the coating with a paint brush) is often sufficient to break up these loose aggregates. However, drying of the wet film can lead to phase separation of colloidal components and clustering, as they come in closer proximity as a result of water evaporation.[11] This is undesirable.

Before we address how the dispersion of our hollow SiO_2 particles can be improved, let's first look at some of the factors which influence the stability of colloids in aqueous media.

Brownian motion (which is something we will deal more comprehensively with in **Chapter 4.1**) is the random movements of colloidal entities due to thermal fluctuations of solvent molecules that bombard the particle surface, transferring kinetic energy. This motion of particles can lead to particle aggregation upon collision with one another. The aggregation process is driven by attractive van der Waals forces between particles.[12] Note that the van der Waals force can be repulsive in nature, when the dielectric constant of the liquid medium is in between that of the two interacting interfaces.[13]

Charges on the surface of a colloidal particle in high dielectric media (e.g. water) lead to the formation of an electrical double layer, whereby oppositely charged ions from solution will associate with the charged surface of the particle. This electric double layer can be sub-divided into two sections. Firstly, there is a

tightly bound "Stern layer" of oppositely charged surface ions to the groups present on the surface of the colloid due to electrostatic interactions.[14] Further out there is a diffuse "Gouy-Chapman layer" of mixed ions (but with a higher concentration of counter-ions with respect to the charge of the surface due to Coulombic interactions).[15,16] The thickness of the double layer is also known as the Debye length, and is dependent on the ionic strength of the medium. A higher ionic strength (either higher concentration of ions or higher valency ions) suppresses the Debye length to a greater extent.

Within the diffuse layer there exists a "slipping plane", which is the boundary of liquid that is effectively attached to the particle. The electric potential at this boundary layer is called the zeta potential, ζ, measured in mV. Potential charge density eventually drops to zero in the bulk medium as the distance from the particle surface increases. These concepts are illustrated in **Figure 2.1**.

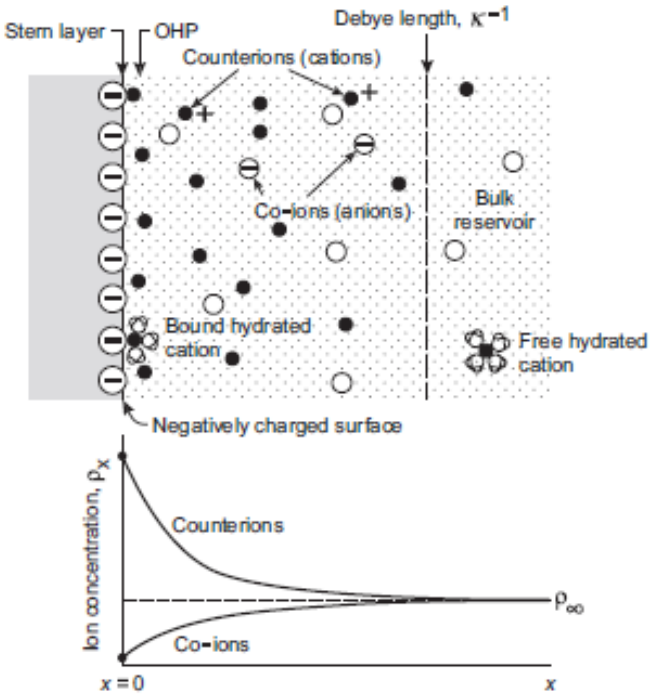

Figure 2.1. Schematic of the electrical double layer of a negatively charged colloidal particle (**top**), with a plot showing the ion concentration as a function of distance from the surface of the particle (**bottom**).Image from reference.[17]

Zeta-potential is a measure of colloidal stability which, from an experimental viewpoint, affords an electrostatically stabilized dispersion of particles when its magnitude is ±20-30 mV. Electrophoretic light scattering is used in the determination of zeta-potential. For more details on the theory behind these measurements the reader is referred to **Appendix I.7**.

Further advancement to the theory of colloidal stability was made by Derjaguin and Landau,[18] and Verwey and Overbeek,[19] in what has become known as DLVO theory. Essentially it is a quantitative method for modelling the stability of colloidal dispersions by adding the electrostatic repulsion contribution to the van der Waals attractive forces, giving a potential energy plot as a function of separation

distance between two approaching bodies in solution, an example of which is shown in **Figure 2.2**.

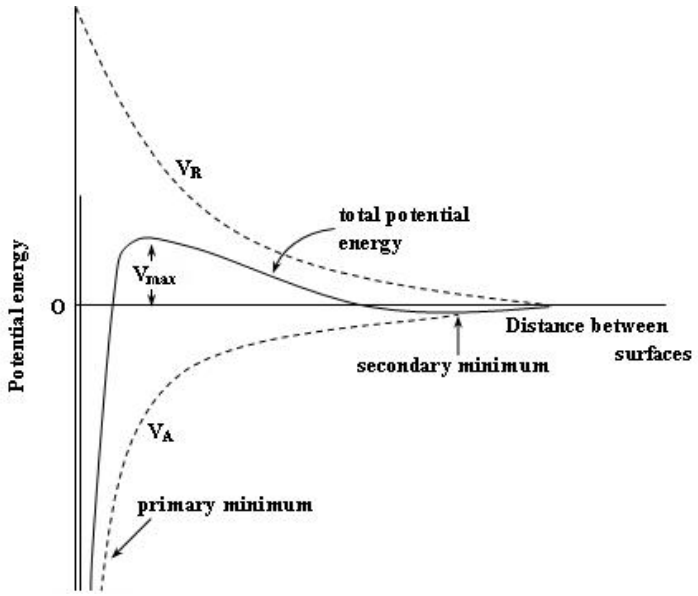

Figure 2.2. DLVO plot of interaction energy as a function of particle distance for two approaching colloidal bodies.[20]

Note that the negative y-axis corresponds to an attractive force and the positive y-axis corresponds to a repulsive force. The height of the repulsive barrier, V_{max}, dictates the amount of energy that must be overcome as particles approach one another for the system to irreversibly coagulate.

When a macromolecule wets the interface of a particle it can spread across and adhere to the surface to give an occupied volume several nanometers thick.[21] However, when the surface density of the macromolecule (or size) is increased, the thickness of the exclusion zone can reach well over 100 nm.[22] Steric stabilization arises when two particles with similar adsorbed macromolecules approach one

another, causing interpenetration of the polymer brushes. This leads to a repulsive force due to the local increase in the concentration of polymer (and hence reduction in the concentration of solvent, causing an increase in the osmotic pressure). Furthermore, the interpenetration of the polymer chains causes them to lose mobility, which is highly unfavorable from an entropic point of view. Strictly speaking, steric stabilization is in the absence of electrostatic interactions, however in most cases these forces contribute to some degree as well. When there is a combination of steric and electrostatic repulsion at the colloid interface then it is said to be electrosterically stabilized.[23] It is widely recognized that electrosteric stabilization of pigment particles can impart enhanced stability over a range of ionic strengths, pH and shear, when compared to pure electrostatic or steric repulsion.[24]

Another phenomenon that one has to keep in mind in colloidal formulations is that of depletion flocculation. Here colloidal particles or macromolecules which are dispersed or dissolved in the water phase induce aggregation of other colloidal particles (e.g. pigment or binder), driven by a locally induced osmotic underpressure between two colloidal particles.[25,26] Bridging flocculation must also be limited. This is where particle flocculation is induced by large macromolecules that can adhere to the surfaces of multiple particles.

Previously we utilized physisorbed PVP-K30 (Mwt. = 40,000 $g \cdot mol^{-1}$) to provide steric stabilization for our hollow SiO_2 colloids. PVP is a non-ionic homopolymer that predominantly provides steric stabilization. Polycarboxylic acids like Orotan N-4045 on the other hand are an effective class of stabilizer for pigments like SOCAL P3 that provide electrosteric repulsion between particles. For this reason

we decided to investigate systems that would confer electrosteric stabilization to our hollow SiO_2 particles, with the aim of improving their degree of dispersion and consequently, their opacity. It is worth noting at this point that Orotan N-4045 is not a suitable dispersion agent for SiO_2. Many of the dispersion agents used in coatings carry negative charges, and for this reason they do not effectively wet the SiO_2 particles, as they also carry a negative charge.

If we were to grow polymeric brushes from the surface so that they are covalently bound to the surface of the hollow SiO_2 particles, then adsorption-desorption kinetics will not be an issue as they would for physisorbed species.[27]

A grafted layer of electrosteric stabilizer would serve as a protective layer, aiding easy dispersion of dried pigment aggregates without the need for high shear dispersion (assuming that the graft density is high enough). The shear stage is a very time and energy intensive process when performed at an industrial scale that also generates a lot of heat.[28]

There are numerous approaches to growing polymeric brushes from silica surfaces.[29–32] Our approach is to use SI-ATRP. We chose negatively charged brushes to confer increased charge stability at the coating pH ~ 9. In this sense we impart electrosteric stabilization to the particles, that is both electrostatic and steric hindrance to aggregation.

In the following discussion we shall look at some of the salient features of ATRP, in particular surface initiated processes.

The proposed mechanism for ATRP involves an equilibrium, K_{ATRP}, between dormant alkyl-halogen species, R-X, and a transition metal-ligand complex, Mt^nL, with the radical R^* species and the higher oxidation state transition metal complex, $X\text{-}Mt^{n+1}L$ (**Figure 2.3**). The forwards reaction is referred to as the activation step and the reverse reaction is referred to as the deactivation step. It is the R^* species which can undergo polymerization with the unsaturated monomer (chain transfer is also possible) via a radical propagation process, having conventional free radical rate coefficients for propagation, k_p, and termination, k_t.[33]

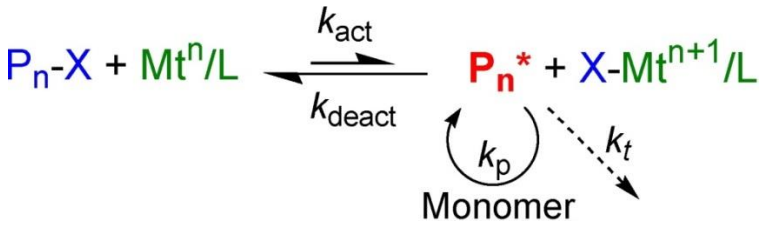

Figure 2.3. Schematic depicting the mechanism behind ATRP, involving a dynamic equilibrium between dormant and active species.[34]

Surface initiated-ATRP (SI-ATRP) as a method to grow polymer brushes from silica particles has been studied widely. For a detailed overview of SI-ATRP on a variety of substrates, including siliceous oxides, the reader is referred to the review by Klok et al.[35]

In order to grow polymer brushes from a silica surface it must first be functionalized with a suitable initiator moiety for the ATRP process. A common route is to react surface silanol groups with a silane agent bearing an ATRP initiator. Alternatively, an ATRP macroinitiator can be physisorbed onto the surface for polymer to be grafted from.

Huang and Wirth were the first to report growth of polymer brushes from silica particles via an ATRP process. In this work they modify the surface silanol groups with a trichlorosilane agent, terminated with a benzyl chloride group that is used as initiator in the growth of polyacrylamide brushes (**Figure 2.4**). The polymerization equilibrium is mediated by a $Cu(bpy)_2Cl$ complex.[36]

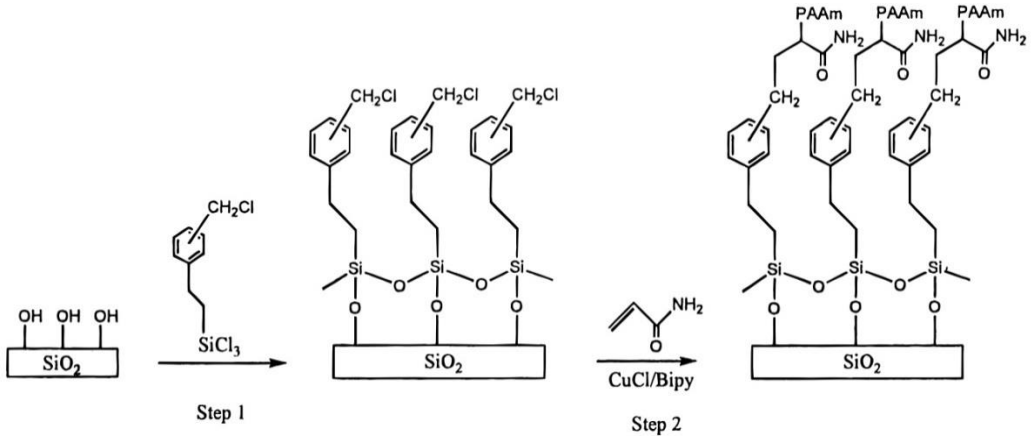

Figure 2.4. Schematic depicting the route taken by Huang and Wirth to functionalize the surface of silica particles with a trichlorosilane, bearing a pendant benzyl chloride used to initiate the ATRP growth of polyacrylamide brushes. Image from reference.[36]

Armes *et al.* demonstrated ATRP from an anionic sol that had been stabilized with a cationic macroinitiator bearing tertiary -bromo groups (**Figure 2.5**). The limitation of this procedure was that monomers bearing anionic charge could not be directly grafted from the cationic macroinitiator on the surface, which they attribute to bridging flocculation.[37]

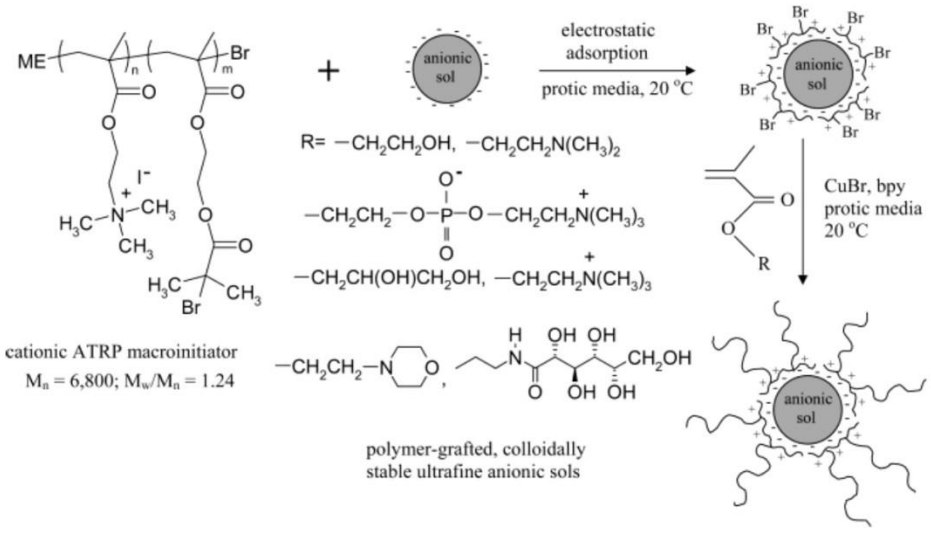

Figure 2.5. Schematic of the process used by Armes et al. whereby they adsorb a cationic macroinitiator for the ATRP process onto anionic colloids. Image from reference. [37]

Another example of SI-ATRP from the Armes group utilized the silane ester 3-(dimethylethoxysilyl)propyl-2-bromoisobutyrate (**Figure 2.6 A**) to covalently modify the surface of SiO_2 particles with a molecule capable of ATRP initiation, from which polymer could be grafted.[38]

A downside of using this specific silane agent is the hydrolytic susceptibility of the ester group. As we have to treat our $CaCO_3$@SiO_2 particles with acid to remove the calcium carbonate core then there is a risk of hydrolysis of the anchoring group, and thus loss of ATRP grown polymer is considerable.

Therefore we chose to use an ATRP initiator with an amide link to the particle surface instead (**Figure 2.6 B**).

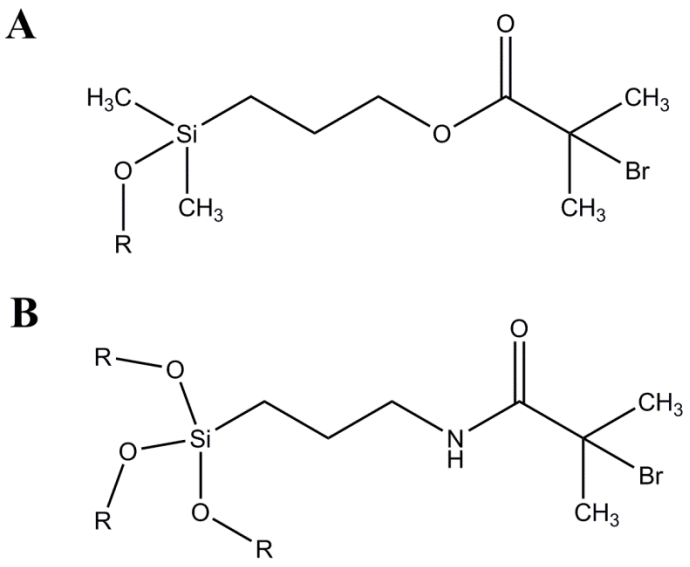

Figure 2.6. Chemical structure of (**A**) A commonly used silane based ATRP initiator containing an ester bond and (**B**) the ATRP initiator that we have made for use in this study containing a more hydrolytically stable amide bond. Where R = siloxane linkages to particle surface.

We used poly(styrene sulfonate) as a polyelectrolyte brush because it is highly charged at the coating pH~9 (its pKa is approximately 2.5), and it also confers steric stabilization i.e. electrosteric stabilization.[39]

A complication of SI-ATRP however is that cross-coupling termination between chains can lead to interparticle cross-linking, which if prevalent eventually leads to the formation of a gel. In order to combat this unwanted effect one can either lower the number of particles per volume of liquid, that is $N_{p,}$ or ensure that the number of active radicals at any one time is kept low i.e. $k_{deact} >> k_{act}$.[40]

In the field of ATRP, a recent breakthrough showed that polymerization in polar solvents could be carried out using Cu(0) instead of Cu(I) as the catalyst. This

process is referred to as SET-LRP (**Figure 2.7**). According to Percec and co-workers,[41] the initiating species is Cu(0) which gets oxidized to Cu(I)XL. Two of these transient and unstable compounds disproportionate into their Cu(0) and Cu(II)X_2L analogues. There is much debate over the mechanism as some would argue that there are issues with the stoichiometry balance in the mechanism proposed.

We therefore decided to use Cu(0) powder alone to generate radicals on the surface of our particles in the presence of water to afford an ultrafast polymerization.

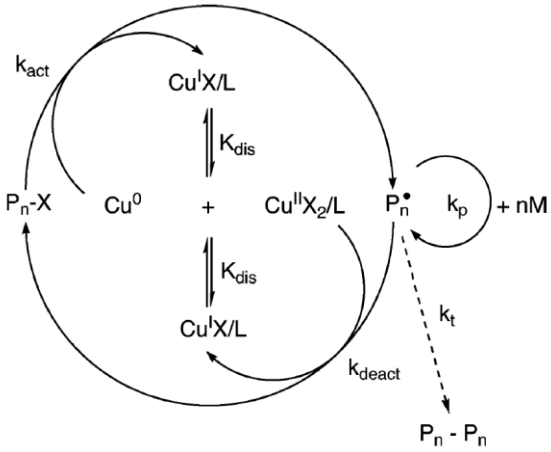

Figure 2.7. Schematic of the process involved in "SET-LRP" that involves the use of Cu(0) to form the transient Cu(I) complex which disproportionates into the corresponding Cu(II) /Cu(0) species.[41]

In this work we demonstrate the synthesis of hollow SiO_2 particles with poly(styrene sulfonate) grafted from the surface via a SI-ATRP type process, with the aim of increasing the colloidal stability of the pigment particles by electrosteric stabilization i.e. vs. predominantly steric PVP used to disperse the hollow SiO_2 particles in **Chapter 1** (and small electrostatic contribution from PVP). By imparting

improved pigment dispersion in the dry film we hope to increase opacity accordingly.

$CaCO_3$@SiO_2 particles are first functionalized with an ATRP initiator anchored to the surface by an amide linkage. We then demonstrate SI-ATRP growth of poly(styrene sulfonate) brushes from the particle surface. It must be stressed that living control was not our aim in this synthesis; we purely wish to grow polymer brushes from the silica surface without interparticle cross-linking, which was achieved.

Colloidal stability of SOCAL P3-Orotan N-4045, hollow SiO_2-PVP and hollow SiO_2-graft-poly(NaSS) was examined by freeze-thaw stability of waterborne dispersions of the particles. Results indicated that grafting the polymeric brushes from the surface was indeed beneficial to colloidal stability as compared to physisorbed PVP.

Paint formulations were made up, as in **Chapter 1**, and the polymer films were analyzed accordingly.

2.2 Results and Discussion

2.2.1 Synthesis and characterization of the $CaCO_3$@SiO_2 particles with ATRP initiator functionalized surface

Before we can grow polymer brushes from the $CaCO_3$@SiO_2 particles, we need to first functionalize the surface with an ATRP initiator. In order to confer hydrolytic stability of the anchoring group we chose to link the initiator to the surface through an amide linkage.

To this end the particles were first reacted with (3-aminopropyl)triethoxysilane (APTES), to functionalize the surface with amine groups (**Figure 2.8**).[42] As functionalized $CaCO_3$@SiO_2 particles were dispersed in a basic ethanol/water solution, similar to that used in the coating procedure. Following a feed of APTES the dispersion was heated to reflux for several hours to enhance the rate of hydrolysis and condensation onto the particle surface. For more details please refer to experimental **Section 2.4.4**.

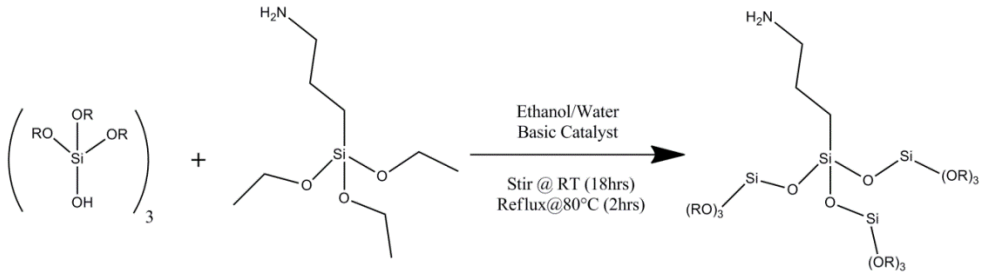

Figure 2.8. Schematic of the reaction between a SiO_2 nanoparticle surface and the organosilane monomer, APTES. Following stirring and reflux to promote covalent bonding, an amine functionalized SiO_2 nanoparticle is obtained.

SEM was used to image the sample following treatment with APTES to check for secondary nucleation, which was not apparent (**Figure 2.9**).

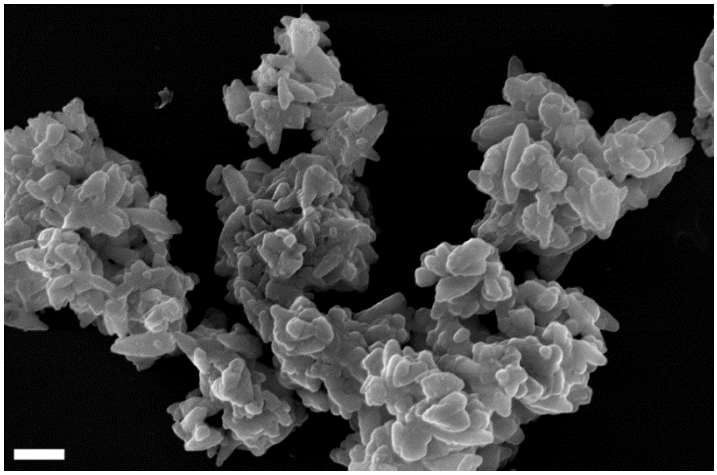

Figure 2.9. SEM image of the SOCAL P3@SiO_2-NH_2 particles. Scale bar = 1 µm.

CHN microanalysis was performed on a sample of hollow SiO_2 particles, and hollow SiO_2 particles that had been modified with APTES (**Table 2.1**). It is clear to see that there is an increase in nitrogen content after surface functionalization with APTES. All three elements tested for are present in both samples. This is reasonable to expect due to the inevitable inclusion of contaminants from the reaction in the amorphous silica matrix i.e. ammonia catalyst, and solvent molecules.[43]

Nevertheless, it would appear that there is a higher weight fraction of nitrogen and carbon in the APTES functionalized silica particles. Whilst this alone is not conclusive proof of functionalization (as some unreacted APTES could be trapped in the silica pores despite cleaning), when taken together with zeta-potential measurements (**Figure 2.12**), the Ninhydrin test (**Figure 2.13**), and the fact that subsequent analyses indicate that the reaction has successfully proceeded beyond this point as proposed, then it serves to reinforce the idea that the surface of the SiO_2 has been functionalized with -NH_2 groups.

Table 2.1. CHN analysis of hollow SiO_2 and hollow SiO_2-NH_2 particles. [a]Averaged over 2 runs.

Element	Sample	Average % wt/wt[a]
C	Hollow SiO_2	0.25
	Hollow SiO_2-NH_2	0.53
H	Hollow SiO_2	1.01
	Hollow SiO_2-NH_2	0.82
N	Hollow SiO_2	0.07
	Hollow SiO_2-NH_2	0.31

TGA measurements were then performed on the $CaCO_3$@SiO_2 nanocomposite, and that functionalized with APTES, in order to determine the mass fraction of SiO_2 (**Figure 2.10**).

Analysis of the APTES functionalized particles indicates that there is a marginal increase in shell thickness after APTES functionalization, but when one takes water loss into account there is likely only a monolayer. Further evidence of APTES functionalization will be demonstrated with zeta potential measurements and the "Ninhydrin" test for primary amines.

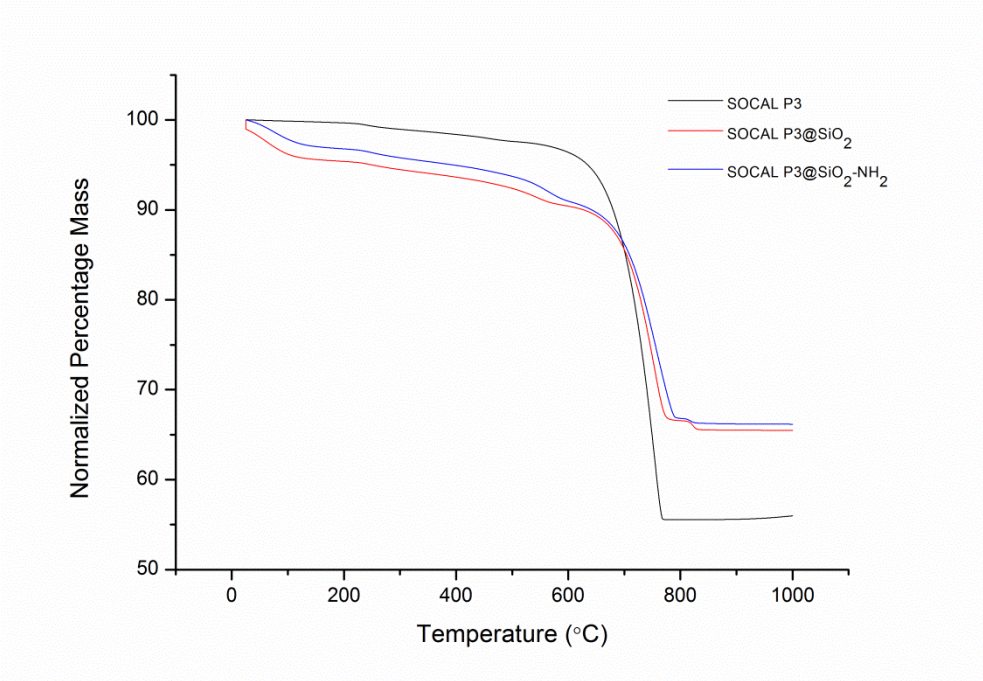

Figure 2.10. TGA plots of the normalized percentage mass for SOCAL P3, SOCAL P3@SiO_2, and SOCAL P3@SiO_2-APTES particles as a function of temperature.

As outlined in **Section 1.2.2.3**, TGA measurements provide us with a convenient way of determining the mass of silica shell in the nanocomposite, by comparing the retained mass with the original template following loss of CO_2 after heating to > 750°C.

The difference in mass between the SOCAL P3 template and the APTES functionalized SOCAL P3@SiO_2 particle is 10.2%. Note that we take the APTES functionalized sample as final SiO_2 conversion. Proceeding with the method outlined in **Section 1.2.2.3**, this gives an effective particle density for the hollow particles of 0.2765 g·cm^{-3}, if we are to assume that all of the air voids remain intact.

Reaction of the amine functionalized SiO_2 particle with α-bromoisobutyryl bromide (BiBB) converts the amine to an amide linkage (**Figure 2.11**). Amine

functionalized SiO_2 nanoparticles are dispersed in anhydrous THF and cooled to between 0-5°C. An excess of BiBB w.r.t. amine groups is then added, after the addition of an equimolar amount of pyridine w.r.t. BiBB as proton scavenger. For more details please refer to experimental **Section 2.4.5**.

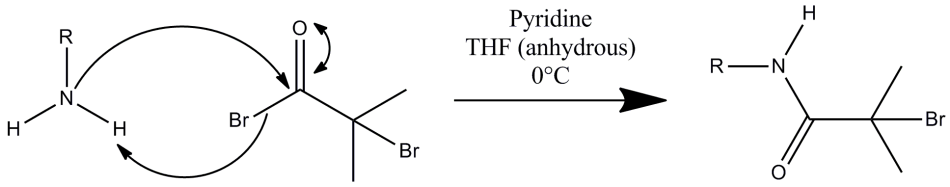

Figure 2.11. Schematic depicting the reaction between an amine functionalized nanoparticle and BiBB to yield an amide linkage and a functional group suitable to act as an initiator for an SI-ATRP polymerization in the subsequent growth of polymeric brushes from the nanoparticle surface.

This amide linkage confers hydrolytic stability to the anchoring group during acid etch of the $CaCO_3$ core. We have also now incorporated a tertiary alkyl bromide group on the surface which can function as an ATRP initiator for the growth of poly(styrene sulfonate) brushes that will confer electrosteric stabilization.

Due to the low mass fraction of functionalized moieties on the surface of the $CaCO_3$@SiO_2 particles, we found it difficult to characterize their presence via some of the more conventional molecular detection methods i.e. NMR and FTIR.

Zeta potential measurements however are a very convenient way of following surface functionalization.[44] For a more in-depth discussion of the theory behind electrophoretic light scattering measurements please refer to **Appendix I.7**. By

measuring the zeta potential of each sample as a function of salt concentration (**Figure 2.12** and **Appendix III.1**, **Tables III.1-III.5**) one can get a good idea of the true potential at the shear plane in the absence of counter-ions i.e. extrapolation to zero ionic strength.[45]

One would expect the sign of the zeta potential of calcium carbonate to be slightly negative at a pH = 6[46] (at which all subsequent measurements were performed). Interestingly, SOCAL P3 actually displays a slightly cationic zeta potential across the range of salt concentrations investigated. Others have found that when the pH is below the isoelectric point of calcite (8.2-8.4), there is an excess of positive cations over negative anions in solution,[47] which may help to explain our result of a positive zeta potential.

The zeta potential then switches sign and magnitude to a strongly negative potential following growth of a SiO_2 shell, as one would expect.[48]

Further functionalization of the shell with APTES then causes the potential to switch sign again to positive due to the primary amine groups at the surface. This is in good agreement with similar investigations in the literature.[49,50]

Reaction of the surface amine groups with BiBB yields an amide linkage with a tertiary alkyl bromide at the surface, causing the zeta-potential to switch sign to negative again as one would expect.[51]

As reference, the zeta potential of SOCAL P3@SiO_2-PVP K30 is given, which shows a retardation in magnitude when compared to bare SOCAL P3@SiO_2 due to screening effects. This phenomenon has been noted by others as well.[52]

All samples display rapid suppression of the double layer at a salt concentration > 0.1 M.

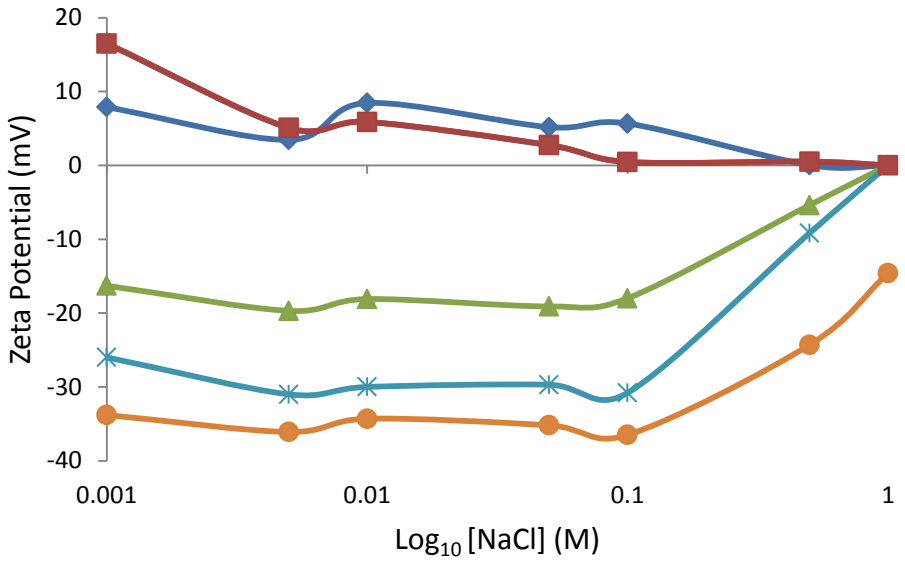

Figure 2.12. Zeta potential as a function of [NaCl] for SOCAL P3 (blue diamond), SOCAL P3@SiO_2 particles (orange circle), -NH_2 functionalized SOCAL P3@SiO_2 particles (red square), and -Br functionalized SOCAL P3@SiO_2 particles (cyan cross). For comparison SOCAL P3@SiO_2 particles with PVP K30 physisorbed is also given (green triangle). All measurements were performed at pH = 6 and averaged over at least 10 runs.

Further proof for the surface functionalization of the $CaCO_3$@SiO_2 particles with amine groups, and subsequently amide groups, can be seen by the change in color of aqueous particle dispersions after adding the reagent Ninhydrin.

When Ninhydrin is exposed to primary amine groups it becomes pink/purple due to the formation of the dye complex known as Ruhemann's purple,[53] and so it is often used to detect the presence of APTES on surfaces.[54] The development of a pink coloring on the nanocomposite particles qualitatively confirms that we have formed SOCAL P3@SiO_2-APTES particles (**Figure 2.13 A**).

When it is exposed to an amide then the imine salt formed with Nihydrin will be orange/yellow,[55] which is what we see following reaction of the primary amine with BiBB (**Figure 2.13 B**).

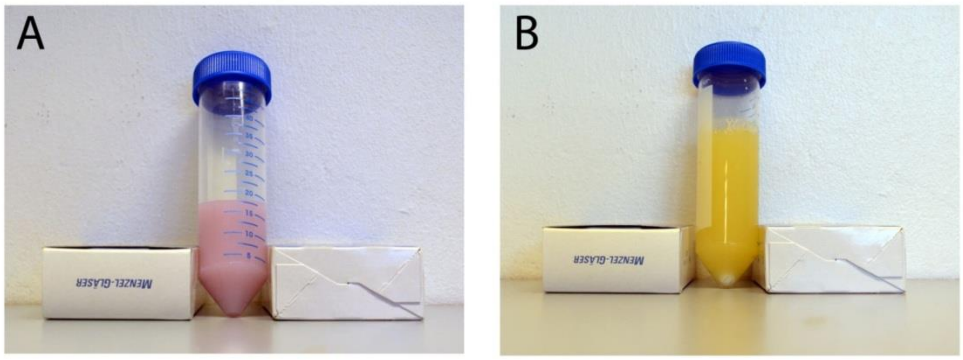

Figure 2.13. Digital photograph of SOCAL P3@SiO_2 particle dispersions exposed to Ninhydrin with (**A**) –NH_2 functionalized SiO_2 shell, and (**B**) -Br functionalized SiO_2 shell.

Testing for elemental bromine was performed by the oxygen flask method. Unfortunately the amount of bromine present in the sample was at the edge of the techniques' detection limit (**Table 2.2**), and makes sense if one considers the low weight fraction of nitrogen detected in the particles (**Table 2.1**).

Table 2.2. Bromine analysis of the hollow SiO_2 particles functionalized with the ATRP initiator using the oxygen flask method. [a] Averaged over 2 runs.

Element	Sample	Average % wt/wt[a]
Br	Hollow SiO_2-Br	$0 < x \leq 0.3$

The sample deviated from the blank over both runs indicating that there was a trace amount present. Again, whilst this is not conclusive proof of the attachment of the ATRP initiator, it still serves to reinforce data from zeta-potential measurements (**Figure 2.12**) and the Ninhydrin test shown above. We shall also see that the ATRP reaction successfully grew polymer brushes from the surface, which is proof enough of surface functionalization as this would not be possible without the presence of the initiator on the surface of the particles. It would be possible to work out graft density by dissolving the silica particles in HF and then analysing the number of polymer chains in solution, assuming that the distribution of the polymer molecular weights was known.

2.2.2 SI-ATRP of sodium styrene sulfonate grafted from $CaCO_3$@SiO_2 particles functionalized with ATRP initiator, and formation of hollow particle analogues

Following covalent attachment of the ATRP initiator onto the surface of the $CaCO_3$@SiO_2 nanocomposite, poly(NaSS) brushes were grown by a SI-ATRP polymerization in the presence of copper and PMDETA (see experimental **Section 2.4.6**). Initially the reaction medium appears white due to light scattering by the nanocomposite particles, however at the end of the reaction a significant amount of copper(II)XL is generated and so the supernatant of a successful reaction turns a dark blue in color (**Figure 2.14**). Note that it is still slightly opaque as there were still some particles present in this solution.

Figure 2.14. Digital photograph of the supernatant from the end of the SI-ATRP reaction, illustrating the formation of copper(II)XL.

Laser diffraction measurements were performed on the sample following APTES functionalization, reaction of the amine with BiBB, and growth of the poly(NaSS) brushes from the surface (**Figure 2.15** and **Appendix III.2**, **Table III.6**).

From the size distribution plot it can be seen that no aggregates are formed in any of the samples, except for a small population of larger particles in the –Br functionalized sample, which subsequently disappears in the product obtained from these particles with the poly(NaSS) brushes. This would indicate that this anomaly is due to dispersion issues present only in the Mie scattering analysis.

Growth of the polyelectrolyte brushes increases the apparent size slightly as one might expect.[56] Note that we are measuring the diffraction of light by the particle here and not the hydrodynamic radius, therefore we do not expect the brushes to scatter light strongly i.e. there will not be a large apparent size increase.

The fact that there are no particle aggregates (as evidenced by Mie scattering) following polymer hair growth would indicate that there is no polymer-polymer

termination between particles during the polymerization, which is what we were intending to avoid.

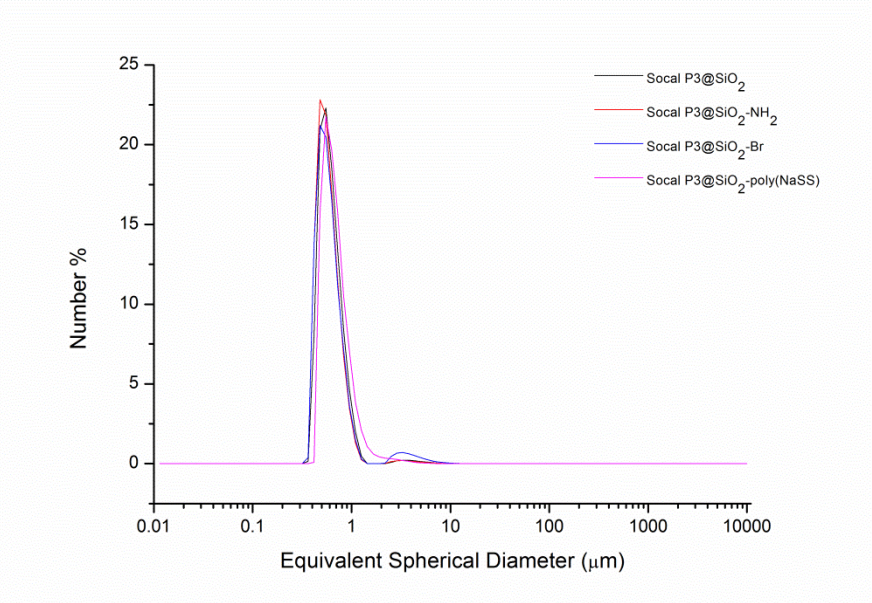

Figure 2.15. Laser scattering measurement (Mie scattering) showing the frequency distribution of equivalent spherical particle diameters (number average), for SOCAL P3@SiO_2 nancomposite particles and those functionalized with –NH_2, –Br, and poly(NaSS) brushes.

Zeta-potential measurements of the hollow SiO_2 particles with poly(NaSS) brushes display an interesting response to altering the [NaCl] (**Figure 2.16** and **Appendix III.3**, **Table III.7**).

In the presence of a very low concentration of counter-ions, the polymer brushes are fully extended into solution, screening the charge from the SiO_2 surface. Due to the negatively charged sulfonate groups at pH = 6, the zeta-potential at the shear plane is negative.

As the concentration of salt is increased, more cations are bound by the negatively charged sulfonate groups, leading to an initial decrease in the magnitude

of the negative potential. At a certain salt concentration (around 5 x 10^{-3} M NaCl in this case) the polymer brushes collapse onto the surface, allowing the surface charges of the SiO_2 to again contribute to the zeta potential. Further addition of salt then suppresses the double layer as usual. Interestingly, the polymer grafted particles still display a large magnitude in zeta-potential at high salt concentration (1 M), unlike the PVP stabilized $CaCO_3$@SiO_2 particles (**Figure 2.12**).

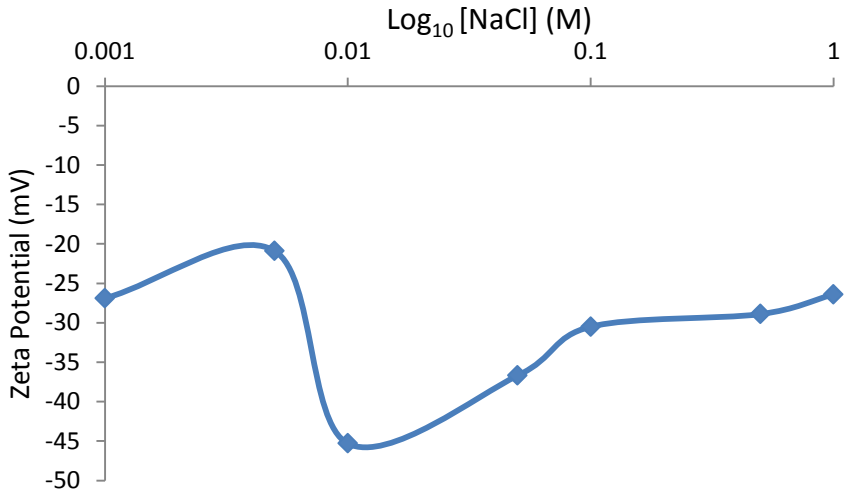

Figure 2.16. Zeta-potential as a function of [NaCl] for SOCAL P3@SiO_2-graft-poly(NaSS). Measurements were performed at pH = 6 and averaged over at least 10 runs.

Cryo-TEM was used to image the hollow SiO_2 particles with the polymer brushes on the surface in their native aqueous environment, in order to corroborate the presence of the polymer brushes and check their length (**Figure 2.17**). Dark brushes can be seen radiating from the surface of the particle into the ice. They

appear have a length of about 200 nm and are not uniform in length, indicating that the polymerization is not "living".

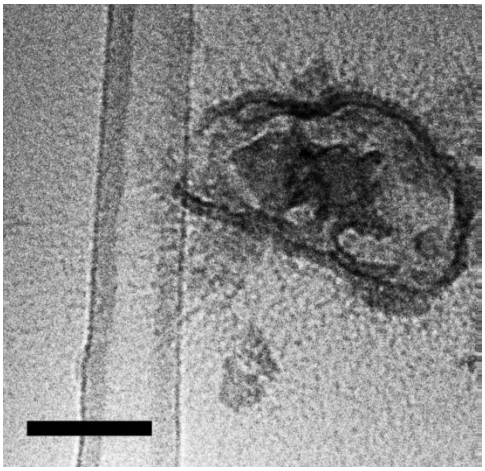

Figure 2.17. Cryo-TEM image of hollow SiO_2 particles with grafted poly(NaSS) brushes. Scale bar = 200 nm.

An SEM-EDAX spectrum of the hollow SiO_2-graft-poly(NaSS) brushes confirmed the presence of sulfur, silica, and oxygen as one would expect, whilst all of the calcium had been removed following the acid etch (**Figure 2.18**).

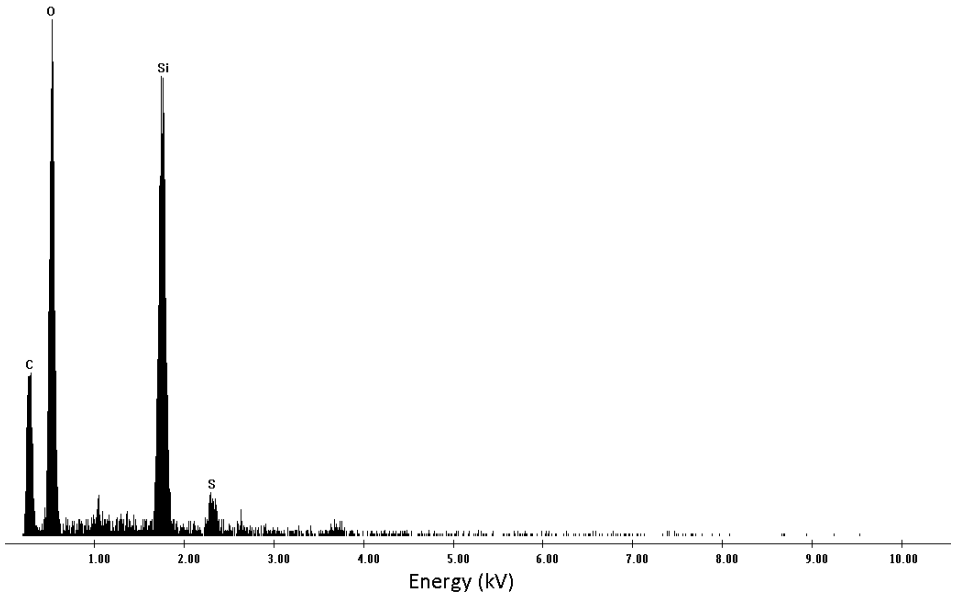

Figure 2.18. EDAX spectrum of the hollow SiO_2 particles with poly(NaSS) brushes, showing the presence of the sulfur group.

FTIR spectra were also recorded for $CaCO_3$@SiO_2 (**Figure 2.19 A**) particles and hollow SiO_2-graft-poly(NaSS) (**Figure 2.19 B**) to confirm the presence of the polystyrene sulfonate brushes.

The peaks at 713, 875 and 1466 cm^{-1} in **Figure 2.19 A** are due to the presence of $CaCO_3$. The lack of peak splitting at 875 and 1466 cm^{-1} confirm that SOCAL P3 is the calcite polymorph.[57]

One of the key differences between the two spectra which indicates the presence of the brushes is the characteristic polystyrene peak at 1601cm^{-1}, that is caused by stretching modes of the C-C bonds in the aromatic ring (**Figure 2.19 B**). The peaks at 1077 cm^{-1} in both spectra are attributable to Si-O-Si stretching modes. The reason for the increase in intensity of the peaks around 1050 cm^{-1} in the polymer modified particle is due to the presence of the sulfonate moieties, with stretching modes at 1000 and 1030cm^{-1} that produce these peaks.[58]

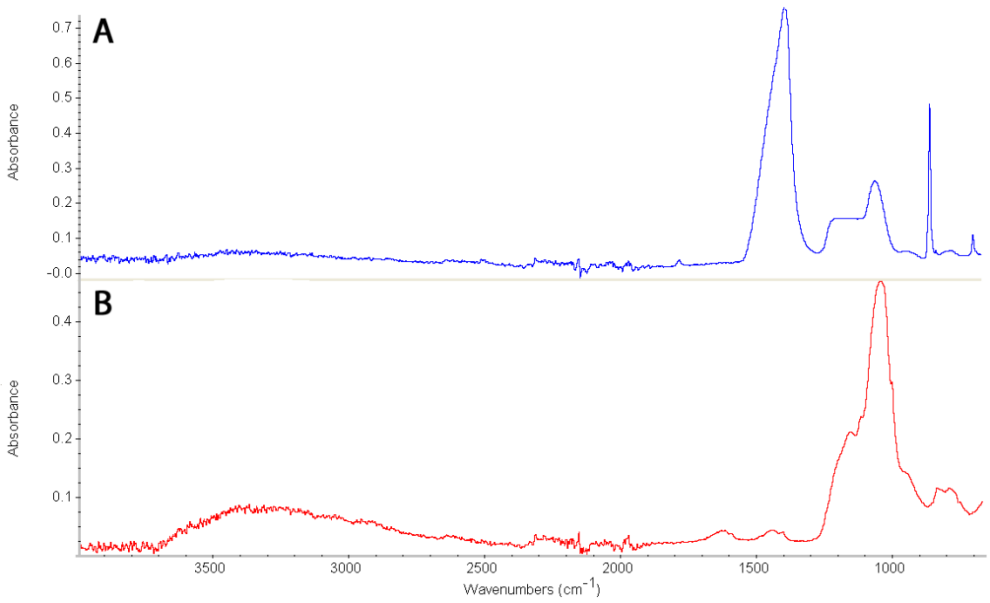

Figure 2.19. FTIR spectra of (**A**) $CaCO_3$@SiO_2 particles, and (**B**) hollow SiO_2-graft-poly(NaSS).

In order to test whether the growth of poly(NaSS) brushes had conferred enhanced dispersion stability to the hollow SiO_2 particles, compared to when PVP was physisorbed, we decided to test their "freeze-thaw" stability over three cycles by measuring particle size distribution with laser diffraction (**Figure 2.20** and **Appendix III.4**, **Tables III.8-III.10**). For comparison we also tested the SOCAL P3-Orotan N-4045 dispersion as well. Essentially when the solution freezes it pushes the particles close together,[59] similar to what happens as a waterborne coating dries. If the particles are well stabilized then they should be able to redisperse following thawing of the dispersion. Note that the original particle size can be seen in the size frequency plot given in **Figure 2.15**.

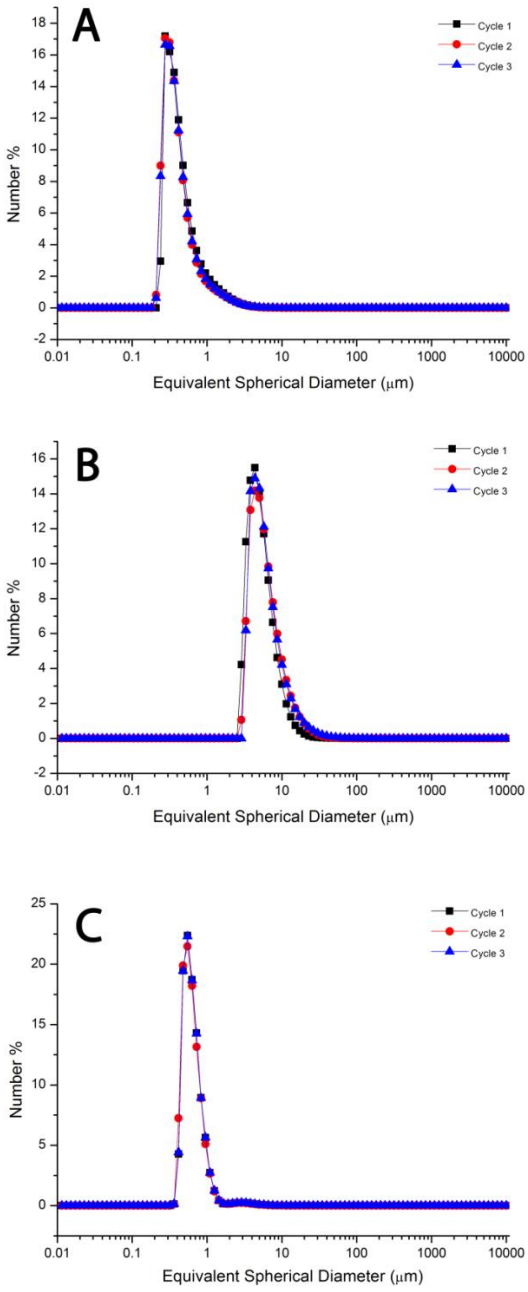

Figure 2.20. Laser scattering measurement (Mie scattering) showing the frequency distribution of equivalent spherical particle diameters (number average), for the pigment systems (**A**) SOCAL P3-Orotan N-4045, (**B**) hollow SiO_2-PVP K30 (2nd generation from **Section 1.2.5**) and (**C**) hollow SiO_2-graft-poly(NaSS), following the "freeze-thaw" dispersion test.

These results would indicate that PVP-K30 is not a suitable dispersion agent for the hollow SiO_2 particles (**Figure 2.20 B**), as evidenced by the increase in particle size after the first freeze-thaw cycle from that of the original template given in **Figure 2.15**. Our grafted poly(NaSS) brushes on the other hand do not increase in size at all from their original size i.e. no aggregates form over three freeze-thaw cycles, which indicates that the brushes confer excellent freeze-thaw stability to hollow SiO_2 particles (**Figure 2.20 A**). Orotan N-4045, also an electrosterically stabilizing agent, is found to be an ideal choice for SOCAL P3 (**Figure 2.20 C**). It is worth noting again at this point that Orotan N-4045 was not found to be an effective dispersant for silica, most likely due to them both carrying a negative charge at the coating pH~9.

2.2.3 Formulation of waterborne coating containing hollow SiO_2-graft-poly(NaSS) brushes as pigment and subsequent opacity testing

It is important to know the weight ratio of polymer brushes:silica so that we can add an accurate volume of light scattering centers (hollow silica component) to the coating, based on gravimetrical measurement of the particle dispersion.

TGA was used to determine the mass ratio between the organic and inorganic parts of the nanocomposite, the plot of which is shown in **Figure 2.21.** It would appear that poly(NaSS) accounts for about 8% by mass of the hollow SiO_2 particle, as it is burnt off sharply between around 450-550°C. The mass lost before this is the removal of trapped water from the structure. Continuous loss of mass at temperatures above the polymer degradation (> 600°C) is ascribed to removal of the carbonaceous residue formed by the incomplete combustion of the polymer.[60]

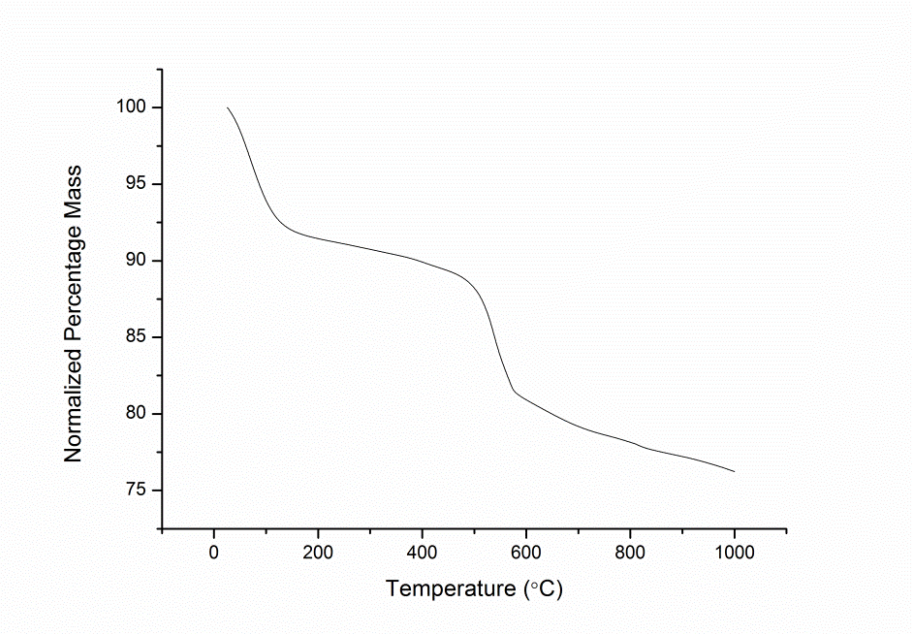

Figure 2.21. TGA plot of the hollow SiO_2-graft-poly(NaSS) particles, showing the mass fraction of polymer brushes to SiO_2.

A waterborne coating was formulated as before to have PVC ~ 30%, and volume solids ~ 17% (**Table 2.3).**

Table 2.3. Key formulation parameters for waterborne coating with hollow SiO_2-graft-poly(NaSS) particles as pigment. [a]Note that these values only hold true when all of the particles are intact, which as we shall is not the case. Corrected values are given later.

	Mass Solids (%)	**Mass fraction Pigment (%)**	**Volume Solids (%)[a]**	**PVC (%)[a]**
Theoretical	13.3	1.24	15.3	29.2
Experimental (TGA)	12.3	1.26	14.7	30.6

In order to get a more accurate value for the PVC and volume solids of the coating, TGA was conducted on the coating **(Figure 2.22).** Water loss by evaporation from the pan, whilst queued for analysis, was corrected for by normalizing the mass of the first measurement to that of the initial weight. Following water loss, which occurs at just over 100°C, the remaining mass is dry latex and pigment. The former is burnt away between ~375-425°C, leaving behind the pigment only. Experimentally determined values for the coating parameters are also given in **Table 2.3.** For a description of the calculations used to work out the experimental PVC and volume solids from TGA measurements, please refer to **Section 1.2.3.**

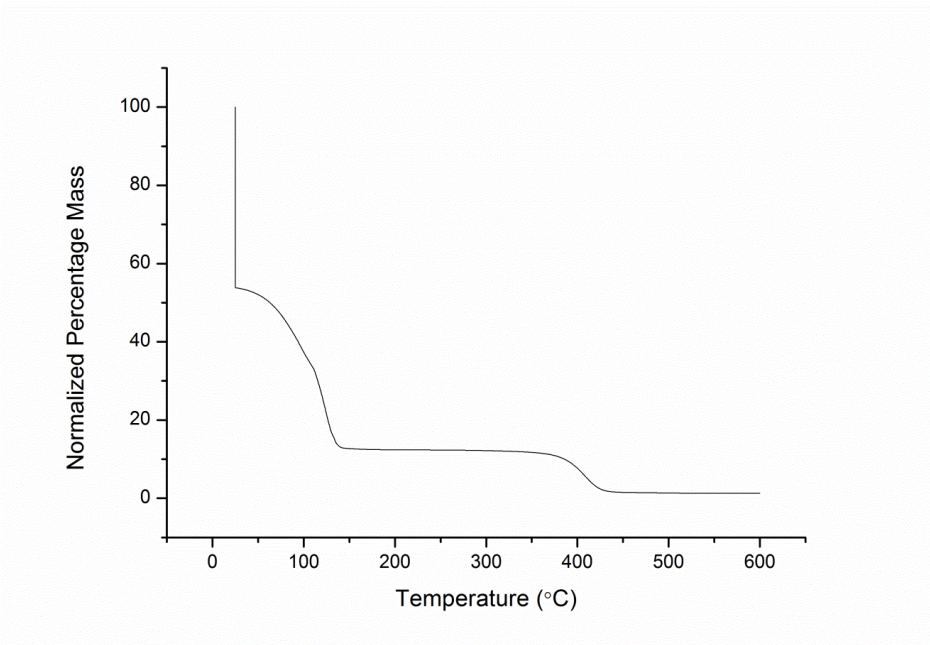

Figure 2.22. TGA plot of the waterborne coating containing hollow SiO_2-graft-poly(NaSS) as pigment.

Optical microscopy of the coating confirmed that the hollow SiO_2-graft-poly(NaSS) particles were well dispersed in the coating, with no observable

aggregates present in the waterborne section seen above the dark line running across the image in **Figure 2.23**.

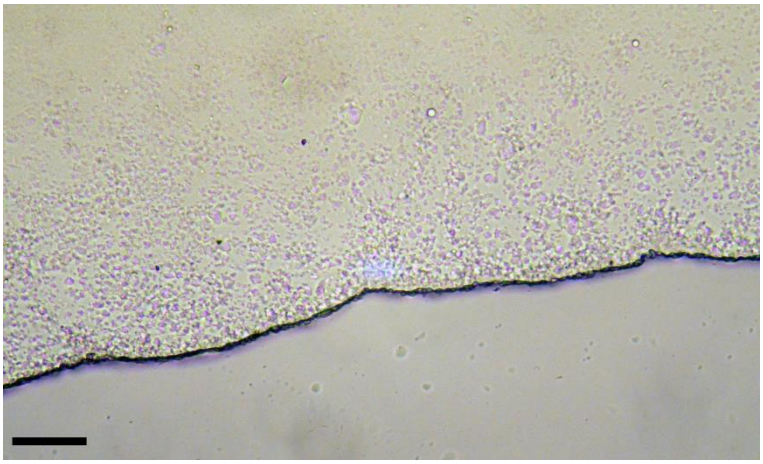

Figure 2.23. Optical microscope image of the coating containing hollow SiO_2-graft-poly(NaSS) as pigment. Scale bar = 10 μm.

Digital photographs showing multifilm thickness drawdowns of the coatings with the hollow SiO_2-graft-poly(NaSS) (**Figure 2.24 A**), and 2nd generation hollow SiO_2-PVP (from **Section 1.2.5**) (**Figure 2.24 B**) particles as pigment.

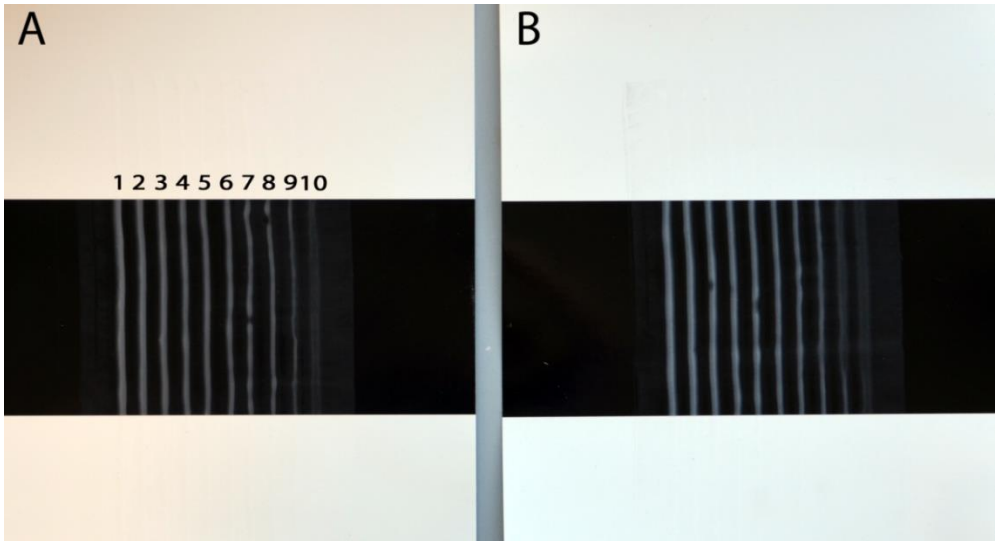

Figure 2.24. Digital photograph of dry films following application of the two pigmented coatings with a multifilm applicator to a Lenetta panel. Pigments in the coatings were (**A**) hollow SiO_2-graft-poly(NaSS) @ 30.6% PVC,[a] 14.7% vol. solids,[a] and (**B**) 2nd generation hollow SiO_2–PVP K30 from **Chapter 1.2.5** @ 31.2% PVC,[b] 19.0% vol. solids.[b] Wet and dry film thickness for (**A**) can be found in **Appendix III.5**, **Table III.11**, and (**B**) in **Appendix II.6**, **Table II.6**. [a//b] These values are assuming that all of the air voids are intact. Following corrections for the amount of broken particles from film density measurements (see following section), a more accurate representation for [a] would be PVC = 0.6%, and vol. solids = 10.8%., and for [b] PVC = 7.4%, and vol. solids = 14.1%

As in **Section 1.2.3** and **1.2.5**, we measured experimental film density by the "DMCPS method" (for a full description of this procedure please refer to **Section 1.2.3**). We compared this to the theoretical film density in the two extreme cases where all of the particles are broken, and when all of the particles are intact (**Table 2.4** and **Appendix III.6**, **Table III.12**). Interpolating where this experimental value lies in the range of the theoretical values gives an estimation for the number of intact

voided particles, which was found to only be 3.3%. This gives an average effective particle density of 2.11 $g \cdot cm^{-3}$, which gives a corrected PVC value of 0.6%, and vol. solids of 10.8%.

It is quite impressive that despite this small volume fraction of air voids, one still gets such a high level of opacity. We could assign opacity to the silica shell although the refractive index difference with the binder is negligible, their thickness is smaller than that which typically scatters light, and the mass fraction of silica in the coating is very low (1.3%).

This is in comparison to the 2nd generation hollow SiO_2-PVP pigment particles used in **Section 1.2.5** that had 19.4% of intact voided particles. Therefore the presence of the polymer hairs must be detrimental to the stability of the particle in the drying film.

Table 2.4. Comparison of the experimental film density for the hollow SiO_2 coating with the theoretical film density in the case where all particles are intact voided structures, and when none of the particles are intact voided structures.

Experimental film density ($g \cdot cm^{-3}$)	**Theoretical film density with all hollow particles ($g \cdot cm^{-3}$)**	**Theoretical film density with no hollow particles ($g \cdot cm^{-3}$)**
1.13	0.84	1.14

Contrast ratio of the coatings was determined by film reflectance measurements as used before in **Section 1.2.5**, and normalized with respect to film thickness. It can be seen that the contrast ratio per micron for the hollow SiO_2-graft-poly(NaSS) pigmented film is slightly better than the 2nd generation hollow SiO_2–

PVP coating used in **Section 1.2.5** (R_B/R_W micron^{-1}= 3.05-3.30). This is impressive considering that the PVC of the polymer grafted hollow SiO_2 coating is 14 times less that of the 2nd generation hollow SiO_2-PVP coating.

Table 2.5. Tabulated reflectance data showing contrast ratio per micron film thickness for coating with hollow SiO_2-graft-poly(NaSS) as pigment.

Dry film thickness (µm)	R_B/R_W	R_B/R_W micron^{-1}
3.02	10.77	3.57
2.86	10.32	3.62
2.81	10.32	3.67
2.78	10.60	3.82
2.74	10.36	3.79

SEM imaging was conducted on the dry films for the three pigment systems investigated; SOCAL P3-Orotan N-4045 (**Figure 2.25 A**), Hollow SiO_2-PVP (**Figure 2.25 B**), and hollow SiO_2-graft-poly(NaSS) (**Figure 2.25 C**). The surface roughness and porosity of the SOCAL P3 film should make the film quite matte, and indeed this is a property that SOCAL P3 is known to impart to dry films.[61] Both of the hollow SiO_2 coatings have smoother film surfaces so should have a higher gloss, which is a desirable property for decorative coatings. The reason for this is likely due to the fact that many of the particles remain broken and these form smaller aggregates in the coating, allowing the binder to coat them fully.

It would also appear that there are less aggregates in the hollow SiO_2-graft-poly(NaSS) coating than in the hollow SiO_2-PVP coating, which is a consequence of the improved particle dispersion as determined by the freeze-thaw experiment.

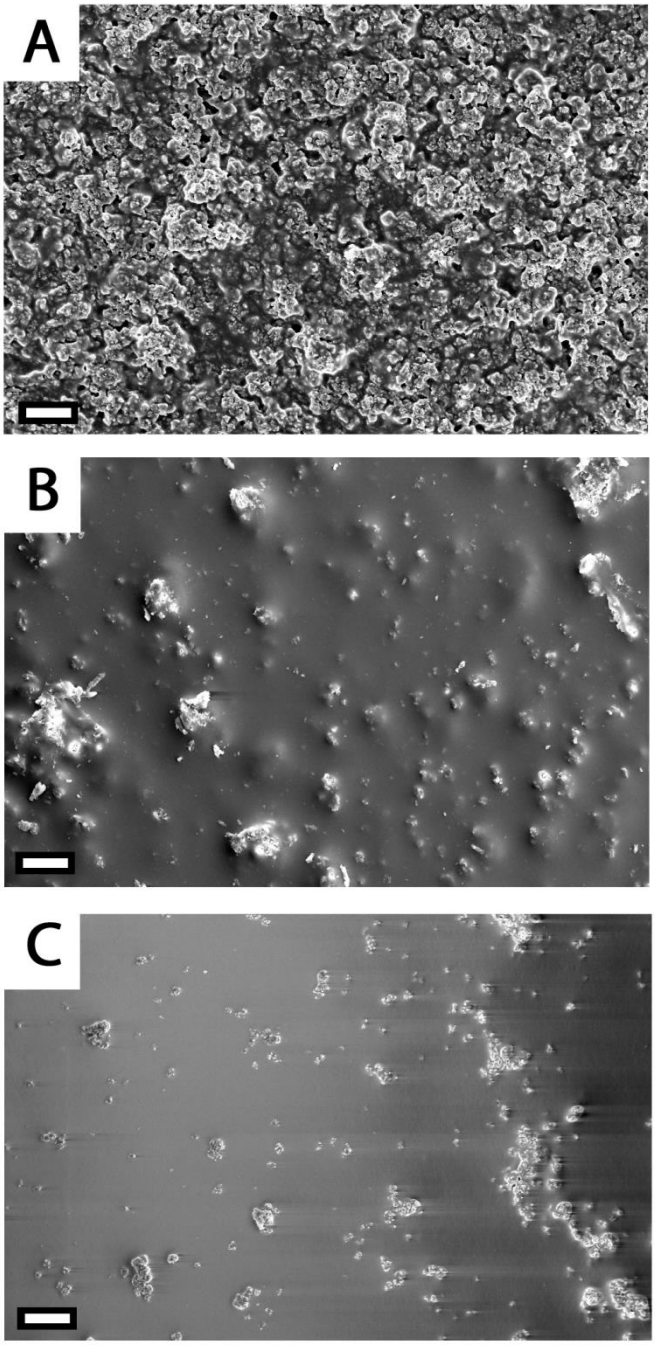

Figure 2.25. SEM images comparing the morphology of the film surface for the coatings with pigment of (**A**) SOCAL P3-Orotan N-4045, (**B**) hollow SiO_2-PVP K30 (2^{nd} generation from **Section 1.2.5**), and (**C**) hollow SiO_2-graft-poly(NaSS), Scale bar = 10 µm.

2.3 Conclusions

In this chapter we grafted poly(styrene sulfonate) hairs from hollow SiO_2 particles functionalized with an ATRP initiator. The aim of this was to improve the colloidal stability of the particles to be used as pigment over those used in **Chapter 1** that had PVP physisorbed onto the surface (providing predominantly steric stabilization).

First we functionalized the SiO_2 surface with APTES to give it $–NH_2$ functionality, and then we reacted this with BiBB to give particles with a tertiary alkyl bromide that could act as ATRP initiator.

Zeta potential measurements were useful for following these reactions due to the low weight fraction of the surface groups. Ninhydrin was also useful to qualitatively deduce the presence of primary amine groups, and their conversion to amide groups.

Sodium styrene sulfonate monomer was then grown from the surface by an SI-ATRP type polymerization, involving PMDETA as ligand and Cu(0) as catalyst. The latter oxidizes to form 2Cu(I)XL, a highly unstable intermediate that breaks down to form the Cu(0)/Cu(II)XL analogues which mediate the equilibrium process.

The presence of the hairs was evidenced by cryo-TEM, EDAX, FTIR, zeta-potential, and TGA measurements.

Freeze-thaw experiments were performed on the three pigmented coatings (with pigments being SOCAL P3-Orotan N-4045, hollow SiO_2-PVP K30 **(**2^{nd} generation from **Section 1.2.5)**, and hollow SiO_2-graft-poly(NaSS)) in order to deduce colloidal stability of the particles. We found that grafting poly(NaSS) brushes from the surface conferred enhanced stability over the hollow SiO_2 particles that only had PVP physisorbed. Orotan N-4045 was also found to be an excellent choice

for providing highly stable dispersions for SOCAL P3, likely due to it providing electrosteric stabilization similar to our grafted polymer brushes.

Films made with the hollow particles had a much smoother and less porous surface than those with SOCAL P3, possibly due to some of the particles having collapsed, which would form smaller aggregates as film formation occurred, facilitating enhanced wetting by the binder.

Film density measurements indicated that a much larger proportion of particles collapsed during film formation (only 3.3% intact voided particles vs. 19.4% for 2nd generation hollow SiO_2 particles). Despite this the contrast ratio of the coating per micron film thickness was actually higher than in the PVP stabilized particles, indicating that the enhanced dispersion of the pigment had indeed conferred enhanced light scattering properties to the film.

Had we more time then studying the polymer composition via gel permeation chromatography (GPC) after removal of the silica with HF would have been the next step, and from this we could deduce graft density of the hairs on the hollow silica particles.

2.4 Experimental

2.4.1 Materials

SOCAL P3, Acrysol SCT-275, Orotan N-4045, and S/BA/AA latex binder were kindly donated by AkzoNobel. Solvay also kindly provided us with SOCAL P3. Tetraethylorthosilicate (reagent grade, 98%), α-bromoisobutyryl bromide (98%), THF (anhydrous, > 99.5%), sodium 4-vinylbenzenesulfonate (technical, > 90%),

N,N,N′,N″,N″-pentamethyldiethylenetriamine (99%), copper(0) powder (99.999%), Ninhydrin (2,2-Dihydroxy-1,3-indanedione), and PVP-K30 (40,000 $g \cdot mol^{-1}$) were used as received from Sigma Aldrich.

3-aminopropyltriethoxysilane (99%) was used as received from Acros Organics.

Ethanol (absolute, 99.9%) and THF (99.9%) was used as received. Acetic acid (100%) and hydrochloric acid (35%) were diluted down to make the appropriate strength solution. All were obtained from VWR international.

Ammonium hydroxide (35%) and pyridine (anhydrous) were used as received from Fisher Scientific.

Deionized water was produced by a Milli-Q purification unit with a conductivity of 18 MΩ.

2.4.2 Analytical techniques

All analytical techniques used that are common with **Chapter 1** (SEM, Mie scattering, TGA, SEM EDAX, film density, optical microscopy and film reflectance measurements) had the same procedure as outlined in **Section 1.4.2**. Analytical techniques unique to this Chapter were conducted as follows.

2.4.2.1 Electrophoretic light scattering measurements (zeta potential)

A dilute solution of nanocomposite particles in water (0.1 mL, ~2 $mg \cdot ml^{-1}$) were dispersed into NaCl solutions of different molarities (1.5 mL). The solution was transferred to a Malvern Zetasizer Nano cell, taking care not to induce any air

bubbles, and sealing with plugs after filling. Measurements were then conducted in a Malvern Zetasizer Nano ZS after equilibration at 25°C for 2 minutes. Results reported are averaged over 3 measurements, each having 100 sub-runs.

2.4.2.2 CHN and Br microanalysis

Both analyses were performed by Warwick Analytical Services (WAS).

2.4.2.3 Cryo-TEM

Aqueous samples were placed onto lacey carbon film grids (300 mesh Cu, Agar Sc. S166-3), and prepared by vitrifying the aqueous suspension of particles in liquid ethane. Imaging was then performed on a Jeol 2011 TEM operating at 200 kV, LaB6, with a 2K Gatan Ultrascan camera.

2.4.2.4 FTIR spectroscopy

FTIR spectroscopy was conducted on samples that had been dried in an oven at 100°C for 24 hours. Spectra were collected on Bruker Alpha Platinum-ATR spectrometer with a ZnSe disc. Background baselines were subtracted and ATR correction was applied.

2.4.2.5 Freeze-thaw experiment

Samples were frozen at -25°C for 24 hours and then allowed to thaw at room temperature for 24 hours, before being analysed with a Malvern Mastersizer 2000S as described in **Section 1.4.2.1**. Three cycles of freeze-thaw-analysis were performed on each of the samples.

2.4.3 Synthesis of SOCAL P3@SiO_2 nanocomposite

Synthesis of the SiO_2 coated SOCAL P3 particles was conducted as outlined in **Section 1.4.4** for the sample A4. Briefly, SOCAL P3 (20 g) was dispersed in ethanol (184 mL), water (20 mL), and ammonium hydroxide (35 % vol., 16 mL). After stirring for 20 minutes a feed of TEOS (20 mL) at a rate of 4 $mL \cdot hr^{-1}$ was started, and the reaction quenched after 5 hours by centrifugation and redispersal of the as-synthesized particles into deionized water. This was repeated three times.

2.4.4 Synthesis of SOCAL P3@SiO_2-APTES nanocomposite

SOCAL P3@SiO_2 particles (22 g, corresponding to ~2 g of SiO_2) were then redispersed into ethanol (186 mL) and ammonium hydroxide (35 % vol., 16 mL). APTES (4 mL, 0.017 mols) was then fed in over an hour and the reaction mixture was left to stir for 18 hours before the reaction was heated to 78°C, where it was left to stir for 3 hours. The reaction was then quenched via centrifugation and redispersed into ethanol three times, before a further 3 rounds of redispersal into THF by centrifugation.

2.4.5 Functionalization of hollow SiO_2-NH_2 with α-bromoisobutyryl bromide

Particles (~22 g) from **Section 2.4.4** above were centrifuged and redispersed in anhydrous THF (200 mL). The solution was degassed with N_2 in a round bottomed flask with magnetic stirrer. An ice bath was used to cool the solution down to 0°C before the addition of pyridine (4.52 mL, 56 mmol), followed by BiBB (7.0 mL, 56 mmol) in a dropwise manner. The reaction was left for 30 minutes before the ice bath was removed and the reaction was allowed to warm to room temperature. Particle purification was conducted by four rounds of centrifugation, redispersing into THF, followed by a further four rounds of centrifugation, dispersing into water.

2.4.6 Growth of poly(NaSS) brushes from the surface, using the $CaCO_3$@SiO_2 particles surface functionalized with ATRP initiator as seed

Cu(0) powder (50 mg, 0.79 mmol) was added to a solution of bromo-functionalized SiO_2 particles (20 g in 150 mL). To this was added the monomer NaSS (4.0 g, 20 mmol) and the solution degassed with N_2 for 1 hour under mild stirring. Simultaneously, a solution of PMDETA (50 g, 2% wt.) was also degassed for 1 hour with N_2. An aliquot of PMDETA (6.76 mL, 0.135 g PMDETA, 0.89 mmol) was then transferred to the solution at RT. Stirring was conducted under inert conditions for 2 hours before the particles were cleaned with several rounds of centrifugation, redispersing into water until the supernatant was colourless. Three further rounds of centrifugation at 1,000 g allowed us to remove the copper powder in the collected solids, keeping and combining the supernatant with our particles in.

The core was then removed with a mild acid etch using a drip feed of acetic acid (500 mL, 0.5 M), before the particles were cleaned a further three times by centrifugation, and redispersal into water.

2.4.7 Formulation of waterborne coatings with hollow SiO_2-graft-poly(NaSS) as pigment

Table 2.6. Formulation for 30% PVC waterborne coating with hollow SiO_2-graft-poly(NaSS) as pigment @15% vol. solids. [a] This is the correct mass of particles to add in order to account for the mass contribution from the polymer brushes. [b] This is assuming that the particles are not fractured and that they still have the internal void volume.

Reagent	**Mass (g)**	**Weight % Solids**	**Density Solids ($g \cdot cm^{-3}$)**	**Volume Solids (cm^3)**	**Density aqueous ($g \cdot cm^{-3}$)**	**Volume aqueous (cm^3)**
Hollow SiO_2	2.02 (2.18)[a]	100	0.28[b]	7.30	-	-
Water	115.0	0	0	0	1	115.0
S/BA/AA Binder	35.2	50	1.08	16.3	-	
Acrysol SCT-275	10.0	17.5	0.90	1.94	1	5.8

2.5 References

(1) Hsu, W. P.; Yu, R.; Matijević, E. *J. Colloid Interface Sci.* **1993**, *156*, 56–65.

(2) Mishchenko, M. I.; Travis, L. D.; Mackowski, D. W. *J. Quant. Spectroc. Radiat. Transfer* **1996**, *55*, 535–575.

(3) Nelson, K.; Deng, Y. *Langmuir* **2008**, *24*, 975–982.

(4) Croll, S. *Prog. Org. Coat.* **2002**, *44*, 131–146.

(5) Brown, R. F. G.; Carr, C.; Taylor, M. E. *Prog. Org. Coat.* **1997**, *30*, 185–194.

(6) Tadros, T. F. In *Dispersions of Powders in Liquids and Stabilization of Suspensions*; Wiley-VCH Verlag GmbH & Co. KGaA, 2012; pp. 1–2.

(7) Clayton, J. *Surf. Coat. Int.* **1997**, *80*, 414–420.

(8) Fujitani, T. *Prog. Org. Coat.* **1996**, *29*, 97–105.

(9) Farrokhpay, S.; Morris, G. E.; Fornasiero, D.; Self, P. *Powder Technol.* **2010**, *202*, 143–150.

(10) Barnes, H. A. *J. Non-Newton Fluid* **1997**, *70*, 1–33.

(11) Nagata, N.; Yamazaki, T. U.S. Pat. 3,652,313, 1968.

(12) Hamaker, H. C. *Physica* **1937**, *4*, 1058–1072.

(13) Lee, S.; Sigmund, W. M. *Colloids Surf. A* **2002**, *204*, 43–50.

(14) Stern, O. *Z. Electrochem.* **1924**, *30*, 508–516.

(15) Chapman, D. L. *Phil. Mag.* **1913**, *6*, 475–481.

(16) Guoy, L. G. *J. Phys. Appl.* **1909**, *149*, 654–657.

(17) Israelachvili, J. N. *Intermolecular and Surface Forces*; 2011; p. 307.

(18) Derjaguin, B.; Landau, L. *Acta Physicochimica U.R.S.S* **1941**, *14*, 633–662.

(19) Verwey, E. J. W.; Overbeek, J. T. G. *Theory of the Stability of Lyophobic Colloids*; Elsevier: Amsterdam, 1948.

(20) Http://depts.washington.edu/solgel/images/ courses/MSE_502/Ch_2/figure_2.16.JPG. Accessed on 15/09/13.

(21) Luckham, P. F.; Klein, J. *J. Colloid Interface Sci.* **1987**, *117*, 149–158.

(22) Klein, J. *J. Colloid Interface Sci.* **1986**, *111*, 305–313.

(23) Fritz, G.; Scha, V.; Willenbacher, N.; Wagner, N. J. *Langmuir* **2002**, *18*, 6381–6390.

(24) Creutz, S.; Jérôme, R.; Kaptijn, G. M. P.; Werf, A. W.; Akkerman, J. M. *J. Coat. Technol.* **1998**, *70*, 41–46.

(25) Rudhardt, D.; Bechinger, C.; Leiderer, P. *J. Phys.: Condens. Matter* **1999**, *11*, 10073–10078.

(26) Kiratzis, N.; Faers, M.; Luckham, P. F. *Colloids Surf. A* **1999**, *151*, 461–471.

(27) Banash, M. A.; Croll, S. G. *Prog. Org. Coat.* **1999**, *35*, 37–44.

(28) Http://www.dispersions-pigments.basf.com/portal/basf/ien/dt.jsp?setCursor=1_556356. Accessed on 13/09/13.

(29) Radhakrishnan, B.; Ranjan, R.; Brittain, W. J. *Soft Matter* **2006**, *2*, 386–396.

(30) Chevigny, C.; Gigmes, D.; Bertin, D.; Jestin, J.; Boué, F. *Soft Matter* **2009**, *5*, 3741–3753.

(31) Wang, Y-P.; Pei, X-W.; He, X-Y.; Yuan, K. *Eur. Polym. J.* **2005**, *41*, 1326–1332.

(32) Li, C.; Benicewicz, B. C. *Macromolecules* **2005**, *38*, 5929–5936.

(33) Wang, J.-S.; Matyjaszewski, K. *J. Am. Chem. Soc.***1995**, *117*, 5614–5615.

(34) Http://www.cmu.edu/maty/development-atrp/development-ATRP.html. Accessed on 20/09/13.

(35) Barbey, R.; Lavanant, L.; Paripovic, D.; Schüwer, N.; Sugnaux, C.; Tugulu, S.; Klok, H-A. *Chem. Rev.* **2009**, *109*, 5437–5527.

(36) Huang, X.; Wirth, M. J. *Anal. Chem.* **1997**, *69*, 4577–4580.

(37) Chen, X. Y.; Armes, S. P.; Greaves, S. J.; Watts, J. F. *Langmuir* **2004**, *20*, 587–595.

(38) Perruchot, C.; Khan, M. A.; Kamitsi, A.; Armes, S. P.; von Werne, T.; Patten, T. E. *Langmuir* **2001**, *17*, 4479–4481.

(39) Saleh, N.; Sarbu, T.; Sirk, K.; Lowry, G. V; Matyjaszewski, K.; Tilton, R. D. *Langmuir* **2005**, 9873–9878.

(40) Pyun, J.; Jia, S.; Kowalewski, T.; Patterson, G. D.; Matyjaszewski, K. *Macromolecules* **2003**, *36*, 5094–5104.

(41) Percec, V.; Guliashvili, T.; Ladislaw, J. S.; Wistrand, A.; Stjerndahl, A.; Sienkowska, M. J.; Monteiro, M. J.; Sahoo, S. *J. Am. Chem. Soc.* **2006**, *128*, 14156–14165.

(42) An, Y.; Chen, M.; Xue, Q.; Liu, W. *J. Colloid Interface Sci.* **2007**, *311*, 507–513.

(43) Mueller, R.; Kammler, H. K.; Wegner, K.; Pratsinis, S. E. *Langmuir* **2003**, *19*, 160–165.

(44) Butterworth, M. D.; Corradi, R.; Johal, J.; Lascelles, S. F. .; Maeda, S.; Armes, S. P. *J. Colloid Interface Sci.* **1995**, *174*, 510–517.

(45) Horikawa, Y.; Murray, R. S.; Quirk, J. P. *Colloids Surf.* **1988**, *32*, 181–195.

(46) Moulin, P.; Roques, H. *J. Colloid Interface Sci.* **2003**, *261*, 115–126.

(47) Chibowski, E.; Hotysz, L.; Szcześ, A. *Colloids Surf. A* **2003**, *222*, 41–54.

(48) Mahon, E.; Hristov, D. R.; Dawson, K. A. *Chem. Comm.* **2012**, *48*, 7970–7972.

(49) Bagwe, R. P.; Hilliard, L. R.; Tan, W. *Langmuir* **2006**, *22*, 4357–4362.

(50) Kecht, J.; Schlossbauer, A.; Bein, T. *Chem. Mater.* **2008**, *20*, 7207–7214.

(51) Wei, X.; Gong, X.; Ngai, T. *Polym. Chem.* **2013**, *4*, 4356–4365.

(52) Badila, M.; Brochon, C.; Hébraud, A.; Hadziioannou, G. *Polymer* **2008**, *49*, 4529–4533.

(53) Joullie, M. M.; Yhompson, T. R.; Nemeroff, N. H. *Tetrahedron* **1991**, *47*, 8791–8830.

(54) Choi, S. Y.; Lee, Y.-J.; Park, Y. S.; Ha, K.; Yoon, K. B. *J. Am. Chem. Soc.* **2000**, *122*, 5201–5209.

(55) Rosen, H. *Arch. Biochem. Biophys.* **1957**, *67*, 10–15.

(56) Chen, X.; Randall, D. P.; Perruchot, C.; Watts, J. F.; Patten, T. E.; von Werne, T.; Armes, S. P. *J. Colloid Interface Sci.* **2003**, *257*, 56–64.

(57) Zhao, H.; Li, Y.; Liu, R.; Zhao, F.; Hu, Y. *Mater. Lett.* **2008**, *62*, 3401–3403.

(58) Chu, C-C.; Wang, Y-W.; Wang, L.; Ho, T-I. *Synth. Metal* **2005**, *153*, 321–324.

(59) Palazolo, G. G.; Sobral, P. A.; Wagner, J. R. *Food Hydrocolloids* **2011**, *25*, 398–409.

(60) Oriakhi, C. O.; Farr, I. V.; Lerner, M. M. *Clay. Miner.* **1997**, *45*, 194–202.

(61) Http://www.solvaychemicals.com/SiteCollectionDocuments/PCC/Solvay%20PCC%20Applications.pdf. Accessed on 20/09/13.

Chapter 3

"Understanding the Multiple Orientations of Hematite Superellipsoidal Pseudocubes at the Oil-Water Interface"[a]

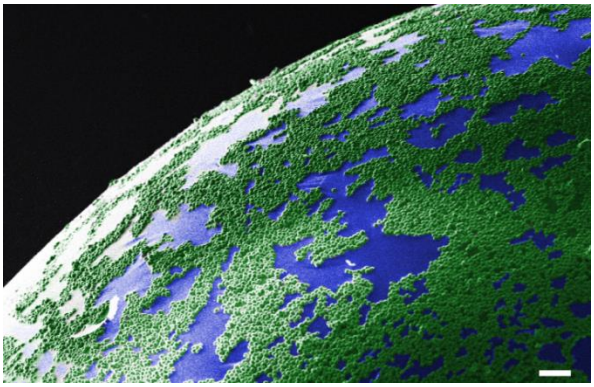

Non-spherical particles have the potential to adopt multiple orientations once adhered to a liquid-liquid interface. In this work we combine simulations and experiments to investigate the behavior of isolated microscopic hematite particles of superellipsoidal (pseudocubic) shape. We show that these microparticles can adopt one of three orientations when adhered to an *n*-hexadecane-water interface. Two of the orientations can be assigned to thermodynamic minima on the energy landscape, as determined by free-energy minimization simulations. Estimates for their relative populations were determined through particle trajectory simulations. The third orientation was found to correspond to a kinetically-trapped state, existing on certain particle trajectories in a region of a negligible gradient in free energy. This is one of

the first observations of such a state in an experimental system and the first geometry with uniform wettability reported to have a kinetic minima.

[a] Part of this work was published

Morgan, A. R.; Ballard, N.; Rochford, L. A.; Nurumbetov, G.; Skelhon, T. S.; Bon, S. A. F., *Soft Matter*, **2013**, *9*, 487-491.

3.1 Introduction

The ability for solid particles to adhere to soft interfaces was first observed by Ramsden[1] and Pickering,[2] who showed that emulsion droplets could be stabilized by solid particles. Although there was some research into the field throughout the early 20th century[3–5] it is fair to say that in the last few decades this area has been undergoing a renaissance. Interest has in part been driven by the numerous industrial applications that Pickering stabilized particles possess. Some examples of the applications that Pickering particles have been used for include silica armored polymer latexes that are used in scratch resistant coatings,[6] titanium dioxide stabilized colloids that can be used for chemical encapsulation/protection/release,[7,8] clay stabilized polyacrylate latexes which have been shown to make efficient gas membranes,[9] and Pickering stabilized poly(vinyl laurate) particles that were assembled into a foam for use in the detection of small molecules.[10]

However, Pickering stabilized systems also serve as models in the study of theoretical problems in Chemistry and Physics, such as the Thomson problem of how to optimally pack spheres or circles onto a spherical surface.[11]

One question of interest to colloid scientists is how a single isolated particle positions itself at an oil-water interface in order to minimize the free energy of the system. Pieranski was the first to report a semi-quantitative model describing the equilibrium position of an isolated smooth spherical particle of micron-scale dimensions at an air-water interface, with the associated energy well as a measure for the strength of adhesion.[12] This model doesn't take into consideration effects such as line tension and capillary bridging however, which have dramatic effects on how

particles orient themselves at an interface. This is something that we shall delve into more detail over later on in this section. If we assume that the particle is a perfectly smooth sphere adhered to a soft interface in the absence of external fields (i.e. gravity, charge etc.), then we can depict the situation as follows (**Figure 3.1**).

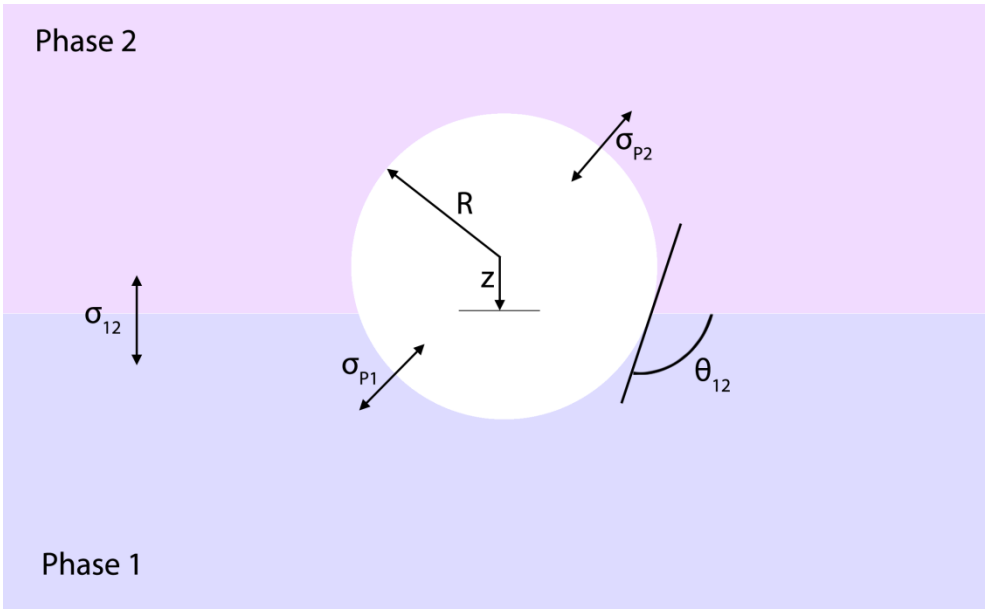

Figure 3.1. Schematic depiction of the variables that underpin how the position of a Pickering particle is defined at a biphasic interface consisting of phase 1 (oil), and phase 2 (water). The particle is assumed to be a micron-sized isolated smooth sphere of radius *R*. Surface tension between the phases is depicted as σ, where σ_{P1}, σ_{P2}, and σ_{12} are the surface tensions between the particle/phase 1, particle/phase 2, and phase 1/phase 2 respectively. The distance between the center of the sphere and the interface between phase 1 and phase 2 is denoted as *z*. The particle has a three-phase contact angle denoted by θ_{12}.

Note that we can define the dimensionless height of the particle, z_0, (**Equation (**3.1), the surface area of the sphere, S_T, (**Equation (**3.2) and the cross-sectional area of the sphere, A_T (**Equation (**3.3).

$$z_0 = \frac{z}{R} \tag{**3.1**}$$

$$S_T = 4\pi R^2 \tag{**3.2**}$$

$$A_T = \pi R^2 \tag{**3.3**}$$

Taking these parameters into account with the respective surface tensions, one can calculate the energetic terms at each interface in the system. There are two energetically unfavorable interactions which relate the interfacial tension and exposed surface area between the particle and each phase (**Equation (3.4**) and **(3.5**)), as well as the energetically favorable removal of interface between the two phases by the particle (**Equation (**3.6).

$$E_{P1} = \sigma_{p1} \cdot \mathrm{S_T} \frac{(1 + z_0)}{2} \tag{**3.4**}$$

$$E_{P2} = \sigma_{p2} \cdot \mathrm{S_T} \frac{(1 - z_0)}{2} \tag{**3.5**}$$

$$E_{12} = -\sigma_{12} . \mathbf{A_T}(\mathbf{1} - \boldsymbol{z_0^2}) \tag{**3.6**}$$

The free energy of the biphasic system when all of the particles are dispersed into one of the phases i.e. not at the interface, can be defined as $E_{Initial}$. In this case we have an interface of area, A_{12}, between the two phases that have an interfacial tension, σ_{12}. There is also an energetic contribution from the particles in phase 1 with an interfacial tension, σ_{P1} (**Equation (**3.7).

$$E_{Initial} = \sigma_{12} \cdot A_{12} + (4\pi R^2 \cdot \sigma_{P1}) \quad \textbf{(3.7)}$$

Addition of a particle to the interface can result in a reduction of the overall energy of the system, E_{Final}, through replacement of the energetically unfavorable interface by the particle (**Equation (**3.8).

$$E_{Final} = E_{Initial} - \pi R^2[\sigma_{12} + 2(\sigma_{P2} - \sigma_{P1})] \quad \textbf{(3.8)}$$

This thermodynamic and thus static behavior of a spherical microparticle is elegantly and straightforwardly solved as a direct result of the geometry and size of the particle (**Equation (**3.9). One can see that the energy of attachment to the interface depends on both the interfacial tensions and the radius of the particle. If a successful Pickering emulsion is formed then z_0 must lie between -1 and +1.

$$E_0 = \frac{E_{P1} + E_{P2} + E_{12}}{k_B T} = \left[\frac{\pi R^2 \sigma_{12}}{k_B T}\right]({z_0}^2 + 2(a-b)z_0 + 2(a+b) - 1) \quad \textbf{(3.9)}$$

Where $k_B T$ = Boltzmann's constant, T = temperature (K) and:

$$a = \frac{\sigma_{P1}}{\sigma_{12}}$$

$$b = \frac{\sigma_{P2}}{\sigma_{12}}$$

This allows us to solve for the particle height at the biphasic interface when minimizing the free energy, z_0^{min}, according to (**Equation (**3.10).

$$z_0^{min} = R(b - a) \quad \textbf{(3.10)}$$

In the following example we will look at the magnitude of energy stabilizing a small adsorbed microparticle at an oil-water interface. We take a spherical particle of radius R = 500 nm covered with poly(n-vinyl-2-pyrrolidone) (PVP), that is sitting at the *n*-hexadecane-water interface. From literature values we know that the respective interfacial tensions are σ_{12} = 52 mN·m^{-1},[13] σ_{P1} = 68 mN·m^{-1},[14] and σ_{P2} = 23·mN m^{-1}.[15] Where phase 1 is the water phase and phase 2 is the oil phase. Using **Equation** (**3.9**) we can generate a plot of how the free energy of the system changes as the particle height varies at the interface (**Figure 3.2**). From **Equation 3.10** we get z_0^{min} = -0.44, which is in good agreement with z_0^{min} found in **Figure 3.2**.

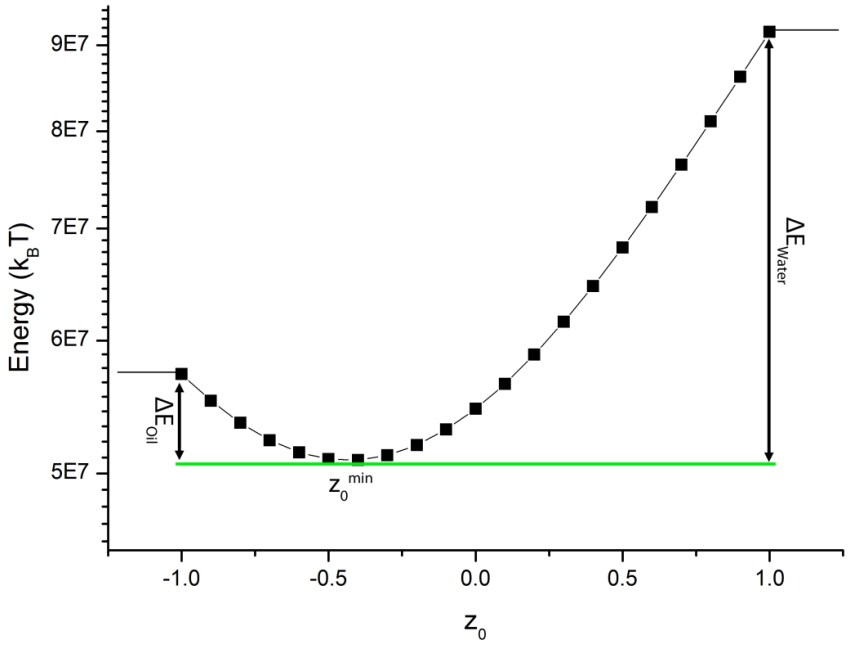

Figure 3.2. Plot showing how the free energy of a system, consisting of a spherical colloid coated in PVP (diameter = 1 µm) being moved through an *n*-hexadecane-water interface, varies with dimensionless height, $\boldsymbol{z_0}$. In this case $\boldsymbol{z_0 = 1}$ corresponds to the particle being fully in the aqueous phase and $\boldsymbol{z_0 = -1}$ is where the particle is fully in the oil phase.

Here $z_0 = 1$ corresponds to the particle being fully in the water phase, whereas $z_0 = -1$ corresponds to the particle being fully in the oil phase. At magnitudes larger than these for the dimensionless height the energy will plateau, as the interfacial energy terms are reduced down to two constants. We can see that in this case z_0^{min} is shifted slightly in favor of the oil phase, such that the particle is sitting further in the oil phase than it is in the water phase. This can be rationalized based on the fact that the physisorbed PVP has a lower interfacial tension with the

oil phase than it does with the water phase. Altering the respective values of the interfacial tensions would thus change the height of the particle in the interface.

Particle adsorption is often a very energetically favorable process, although it is technically a reversible process. It can be seen from **Figure 3.2** that the activation energy required to push the particle from its energy minima and into the oil phase is 6.4 x 10^6 k_BT, whereas the amount of energy required to push the particle off the interface, and into the water phase, would require 4 x 10^7 k_BT. These are large quantities of energy and so we can say that the particle is quite stable at the interface. Sonication and the addition of surfactants are both methods that one could employ to destabilize the Pickering system however. Sonication supplies energy to the particles at the interface and alters the contact angle if the interface is soft. Surfactants lower the interfacial tensions at the respective interfaces that they adsorb to; altering the balance of what is most energetically favorable.

The strength with which a particle adheres to an interface is also a function of its three-phase contact angle, θ_{12}, and the surface tension of the oil/water interface. [16] Following the constraints of the Pieranski system, and the argument of Binks and Lumsdon,[17] we can define the particle depth, *d*, into the aqueous phase (Phase 1 in **Figure 3.1**) as (**Equation (**3.11).

$$d = R\,(1 + cos\theta_{12}) \qquad \textbf{(3.11)}$$

The area of contact between the particle and the water is simply *d* multiplied by 2πR. Therefore, the area of oil-water interface that is eliminated by the particle can be expressed as in **Equation** (**3.12**).

$$A = \pi R^2(1 - cos^2\theta) \quad \textbf{(3.12)}$$

Now we can define the energy required to remove the particle from the interface in terms of each surface tension and the three-phase contact angle (**Equation (**3.13).

$$E = 2\pi R^2(1 + cos\theta_{12})(\sigma_{P1} - \sigma_{P2}) + \pi R^2(1 - cos^2\theta_{12})\sigma_{12} \quad \textbf{(3.13)}$$

We also know that the surface tension is related to the contact angle by Young's equation (**Equation (**3.14).

$$\sigma_{P2} - \sigma_{P1} = \sigma_{12}\cos\theta_{12} \quad \textbf{(3.14)}$$

Equation 3.13 then simplifies down to give us an expression for the energy required to remove the particle from the interface, either into the oil phase (**Equation (**3.15), or into the aqueous phase (**Equation (**3.16).

$$E_{oil} = \pi R^2\sigma_{12}(1 + \cos\theta_{12})^2 \quad \textbf{(3.15)}$$

$$E_{water} = \pi R^2\sigma_{12}(1 - \cos\theta_{12})^2 \quad \textbf{(3.16)}$$

In a Pickering emulsion system, the type of emulsion formed i.e. water-in-oil (W/O), or oil-in-water (O/W), depends on the particle wettability; in that the phase which preferentially wets the particle is usually the continuous phase. This is known as the Bancroft rule.[18] Referring back to **Figure 3.1**, hydrophilic particles therefore

have a θ_{12} < 90° when measured into the aqueous phase, whereas hydrophobic particles have a θ_{12} > 90°. A crossover in the type of emulsion occurs when θ_{12} = 90°.[19] As with many "rules" in science there are violations, with notable exceptions including the water-in-oil emulsions formed in the presence of sulfate stabilized polystyrene latex particles (initially dispersed in the aqueous phase) demonstrated by Lips and co-workers.[20]

Pieranski's model for the equilibrium orientation of a particle, and its associated energy well, is somewhat limited in its application to experimental systems as it doesn't account for the influence of other important interfacial phenomena. Curvature of the soft interface distorts the three-phase contact angle from that seen in the planar system, which in turn effects the free energy of adsorption.[21] Other effects that influence particle behavior at the interface include line tension, externally imposed fields (such as gravity) that cause distortions of the interface (especially for larger/denser particles), particle roughness, van der Waals and electrostatic forces (such as image charges), particle anisotropy, and capillary bridging interactions between multiple particles. We shall explore each of these phenomena in the following discussion and examine how they affect the free energy of particle adsorption, which subsequently impacts their relative positioning at the oil-water interface.

Further miniaturization of the particle down to nanoscale dimensions complicates matters of understanding the adhesion behavior of particles to soft interfaces due to the increasing importance of line tension, τ,[22–24] capillary waves[25] and Brownian motion/rotation. Line tension is an energy term expressed in one-

dimension ($J \cdot m^{-1}$) along the three-phase contact line, which can alter the contact angle that the particle makes with the interface and in some cases prevents the particle from entering the interface. Deformations can arise due to either van der Waals, hydrophobic, or electrostatic interactions. The interplay of how the line tension affects the free energy of a particle at equilibrium in the interface changes as particle *R* is decreased, as can be seen from **Equation** (**3.17**).[26]

$$E(z_0) = -\pi R^2 \sigma_{12}(1 - {z_0}^2) + 2\pi R^2(\sigma_{P1} - \sigma_{P2})(1 - z_0) + 2\pi R\tau\sqrt{1 - z_0^2} \quad \textbf{(3.17)}$$

At the micron-scale, capillary waves arise from the statistical fluctuations caused by thermal motion of the molecules in each phase. As the height of the capillary wave is on the order of a fraction of a nanometer, this phenomenon alters the contact angle of very small nanoparticles to a much greater extent than larger micron-sized colloids.[27] Similarly, the energy/motion of smaller nanoparticles is influenced to a greater extent by the forces of thermal (Brownian) motion of the solvent molecules, which makes the activation energy for particle desorption from the interface easier to overcome than for a larger particle (for a more thorough discussion of Brownian motion the reader is referred to **Chapter 4.1**).

Introducing nanoscale roughness to a surface has been shown to dramatically alter wettability. A good example of this is the superhydrophobic properties of the rough leaves of the Lotus plant, which many groups have taken as biomimetic inspiration.[28] Similarly, wettability of a particle adsorbed to a liquid-liquid interface and hence the positioning and strength of adsorption is also strongly influenced by

the nanoscale roughness of the surface. There is some controversy as to whether increasing the surface roughness of the particles confers increased stability of the emulsion however. Tsujii and co-workers believe that by increasing the roughness of the surface, one is exacerbating the preference for the particle to sit in the phase which preferentially wets it, thus decreasing stability by pushing the particle away from the ideal θ_{12} = 90°.[29] Contrary to this, San-Miguel and Behrens conducted a study where they created particles with varying degrees of surface roughness and found a non-monotonic relationship between contact angle hysteresis and capillary pressure of the emulsion. Increasing roughness improved emulsion stability in the case of homogenous (Wenzel regime)[30] wetting to a point, upon which there was a transition to the Cassie-Baxter regime[31] where wetting was heterogeneous and emulsion stability decreased.[32] One plausible explanation for the observation of increased emulsion stability upon increasing surface roughness can be found in the work of Brenn and co-workers, whereby they theoretically demonstrate that contact line undulations, as a result of surface roughness, can induce favorable capillary interactions between multiple particles (known as capillary multipoles), which increases the energy well of the particles at the interface.[33]

When dealing with larger particles of dimensions near or exceeding the capillary length of a fluid interface, λ_c, gravitational forces, g, can no longer be ignored (**Equation (**3.18).[34]

$$\lambda_c = \sqrt{\frac{\sigma_{12}}{g\Delta\rho}} \qquad \textbf{(3.18)}$$

Where $\Delta\rho$ is the density difference between the two phases.

This capillary length is typically on the order of a few mm for a water-oil interface. However, addition of particles to the interface lowers the local surface tension, causing a decrease in the capillary length to the micron-scale.

Another way to assess the importance of gravity compared to the surface tension forces is by looking at the magnitude/regime of the Bond number, B_0,[35] which is defined as the ratio of the force induced by gravity on one particle (that can interact with others and modify this term), to the capillary force which holds it at the interface (**Equation (**3.19).[36]

$$B_0 = \frac{L^2 \Delta\rho g}{\sigma_{12}(1 - \cos\theta)} \quad \textbf{(3.19)}$$

Where L is the characteristic length scale of the particle.

There are two regimes - one where $B_0 > 1$ and gravity will pull the particle off the interface, and then when $B_0 < 1$ where surface tension forces dominate.

Various electrostatic particle-surface and particle-particle interactions play an important role in the interaction energy of Pickering systems. The van der Waals interaction energy for a sphere at a separation distance, $D << R$ (particle radius), away from a planar surface can be expressed as (**Equation (**3.20).

$$E(D) = -\pi^2 C\rho^2 R/6D \quad \textbf{(3.20)}$$

Where C = van der Waals constant and ρ = number density of molecules in the sphere.

Further to this van der Waals contribution there is also an energy term from what is known as the image-charge effect.[37] Imagine that we have a sphere with charge, Q, in a medium denoted as phase 3 with dielectric constant, ε_3, at a distance from a planar interface, D, that is formed with another medium denoted phase 2, having a dielectric constant, ε_2 (**Figure 3.3**).

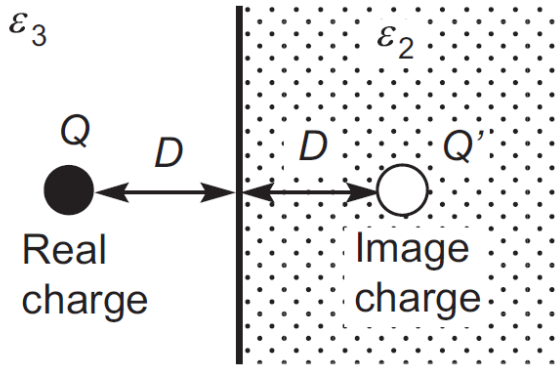

Figure 3.3. Schematic illustrating the concept of an image charge formed when a charged sphere interacts with its field reflection off a planar interface that separates two liquids of different dielectric constant. Image from reference.[38]

The particle will experience a force as if there were an image charge the same distance away for the interface in medium 2 i.e. it is $2D$ away from the real charge.

The interaction energy for this can then be defined as in **Equation** (**3.21**). Note this is a problem-solving tool for a much more complicated electrostatic phenomenon.

$$E(D) = \frac{-Q^2}{4(4\pi\varepsilon_0\varepsilon_3)D}\left(\frac{\varepsilon_2 - \varepsilon_3}{\varepsilon_2 + \varepsilon_3}\right) \quad \textbf{(3.21)}$$

Where ε_0 = permittivity of free space. So we can see that when $\varepsilon_2 < \varepsilon_3$ the interaction energy is repulsive and when $\varepsilon_2 > \varepsilon_3$ the interaction is attractive.

Interesting behavioral effects of colloidal particles at soft interfaces arise when morphological or chemical anisotropy of the particle is introduced.[39–44]

It has been shown recently through simulations by Lee *et al.* that an isolated Janus ellipsoid can adopt two stable equilibrium orientations; one being the global energetic minimum and the other being a local minimum (and thus thermodynamically metastable state). Ultimately the orientational preference depends on the aspect ratio of the particle, and the wettability characteristics of each side with the two liquid phases.[45]

Morris *et al.* modeled the equilibrium orientations of isolated, sharp-edged, polygon-shaped particles at an air-water interface. They demonstrated that, in theory, multiple orientations can exist for isolated cubic-like particles as the result of thermodynamic minima in the energy landscape.[46]

Similarly, work by van Roij and co-workers demonstrated the possibility of multiple orientations for a cylindrical particle at an interface when modeled with the triangular tessellation methodology[47] - a very powerful tool which we shall be using in this work.

So far we have discussed some of the forces that affect the adsorption behavior of singular particles to the interface, in particular spheres. Now we shall briefly discuss some of the interactions that can occur between multiple particles at the interface, as this can affect positioning and adsorption energy significantly. This is something which we had to be aware of in the work presented in this chapter.

Coulombic repulsion between like-charged particles at the oil-water interface leads to repulsion with long-range ordering. Interestingly, Aveyard *et al.* noted that the repulsion between the particles is not affected by the addition of ionic species, as is seen in bulk colloidal dispersions of electrostatically stabilized colloids. Therefore the charges must be operating through the oil phase, which they attribute to pockets of water of hydration, stabilizing negative sulfonate groups on the rough particle surface in contact with the oil phase. This allows for a residual surface charge at the interface.[48]

Capillary attractions between like particles that are either rough or anisotropic can arise when overlapping capillary distortions of the interface between particles drive their assembly through minimization of the area/energy if they come together.[49,50] Stebe and co-workers utilized capillary bridging interactions between cylindrical colloids at the air-water interface to assemble them end-to-end in highly ordered chains (**Figure 3.4**).[51]

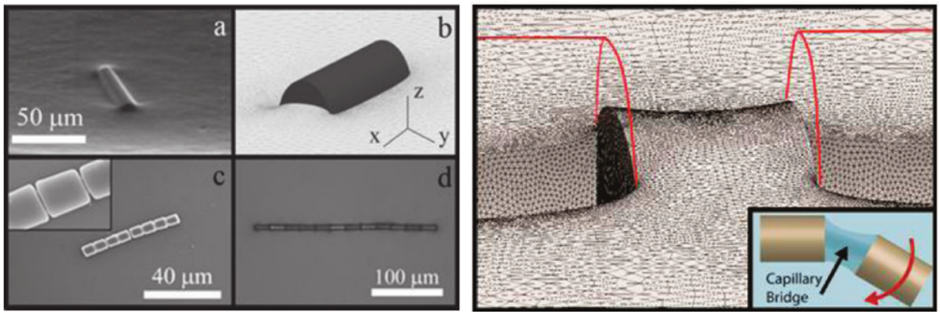

Figure 3.4. (**Left**) (**a**) Environmental scanning electron microscopy (ESEM) of a cylindrical colloid at the air-water interface with visible deformation of the interface, (**b**) Surface evolver simulation of a cylinder at the interface, (**c/d**) SEM images of assembled cylinders trapped at the interface. (**Right**) Surface evolver simulation of the deformed interface forming a capillary bridge between the ends of two cylinders. Images from reference.[51]

Capillary forces were also used in the assembly of mesoscale objects by Whitesides and co-workers.[52]

Herein, we show through a combination of experiments and simulations that isolated superellipsoidal (pseudocubic) hematite microparticles trapped at the *n*-hexadecane-water interface can adopt multiple orientations. Three different orientations were observed experimentally, only two of which could be explained computationally as the result of two thermodynamic minima on the energy landscape - one being the global minima, the other a local minima. The third orientation of the superellipsoidal particle at the interface is what we postulated to be a kinetically-trapped state. This is explained by the particle being trapped on a local plateau with a negligible negative energy gradient, as found by simulations. This negligible

gradient toward a lower energetic conformation inhibits further re-orientation, effectively trapping the particle in this metastable kinetic state. To the best of our knowledge this is the first time such behavior has been observed experimentally for an isolated particle at a soft interface.

3.2 Results and Discussion

3.2.1 Preparation and characterization of oil-water interface with superellipsoidal hematite pseudocubes adsorbed

Superellipsoidal hematite particles of micron-scale dimensions, with a monomodal particle size distribution, were prepared by a hydrothermal synthetic route[53] (See **Section 3.4.2**). From analysis of 100 particles in SEM images (**Figure 3.5**) the particles were found to have an average characteristic length of 1.36 ± 0.12 μm. Standard deviations from the mean were within 9%.

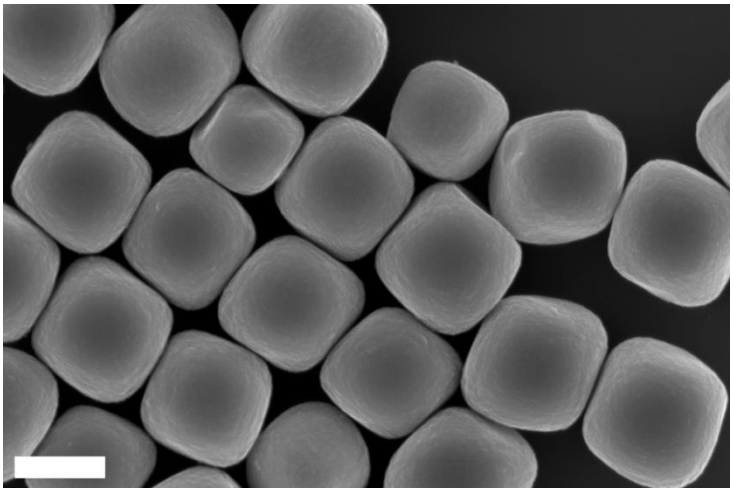

Figure 3.5. SEM image of monodisperse hematite particles with dice-like morphology (superellipsoidal pseudocubes). Scale bar = 1 μm.

Laser diffraction was used to measure the spherical equivalent volume average particle diameter and particle size distribution of the hematite superellipsoidal pseudocubes, that were stabilized with PVP-K30 (Mwt. = 40,000 $g \cdot mol^{-1}$) (**Figure 3.6** and **Table 3.1**).

The d(0.5) volume average equivalent spherical particle diameter was 1.38 μm and the uniformity (for a definition of both the reader is referred to **Appendix I.3**, **Equation I.2**) was 0.36, confirming the samples good colloidal stability i.e. no aggregates are formed, and corroborating the size analysis from SEM imaging.

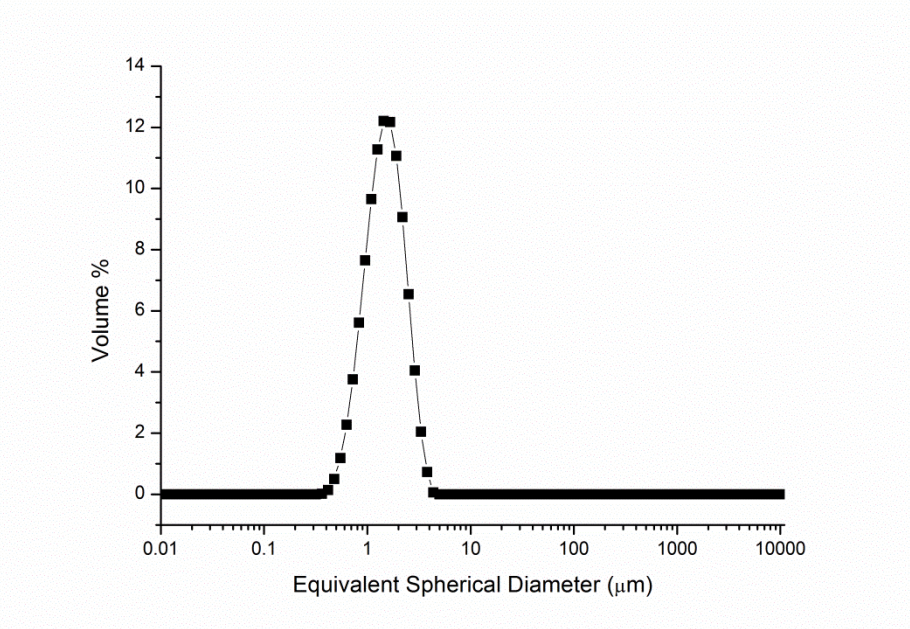

Figure 3.6. Laser diffraction measurement showing the frequency of volume equivalent spherical particle diameters for the hematite superellipsoidal pseudocubes stabilized with PVP-K30.

Table 3.1. Statistical data for laser diffraction measurements for hematite superellipsoidal pseudocubes stabilized with PVP-K30 plotted in **Figure 3.6**.

d(0.1) (μm)	**d(0.5) (μm)**	**d(0.9) (μm)**	**Uniformity**	**Weighted Residual (%)**
0.77	1.38	2.34	0.36	2.83

This synthetic approach allows for control of particle shape by varying the relative amounts of iron(III) chloride to sodium hydroxide, and other ionic species, used in the synthesis (See **Chapter 1.1**). Colloidal stability of the hematite particles was warranted through use of PVP-K30 as macromolecular surfactant, which is

strongly adhered to the surface of the particles by physisorption.[54] Coverage of the surface of the particles with the polymeric stabilizer masks underlying variations in wettability of the different crystal faces,[55] which simplifies matters in subsequent simulation of particle orientation as it removes chemical anisotropy and provides us with a straightforward set of three interfacial tension values.

The orientation of isolated hematite particles with respect to an *n*-hexadecane-water interface was studied by addition of a minute quantity of a dilute sol of the particles, dispersed in isopropyl alcohol, into the *n*-hexadecane phase which was in planar contact with the water phase underneath (both phases kept at 50 °C). The elevated temperature allowed for swift evaporation of the isopropyl alcohol. Sedimentation of the particles from the *n*-hexadecane phase allowed the particles to approach and interact with the *n*-hexadecane-water interface. The water phase contained 2.0% wt. Phytagel, which has proven not to interfere with the adhesion behavior,[56] and allows for investigation of the orientation of the particles at the liquid-liquid interface once trapped there upon cooling. Replacement of the *n*-hexadecane phase with curable poly(dimethyl siloxane) (PDMS) resin allowed for fixation of the particles and study of their orientation. This technique was developed by Paunov, and is referred to as the "gel-trapping" technique.[56]

We investigated the orientation of 100 isolated superellipsoidal hematite particles at the *n*-hexadecane-water interface by SEM analysis of our samples in which the particles were fixed into the PDMS matrix. Care was taken only to look at isolated particles in order to avoid complications arising from particle-particle interactions, for example through capillary bridging, which could potentially alter the orientation. From our collection of SEM images (see accompanying CD, **ESI 3.1**) it became evident that three categories of orientations emerged, of which two

orientations predominated (**Figure 3.7**). From the set of 100 particles, 59 adopted a conformation where two of the faces lay parallel to the interface (flat), with an average penetration depth into the water phase of 1.05 ± 0.08 μm. 35 particles showed a titled orientation relative to the oil-water interface, with an average tip-to-surface distance of 0.86 ± 0.08 μm. A small ternary population of 6 particles also exhibited a tilted orientation but they were lying distinctly deeper into the oil phase, with an average tip-to-surface distance of 0.54 ± 0.08 μm.

The three orientation categories were also looked at with atomic force microscopy (AFM). Overall, SEM analysis was more practical than AFM in assessing the orientation of our sample set of hematite particles due to their respective image acquisition times. AFM measurements were used to corroborate particle penetration depths for the three orientations observed. Note that only isolated particles were observed as we wanted to avoid the effects of capillary bridging interactions between particles to ensure that our experimental system applied the conditions we had allowed for in the subsequent simulations.

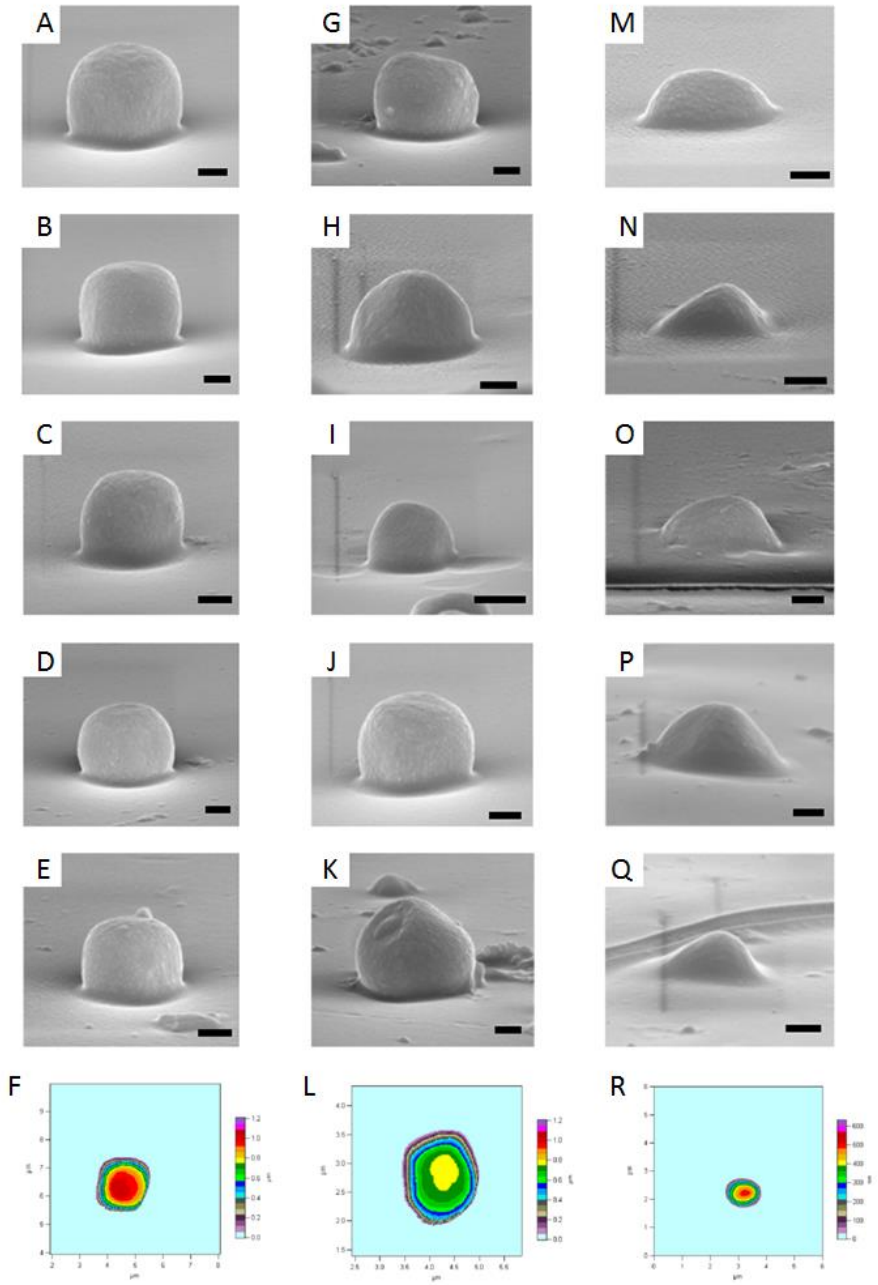

Figure 3.7. Representative SEM images of the three observed orientations in our sample set of 100 isolated superellipsoidal hematite particles fixed into a PDMS matrix (See also **ESI 3.1** on CD). (**A-E**) Flat orientation = 59% of population. (**G-K**) Tilted orientation = 35%. (**M-Q**) Tilted but sunken orientation = 6%. Scale bar = 400 nm. (**F, L, R**) Representative AFM height contour maps of the three orientations shown above the respective images.

3.2.2 Free energy simulation of a superellipsoidal pseudocubic hematite particle at an oil-water interface

In order to explain our experimental observations of three distinct particle orientations we calculated the free energy landscape of a single superellipsoidal cube by a numerical method, which calculates the free energy of a given particle orientation with respect to the liquid-liquid interface. The method is similar to the triangular tessellation scheme introduced by van Roij *et al*.[57] Firstly, we define mathematically the shape of a superellipsoid as follows (**Equation (**3.22).

$$\left(\frac{x^{2/n_2}}{r_x}+\frac{y^{2/n_2}}{r_y}\right)^{n_2/n_1}+\frac{z^{2/n_1}}{r_z}=1 \qquad \textbf{(3.22)}$$

Where x, y and z are Cartesian coordinates. r_x, r_y, and r_z are the particles x, y and z radii respectively. n_1 and n_2 act as the "squareness" parameters in the z axis and the xy plane respectively, with $0 < n_1, n_2 < \infty$. In our calculations we used values of $r_x = r_y = r_z = 680$ nm, and $n_1 = n_2 = 0.5$ in order to represent the shape of the hematite particles used in our experiments, as determined from SEM image analysis. The surface created by **Equation** (**3.22**) can be bound by a sphere of minimum radius (R) centered at the origin, which can be rotated about the $x(\theta_1)$ and $y(\theta_2)$ axes (See **Figure 3.8 A**). It is then translated in the z direction to define its position and orientation with respect to the interface, represented by the thick black line in **Figure 3.8 B**.

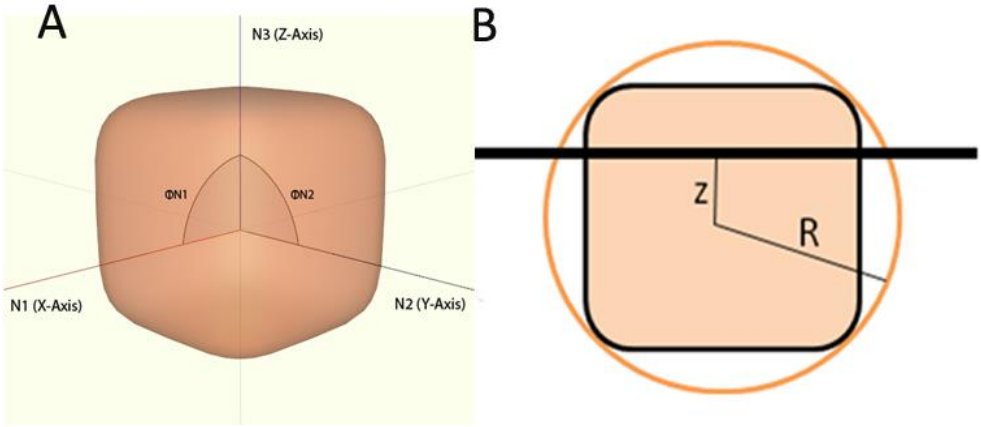

Figure 3.8. (**A**) Schematic of how particle rotation is defined with respect to the xy plane of the interface. (**B**). Diagram of how the radius of the surface bound sphere, ***R***, and the height from the liquid-liquid interface, ***z***, are defined.

Particle movement along the z axis is set by its dimensionless vertical coordinate, ž**,** as defined by **Equation (3.23**).

$$ž = {}^{z}/_{R} \tag{3.23}$$

Where z is the distance from the center of the sphere bounding the particle to the interface, and R is the radius of the bounding sphere. When $ž = 1$ the particle is in the oil and where $ž = -1$ the particle is immersed in water.

A specific orientation of the superellipsoidal particle with respect to the planar interface can now be expressed using the three parameters θ_1, θ_2, and ž. The total free energy at each orientation can be calculated through summation of the

products of the respective interfacial/surface tensions and the areas of contact, as in **Equation (3.24**).

$$E = \sigma_{P1}A_{P1} + \sigma_{P2}A_{P2} - \sigma_{12}A_{12} \quad \textbf{(3.24)}$$

The subscripts $P1, \mathrm{P2}$ and 12 denote the particle-oil, particle-water, and oil-water interface respectively. The interfacial tension values used in our work were σ_{P1} = 68 mN·m^{-1},[14] σ_{P2} = 23 mN·m^{-1},[15] and σ_{12} = 52 mN·m^{-1}.[13] This allowed us to simulate the free energy landscape for a PVP covered hematite particle at the *n*-hexadecane-water interface.

Note that our method falls in line with Pieranski's model[12] and does not take into account several factors which may contribute to the overall adsorption energy. We ignore effects due to gravity (such as interfacial deformation) because of the low energy involved compared to the adsorption energy in the low Bond number regime used here (< 5 x 10^{-11}). The effect of capillarity on deforming the interface is also ignored. This assumption is somewhat validated by the negligible interfacial distortion observed in experimental measurements and the fact that we deal with isolated particles - ruling out the effects of interparticle capillary bridging.[33] We also ignore the effects of line tension since the magnitude of this force is negligible for particles with a characteristic size exceeding the order of 10 nm.[26] Potential effects of surface charges, for example the intrinsic charge of the *n*-hexadecane-water interface, are also not taken into account. We believe that these assumptions are justified in this system, supported by the excellent correlation between experiments and simulated results.

The energy profile for the adhesion of superellipsoidal hematite particles at the *n*-hexadecane-water interface, calculated by our method, predicts two energy minima and thus two thermodynamic equilibrium orientations. These are in excellent agreement with two of our experimentally observed orientations (**Figure 3.7 A-F** and **Figure 3.7 G-L**). One orientation corresponds to the particle lying flat with respect to the interface (θ_1 = 0°, θ_2 = 0°, ž = -0.52), which corresponds to the global energy minimum (**Figure 3.9 A**). The other orientation is lying at a tilted angle corresponding to θ_1 = 45°, θ_2 = 35°, ž = -0.21 (**Figure 3.9 B**), which is a local minimum. The overall energy contour plot as a function of the angles θ_1 and θ_2 for the minimum ž value, E(θ_1, θ_2, $ž_{min}$), is also given (**Figure 3.9 C**).

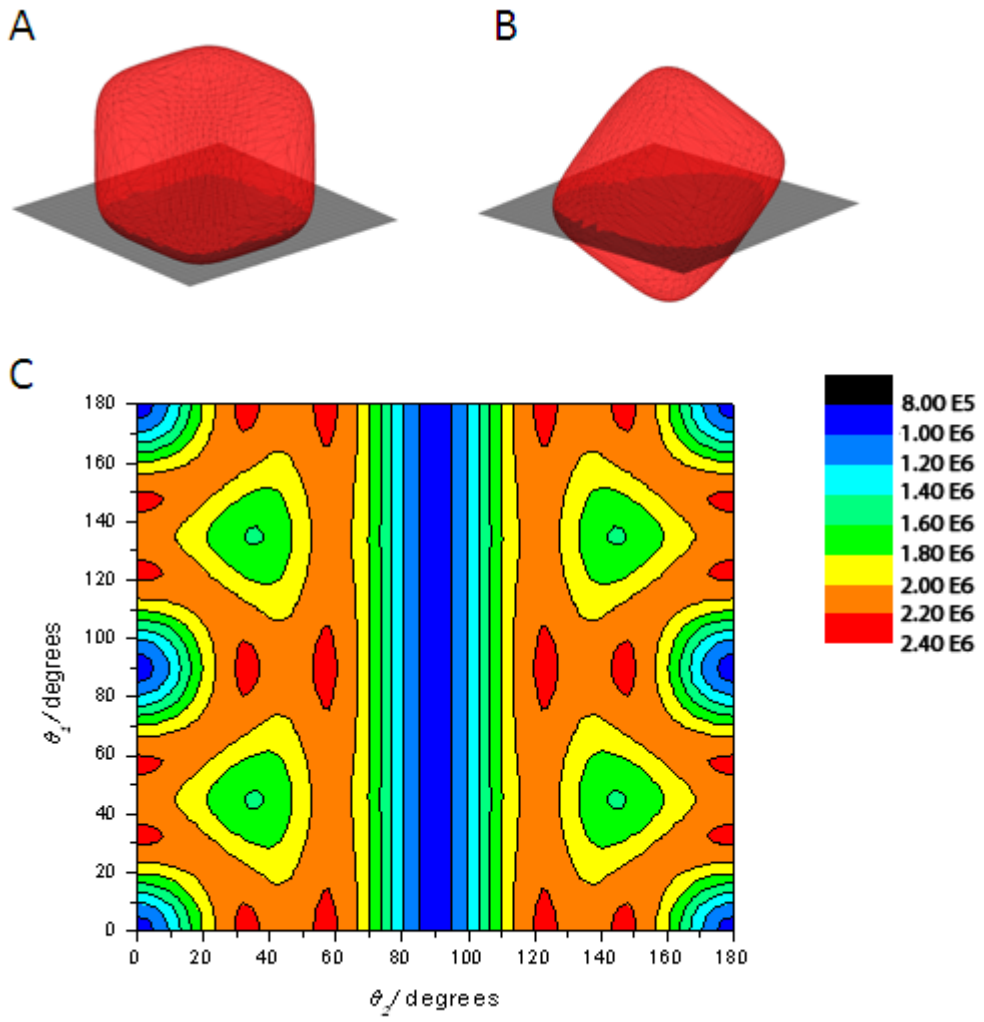

Figure 3.9. (**A**) Representation of a particle trapped at the global energy minimum, corresponding to the observed flat orientation found at $\boldsymbol{\theta_1}$ = 0°, $\boldsymbol{\theta_2}$ = 0°, ž = -0.52. See also **Figure 3.7 A-F**. (**B**) A second thermodynamically metastable tilted state is also observed at the local minimum found at $\boldsymbol{\theta_1}$ = 45°, $\boldsymbol{\theta_2}$ = 35°, ž = -0.21. See also **Figure 3.7 G-L**. (**C**) Energy profile of a superellipsoidal pseudocubic hematite particle at the *n*-hexadecane-water interface at its minimum ž value as a function of $\boldsymbol{\theta_1}$ and $\boldsymbol{\theta_2}$. Scale bar is in units of $\boldsymbol{k_BT}$.

3.2.3 Explanation of the third kinetically-trapped orientation

A third orientation that was found experimentally (See **Figure 3.7 M-R**) could not be assigned to any minima in the free energy landscape as determined by our simulations. In order to understand the existence of this orientation we looked closer at the dynamics of the transition of the particle from the oil phase into the interface. For this we initialized 100 particles at random orientations in the *n*-hexadecane phase with respect to the interface and calculated the associated energetic trajectories (**Figure 3.10**).

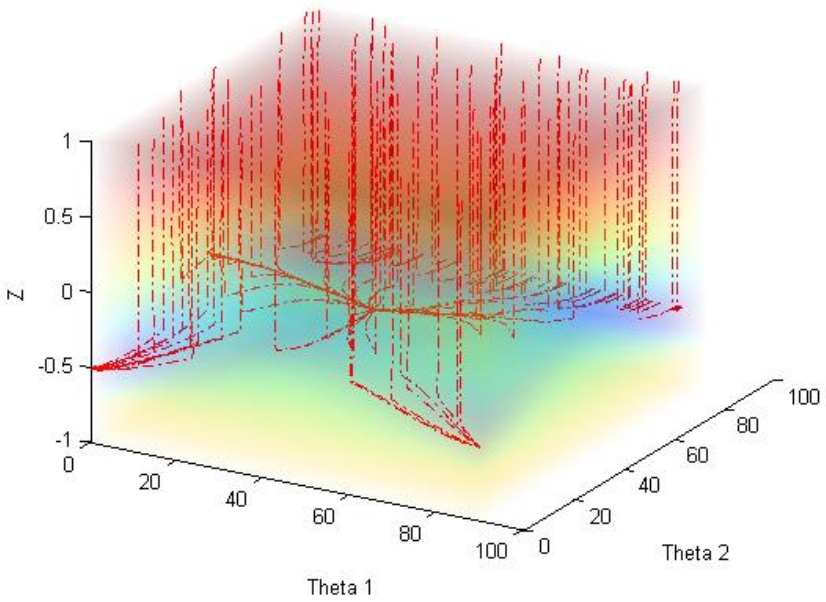

Figure 3.10. Simulation of energetic trajectories taken by 100 particles dropped towards the interface from a random starting orientation in the oil phase.

Trajectories that follow the path of steepest descent in terms of energy from an initial point $P^0(\theta_1{}^0, \theta_2{}^0, z^0)$ are calculated by interpolating between the values of the gradient of the free energy profile and using the constituent $d\theta_1$, $d\theta_2$, and dz

values to determine the direction of particle motion. In all cases the simulated trajectories of the particle could be discerned into two separate stages. First, a rapid "sinking" of the particles into the interface is observed, as the energy involved in translation of the particle from the oil phase into the interface (movement in the *z* axis) is significantly more favorable than the energy involved in particle rotation. Following this the particle undergoes rotation into an orientation that corresponds to an energy minimum. In certain cases it was observed that the energy profile contained a region between these two stages in which the gradient was negligible, which would allow for a kinetically-trapped (or transition) state (**Figure 3.11**). Closer examination indicated that this region relates to the third 'unknown' orientation that had been observed experimentally.

A movie depicting this transition is provided on the accompanying CD (See **Video ESI 3.1**) and clearly shows that the orientation the particle has in the plateau region of the energy profile corresponds with the sunk and tilted state as was experimentally observed for a small population of particles (See **Figure 3.7 M-R**).

To the best of our knowledge this is the first report of such a kinetic metastable state being observed experimentally for a particle at liquid-liquid interfaces. It must be mentioned that van Roij also noted that the orientation of anisotropic particles at the point of contact with the interface plays a crucial role on the dynamics of which minima the particle will end up in on the free energy landscape.[47]

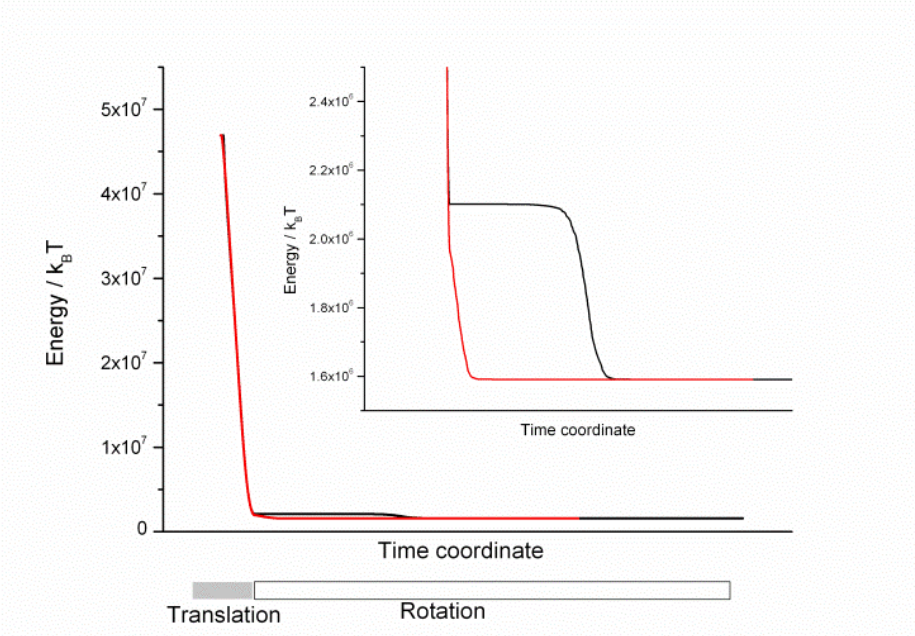

Figure 3.11. Plot of the total free energy involved in two specific hematite superellipsoidal pseudocubic particle trajectories into an *n*-hexadecane-water interface. Some particles experience a negligible gradient in free energy when re-orientating (black energy trajectory vs. the red energy trajectory), corresponding to the third observed kinetically-trapped transition state (See **Video ESI 3.1** on the supplied CD).

When we simulate a set of 100 different particles falling into the interfacial energy wells, and allow all of them to reach a thermodynamic equilibrium minimum (see **Figure 3.10**), 56% of the particles fall into the global energy minimum and thus adopt the flat orientation, whereas 44% get trapped in the local minimum, corresponding to the tilted orientation. The experimental observation of 59% of particles lying flat and the rest tilted is in excellent agreement with this data. This implies that our initial assumption, that is the particles can be modeled to have a random orientation prior to contact with the interface, is valid. Note that starting the

process of the particle interacting with the liquid-liquid interface from two orientations differing only slightly can have a huge impact on their final orientation, as demonstrated in the accompanying video on the CD (**Video ESI 3.2**). In this video two particles start their trajectories from similar orientations in the oil phase, being θ_1 = 20°, θ_2 = 55°, and θ_1 = 20°, θ_2 = 65° respectively. Upon contact they follow different pathways ending up in different final orientations. Thus the distribution of particle orientations observed once adhered to the oil-water interface is a result of the random tumbling of particles, the specific orientation the particle has when it comes into contact with the oil-water interface, and a potential plateau region in the energy profile of the trajectory; rather than a distribution predicted on the basis of the relative energy levels of the respective minima.

One outstanding question is if the hematite particles which are found in the kinetically-trapped state can eventually reach one of the two orientations that correspond to a minimum value in free energy. We believe that due to hysteresis effects (pinning) these particles by themselves may not have the ability to overcome this barrier.

3.3 Conclusions

We have shown through combination of simulation and experimental observations that hematite particles with a superellipsoidal pseudocubic shape can adopt one of three orientations when adhered to an oil-water interface. The favored orientation is the global energy minimum, which corresponds to a “flat” orientation.

Tilted particles comprise the other two conformations, both of which are metastable states; one being thermodynamic (a local minimum), the other being a kinetically-trapped transition state. The relative populations of each orientation observed experimentally were verified through simulation of particle trajectories. From this it was clear that some particles went through a negligible gradient in free energy during the transition from a high-energy state to a lower-energy state. This is the reason for the observation of a small ternary, kinetically-trapped, population of sunken and tilted particles.

Finally, we demonstrated that the distribution of the three populations is governed by the particle orientation upon contact with the interface, as well as the overall shape of the energy landscape. We believe that our findings contribute to a greater understanding of the behavior of solid particles when they interact with soft interfaces.

3.4 Experimental

3.4.1 Materials

Reagent grade iron(III) chloride hexahydrate, *n*-hexadecane, methanol, sodium hydroxide, Phytagel, polydimethylsiloxane (PDMS, 200 fluid, 10 cSt), Sylgard 184 elastomer, and PVP-K30 (40,000 $g \cdot mol^{-1}$) were all used as received from Sigma Aldrich. Deionized water was produced by a Milli-Q purification unit with a conductivity of 18 MΩ. Beer bottles and their swing tops were obtained from JBC glassware.

3.4.2 Preparation of hematite superellipsoidal pseudocubes

Superellipsoidal hematite particles were prepared by the route originally described by Muramatsu.[53] Iron(III) chloride hexahydrate (2.0 M, 100 mL) was added to a 200 mL beer bottle fitted with a ceramic swing top, and sealed with a Teflon-lined rubber seal. Sodium hydroxide solution (5.4 M, 90 mL) was slowly fed into the iron chloride solution under vigorous stirring over a period of 5 minutes before a small aliquot of deionized water (10 mL) was added. The bottle was sealed and transferred to an oven at 100°C where it was left for 8 days.

The amber-colored supernatant was removed and the sediment re-dispersed in water before 3 rounds of centrifugation at 2,500 g, re-dispersing in water each time. PVP-K30 (10.0 g) was added and the solution was allowed to stir for 48 hours to ensure complete adsorption before they were cleaned by a further 3 rounds of centrifugation/dispersion in water, and drying in an oven under vacuum at 60°C for 48 hours.

3.4.3 Assembly and immobilization of particle at the oil-water interface

A 2.0% wt. solution of Phytagel was made up by dissolving in water at 80°C with vigorous stirring and then left to cool to 50°C with light stirring, until no bubbles remained in the system. This solution was placed in a Petri dish and *n*-hexadecane at 50°C was layered on top. 100 μL of a 1.0% wt. hematite particle suspension in isopropanol was injected at the oil-water interface by syringe, and the Petri dish was left to cool for 30 minutes at room temperature until the aqueous phase gelled. The oil layer was gently removed by pipette and replaced by a Sylgard

184 elastomer at a mass ratio of 9:1 PDMS:curing agent ratio, which had previously been degassed under vacuum. The liquid PDMS was gently poured over the gel surface and left to cure for 2 days at room temperature. At this point the PDMS layer was peeled from the hydrogel surface and immersed in hot water for two minutes to remove any residual phytagel.

3.4.4 Imaging of trapped hematite particles

Squares of PDMS (1 cm x 1 cm) were cut before cleaning in boiling deionized water for 2 minutes. AFM images were obtained using an Asylum Research MFP-3D (Santa Barbara, USA) in AC mode using AC240TS cantilevers (Olympus).

SEM sample were prepared by sputter-coating PDMS squares with platinum at a 45° angle. An operating voltage of 1.5 kV was used, calculated to give a surface thickness of 5 nm. Imaging was performed at a 14.1° angle with respect to the plane of the interface on a FEG-SEM Zeiss Supra 55VP, operated at 10 kV. A simple trigonometric correction factor was applied when measuring particle height in order to account for the tilt of the stage. See **ESI**

3.1 on the accompanying CD for tabulated analysis of all SEM images, which can also be found in the same folder on the CD.

3.4.5 MATLAB simulations of stable particle orientations

Simulations were performed in MATLAB using a triangular tessellation method similar to that described by van Roij *et al*.[57] The particles are created from a series of points which all fit the unique expression for a superellipsoid (**Equation (**3.22).

$$\left(\frac{x^{2/n_2}}{r_x}+\frac{y^{2/n_2}}{r_y}\right)^{n_2/n_1}+\frac{z^{2/n_1}}{r_z}=1 \qquad \textbf{(3.22)}$$

Where x, y, and z denote the coordinates of the point r_x, r_y, and r_z, which are the particles x, y, and z radii. n_1 and n_2 act as the "squareness" parameters in the z axis and the xy plane respectively, with $0 < n_1, n_2 < \infty$. From the input parameters of r_x, r_y, r_z, n_1, n_2, and the number of points to be created, the particle shape is computed. The point coordinates are obtained by first generating an evenly distributed set of points around a sphere with $r_x = r_y = r_z = 1$ using the golden section spiral method. The x, y, and z coordinates from the sphere are converted into spherical coordinates and the x, y, and z values for the superellipsoid are calculated from the parametric equations (**Equation** (**3.25**)-**(**3.27).

$$x = r_x \cos^{n_1}\theta \cos^{n_2}\varphi \qquad \textbf{(3.25)}$$

$$y = r_y \cos^{n_1}\theta \sin^{n_2}\varphi \quad \textbf{(3.26)}$$

$$z = r_z \sin^{n_1}\theta \quad \textbf{(3.27)}$$

The surface of the particle is obtained from this set of data points by taking the convex hull of the data set, resulting in a series of triangles that connect the points.

The surface created by the above equation is bound by a sphere of minimum radius (R) centered at the origin, which can be rotated about the $x(\theta_1)$ and $y(\theta_2)$ axes, and translated in the z axis to give any position and orientation of the particle with respect to the interface. The particle movement in the z axis is defined by the vertical coordinate ž (**Equation 3.23**).

$$\check{z} = {}^{z}/_{R} \quad \textbf{(3.23)}$$

Where z is the distance from the center of the sphere bounding the particle to the interface, and R is the radius of the bounding sphere (where $\check{z} = 1$ the particle is in the oil phase and where $\check{z} = -1$ is in the water phase). The particle is scanned through various positions by translating and rotating the points, and at each position the associated energy is calculated. The energy is calculated by summing the area of triangles above and below the interface and multiplying by the interfacial tension. Triangles which intersect the interface are subdivided further and the new triangles are designated into the appropriate phase in a method analogous to that of van Roij *et*

al. The area of the interface that is "removed" upon adsorption of the particle is determined by connecting the points where lines from the triangular tessellation intersect the liquid-liquid interface, and then the areas of the described polygon are calculated. This can be summarized mathematically (**Equation (**3.24).

$$E = S_{P1}A_{P1} + S_{P2}A_{P2} - S_{12}A_{12} \quad \textbf{(3.24)}$$

Where E is the energy, S is the surface tension, and A is the area. The subscripts $P1$, $P2$ and 12 denote the particle-oil, particle-water, and oil-water interface respectively.

Particle trajectories and transitions between states were calculated by taking the negative gradient at each point in the 3-dimensional free energy landscape (**Equation (**3.28), calculated in the above section.

$$-\nabla E\ (\theta_1, \theta_2, z) = -\left(\frac{d\theta_1}{dE} + \frac{d\theta_2}{dE} + \frac{dz}{dE}\right) \quad \textbf{(3.28)}$$

Trajectories that follow the path of the steepest descent in terms of energy from an initial point, $P^0({\theta_1}^0, {\theta_2}^0, z^0)$, are calculated by interpolating between the values of the recorded gradient, and using the constituent $d\theta_1$, $d\theta_2$, and dz values to determine direction of particle motion. A zero-temperature string method was used to find pathways with an energy barrier, which allows one to calculate the minimum energy pathway between two energy minima.[58]

3.5 References

(1) Ramsden, W. *Proc. R. Soc. Lond.* **1903**, *72*, 156–164.

(2) Pickering, S. U. *J. Chem. Soc.* **1907**, *91*, 2001–2021.

(3) Finkle, P.; Draper, H. D.; Hildebrand, J. H. *J. Am. Chem. Soc.* **1923**, *45*, 2780–2788.

(4) Scheludko, A.; Toshev, B. V; Bojadjiev, D. T. *J. Chem. Soc. Faraday Trans. 1* **1975**, *72*, 2815–2828.

(5) Wiley, R. M. *J. Colloid Sci.* **1954**, *72*, 427–437.

(6) Sandmeyer, F.; Barthel, H.; Gottschalk-Gaudig, T. U.S. Pat. 8409710 B2 **2013**.

(7) Chen, T.; Colver, P. J.; Bon, S. A. F. *Adv. Mater.* **2007**, *19*, 2286–2289.

(8) Dinsmore, A. D.; Hsu, M. F.; Nikolaides, M. G.; Marquez, M.; Bausch, A. R.; Weitz, D. A. *Science* **2002**, *298*, 1006–1009.

(9) Herrera-Alonso, J. M.; Sedláková, Z.; Marand, E. *J. Membrane Sci.* **2010**, *363*, 48–56.

(10) Colard, C. A. L.; Cave, R. A.; Grossiord, N.; Covington, J. A.; Bon, S. A. F. *Adv. Mater.* **2009**, *21*, 2894–2898.

(11) Fortuna, S.; Colard, C. A. L.; Troisi, A.; Bon, S. A. F. *Langmuir* **2009**, *25*, 12399–12403.

(12) Pieranski, P. *Phys. Rev. Lett.* **1980**, *45*, 569–572.

(13) Wang, D.; Yordanov, S.; Paroor, H. M.; Mukhopadhyay, A.; Li, C. Y.; Butt, H-J.; Koynov, K. *Small* **2011**, *7*, 3502–3507.

(14) Águila-Hernández, J.; Trejo, A.; García-Flores, B. E. *J. Chem. Eng. Data* **2011**, *56*, 2371–2378.

(15) Çaykara, T.; Yerlikaya, Z.; Kantoğlu, Ö. *J. Appl. Polym. Sci* **2004**, *91*, 1893–1897.

(16) Ballard, N.; Bon, S. A. F. *Polym. Chem.* **2011**, *2*, 823–827.

(17) Binks, B. P.; Lumsdon, S. O. *Langmuir* **2000**, *16*, 8622–8631.

(18) Bancroft, W. D. *J. Phys. Chem.* **1913**, *17*, 501–519.

(19) Binks, B. P.; Clint, J. H. *Langmuir* **2002**, *18*, 1270–1273.

(20) Golemanov, K.; Tcholakova, S.; Kralchevsky, P. A.; Ananthapadmanabhan, K. P.; Lips, A. *Langmuir* **2006**, *22*, 4968–4977.

(21) Aveyard, R.; Clint, J. H.; Horozov, T. S. *Phys. Chem. Chem. Phys.* **2003**, *5*, 2398–2409.

(22) Aveyard, R.; Beake, B. D.; Clint, J. H. *J. Chem. Soc. Faraday Trans.* **1996**, *92*, 4271–4277.

(23) Scheludko, A.; Toshev, B. V.; Bojadjiev, D. T. *J. Chem. Soc. Faraday Trans.* **1976**, *72*, 2815–2828.

(24) Aveyard, R.; Clint, J. H. *J. Chem. Soc. Faraday Trans.* **1996**, *92*, 85–89.

(25) Lehle, H.; Oettel, M. *J. Phys.: Conens. Matter* **2008**, *20*, 404224 (10).

(26) Cheung, D. L.; Bon, S. A. F. *Phys. Rev. Lett.* **2009**, *102*, 066103 (4).

(27) Aarts, D. G. A. L.; Schmidt, M.; Lekkerkerker, H. N. W. *Science* **2004**, *304*, 847–850.

(28) Zorba, V.; Stratakis, E.; Barberoglou, M.; Spanakis, E.; Tzanetakis, P.; Anastasiadis, S. H.; Fotakis, C. *Adv. Mater.* **2008**, *20*, 4049–4054.

(29) Nonomura, Y.; Komura, S.; Tsujii, K. *Langmuir* **2005**, *21*, 9409–9411.

(30) Wenzel, R. N. *Ind. Eng. Chem.* **1936**, *28*, 988–994.

(31) Cassie, A. B. D.; Baxter, S. *Trans. Faraday Soc.* **1944**, *40*, 546–551.

(32) San-Miguel, A.; Behrens, S. H. *Langmuir* **2012**, *28*, 12038–12043.

(33) Danov, K. D.; Kralchevsky, P. A.; Naydenov, B. N.; Brenn, G. *J. Colloid Interface Sci.* **2005**, *287*, 121–134.

(34) Xu, H.; Melle, S.; Golemanov, K.; Fuller, G. *Langmuir* **2005**, *21*, 10016–10020.

(35) Kim, E. G.; Stratford, K.; Clegg, P. S.; Cates, M. E. *Phys. Rev. E.* **2012**, *85*, 020403 (4).

(36) Tavacoli, J. W.; Katgert, G.; Kim, E. G.; Cates, M. E.; Clegg, P. S. *Phys. Rev. Lett.* **2012**, *108*, 268306 (5).

(37) Wang, H.; Singh, V.; Behrens, S. H. *J. Phys. Chem. Lett.* **2012**, *3*, 2986–2990.

(38) Israelachvili, J. N. *Intermolecular and Surface Forces*; 2011; pp. 256–260.

(39) Cheung, D. L.; Bon, S. A. F. *Soft Matter* **2009**, *5*, 3969–3976.

(40) Li, T.; Niu, Z.; Emrick, T.; Russell, T. P.; Wang, Q. *Small* **2008**, *4*, 1624–1629.

(41) Loudet, J. C.; Alsayed, A. M.; Zhang, J.; Yodh, A. G. *Phys. Rev. Lett.* **2005**, *018301* (4).

(42) Binks, B. P.; Fletcher, P. D. I. *Langmuir* **2001**, 4708–4710.

(43) Aveyard, R. *Soft Matter* **2012**, *8*, 5233–5240.

(44) Ruhland, T. M.; Gröschel, A. H.; Walther, A.; Müller, A. H. E. *Langmuir* **2011**, *27*, 9807–9814.

(45) Park, B. J.; Lee, D. *ACS nano* **2012**, *6*, 782–790.

(46) Morris, G.; Neethling, S. J.; Cilliers, J. J. *J. Colloid Interface Sci.* **2011**, *354*, 380–385.

(47) De Graaf, J.; Dijkstra, M.; van Roij, R. *J. Chem. Phys.* **2010**, *132*, 164902 (14).

(48) Aveyard, R.; Clint, J. H.; Nees, D.; Paunov, V. N. *Langmuir* **2000**, *16*, 1969–1979.

(49) Di Leonardo, R.; Saglimbeni, F.; Ruocco, G. *Phys. Rev. Lett.* **2008**, *100*, 106103 (4).

(50) Danov, K. D.; Kralchevsky, P. A. *Adv. Colloid Interface Sci.* **2010**, *154*, 91–103.

(51) Lewandowski, E. P.; Cavallaro, M.; Botto, L.; Bernate, J. C.; Garbin, V.; Stebe, K. J. *Langmuir* **2010**, *26*, 15142–15154.

(52) Bowden, N.; Terfort, A.; Carbeck, J.; Whitesides, G. M. *Science* **1997**, *276*, 233–235.

(53) Sugimoto, T.; Khan, M. M.; Muramatsu, A. *Coll. Surf. A* **1993**, *70*, 167–169.

(54) Rufier, C.; Reufer, M.; Dietsch, H.; Schurtenberger, P. *Langmuir* **2011**, *27*, 6622–6627.

(55) Shchukarev, A.; Boily, J.-F.; Felmy, A. R. *J. Phys. Chem. C* **2007**, *111*, 18307–18316.

(56) Paunov, V. N. *Langmuir* **2003**, *19*, 7970–7976.

(57) De Graaf, J.; Dijkstra, M.; van Roij, R. *Phys. Rev. E* **2009**, *80*, 1–19.

(58) E, W.; Ren, W.; Vanden-Eijnden, E. *J. Chem. Phys.* **2007**, *126*, 164103 (8).

Chapter 4

"Chemotaxis of Catalytic Silica-Manganese Oxide 'Matchstick' Particles"[a]

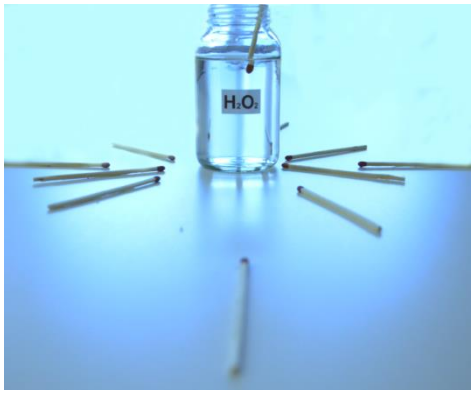

In this chapter we use a water-in-oil emulsion strategy in the fabrication of silica rods that contain a hollow manganese oxide sphere at one end. Incorporation of the manganese oxide particles allows us to tune the diffusion coefficient of the particles in solution by varying the amount of hydrogen peroxide added as fuel. We find this to be a first-order relationship. Chemotaxis of the particles is then demonstrated when they are placed into a gradient of hydrogen peroxide that acts as chemoattractant.

Convection is ruled out as the force behind the directional movement of the rods by including catalytically inert polymer microspheres, which move under convection in the opposite direction to the catalytically active rods. This is the first example of a synthetic strategy that enables large quantities of "swimmers" to be synthesized out of low cost materials, and with a diverse range of facile surface

modifications possible to enhance functionality, such as the potential for self-assembly by introducing Janus type wettability across the particle.

[a] Part of this work was published

Morgan, A.R.; Dawson, A.B.; McKenzie, H.S.; Skelhon, T.S.; Beanland, R.; Franks, H.P.W.; Bon, S.A.F.; *Materials Horizons*, **2014**, Advance Article, DOI: 10.1039/C3MH00003F.

4.1 Introduction

Autonomous movement of microscopic particles and microorganisms in liquids operates in a low Reynolds' number (*Re*) regime where inertial forces are outweighed by viscous forces due to the small dimensions of the object (**Equation 4.1**).

$$\boldsymbol{Re = \frac{av\rho}{\eta} = \frac{Inertial\ Forces}{Viscous\ forces}} \quad \textbf{(4.1)}$$

Where a = characteristic particle dimension, v = velocity of the object, ρ = density of the fluid, and η = dynamic viscosity of the fluid.

In the submicron size regime colloidal matter undergoes Brownian motion, whereby the root mean squared displacement ($\sqrt{MSD}$) is diffusive in character at long time intervals. This phenomenon of seemingly random motion by microparticles was first noted by a Roman, Lucretius, in 60 BC when he observed dust particles in a light beam being perturbed by convection currents in the air. Later on, in 1674, Anthony van Leeuwenhoek observed motion of what he believed to be "animalcules" in a drop of water when observed through one of his newly invented magnifying glasses, attributing the motion of the particles to the fact that they must be alive. Then, in 1828 botanist Robert Brown produced a manuscript on the random motion of pollen grains and other inorganic particles in water when observed under a microscope.[1] It was somewhat unfortunate for Adolphe Brongniart that the namesake is attributed to Brown however, as he made similar observations a year before in 1827.[2]

The underlying reason for the random Brownian motion of colloids is due to the thermal motion of solvent molecules that bombard the particles' surface, something realized by Gouy in 1888.[3] It was in 1905 that Einstein quantified this translational motion for the case of a spherical "Stokes" particle in one-dimension, by applying the drag equation with the van't Hoff equation to particles in suspension, giving the Stokes-Einstein equation (**Equation 4.2**).[4] This was derived later on by Langevin in a very elegant fashion on just one page and later translated by Lemons and Gythiel[5] (Note that Sutherland[6] and von Smoulochowski[7] derived similar results in 1905-1906 as well).

$$D = \frac{RT}{N_A}\frac{1}{6\pi\eta a} \tag{4.2}$$

Where D = Diffusion coefficient, R = Molar gas constant, T = temperature, N_A = Avogadro's number.

Through knowledge of the diffusional coefficient it is then possible to calculate the $\sqrt{MSD}$ of a sphere in one Cartesian dimension, x_{rms}, as a function of time, *t*, as follows (**Equation 4.3**).

$$\boldsymbol{x_{rms} = < x^2(t) >^{1/2} \ (= \sqrt{2Dt})} \tag{4.3}$$

The importance of this equation in tying together macroscale thermodynamics and atomic theory was then demonstrated experimentally by Perrin

wherein he measured the $\sqrt{MSD}$ as a function of time to derive an exact value for N_A (**Equation 4.4**).[8]

$$N_A = \frac{t}{< \Delta x(t)]^2 >} \frac{RT}{3\pi\eta a} \quad \textbf{(4.4)}$$

And so it can be seen that investigations pertaining to Brownian motion clearly had profound implications for thermodynamics and atomic theory.

The diffusive nature of a particle is only true at long time scales (diffusive regime), where motion is averaged out. If one were to look at very small time intervals then it is in fact dominated by inertia (ballistic regime), where one can imagine the process as a particle being moved by collision with solvent molecules, causing it to coast until it comes to a stop, and the process repeating. Over long time intervals it appears that the particle is constantly diffusing, however when you look closer it actually stops and starts. This was postulated by Einstein in 1907 and only experimentally verified in 2010 by Raizen and co-workers when they studied the instantaneous velocity of a 3 μm silica sphere trapped in air with optical tweezers.[9] For a more in-depth history of Brownian motion the reader is referred to Haw.[10]

Certain particles and microorganisms also have the ability to undergo self-propulsion, which can be expressed in the form of "enhanced diffusion coefficients".

Some of these particles can also undergo directional motion when exposed to a directional stimulus (-taxis), but this is something we will discuss later on in this section.

Broadly speaking there are two ways that small objects dispersed in fluids can self-propel:

(1) They undergo a time-irreversible mechanical deformation in order to undergo motion. In the low Reynolds' number regime inertial forces are irrelevant and so, if we were to cancel the inertial components on the right of **Equation 4.5** (Navier-Stokes equation for isochoric flow), then time is also irrelevant.

$$-\nabla p + \eta\nabla^2 \vec{\upsilon} = \rho\frac{\partial \vec{\upsilon}}{\partial \mathrm{t}} + \rho(\vec{\upsilon}\cdot\nabla)\vec{\upsilon} \qquad \textbf{(4.5)}$$

On the left-hand side of the equation $-\nabla p$ is the pressure gradient, and $\eta\nabla^2 \vec{\upsilon}$ describes the viscosity. On the right-hand side of the equation the whole term corresponds to inertia per volume, itself being comprised of local and convective acceleration following a particle at a location and time of interest.

Consequently reciprocal motion is the same backwards as it is forwards and so this is not a valid mechanism for propulsion of "mechanical swimmers". Particles that propel themselves using a time-irreversible deformation mechanism are commonly referred to as "Purcell swimmers", following the lecture by Purcell on this phenomenon.[11] Perhaps the most familiar example of this type of motion is that of bacteria's flagella.

Bibette and co-workers utilized the propulsion mechanism of initiating a time-irreversible deformation in order to propel a particle which consisted of a red blood cell attached to a flexible chain of magnetic particles (joined together by a streptavadin-biotin interaction) in an oscillating magnetic field.[12]

Ghosh and Fischer utilized a homogenous magnetic field with rotating frequency to propel corkscrew shaped SiO_2 particles in a time-irreversible fashion, with precise control over their spatial movement.[13]

(2) The propelling particles generate a gradient field onto their local environment, of which there are an abundance of different paradigms with various mechanisms proposed.

Examples include the traditional camphor/soap boat[14,15] that consists of a small well of material confined on a macroscale object and allowed to diffuse out; thereby creating an asymmetrical gradient in surface tension with subsequent propulsion in the opposite direction to diffusion.

A popular mechanism for the propulsion of smaller objects is bubble propulsion, whereby a catalytic engine is included on the particle that can facilitate the breakdown of a fuel (typically a fairly concentrated solution of hydrogen peroxide, which is decomposed into oxygen and water). In doing so there is a gas bubble generated on the particle that displaces surrounding fluid during its growth and detachment (**Figure 4.1**).[16–18]

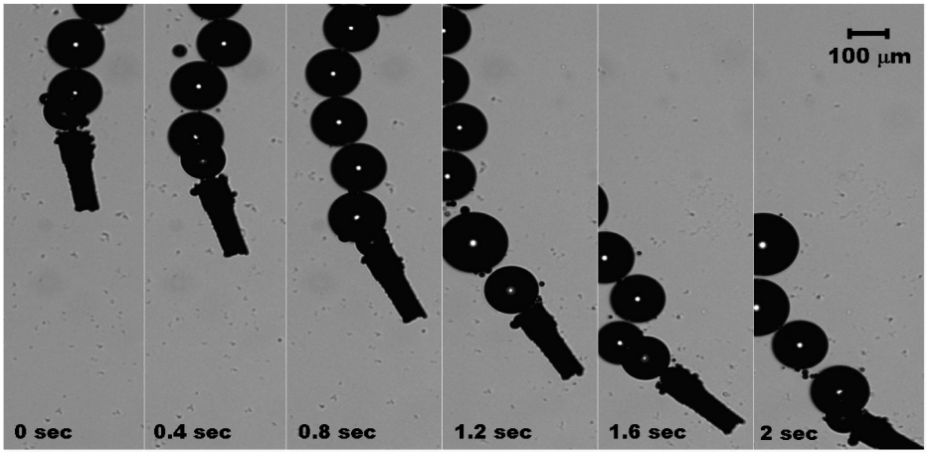

Figure 4.1. A Pt-Au microparticle, with the ability to catalytically convert hydrogen peroxide into oxygen and water. It can undergo propulsion due to the fluid displaced by the formation and detachment of the gas bubble. Image from reference.[16]

Diffusiophoresis is a colloidal propulsion mechanism in which particles that are exposed to a non-homogenous solution of molecular solutes migrate to regions of higher solute concentration, as a result of the molecules' interaction with the slip plane of the colloids' double layer.[19] A flow is created at the interfacial region of the double layer due to charge-mediated adsorption or repulsion of solutes, which can be modeled using the Nernst-Planck equation.[20,21]

Other mechanisms that would fall into this category include induced electrophoresis[22] and catalytic fluid pumping.[23]

Self-propulsion can be made directional when external gradients are imposed on the particles.[24–28] In man-made systems direction of motion is the apex of colloidal delivery of cargo and self-assembling systems. An elegant example that achieves this by using an external magnetic field to direct particle motion has been described by Sanchez and co-workers. They show that catalytic microtubes

undergoing bubble propulsion can be guided against the direction of fluid flow in microfluidic channels.[29]

Light-induced self-propulsion and dynamic assembly of photoactivated colloidal particles into colloidal crystals was recently demonstrated by Palacci and co-workers.[30]

When the external gradient is of a chemical origin one speaks of (chemo)taxis. This is crucial to the movement of microorganisms in their quest to out swim diffusion. They use "temporal sensing" as an internal feedback loop to determine the direction of the gradient.

Velegol and co-workers showed that bimetallic colloidal rods could undergo chemotaxis, causing them to accumulate in a gel that was soaked in hydrogen peroxide as the attractant and fuel (**Figure 4.2**).[31]

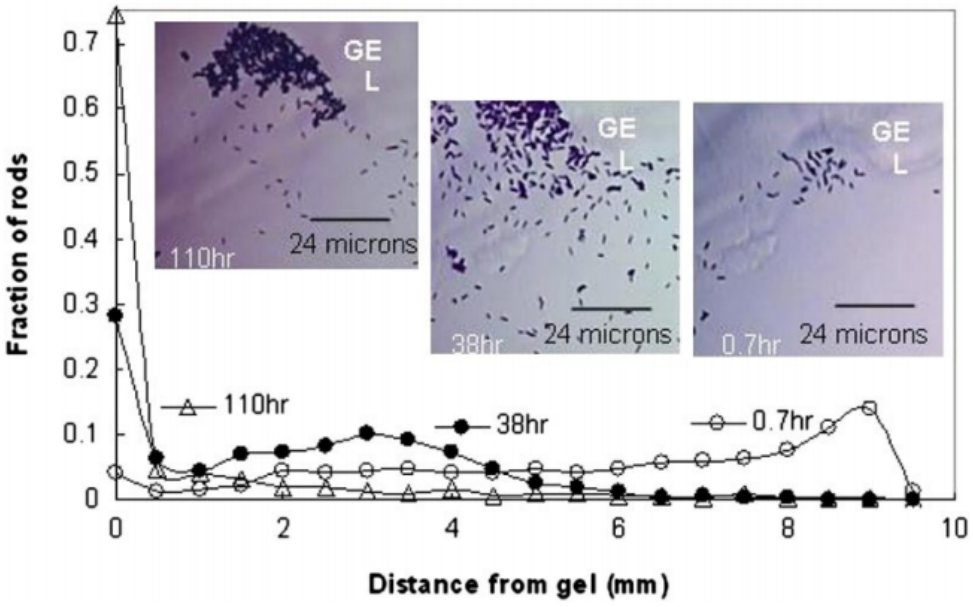

Figure 4.2. Velegol and co-workers used a hydrogen peroxide soaked gel to attract Pt-Au microrods via chemotaxis. Image from reference.[31]

We set out to develop "matchstick" shaped particles with a catalytic head that can undergo chemotaxis. The reason for this design was two-fold. First, high aspect ratio rod-like particles are a favorable geometry for efficient propulsion, as seen for example in nature, in the shapes of highly motile bacterial cells.[32]

Zerbetto *et al.* used dissipative particle dynamics as a modeling tool to show that that rods with an aspect ratio of 5 were more efficient propulsion devices than catalytic Janus spheres, rods with a lower aspect ratio (1.76), and disk-like particles (**Figure 4.3**).[33]

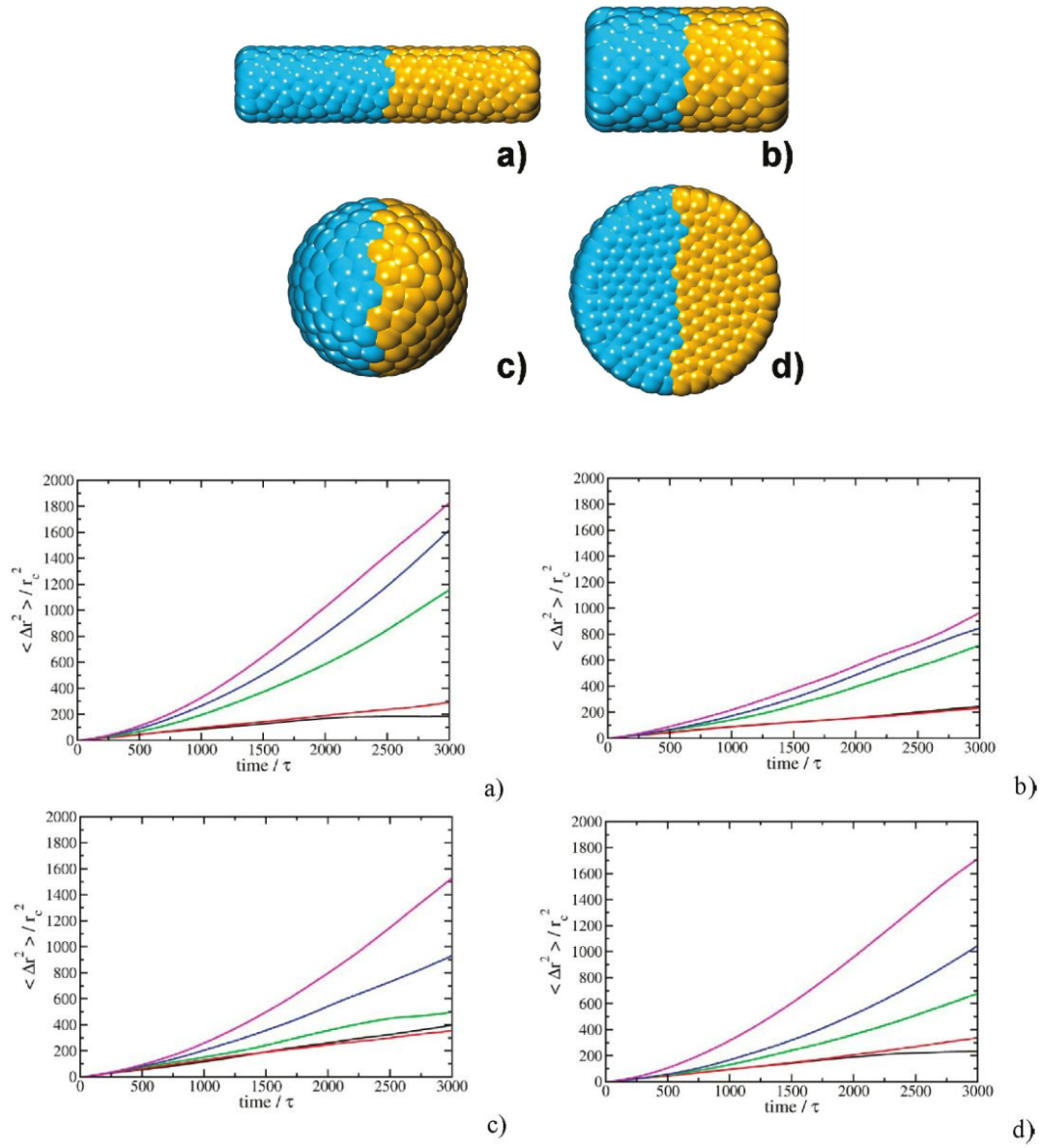

Figure 4.3. Zerbetto and co-workers simulated the motion of four Janus micromotors with dissipative particle dynamics. The geometries of the particles studied are shown in the top image, and correspond to (**a**) long rod (aspect ratio, AR = 5.00), (**b**) short rod (AR = 1.76), (**c**) sphere (AR = 1.00) and (**d**) disk (AR = 0.17). In the plots below one can see the MSD as a function of time interval for the four particles at different fuel concentrations. Images from reference.[33]

High aspect ratio rod-shaped particles have their rotational diffusion suppressed due to asymmetrical drag coefficients, which in turn facilitate the efficiency of translational motion that is desirable for chemotaxis.[34,35] Examining the translational diffusion coefficient of a rod indicates that a higher aspect ratio shape is favorable, but this is in an interplay with the length of the rod as well (**Equation 4.6**).

$$D^t = \left[\left(\left(D_{\parallel}^t + 2D_{\perp}^t\right)/3\right) = \left((k_B T \ \ln p)/(3\pi\eta L)\right)\right] \quad \textbf{(4.6)}$$

Where p = aspect ratio, L = length of rod, and $D_{\parallel}^t$= motion parallel to the axis of the rod, which is equal to **Equation 4.7**.

$$D_{\parallel}^t = \left((k_B T \ \ln p)/(2\pi\eta L)\right) \quad \textbf{(4.7)}$$

$D_{\perp}^t$ = motion perpendicular to the axis of the rod and is equal to **Equation 4.8**.

$$D_{\parallel}^t = \left((k_B T \ \ln p)/(4\pi\eta L)\right) \quad \textbf{(4.8)}$$

The second reason for our matchstick design was that the engine which drives the self-propulsion needs to have at least one degree of asymmetry along the particle to have directional motion. A "matchstick" design, whereby the head contains the engine (in our case a metal oxide catalyst), is ideal as it shows asymmetry perpendicular to the direction of self-propulsion and at the same time it maintains rotational symmetry parallel with the plane of motion.

Herein we demonstrate the synthesis of silica rods that contain a manganese oxide head located at one end from a water-in-oil emulsion. The manganese oxide head is formed by doping the water droplets in the emulsion with manganese sulfate, and subsequently oxidizing these species to nanoparticles in order to generate Pickering stabilized droplets that serve as nuclei for silica rod growth.

We explore the mechanism behind their formation and demonstrate an enhanced diffusion coefficient for the particles by adding hydrogen peroxide as a fuel source, which is broken down into water and oxygen by the manganese oxide head. It is also demonstrated that the particles display chemotactic behavior when exposed to a hydrogen peroxide gradient. Convection is ruled out as a possible source of directional movement for the rods by including catalytically inert polymer microspheres, which move under convection in the opposite direction to chemotactic rod movement.

4.2 Results and Discussion

4.2.1 Synthesis and characterization of SiO_2-Mn_xO_y "matchstick" particles

Our strategy for the fabrication of catalytically self-propelling "matchstick" particles found its origin in a versatile procedure for the preparation of micron-scale silica rods which use water droplets as seeds for silica growth.[36] The synthetic twist that we have developed, which led to the design of a distinct "matchstick" head, was to introduce a metal oxide engine into the silica rods by templating the water droplets with *in situ* generated manganese oxide nanoparticles. These nanoparticles served as Pickering stabilizers, thus decorating the emulsion droplets prior to silica growth from the droplet.

In a typical reaction 0.20 mL of a 0.18 M aqueous sodium citrate solution, 0.84 mL of a 0.10 M manganese sulfate solution, and 3.00 mL of ethanol were added to 30.00 mL of a 1-pentanol solution containing 100 $g \cdot L^{-1}$ poly(vinyl pyrrolidone) (PVP-K30, Mwt. 40,000 $g \cdot mol^{-1}$). This mixture was emulsified by vigorous hand shaking after which a 0.40 mL solution of 18.10 M ammonia was added to initiate the formation of manganese oxide nanoparticles via reduction of the metal sulfate species. After 2 minutes 0.30 mL of tetraethylorthosilicate (TEOS) was added to start silica growth.

Scanning electron microscopy (SEM) characterization clearly shows that our target "matchstick" shaped particles had been formed (**Figure 4.4**). The mean average and standard deviation of the overall length (1702 ± 208 nm), head width (327 ± 107 nm), and tail width (234 ± 93 nm) were calculated from analysis of 100 particles in SEM images. The aspect ratio of our particles tapers along the long axis of the rod, averaging at 5.2 at the end containing the "matchstick" head, and 7.3 at the opposite end. These aspect ratios approximate the morphological criteria outlined by Zerbetto and co-workers for efficient self-propulsion.

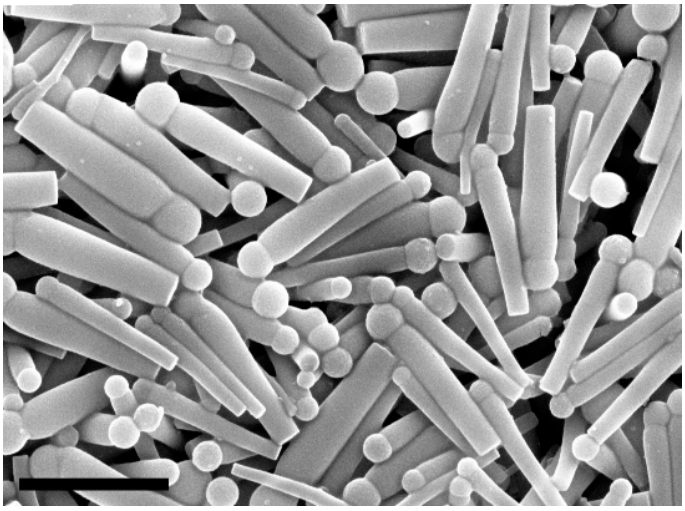

Figure 4.4. SEM image of SiO_2-Mn_xO_y "matchstick" rods. Scale bar = 2 μm.

If our synthesis strategy is correct, that is the manganese oxide nanoparticles act as Pickering stabilizers and thus armor the water droplets, then the manganese oxide should be concentrated predominantly in the head of our "matchstick" particles (**Figure 4.5**, Spot 1), with a small enrichment at the flat tail end (**Figure 4.5**, Spot 4). This is due to silica asymmetrically phase separating from the armored droplet, taking some of the metal oxide species with it. Furthermore, we believe that the water droplet containing the metal species phase separates out from inside the hydrophobic manganese oxide cavity once formed, and onto the end of the growing silica tail; thus leading to a distribution of manganese along the rod.

This distribution of manganese oxide is indeed confirmed by spatial transmission electron microscopy-energy dispersive x-ray spectroscopy (TEM-EDAX) analysis of a single rod (**Figure 4.5** and **Table 4.1**). Note that although the manganese oxide species is not Mn_2O_3 (we shall see that it is in fact a complex mixture of manganese, oxygen, and silica that resembles Braunite-1Q, Syn), we use this stoichiometry as a base model to enable detection of manganese in the particles.

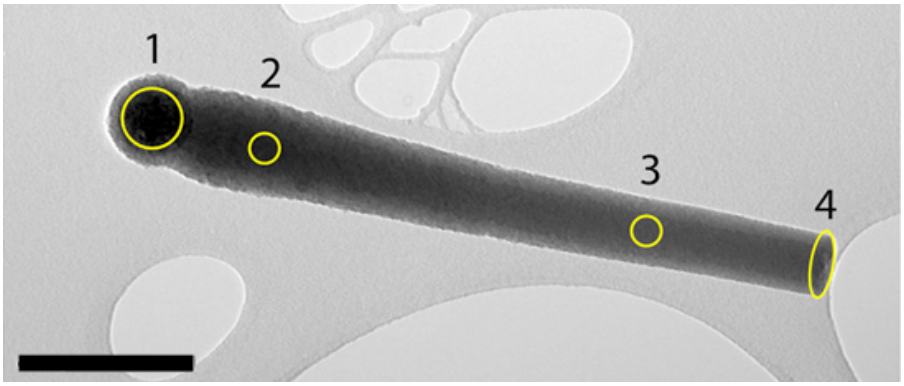

Figure 4.5. TEM image of an individual SiO_2-Mn_xO_y rod that was analyzed via EDAX at each area highlighted. The results of the analysis are summarized in **Table 4.1**. Scale bar = 400 nm.

Table 4.1. Distribution of manganese oxide within the SiO_2 rods as analyzed via EDAX in TEM mode (**Figure 4.5**).

Analysis Area	Weight % Mn_2O_3	Weight % SiO_2
1	19.4	80.6
2	1.0	99.0
3	2.0	98.0
4	3.3	96.7

Additional EDAX measurements of other matchstick particles can be found in **Appendix IV.1**, **Figure IV.1** and **Table IV.1**. The results are in good agreement with those reported in **Table 4.1**.

XRD patterns of our catalytic microrods were measured as function of temperature up to 850°C, during which the particles transitioned from being of

amorphous composition, into a complex mixture of silicon, oxygen, and manganese crystalline polymorphs. No crystallinity is observed below 800°C for the manganese oxide or silica oxide phases. However, crystallinity is induced above 800°C; as can be seen from the plot of scattering intensity as a function of temperature (**Appendix IV.2, Figure IV.2**).

The XRD pattern of the sample calcined in air at 850°C shows it to be predominantly crystalline silicon oxide (some hydrated). There is also a complex mixture of manganese oxides/silicates present including Braunite-1Q, Syn, which is a mixture of all three elements Mn, Si, and O (**Figure 4.6**).

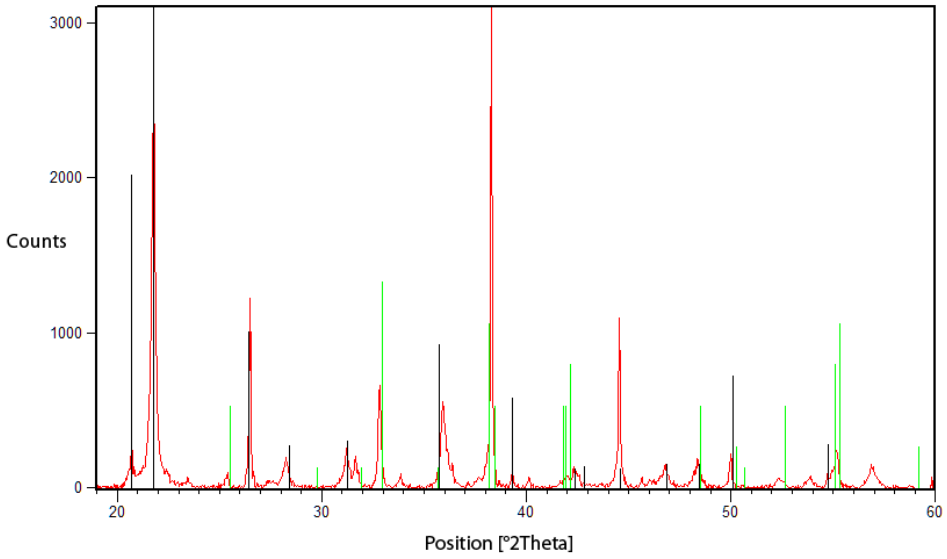

Figure 4.6. XRD pattern of silica-manganese oxide rods following calcination in air at 850°C (**Red trace**). Crystallized forms of silicon oxides could be assigned, namely Opal-A ($SiO_2.xH_2O$) and silicon dioxide (SiO_2) (**Black lines**). The best fit for the manganese oxide species was Braunite-1Q, Syn (Mn_7SiO_{12}) (**Green lines**).

4.2.2 Mechanistic features of particle growth

Initially we propose that the aqueous droplets containing the metal salts are emulsified in the pentanol reaction medium, with added stabilization from the PVP-K30 physisorbed at the oil-water interface. Addition of ammonia to the emulsion causes a rapid oxidation of the hydrated metal sulfate to the hydroxide, which then decomposes in the presence of oxygen to form the metal oxide. As-formed metal oxide nanoparticles then migrate to the interface where they act as Pickering stabilizer.

From XRD analysis it is clear that the manganese oxide formed is a complex amorphous material, however a simplified reaction scheme can be given as follows in **Scheme 4.1**.

$$[Mn(H_2O)_6]^{2+}.SO_4^{2-} + 2NH_3 \rightarrow [Mn(H_2O)_4OH_2] + 2NH_4^+$$

$$[Mn(H_2O)_4OH_2] + O_2 \rightarrow 2Mn_2O_3 + 4H_2O$$

Scheme 4.1. Hydrated manganese sulfate is converted to the hydroxide upon the addition of ammonia. Then, it decomposes in the presence of oxygen to form manganese oxide nanoparticles that migrate to the water-oil interface to act as Pickering stabilizer.

The reason for this amorphous nature is likely due to the fact that the Mn(III) species rapidly polymerizes to form the oxide, which further catalyzes reaction of the Mn(II) species, making separation of the reaction pathways very difficult as they occur simultaneously.[37]

In the original papers outlining the silica rod synthesis sodium citrate is a critical component of the reaction as it confers colloidal stability of the droplet through electrostatic repulsion.[36] We found that the reaction works in our system

even in the absence of sodium citrate, which would indicate that Pickering stabilizer particles provide adequate colloidal stability. We propose the following reaction mechanism for the formation of the SiO_2-Mn_xO_y rods (**Figure 4.7**).

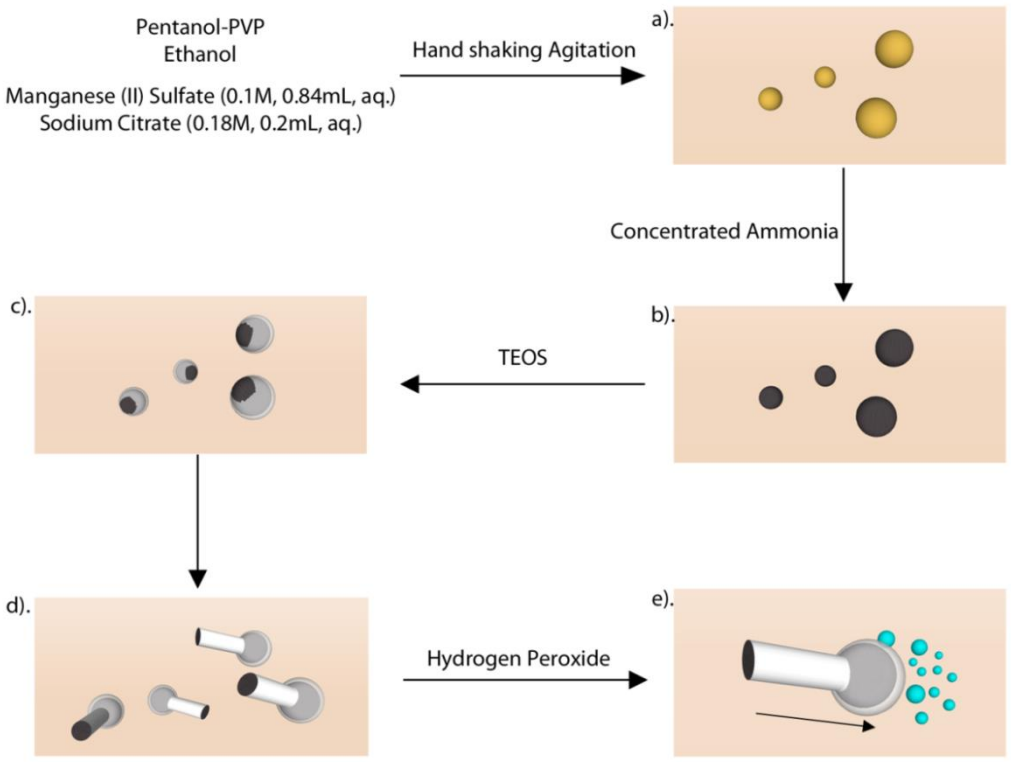

Figure 4.7. Proposed mechanism for hybrid rod growth (**a**) Water-in-oil emulsion is formed upon hand shaking agitation after addition of the reagents. (**b**) Addition of ammonia causes oxidation of the metal salts in the water phase to metal oxide nanoparticles, which migrate to the interface to stabilize it (Pickering). (**c**) TEOS migrates through the oil phase and begins to hydrolyze upon contact with the basic water phase. Condensation of the species at the interface then begins. A nucleation site develops which hydrolyzed reactants preferentially condense on to. (**d**) The basic water droplet phase separates out of the hydrophobic manganese oxide head. Further condensation of the silica onto the growing nucleus results in the formation of a silica rod, thus creating the "matchstick" shaped particles. (**e**) Addition of hydrogen peroxide allows the particles to self-propel by either diffusiophoretic or bubble detachment mechanisms, depending on the concentration of the fuel.

In order to corroborate our proposed mechanism involving manganese oxide particles as Pickering stabilizers at the water-oil interface, we carried out the reaction in the absence of TEOS. Analysis of the resulting particle morphology via SEM (**Figure 4.8 A** and **B**) and TEM (**Figure 4.8 C**) confirmed that hollow spheres templated around the water droplets are formed.

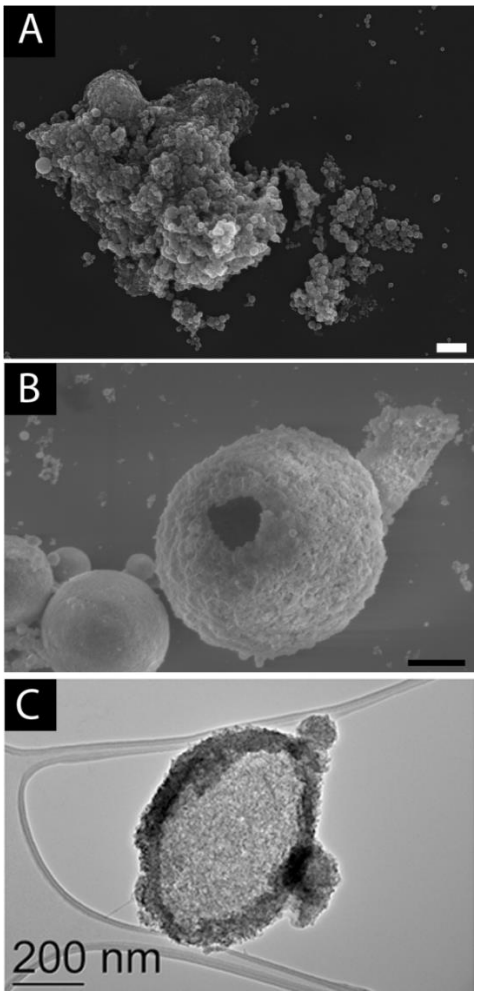

Figure 4.8. (**A/B**) SEM (scale bar = 1 µm) and (**C**) TEM (scale bar = 200 nm) of hollow manganese oxide spheres obtained from carrying out the reaction without the addition of the silica precursor, TEOS.

Analysis of the resulting hollow manganese oxide spheres with dynamic light scattering (DLS) shows that the Z-average spherical diameter by volume is 351 ± 53

nm, with a polydispersity (PdI) of 0.484 ± 0.03 (**Figure 4.9**). Polydispersity is a measure of how wide the particle size distribution is and is defined in **Appendix II.1**, **Equation II.1.**

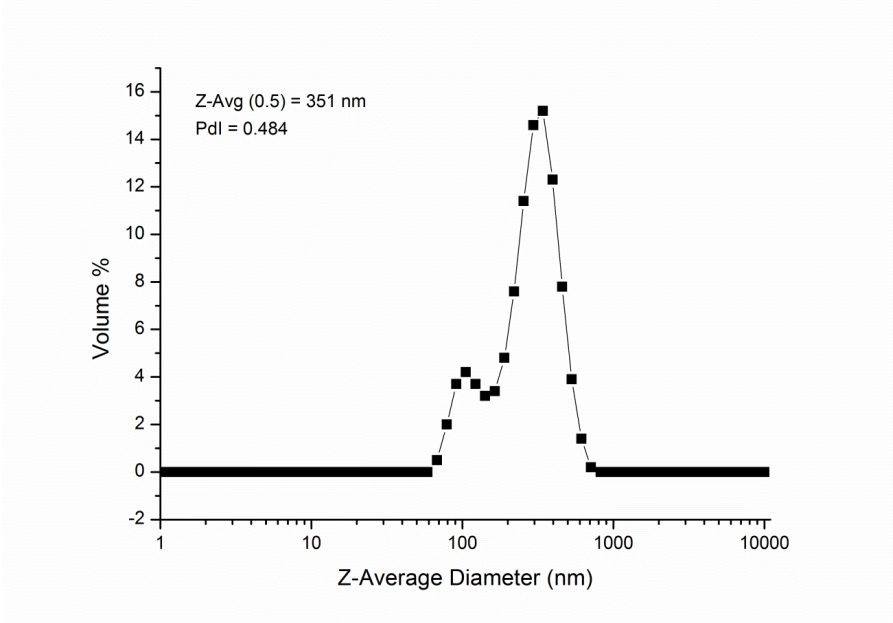

Figure 4.9. Relative particle population of hollow manganese oxide spheres by volume that have a given Z-average diameter.

This result correlates well with the diameter of the head measured from SEM image analysis of the matchstick particles (**Figure 4.4**). The light scattering result also corroborates the majority of the particles seen in **Figure 4.8 A**, although it doesn't account for the small population of particles larger than 1 μm (**Figure 4.8 B**), which is most likely due to sedimentation issues during the light scattering measurement. The PdI of the size distribution is quite broad, which reflects the polydisperse nature of the rods as-synthesized without further selective centrifugation applied.

We found that it was also possible to incorporate other metal oxides into the silica rods, such as iron oxide (**Figure 4.10**), by a similar method outlined for the manganese oxide matchstick particles. However, small hollow spheres are formed besides the matchstick particles. This general technique of using Pickering particles to stabilize the water droplets indicates that a wide range of materials could be asymmetrically incorporated into silica rods, which may allow for magnetic control over particle motion as well for example.

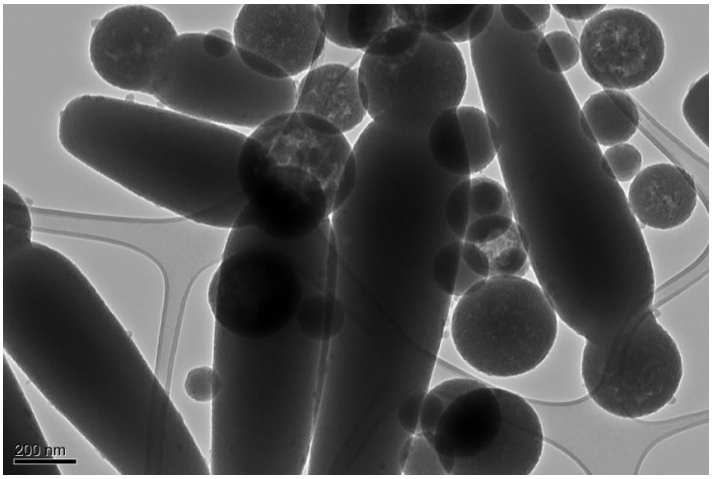

Figure 4.10. TEM image of iron oxide loaded silica rods and hollow spheres. Scale bar = 200 nm.

4.2.3 Enhanced diffusion coefficient of SiO_2-Mn_xO_y rods in the presence of hydrogen peroxide

The use of manganese oxide as catalytic engine in the head of our micro-matchsticks allows the particles to self-propel in the presence of hydrogen peroxide as fuel. This is possible as the catalyst decomposes the fuel into oxygen and water, thus setting up an asymmetric diffusion gradient around the particle.

Particle tracking was used to study the enhanced diffusion coefficient of the particles in the presence of varying concentrations of hydrogen peroxide as fuel. One of the inherent problems with particle tracking of catalytically motile particles is that they have the potential to generate bubbles upon consumption of hydrogen peroxide, which can lead to erroneous data in laser scattering measurements conducted in closed sample chambers. These errors arise either from direct tracking of bubbles, or the generation of convection gradients induced by bubble formation, Ostwald ripening, or buoyancy. To avoid bubble formation we decided to keep the concentrations of fuel low (0%, 0.2%, 0.4%, 0.6%, and 0.8% H_2O_2 by volume), to ensure oxygen generation was kept below water saturation levels.

An excellent discussion on the methodology used to distinguish propulsion from other motion-inducing phenomena such as Brownian motion, convection, and sedimentation or creaming, was recently outlined by Howse and co-workers.[38]

Propulsion can be distinguished from the above mentioned phenomena by observing a crossover in the gradient of a plot of MSD vs. time interval (Δt). One should observe a crossover from ballistic propulsion at short time intervals, to a combination of Brownian motion and propulsion at longer time intervals. This transition from ballistic to diffusive behavior is linked to rotational diffusion.[39]

We tracked 50 individual particles over at least 120 frames for each concentration of hydrogen peroxide. This corresponds to at least 4 seconds in real-time. The individual tracking profiles of the particles display a random walk behavior, which means that motion due to other phenomena such as convection can be qualitatively ruled out (**Appendix IV.3**; **Figure IV.3**). For this it is important to state that no bulk concentration gradient of hydrogen peroxide is imposed.

The data at each time interval was averaged over all particles at that concentration to provide a single plot of MSD vs. Δt at each concentration (**Figure 4.11 A**). Processed raw data can be found on the accompanying CD as **ESI 4.1-4.5**. The custom .jar file used to convert the raw Cartesian coordinates to the MSD values can also be found on the accompanying CD as **ESI 4.7**.

It can be observed that each of the data sets are curved in a way such that two separate linear regimes can be identified, spanning short and long time intervals respectively. The slope of the linear region at short time intervals is the ballistic component. Increase in the value of the gradient as a function of hydrogen peroxide concentration can be assigned to catalytic self-propulsion of our matchsticks. The calculated effective diffusion coefficient shows apparent first-order kinetic behavior with respect to the overall hydrogen peroxide concentration in the water (**Figure 4.11 B**). In the absence of hydrogen peroxide the Brownian diffusion coefficient is 2.74 $\mu m^2 \cdot s^{-1}$. Adding hydrogen peroxide leads to an increase in the effective diffusion coefficient. For example, at a concentration of 0.8% vol. H_2O_2 an experimental value of 4.52 $\mu m^2 \cdot s^{-1}$ is obtained. Therefore we see an increase of the effective diffusion coefficient equal to 2.18 $\mu m^2 \cdot s^{-1}$ per unit % by vol. of H_2O_2.

To put this result into context, Golestanian *et al.* investigated the MSD of polymer microspheres (1.62 ± 0.13 μm diameter) that were coated with a hemisphere of platinum. In the absence of fuel i.e. purely Brownian motion, they have a MSD = 0.9 $\mu m^2 \cdot s^{-1}$. At 1% vol. H_2O_2 they have a MSD ~1.4 $\mu m^2 \cdot s^{-1}$, giving an enhanced diffusion coefficient of ~0.5 $\mu m^2 \cdot s^{-1}$.[39] On the other hand, if we were to look at the MSD for a wild-type *E. Coli* then they can reach highly impressive displacements of around 400 $\mu m^2 \cdot s^{-1}$.[40]

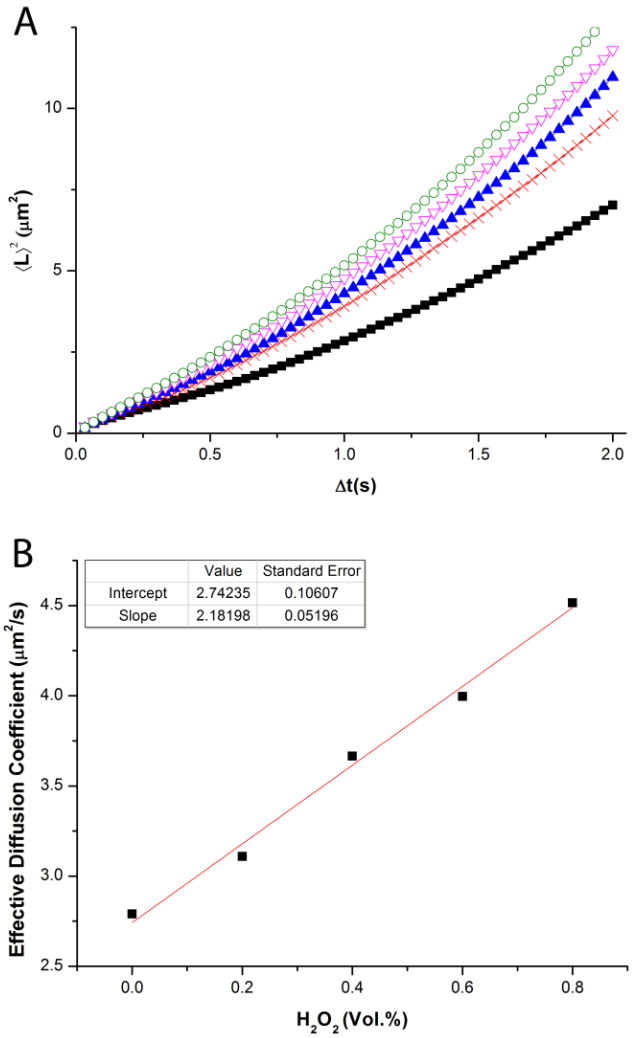

Figure 4.11. (**A**) Plot of MSD vs. Δt over long time interval for the five different % vol.'s of H_2O_2 in water (black filled square = 0%, red cross = 0.2%, blue filled triangle = 0.4%, pink open inverted triangle = 0.6%, green open circle = 0.8%), and (**B**) the enhanced diffusion coefficient as a function of H_2O_2 concentration at short time intervals (Δt = 0.5s).

Calculated MSD's for each time interval do not have a normal distribution, making error analysis through calculation of the standard deviation, or margin of error at confidence levels, inapplicable. Similarly, it would be invalid to transform the data to a normal distribution, calculate the error, and then invert the

transformation function. Instead we have plotted the mean with upper and lower error bars corresponding to the 75th and 25th percentile respectively (**Figure 4.12**). In this way we eliminate some of the more extreme outliers due to both polydispersity of the sample and the fact that motion is in fact in 3D in the cell, as opposed to the observed 2D traces. This problem is compounded at longer time intervals, especially as there are less data points at larger time intervals than at short.

From the plot of 0% vol. H_2O_2 and 0.8% vol. H_2O_2 (**Figure 4.12** blue and red plot respectively) we can deduce a couple of things. First, although there is overlap between the MSD's at the two concentrations, the majority of particles in the presence of a higher concentration of fuel are above the 75th percentile of particles in the absence of fuel, confirming that enhanced diffusion is occurring. Second, we can see that the range of MSD's is larger in the presence of fuel than in its absence, possibly due to a magnification of the previously mentioned effects of polydispersity and 3D motion combined with a greater range of displacements possible.

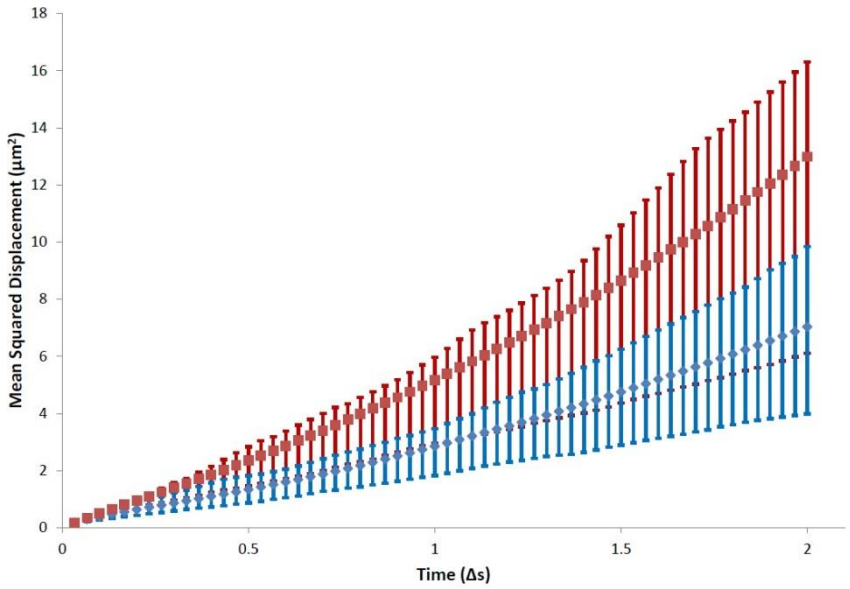

Figure 4.12. MSD as a function of time interval for particles in the absence of fuel (blue plot) and in the presence of 0.8% vol. of H_2O_2 (red plot). The upper and lower bounds correspond to the 75th and 25th percentile respectively.

At higher concentrations of fuel (~ > 1% vol.) one starts to get propulsion through formation of bubbles, followed by detachment. A series of optical microscope images at 10x magnification show a dilute solution of silica-manganese oxide particles (5 mg·mL^{-1}) as a function of time after the addition of 5% vol. H_2O_2 (**Figure 4.13)**.

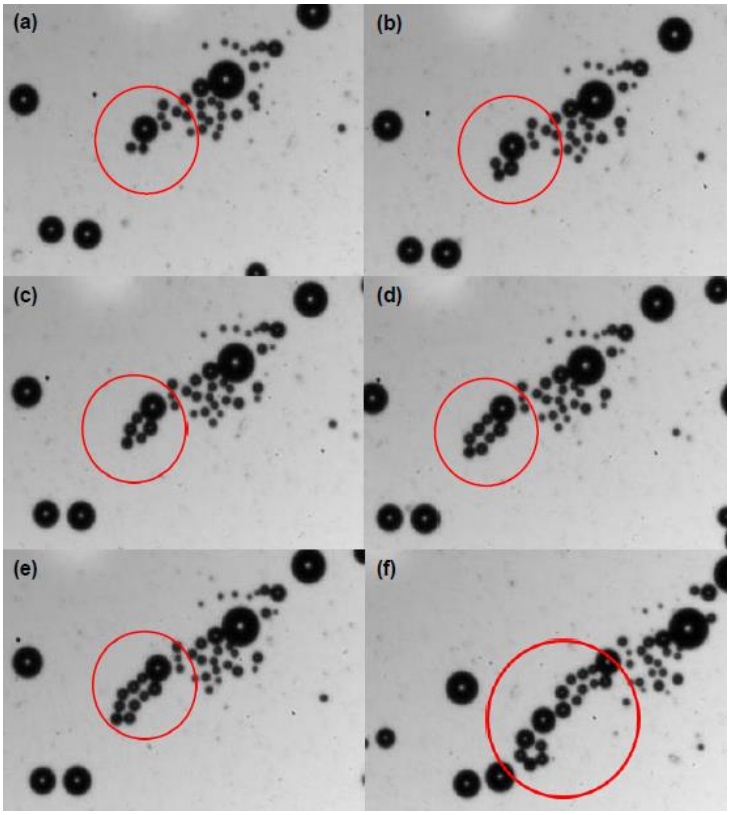

Figure 4.13. A series of optical microscope frames at x10 magnification showing the evolution of oxygen bubbles after addition of H_2O_2 (5% vol.) to a dilute solution of particles at (**a**) 1 s, (**b**) 2 s, (**c**) 3 s, (**d**) 4 s, (**e**) 5 s, (**f**) 15 s.

4.2.4 Chemotaxis of SiO_2-Mn_xO_y rods in presence of a fuel gradient

One phenomenon of interest in the motion of microparticles and organisms is the capability to control their direction. In our case, an imposed gradient of hydrogen peroxide should cause our matchstick particles to undergo chemotaxis. Experiments were conducted in a wax-sealed Dunn cell (**Appendix IV.4**, **Figure IV.4**) with the aqueous hydrogen peroxide solution (0.75% vol. H_2O_2) placed in the outer well and particles seeded onto the coverslip occupying the bridge region of the cell.

In order to prove that the motion of the particles was indeed caused by chemotaxis, and not as a result of convection, we added catalytically inert

polystyrene microspheres to the experiment as a control. A movie of this chemotaxis experiment is provided on the accompanying CD (a sped-up version as well as the real-time original - **ESI Video 4.1/4.2**).

Three snapshots taken at different times are given (**Figure 4.14)**. Note that the hydrogen peroxide containing well is the dark region in the top right of the images. To guide the eye, vectors are overlaid that track three catalytic matchstick rods (red arrows) and three polystyrene microspheres (yellow arrows). It can be seen that the "inert" microspheres undergo convection in a direction away from the hydrogen peroxide filled well, whereas the catalytic rods counteract this force in order to reach the higher concentrations of fuel located in the well i.e. the hydrogen peroxide acts like a chemoattractant. This is logical as the effective diffusion coefficient of the catalytic matchstick particles increases at higher hydrogen peroxide concentrations (**Figure 4.11 B**).

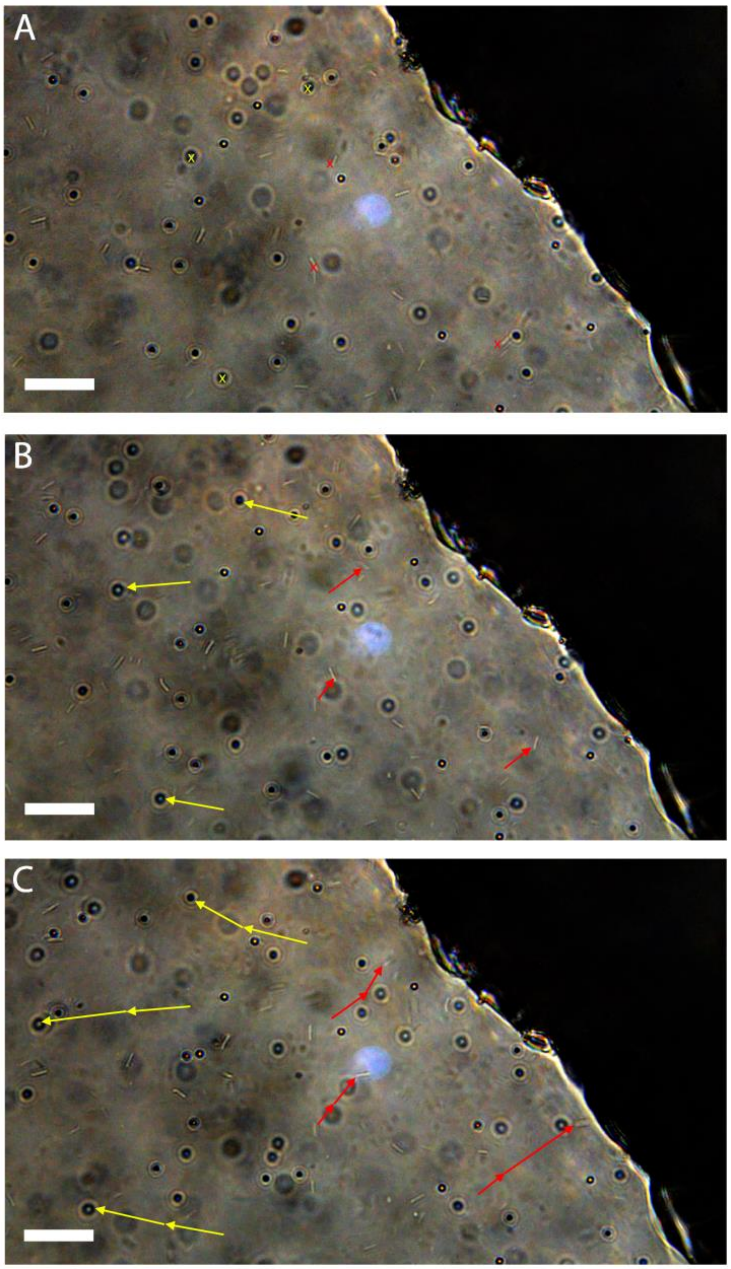

Figure 4.14. Optical Micrographs taken from **ESI Video 4.2** showing a mixture of chemically "inert" polystyrene microspheres and self-propelled catalytic silica-manganese oxide rods in the presence of a hydrogen peroxide gradient (H_2O_2 well is on the right of the images) at (**A**) t = 0 s, (**B**) t = 35 s, (**C**) t = 70 s. Red vectors show rod displacement between each image whereas yellow vectors indicate motion of microspheres between each image. Scale bar = 10 μm.

In order to deduce the average orientation of the particles we proceeded as follows. A tangent line to the edge of the well containing hydrogen peroxide was drawn in order to demark the "finish line" (red line in **Figure 4.15**). We can then denote that when the particle is perpendicular to this tangent line, with the head facing forward, then this corresponds to an angle of 0°. In the opposite case, where the particle is perpendicular to the tangent but the head is at the back, this corresponds to an angle of 180°. Any other angle can be deduced by drawing a line normal to the red line from the flat end of the particle, and measuring the corresponding angle (yellow lines **Figure 4.15**).

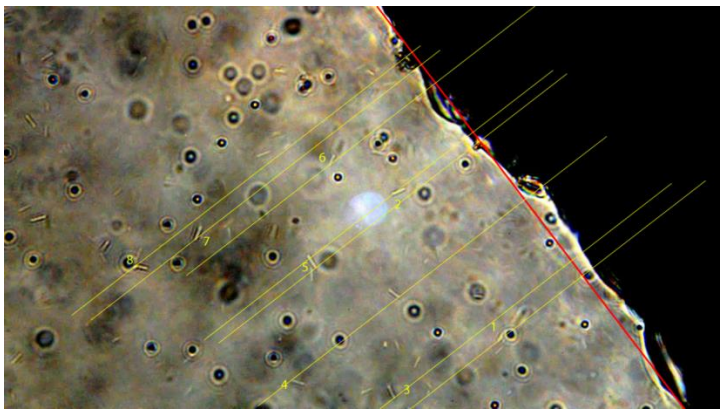

Figure 4.15. Schematic for how the particle orientation was determined during the chemotaxis experiment. A total of 8 particles were tracked over 10 frames, from t_0 to t_{90} seconds at 10 second intervals.

By taking the cosine of the angle in radians when the catalytic head is facing forward i.e. 1st and 4th quadrant, it returns a positive value. When it is facing backwards i.e. 2nd or 3rd quadrant, one gets a negative value. 8 Particles were analyzed at 10 second time intervals over 90 seconds (raw data on CD, **ESI 4.6**).

Looking at the distribution we obtain for the cosine of particle angle (**Figure 4.16**), it is apparent that there is a significant bias towards the case in which the head is facing forwards during chemotaxis. It is quite impressive that over half of the particles never actually reverse orientation over 90 seconds, even though there is significant convection and Brownian rotation.

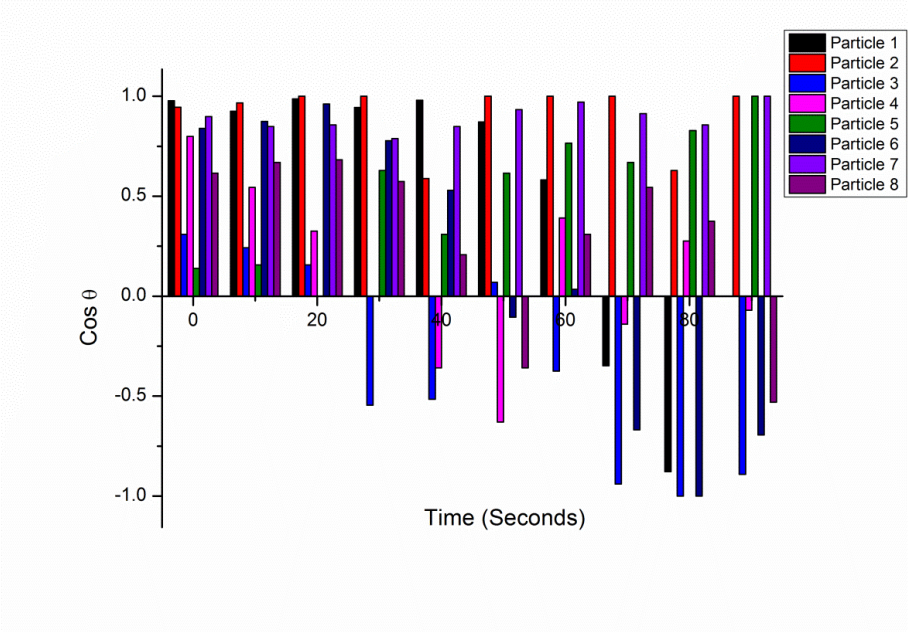

Figure 4.16. Plot of cosine of the particle angle (with respect to the direction of chemotaxis) as a function of time for 8 individual particles. From this we can deduce that the preferred particle orientation during chemotaxis is with the catalytic engine facing forwards.

There also appears to be a correlation between the initial distance of the particles from the well and the distance travelled due to chemotaxis (**Figure 4.17**), which can be rationalized in terms of the higher effective diffusion coefficient at higher concentrations of fuel.

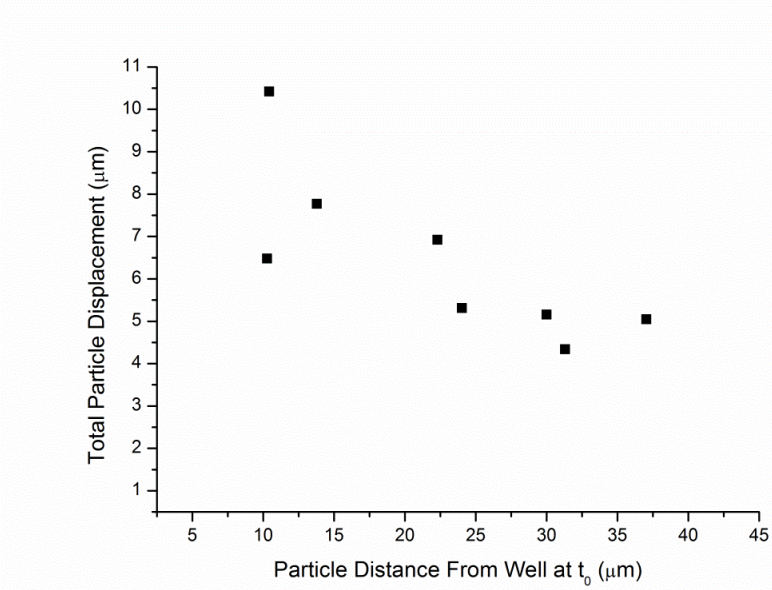

Figure 4.17. Total particle displacement in the direction of chemotaxis as a function of initial particle distance from the tangent to the well. Distances were measured from the centre of the particle to the well tangent line.

4.3 Conclusions

In conclusion, we have reported a method for the synthesis of matchstick shaped silica-based microparticles that have an asymmetric inclusion of manganese oxide nanoparticles, predominantly concentrated in the head of the rods. By doping water droplets in a water-in-oil emulsion with metal salts, and then oxidizing them with the addition of a base, we generate *in situ* Pickering armored water droplets. These basic water droplets then serve as the nucleus for TEOS hydrolysis and condensation, which grows preferentially onto a nucleation site on the particle surface to give a rod-like structure, following phase separation of the water droplet out of the hydrophobic manganese oxide head.

We showed that this particle design is an effective self-propelling object in the presence of hydrogen peroxide as a fuel source and that the effective diffusion coefficient can be tuned by adding different concentrations of hydrogen peroxide. The effective diffusion coefficient is found to follow first-order kinetics as a function of hydrogen peroxide concentration.

It is also possible for the particles to undergo directed motion by chemotaxis when placed in a gradient of fuel. Convection was ruled out as the propulsion mechanism by including inert polymer microspheres that moved under convection, which was in the opposite direction to chemotactic rod movement.

We believe that our synthesis approach is versatile and should allow for future fabrication of micro objects of added complexity. The ability to direct motion of these colloidal structures can form a platform for advances in supracolloidal science. See **Chapter 5** for a brief discussion on amphiphilic matchstick particles that we have also synthesized.

4.4 Experimental

4.4.1 Materials

PVP-K30 (average Mwt. = 40,000 g·mol^{-1}), 1-pentanol (99%), sodium citrate dihydrate (99%), manganese(II) sulfate (> 99%), TEOS (99%), hexadecyltrimethoxysilane (HDTMOS, ≥ 85%) hydrogen peroxide (30% vol.) and paraffin wax (m.p. 73-80°C) were obtained from Sigma-Aldrich and used as received.

Ethanol was of AR grade (99.7-100%) and concentrated ammonia (18.10 M) was no older than 2 months (Important in the rod synthesis). Both were obtained from Fisher Scientific.

Briwax and Vaseline were obtained from local hardware shops.

4.4.2 Synthesis and purification of SiO_2-Mn_xO_y composite matchstick particles

4.4.2.1 Hydrophilic SiO_2-Mn_xO_y rods

A modified recipe to that outlined by Van Blaaderen[36] was adopted, whereby the modification involved doping of the aqueous phase with a metal (manganese or iron) sulfate. Stock solutions of PVP-K30 (100 $g \cdot L^{-1}$) in 1-pentanol, sodium citrate (0.18 M aq.), and metal sulfate (0.10 M, aq.) were made. Note that the PVP-K30 was dissolved by 2 hours of sonication followed by stirring overnight. Then, in a 50 mL Eppendorf centrifuge tube the following were added: Pentanol-PVP (30 mL), ethanol (3 mL), sodium citrate solution (0.2 mL, 0.18 M), and metal sulfate solution (0.84 mL, 0.10 M). The mixture was shaken well by hand for 30 seconds to generate a slightly opaque emulsion of water in pentanol. At this point ammonia was added (0.5 mL, 18.10 M) and the emulsion turned orange/brown in color. Note that the reaction could be left at this point in order to generate hollow metal oxide spheres. In order to generate the silica-metal oxide particles the sample was left for one minute before the addition of TEOS (0.3 mL). The reaction was left to stand for 24 hours. Particles were cleaned by three rounds of centrifugation for 15 minutes at 4,200 g into ethanol/water (50/50% vol.). As the direct synthesis results in a fairly polydisperse size range of metal oxide loaded silica rods, a selective centrifugation procedure was applied to the solution to achieve a narrower polydispersity for analysis. Three

rounds of centrifugation were performed for 15 minutes at 120 g, redispersing in water (keeping solids), followed by a further three rounds of centrifugation for 15 minutes at 30 g (keeping supernatant).

4.4.2.2 Amphiphilic SiO_2-Mn_xO_y rods (see **Chapter 5**)

The synthesis was carried out as above in **Section 4.4.2.1** but 24 hours after the addition of TEOS, HDTMOS (0.03 mL) was added and the solution agitated by hand for 30 s. Growth was then allowed to proceed for 24 hours before purification via centrifugation as outlined above, except that they were redispersed in ethanol/ water (80/20% vol.) between runs.

4.4.3 Characterization of the SiO_2-Mn_xO_y rods

SEM samples were prepared by diluting the matchstick solutions to around 0.01% wt. in DIW and allowing them to dry on silicon wafers supported by an aluminium stub. Sputtering was then performed with a platinum target at 1.5 kV for 40 seconds to give a calculated layer thickness of 5 nm. SEM Imaging was performed on a Zeiss Supra 55VP at 10 kV. TEM image analysis and EDAX samples were mounted on a lacey carbon copper grid and imaged with a JEOL 2000FX TEM equipped with an EDAX detector. XRD measurements were performed on a Bruker D5000 from 25-850°C, between scattering angles of 10-80°. For higher resolution patterns the signal was collected over 24 hours, following calcination of the sample at 850℃ in air.

4.4.4 Studying the ballistic propulsion of the particles

Particle tracking measurements were performed with a Nanosight LM10 running NTA 2.3 software at 20x magnification and with a calibration of 170 nm pixel^{-1} (1 pixel^2 = 0.029 μm^2). The particle concentration of the rods was approximately 5 x 10^8 mL^{-1}. To investigate the effect of the concentration of H_2O_2 on ballistic propulsion, suitable concentrations of H_2O_2 solutions were made up immediately prior to analysis and kept wrapped in tin foil. H_2O_2 solution (0.3 mL), and particle solution (0.5 mL) were mixed together in a vial before injection into the sample cell.

Video clips were typically taken for either 90 or 160 seconds at 30 frames s-^{1}, and filters were put in place to only track particles present in at least 121 frames (~ 4 seconds). This was to ensure a large number of data points were included in the plots of Δt ranging from 1/30 – 2 s.

Following analysis of the video clips, the x and y coordinates for each particle were output as a function of frame number and a custom java script was run on each separate particle file (CD provided, **ESI 4.7**) to calculate the mean-squared displacement at each time interval = 1/(frame rate) (**Equation 4.10**).

$$MSD = \sum_{i=0, j=i+\Delta t}^{F \times \frac{1}{f.r.}} \left(x_j - x_i\right)^2 + \left(y_j - y_i\right)^2 \qquad \textbf{(4.10)}$$

Where F = total number of frames, Δt = time interval, and f.r. = frame rate. Mean averages of the squared displacement were taken over 50 particles to ensure an accurate average representation of particle motion. The MSD's were then converted from pixels^2 to μm^2.

4.4.5 Chemotaxis experiments of silica-manganese oxide rods

Chemotaxis experiments were performed in a Dunn chemotaxis cell obtained from Hawksley medical and laboratory equipment. Imaging was performed with a Leica DM2500M optical microscope using a 40x ph2 objective. Videos were captured with a Nikon D5100 SLR camera. Briefly, a mixture of Paraffin wax:Vaseline:Briwax (1:1:1% wt.) was made up in a beaker and heated to 75°C. Then a solution of hydrogen peroxide (30% vol.) in water was made up to have 0.75% vol. fuel. An aqueous suspension of rods (5 $mg \cdot mL^{-1}$) was added to the central well (or a mixture of rods/spheres), whilst the outer well was filled with deionized water. A thick cover slip was seeded with the particle solution, and used to cover the wells and bridge (save for a sliver of outer well which was left uncovered). It is essential to make sure no air bubbles are present. Once in place the wax mixture was applied with a paintbrush to seal the coverslip in place and ensure there was no convection from the edges of the coverslip. Deionized water was then drained from the outer well via the exposed slit and replaced with the hydrogen peroxide solution. The gap that was left in the outer well was then sealed with the wax mixture and imaging performed across the bridge region in the middle of the concentric wells.

4.5 References

(1) Brown, R. *Phil. Mag.* **1828**, *4*, 161–173.

(2) Brongniart, A. T. *Ann. Sci. Naturelles* **1827**, *12*, 44–46.

(3) Guoy, L. *J. Physique* **1888**, *7*, 561–564.

(4) Einstein, A. *Annalen der Physik* **1905**, *17*, 549–560.

(5) Lemons, D. S.; Gythiel, A. *Am. J. Phys.* **1997**, *65*, 1079–1081.

(6) Sutherland, W. *Phil. Mag.* **1905**, *9*, 781–785.

(7) Von Smoluchowski, M. *Ann. Phys. Paris* **1906**, *21*, 757–779.

(8) Perrin, J. *Atoms*; 1916; pp. 1–240.

(9) Li, T.; Kheifets, S.; Medellin, D.; Raizen, M. G. *Science* **2010**, *328*, 1673–1675.

(10) Haw, M. D. *J. Phys.: Condens. Matter* **2002**, *14*, 7769–7779.

(11) Purcell, E. M. *Am. J. Phys.* **1977**, *45*, 3–11.

(12) Dreyfus, R.; Baudry, J.; Roper, M. L.; Fermigier, M.; Stone, H. A.; Bibette, J. *Nature* **2005**, *437*, 862–865.

(13) Ghosh, A.; Fischer, P. *Nano Lett.* **2009**, *9*, 2243–2245.

(14) Tomlinson, C. *Proc. R. Soc. Lond.* **1860**, *11*, 575–577.

(15) Suematsu, N. J.; Ikura, Y.; Nagayama, M.; Kitahata, H.; Kawagishi, N.; Murakami, M.; Nakata, S. *J. Phys. Chem. C* **2010**, *114*, 9876–9882.

(16) Manesh, K. M.; Cardona, M.; Yuan, R.; Clark, M.; Kagan, D.; Balasubramanian, S.; Wang, J. *ACS nano* **2010**, *4*, 1799–1804.

(17) Solovev, A. A.; Mei, Y.; E., B. U.; Huang, G.; Schmidt, O. G. *Small* **2009**, *5*, 1688–1692.

(18) Solovev, A. A.; Sanchez, S.; Pumera, M.; Mei, Y. F.; Schmidt, O. G. *Adv. Func. Mater.* **2010**, *20*, 2430–2435.

(19) Derjaguin, B. V.; Sidorenko, G. P.; Zubashchenko, E. A.; Kiseleva, E. V. *Kolloidn. Zh.* **1947**, *9*, 335–348.

(20) Keh, H. J.; Wei, Y. K. *Colloid Polym. Sci.* **2000**, *278*, 539–546.

(21) Ebel, J. P.; Anderson, J. L.; Prieve, D. C. *Langmuir* **1988**, *4*, 396–406.

(22) Paxton, W. F.; Sen, A.; Mallouk, T. E. *Chem. Eur. J.* **2005**, *11*, 6462–6470.

(23) Kline, T. R.; Paxton, W. F.; Wang, Y.; Velegol, D.; Mallouk, T. E.; Sen, A. *J. Am. Chem. Soc.* **2005**, *127*, 17150–17151.

(24) Burdick, J.; Laocharoensuk, R.; Wheat, P. M.; Posner, J. D.; Wang, J. *J. Am. Chem. Soc.* **2008**, *130*, 8164–8165.

(25) Zhao, G.; Sanchez, S.; Schmidt, O. G.; Pumera, M. *Chem. Comm.* **2012**, *48*, 10090–10092.

(26) Kline, T. R.; Paxton, W. F.; Mallouk, T. E.; Sen, A. *Angew. Chem. Int. Ed.* **2005**, *44*, 744–746.

(27) Gao, W.; Pei, A.; Feng, X.; Hennessy, C.; Wang, J. *J. Am. Chem. Soc.* **2013**, *135*, 998–1001.

(28) Sundararajan, S.; Lammert, P. E.; Zudans, A. W.; Crespi, V. H.; Sen, A. *Nano Lett.* **2008**, *8*, 1271–1276.

(29) Sanchez, S.; Solovev, A. A.; Harazim, S. M.; Schmidt, O. G. *J. Am. Chem. Soc.* **2011**, *133*, 701–703.

(30) Palacci, J.; Sacanna, S.; Steinberg, A. P.; Pine, D. J.; Chaikin, P. M. *Science* **2013**, *339*, 936–940.

(31) Hong, Y.; Blackman, N. M. K.; Kopp, N. D.; Sen, A.; Velegol, D. *Phys. Rev. Lett.* **2007**, *99*, 178103–178106.

(32) Young, K. D. *Curr. Opin. Microbol.* **2007**, *10*, 596–600.

(33) Lugli, F.; Brini, E.; Zerbetto, F. *J. Phys. Chem. C* **2012**, *116*, 592–598.

(34) Ortega, A.; García de la Torre, J. *J. Chem. Phys.* **2003**, *119*, 9914–9919.

(35) Tao, Y.-G.; den Otter, W. K.; Padding, J. T.; Dhont, J. K. G.; Briels, W. J. *J. Chem. Phys.* **2005**, *122*, 244903 (10).

(36) Kuijk, A.; van Blaaderen, A.; Imhof, A. *J. Am. Chem. Soc.* **2011**, *133*, 2346–2349.

(37) Grassian, V. H.; Martin, S. T. In *Environmental Catalysis*; CRC Taylor & Francis: Boca Raton, 2005; pp. 61–122.

(38) Dunderdale, G.; Ebbens, S.; Fairclough, P.; Howse, J. *Langmuir* **2012**, *28*, 10997–11006.

(39) Howse, J.; Jones, R.; Ryan, A.; Gough, T.; Vafabakhsh, R.; Golestanian, R. *Phys. Rev. Lett.* **2007**, *99*, 8–11.

(40) Berg, H. C. *E. Coli in Motion*; Springer, 2004; pp. 54–56.

Chapter 5

Conclusions and Future Outlook

In this chapter we summarize the findings of each results chapter and put this into context of the original aims of the work. We will then briefly discuss other potentially interesting avenues of research that stem from this work.

5.1 Conclusions and Future Work

In **Chapter 1** our aim was to synthesize hollow silica particles that could be used as opacity modifiers in dry polymer films that were formed after drawdown of waterborne coatings containing the hollow particles as pigment. Our reasoning for this was that there is an industrial drive to reduce the amount of titanium dioxide in coatings formulations due to economic and environmental pressures.

Synthesis of a variety of hollow silica particles with different morphologies was demonstrated by a sacrificial templating method. Cuprous oxide, hematite, and ultimately calcium carbonate were used as template for sol-gel coating with the reagent TEOS to afford core-shell particles. Removal of the core with acid furnished the desired hollow silica particle in each case.

Unfortunately, due to the necessity for large quantities of pigment, only the calcium carbonate template was viable for generating a large enough quantity of hollow particles to be studied as opacity modifier by the AkzoNobel global test method.

Initial investigations into the opacity of these "1st generation" hollow silica particles indicated that they were completely ineffective at scattering light. By measuring the film density and comparing this to the theoretical values, we deduced that many of the air voids had disappeared, indicating that the particles had either broken or collapsed.

Tuning the reaction parameters gave us particles with thicker silica shells (2nd generation) which displayed a marked improvement over the 1st generation of hollow silica particles, although particle collapse was still an issue. Reflectance measurements indicated that the contrast ratio of the 2nd generation hollow SiO_2 particles per micron film thickness was superior to the SOCAL P3 template, even though they were present at a PVC a quarter that of the SOCAL P3 particles.

We would anticipate that the light scattering power of the hollow particles would be even higher if all of the particles could be prevented from fragmentation, which may be possible by increasing the pore dimensions in the shells with a porogen. This should lower the osmotic shock on the shell upon acid etch and capillary pressures upon drying.

Ultimately, we would then investigate the contrast ratio as a function of film thickness at different coating PVC's. From this we data we could fit the Kubelka-Munk model and obtain a scattering coefficient independent of particle volume for comparison with other light scattering pigments.

Investigations into hollow platelet-like morphologies would be another sensible line of inquiry as these materials are commonly used as metal effect pigments due to their high lustre i.e. high degree of light scattering. This is partially due to their preference for orientation parallel to the substrate due to their high aspect ratio.[1] Sacrificial templating of materials like the aluminium oxide platelets

Ronaflair® white sapphire (**Figure 5.1**) could therefore be anticipated to yield very opaque hollow structures.

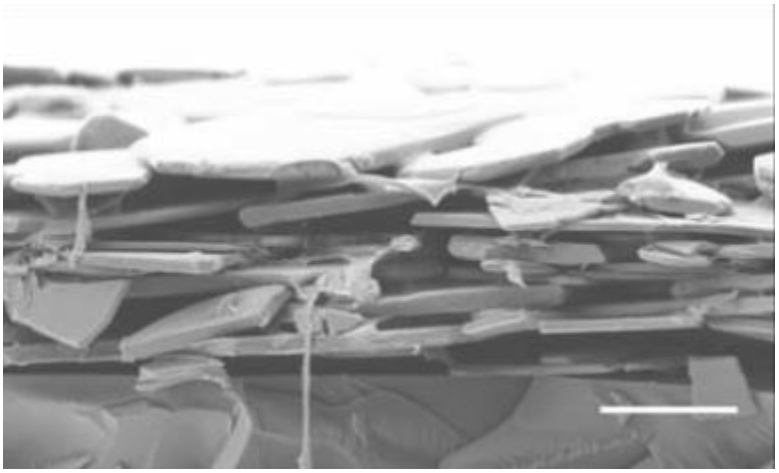

Figure 5.1. SEM image of stacked alumina platelets, which could be expected to make a very effective sacrificial template for achieving high opacity voided pigments. Scale bar = 2 μm.[2]

Chapter 2 was an extension of the work conducted in **Chapter 1**. Our aim was to improve the colloidal stability of the hollow silica particles, previously stabilized with PVP-K30 (predominantly steric stabilization) in **Chapter 1**, by grafting an electrosterically stabilizing polymer from the surface by SI-ATRP.

It's worth noting that it is difficult to find suitable stabilizers that wet silica at the high pH used in a waterborne coating as they are generally both negatively charged, which makes physisorption electrostatically unfavourable.

$CaCO_3$@SiO_2 particles were functionalized with APTES to give amine functionality to the surface, followed by reaction with BiBB to yield an amide linkage with a terminal tertiary alkyl bromide that was capable of ATRP initiation. We chose an amide linkage as it provides good stability to hydrolysis over a wide range of pH.

Zeta-potential measurements proved very useful in following conversion of the surface functionality.

SI-ATRP was conducted with Cu(0) as catalyst, PMDETA as ligand and NaSS as monomer. We chose this monomer to confer electrosteric stabilization over the pH range generally used in waterborne coatings (7-10). Presence of polymer brushes on the surface of the particles was determined by a number of methods including cryo-TEM, which visually confirmed the presence of the brushes.

Freeze-thaw testing of aqueous pigment dispersions, followed by laser diffraction measurements, indicated that the poly-(NaSS) hairs grafted from the particle surface did indeed provide enhanced colloidal stability when compared to the hollow particles with physisorbed PVP. The presence of the hairs led to increased particle fracture during film formation. Despite this the contrast ratio per unit film thickness indicated that these particles with enhanced dispersion were more effective than the 2^{nd} generation hollow SiO_2 particles stabilized with PVP from **Chapter 1**.

We briefly looked into the possibility of using a gas phase silanization to selectively modify the interior of the hollow silica particles with hexamethyldisilazane (HMDS). As the outside silanol groups of the particle are blocked with hydrophilic hairs (that extend well out from the particle surface) it should allow selective functionalization of the silanol groups on the interior of the hollow silica particles with hydrophobic character. Following cleaning of the particles with acetone, drying, and redispersing in water we found the particles to float on water (**Figure 5.2 A**). Mild sonication causes the particles to form a second aqueous phase that phase separates out into two distinct layers of water, one containing the particles (top phase) and the other absent of particles (bottom phase).

This would imply that it is possible to trap gas bubbles inside the particles, which would make them highly effective pigments for generating wet opacity (if buoyancy can be retarded through increasing low shear viscosity).

It should also be possible to absorb hydrophobic reagents inside the cavity and to use the particles as nanoreactors for the generation of novel anisotropic colloids. After addition of 1-bromooctane to the phase separated mixture, the particles gradually began to sediment (as they filled with the hydrophobic oil). Very mild agitation (to prevent emulsification) allowed the oil filled hollow SiO_2 particles to be dispersed in the aqueous phase (**Figure 5.2 B**).

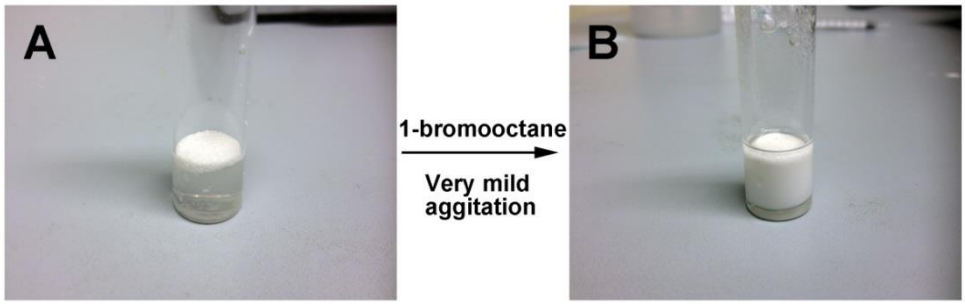

Figure 5.2. Digital photograph of (**A**) hollow SiO_2-graft-poly(NaSS) with HMDS hydrophobic interior floating on top of water due to trapped air bubbles and (**B**) after addition of 1-bromooctane particles sediment as they fill. Very mild agitation a few days later dispersed the oil filled hollow silica particles into water.

In **Chapter 3** we looked at the orientational behavior of superellipsoidal (pseudocubic) hematite particles trapped at a planar oil-water interface through a combination of experimental and simulation based methods.

We found three stable configurations, of which two could be assigned to thermodynamic minima. The most stable and consequently most abundant

population were the particles which lay flat with respect to the interface. A secondary minima was found that corresponded to a tilted orientation. These were the second most abundant present. A third sunken and tilted orientation corresponded to a kinetically trapped state, which was due to some particles going through a negligible gradient in free energy during the transition from a high energy state to a lower energy.

Finally, it was shown that the particle orientation depended on both the shape of the free energy landscape and the specific orientation of the particles at the point of contact with the interface. Our experimental findings for the population distribution were in good agreement with those predicted from simulation.

This work contributes to the understanding of particle stabilized interfaces (Pickering stabilization) and is one of the first examples of a kinetically trapped particle orientation.

Another phenomenon which we observed that warrants further investigation was that application of an ultrasonic wave across the oil-water interface, followed by particle trapping, gave a monomodal distribution of particle orientation, whereby all of the particles fall into the same orientation (analyzed by accounting for 100 particles). Intriguingly the particles do not adopt the orientation which corresponds to the global free energy minima, but rather that of the local free energy minima (**Figure 5.3**).

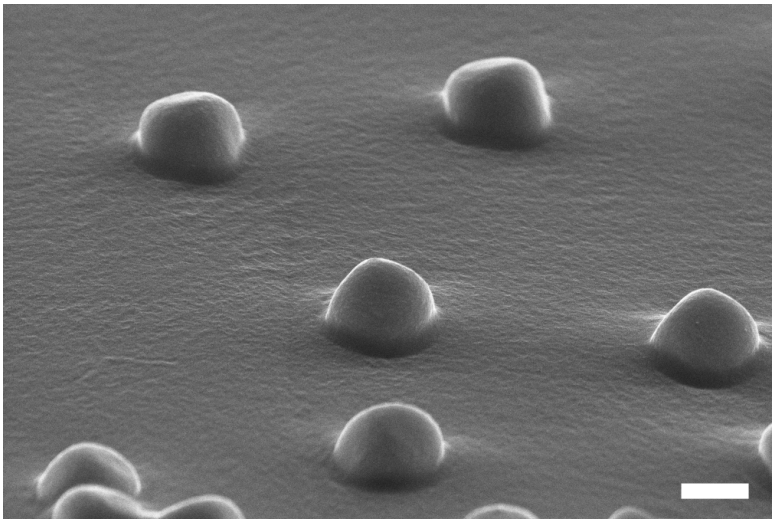

Figure 5.3. SEM image of hematite superellipsoids trapped at the oil-water interface in PDMS under the application of ultrasound. Interestingly they all adopt the same orientation although not the global free energy minima, but rather the local free energy minima. Scale bar = 1 μm.

In **Chapter 4** we demonstrated a modified synthesis of silica rod growth from an oil-in-water emulsion, where we incorporated a catalytic manganese oxide head into one end of the particle, giving a "matchstick" type morphology to the particles. This was achieved by doping the water droplet with manganese sulphate before oxidizing it to manganese oxide, which migrated to the oil-water interface where it acts as Pickering stabilizer. Rod growth by the hydrolysis and condensation of TEOS then yielded the SiO_2-Mn_xO_y matchstick particles.

These particles were used as catalytically active motile particles in the presence of hydrogen peroxide as fuel, whereby they propel through decomposition of fuel into water and oxygen that generates an asymmetric gradient around the particle. Furthermore we demonstrate that the effective diffusion coefficient could be

tuned by varying the concentration of fuel, which it displayed a first-order relationship with.

Placing the particles into a gradient of fuel showed that the particles can undergo chemotaxis, that is directed motion towards a higher concentration of fuel. Convection and other external forces were ruled out as the cause of directed motion by incorporating catalytically inactive polymer spheres into the solution, which moved in the opposite direction to the catalytically active matchstick particles.

Our goal for the next part of this project is to endow the particles with self-assembly capability. We have already made amphiphilic matchstick particles (**Figure 5.4**) by combining our synthetic procedure with that developed by Nie et al.[3] Incorporating a hydrophobic domain at the tail end with the addition of HDTMOS, after TEOS condensation, allows the particles to associate with one another through their hydrophobic domains when they are above a certain concentration i.e. after completing chemotaxis towards a point source.

Other avenues we wish to explore are whether the particles can "impregnate" a polymersome that is filled with fuel and whether we can graft enzymes to the surface to enable them to use glucose as a fuel instead of hydrogen peroxide, similar to the work done by Feringa and co-workers.[4]

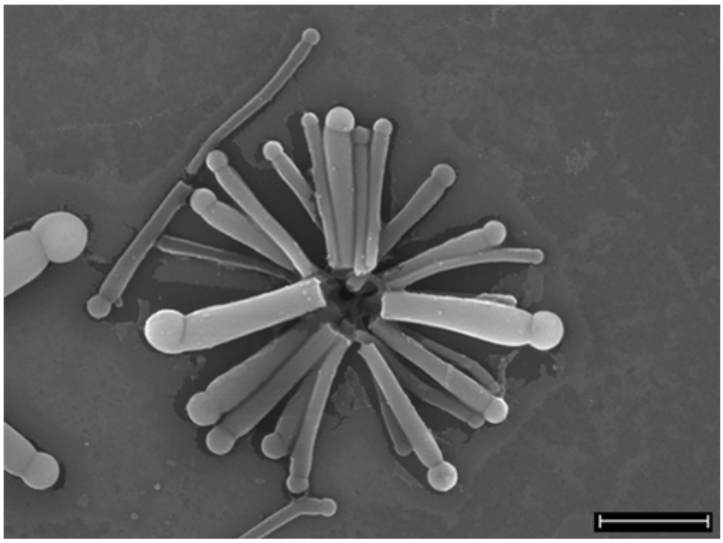

Figure 5.4. SEM image of assembled matchstick colloids that have been functionalized at one end with HDTMOS. Scale bar = 1 µm.

5.2 References

(1) Maile, F. J.; Pfaff, G.; Reynders, P. *Prog. Org. Coat.* **2005**, *54*, 150–163.

(2) Bonderer, L. J.; Studart, A. R.; Gauckler, L. J. *Science* **2008**, *319*, 1069–1073.

(3) He, J.; Yu, B.; Hourwitz, M. J.; Liu, Y.; Perez, M. T.; Yang, J.; Nie, Z. *Angew. Chem. Int. Ed.* **2012**, *51*, 3628–3633.

(4) Pantarotto, D.; Browne, W. R.; Feringa, B. L. *Chem. Comm.* **2008**, 1533–1535.

Appendix I

"Characterization Techniques"

This appendix serves to cover the theory behind some of the analytical techniques used in the work reported in this thesis. This will include how values are generated, the models that are employed in this process, what constitutes a reliable result, and the limitations of the techniques.

I.1 Scanning Electron Microscopy (SEM)

Optical microscopes have a resolution limited by the diffraction of the visible light source i.e. it is wavelength dependent. The minimum size feature that it can possibly resolve in normal transmission mode is ~ 200 nm with certain lenses and light sources (However some cutting edge techniques involving interference based spectroscopy and multiple lenses allow for far greater resolution).

Generally, if one wants to resolve colloidal particles and investigate their surface morphology on the submicron length scale, then scanning electron microscopy is used to image the sample. Instead of using a photon source, the SEM employs a tungsten filament and magnetic lenses to generate a focused beam of accelerated electrons, which have a much smaller wavelength than photons, and thus greater resolution capabilities. Practically the resolution of a SEM instrument is generally 1-20 nm and depends on the accelerating voltage used (typically 1-20 kV), with higher accelerating voltages giving greater resolution i.e. shorter electron

wavelengths. However, radiation damage to the sample can be severe, particularly at higher accelerating voltages. Therefore accelerating voltage must be carefully selected depending on the nature of the sample.

Imaging is done under vacuum as the mean free path of electrons in air is very short.

For this reason the sample must not be damaged by vacuum conditions for successful analysis.

There are a number of electron-sample interactions that can arise. Signals that are used in imaging are typically secondary electrons and back-scattered electrons.

Samples for imaging must be electrically conducting and grounded in order to prevent electrostatic charge build-up. For this reason non-conducting samples must be coated with a thin layer of carbon, gold, or platinum (amongst others) in a sputter chamber under vacuum. It is worth noting that some metals such as gold can deposit in clumps on the surface, which can be a source of image artefacts.

Advantages of SEM over TEM are that large areas of a sample can be imaged and analyzed via EDAX. Disadvantages are that internal structure i.e. pores, cannot be resolved, and the resolution is lower than that of TEM.

I.2 Transmission Electron Microscopy (TEM)

In TEM, electrons are detected by a CCD camera after passing through the sample, interacting with it on the way. Samples are mounted onto very thin grids, typically made of copper. Accelerating voltages are much higher (typically ~200 kV) than those used in SEM and consequently much greater resolution of the sample is possible. Assuming the sample is thin enough and not made of an electron dense material then internal structure of the sample can be analyzed, which is particularly

useful for hollow colloids and those with pores. One of the disadvantages when compared to SEM is that information regarding surface morphology is difficult to obtain and it might not be possible to image dense or thick samples due to the electrons being fully adsorbed or back scattered before passing through to the detector.

I.3 Laser Diffraction – Mie Scattering

When a dispersed colloidal particle passes through a coherent laser beam it scatters the light at an angle which is dependent upon its size, with the angle increasing logarithmically as size decreases. Decreasing the cross-sectional area of the particles also causes a decrease in the intensity of the scattered light. Therefore large particles scatter light at narrow angles but with high intensity, whereas smaller particles have a wider scattering angle and lower intensity.

The scattering pattern that is generated is then compared to the predictions of an appropriate model; typically the Mie scattering model, which is based around electrodynamic theory outlined by Maxwell. The reason for the choice of Mie scattering over other models, such as the Fraunhofer approximation, is that it is very robust – in that it can deal with small or large particles and transparent or opaque colloids. There are some general assumptions which apply to using this model however, which are:

- Particles are spherical in shape.
- The sample is dilute i.e. there are limited, or no, multiple-scattering events.

- Optical properties of both the sample and the dispersion are known. Optical properties that are required include the refractive index at a given wavelength (or two wavelengths in the case of the Mastersizer 2000S), and the corresponding absorption coefficient (imaginary refractive index) at these wavelengths.

It is the refractive index contrast between the dispersion and the sample that will dictate the intensity of the scattering from the surface of the sample. It also underpins the way in which light is scattered inside the particle following absorption, which is especially important in the <50 μm range of particle size.

It was mentioned that one of the assumptions of Mie theory is that the particles to be analyzed are spherical in shape, however there are models built into the Mastersizer software which allows one to compare the scattering pattern with that of an "equivalent sphere".

The absolute size of a spherical particle can be described with one dimension, its diameter. However, many colloidal particles are irregular three-dimensional objects and so one must be careful in choosing the most appropriate metric to describe the size of these particles. Most light scattering techniques report the size of non-spherical objects as being that of the diameter of the "equivalent sphere" that has a certain property the same as the irregular object i.e. they have the same volume or cross-sectional area for example. Some more examples of particle properties that are used as a basis for comparison are given in **Figure I.1**.

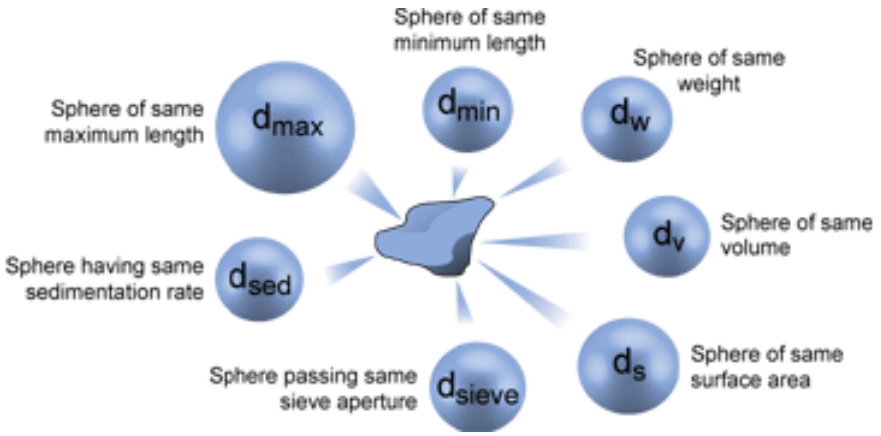

Figure I.1. Diagram illustrating the properties that are used to compare an irregular object with its equivalent sphere.[1]

Following the acquisition of the scattering pattern, the equivalent spherical diameter must be reported using an appropriate statistical distribution. These are typically given as a frequency distribution curve with a table of values known as d(0.1), d(0.5), and d(0.9). Essentially, what these correspond to are the diameters within a population that are in the bottom 10%, in the middle (50%), and in the bottom 90% of all particles in the sample. Different weightings are assigned to each particle based on the statistical average used. A generalized formula for calculating the weighted mean of a sample is given in **Equation I.1**.

$$\overline{D}_{xy}{}^{(x-y)} = \frac{\sum D_i{}^{x}}{\sum D_i{}^{y}} \qquad \textbf{(I.1)}$$

Some of the more common weighted means are the number average ($\overline{D}$ = 10), volume/surface mean ($\overline{D}$ = 32), diameter/volume mean ($\overline{D}$ = 43).

Weighted residuals reflect the deviation of a samples' experimentally observed scattering pattern and that obtained by fitting the Mie scattering model. Lower weighted residuals mean a better agreement between the model and the data. Values lower than about 4-6% are considered acceptable.

Please note that the uniformity of the sample is defined as follows (**Equation I.2**).

$$Uniformity = \frac{\sum X_i \, |d(n,0.5) - d_i|}{d(n,0.5) \sum X_i} \qquad \textbf{(I.2)}$$

Where $d(n,0.5)$ = mean number size of the distribution, d_i = mean diameter in size class i and $X_i = V_i/d_i^3$ (Where V_i = mean volume in size class i).

I.4 Nitrogen Porosimetry

I.4.1 Nitrogen adsorption isotherms and hysteresis

Before any models are used to determine the surface area, the nitrogen adsorption isotherm of the material needs to be obtained as this is the source of the data which the models use to extrapolate their values (and as a consequence different models are only applicable to certain types of materials). The sample is first cooled to cryogenic temperatures because physisorption of gases on solid surfaces is increased at lower temperatures. A quantity of gas is then dosed into the sealed sample tube under vacuum at a given pressure, and the amount of gas adsorbed at different pressures is measured. More specifically this is represented as a plot of molar quantity of gas adsorbed, V_a ($cm^3 \cdot g^{-1}$) under standard conditions (0°C, 760

Torr) as a function of relative pressure, which is the actual gas pressure, P, divided by the vapor pressure of the adsorbing gas, P_0, (P/P_0).

Although there are a wide range of pore sizes, geometries, distributions, and surface affinities for the adsorptive used, it is interesting to note that most materials can be classified into one of six different isotherms types, five of which were first reported by Brunauer.[2] Depending on the shape of the isotherm and any hysteresis present, the nature of the pore size can be qualitatively inferred i.e. nonporous, microporous, mesoporous, or macroporous. Hysteresis arises from the fact that condensation and evaporation rates of gas in a pore are different. This is also why nonporous materials will not exhibit hysteresis in the isotherm plot, as the respective rates of evaporation and condensation are equivalent. However, one must be careful as some pore geometries can also yield an isotherm without hysteresis.

A false hysteresis can also arise from insufficiently long equilibration times for each data point, however it can be spotted with relative ease as the hysteresis tends not to "close" on decreasing relative pressure due to gas adsorption for a non-equilibrated data point, x, being attributed to the next data point, y. The same then happens on the desorption branch, shifting the features of the isotherm and widening the hysteresis.[3]

I.4.2 Surface area measurements with BET theory

BET theory is an extension of the Langmuir adsorption theory. This enables multi-layer gas adsorption to be accounted for by equating the rate of gas condensing onto an already adsorbed layer, to the rate of evaporation from that layer, then

summing for an infinite number of layers. The linear form of the equation is given in (**Equation I.3**).[4]

$$\frac{P}{V_a(P_0 - P)} = \frac{1}{V_m C} + \frac{C - 1}{V_m C}\left(\frac{P}{P_0}\right) \quad \textbf{(I.3)}$$

Where all quantities are as defined before other than P_0= saturation pressure of the gas, V_m = Volume of gas adsorbed when the entire surface is covered by a monomolecular layer. C is a constant which is defined in **Equation I.4**.

$$C \propto \exp \frac{q_1 - q_L}{RT} \quad \textbf{(I.4)}$$

Where q_1= heat of adsorption of the first layer and q_L= heat of liquefaction of the adsorptive.

A plot of $1/[V_a\left(\frac{P_0}{P} - 1\right)]$ vs. P/P0 and fitting with a linear regression allows one to determine both V_m (**Equation I.5**) and C (**Equation I.6**) by knowing the slope, m, and the intercept, i.

$$V_m = \frac{1}{m + i} \quad \textbf{(I.5)}$$

$$C = 1 + \frac{m}{i} \quad \textbf{(I.6)}$$

The BET surface area can then be determine by knowing the value of V_m and the area occupied by a single N_2 molecule, σ, on the surface assuming close packing (**Equation I.7**).

$$\sigma = (4)(0.866)\left[\frac{M}{4(2N_A\rho}\right]^{2/3} \quad \textbf{(I.7)}$$

Where M = molecular weight of N_2, N_A = Avogadro's Constant, and ρ = density of the liquid N_2. A standard value of $\sigma(N_2)$ = 16.2 Å.

BET theory assumes that the material doesn't contain any micropores and that there is uniform coverage of the solid surface with no preferential adsorption sites. By looking at the magnitude of the C-value one can determine whether the result obtained is appropriate given the material being analyzed. Generally the value needs to fall between 5-300. A value less than 5 indicates that the gas-gas affinity is strongly competing with gas-solid affinity. Values greater than 350 indicate either preferential adsorption at sites on the surface, or similarly, the presence of micropores.

I.4.3 Lippens and deBoer t-plot method: micropore area, external surface area, and micropore volume

The Lippens and deBoer-plot allows for the determination of micropore volume and surface area (both micropore and external).[5]

Essentially, the model compares the obtained isotherm of a microporous sample with that of a standard nonporous reference that has a similar BET C-constant to the material under analysis.

In practice the number of gas layers adsorbed on a surface is never uniform but instead can be described by a density profile, which depends largely on the temperature. If we are to assume that the coverage is uniform then one can obtain the statistical thickness, t, from analysis of the adsorption isotherm. Thickness equations are used to work out the standard multilayer thickness at a given relative pressure. An example is given in **Equation I.8**, which we use in this work. It describes the statistical thickness of N_2 adsorption at 77 K on siliceous oxides (**Equation I.8**).

$$t\,(\text{Å}) = \left[\frac{13.99}{\log\left(\frac{P_0}{P}\right) + 0.034}\right]^{1/2} \qquad \textbf{(I.8)}$$

The experimental isotherm is then redrawn as a t-curve, which is a plot of volume of gas adsorbed, V_A, as a function of statistical thickness of gas layers observed at each relative pressure on the nonporous standard.

This is best illustrated by the following example; **Figure I.2 A** shows a nitrogen adsorption isotherm for a nonporous sample, displaying type II behavior. In comparison **Figure I.2 C** shows a material that has a small population of micropores. Notice how the slope of **Figure I.2 C** rises faster than **Figure I.2 A** - this is due to increased gas uptake through condensation of nitrogen in the micropores. If we take a look at a plot of $V_A(t)$ for the two samples then we see that the slope of the nonporous material goes through the origin (**Figure I.2 B**), whereas there is a

deviation of the intercept on the y-axis from the origin when we extrapolate back to t = 0 for the microporous sample (**Figure I.2 D**).

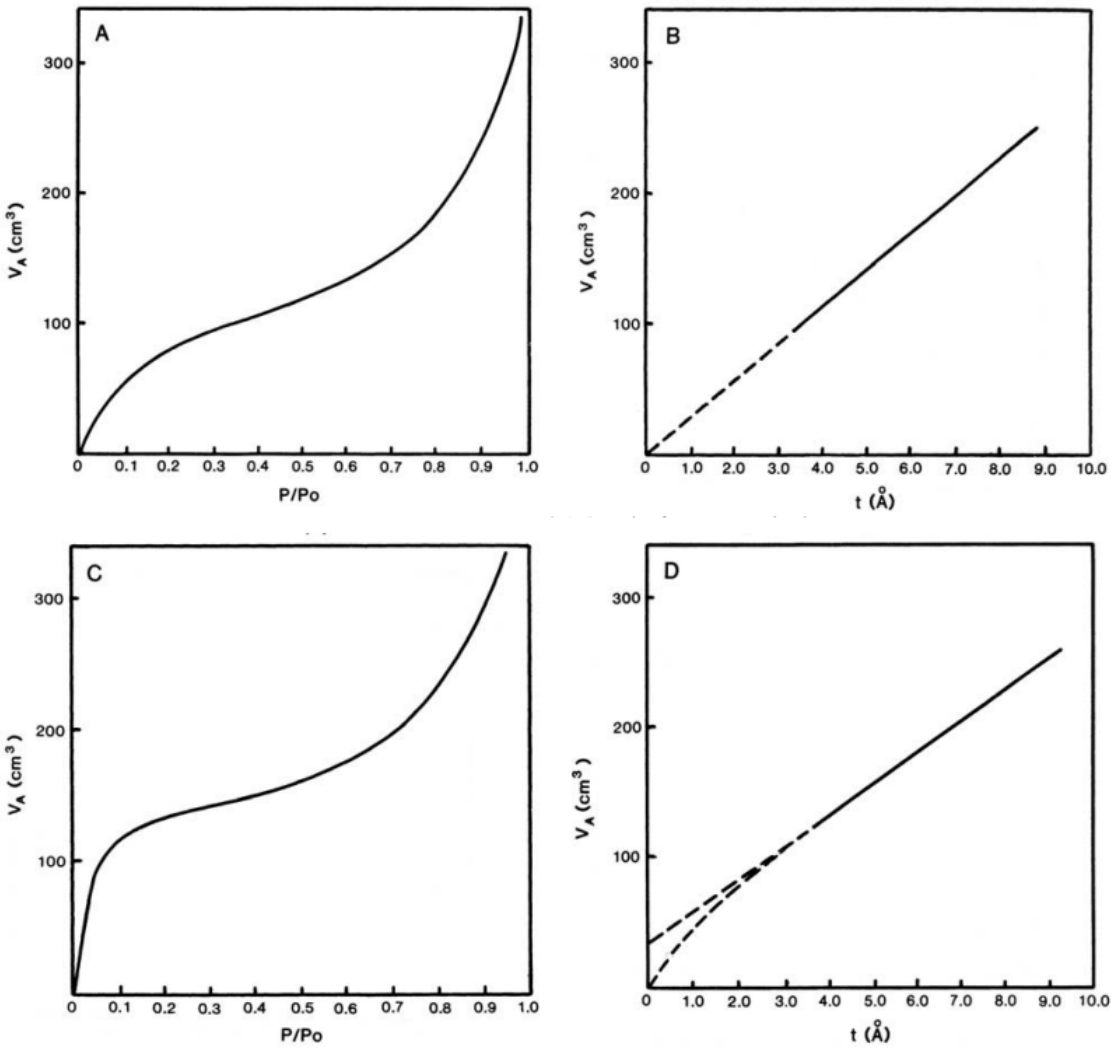

Figure I.2. (**A**) Nitrogen adsorption isotherm for a nonporous material, (**B**) Corresponding $V_A(t)$ plot for (**A**), (**C**) Nitrogen adsorption isotherm for a microporous material (**D**) Corresponding $V_A(t)$ plot for (**C**) with (**B**) overlaid for comparison. Images adapted from.[6]

The slope of the nonporous material in **Figure I.2 B** is equal to the surface area, and should be comparable with the value obtained from BET analysis. The

slope for the microporous material in **Figure I.2 D** is equal to the external surface area - that is the surface area of all flat surfaces and larger pores following micropore filling. Likewise, the surface area of the micropores can be calculated by subtracting that of the external surface from the BET surface area.

Micropore volume is calculated from the positive intercept, *y*, of the plot of $V_A(t)$ for the microporous sample (**Figure I.2 D**) as follows in **Equation I.9**.

$$V_{MP}(cm^3) = y \times 0.001547 \quad \textbf{(I.9)}$$

I.5 Energy Dispersive X-ray Analysis (EDAX)

When a sample is bombarded with electrons it knocks off electrons from the inner shells of some atoms in the sample. Following this, higher energy electrons will move from an outer shell to fill the vacant position. In this process energy is released as an X-ray that is characteristic to both the element and the nature of the transition.

The detector is made up of a crystal, often Si(Li), which converts the energy of the X-ray into an electrical voltage, that is then processed by the software. A plot of the intensity of a certain energy X-ray then allows one to determine the relative abundance of the elements in a sample, however resolution is limited to about 1% by mass of the sample, and some of the lighter elements are not possible to detect. Also the analysis is only really quantitative on homogenous smooth films that have a suitable standard available to calibrate the machine against, which is not the case for most synthesized samples meaning that results are semi-quantitative at best.

Penetration depth as a function of accelerating voltage must also be considered, using software such as CASINO to model these interactions.[7]

EDAX with the SEM is best for analysis over large areas of sample, including elemental mapping of such areas, whereas TEM is better suited to highly spatially resolved elemental analysis.

I.6 Dynamic Light Scattering (DLS)

Also known as photon correlation spectroscopy (PCS), or quasi-elastic light scattering (QELS). The hydrodynamic radius of particles, *d(H)*, in the 1 nm-10 μm range is calculated with the Stokes-Einstein equation (**Equation I.10**) for a sphere through measurement of the translational diffusion coefficient, *D*, itself a result of Brownian motion (discussed in more detail in **Section 4.1**).

$$d(H) = \frac{kT}{3\pi\eta D} \qquad \textbf{(I.10)}$$

Where k = Boltzmann's constant, T = temperature and η = viscosity.

Larger particles have a lower diffusion coefficient whereas smaller particles have a higher diffusion coefficient. It is paramount that one knows the viscosity and temperature of solution as these will impact upon the hydrodynamic radius. It is also important to know the concentration of ions in solution and surface structure as these may also affect *D*, and consequently *d(H)*. It must also be noted that for non-spherical particles, *d(H)* is reported as that of a sphere which has the same *D*.

With regards to how the measurement of *D* is performed, a laser (He-Ne λ = 633 nm for our Malvern Zetasizer Nano ZS) illuminates the sample, and the

backscattered light is picked up by a detector at 173° to the angle of incidence. Fluctuations in the intensity of the scattered light as a function of time are fed into an autocorrelator which compares the signal at very small time intervals. Depending on the size of the particles, the strength of the correlation will persist over different time frames. Various algorithms are applied to the correlation function in order to extract information about the diffusion coefficient and particle size therein. For more information the reader is referred to the Malvern technical notes.[8]

I.7 Electrophoretic Light Scattering

Charged particles move in solution under the application of an electric field (on top of Brownian motion). When this field is applied the particles eventually reach a constant velocity, which is known as the electrophoretic mobility, U_E, that is dependent on the strength of the field. This is measured by a technique known as Laser Doppler velocimetry where two laser beams are crossed at a point in the sample cell to create an interference fringe with known spacing. After application of an electric field the particles move through these fringes and the intensity of light scattering fluctuates with a frequency related to the electrophoretic mobility.

Zeta potential, ζ, is related to the electrophoretic mobility by the Henry **Equation I.11**.

$$U_e = \frac{2\varepsilon\zeta f(Ka)}{3\eta} \quad \textbf{(I.11)}$$

Where ε = dielectric constant of medium, $f(Ka)$ = Henry's function and η = solution viscosity.

For a full discussion on the nature of the zeta potential and the electrical double layer the reader is referred to **Section 2.1**.

In our measurements, the Smoluchowski approximation was used, in which the thickness of the double layer is assumed to be negligible compared to the size of the particle. In this specific model the Henry function has a value of 1.5. This approximation holds for solutions with ionic concentration >1x 10^{-3} M for monovalent ions.

As the surface potential is modified by the pH of the solution and the thickness of the diffuse layer is regulated by ionic strength, it is important to quote both of these parameters when reporting a z eta potential.

I.8 References

(1) Http://www.malvern.com/labeng/technology/laser_diffraction /what_is_particle_size.htm, Accessed on 03/10/13.

(2) Brunauer, S. *The Adsorption of Gases and Vapors. Vol. I, Physical Adsorption*; Princeton University Press, 1943.

(3) Webb, P. A.; Orr, C. *Analytical Methods in Fine Particle Technology*; Micromeritics, 1997; pp. 137–138.

(4) Brunauer, S.; Emmett, P. H.; Teller, E. *J. Am. Chem. Soc.* **1938**, *60*, 309–319.

(5) De Boer, J. H.; Lippens, B. C.; Linsen, B. G.; Broekhoff, J. C. P.; Van den Heuvel, A.; Osinga, T. J. *J. Colloid Interface Sci.* **1966**, *21*, 405–414.

(6) http://www.atomikateknik.com/pdf /Micropore%20Analysis.pdf, Accessed on 20/08/13.

(7) Hovington, P.; Drouin, D.; Gauvin, R. *Scanning Vol.* **1997**, *19*, 1–14.

(8) Http://www.malvern.com/labeng/technology /dynamic_light_scattering/dynamic_light_scattering.htm, Accessed on 03/09/13.

Appendix II

"Chapter 1 Supporting Information"

II.1 Characterization of PS-DVB-AA Latex Particles

SEM image of PS-DVB-AA latex particles used as directing agent in the formation of multi-faceted Cu_2O particles in **Figure 1.8**.

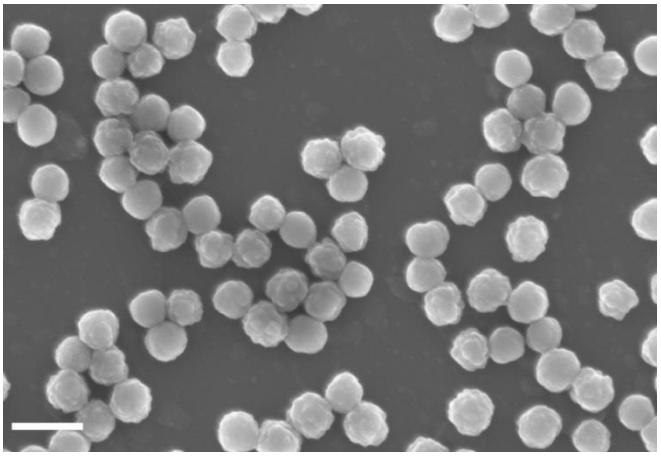

Figure II.1. SEM image of PS-DVB-AA latex particles. Scale bar = 400 nm.

Table II.1. Particle sizing and electrophoretic characterization of the PS-DVB-AA particles shown in **Figure II.1**. [a] PdI is defined below in **Equation II.1**.

Z-average d (nm)	PdI[a]	ζ (mV)
223.5 ± 2.66	0.024 ± 0.021	-58.2 ± 1.27

PdI defines how wide the particle distribution is and is defined below in **Equation II.1**.

$$PdI = \left(\frac{\sigma}{d}\right)^2 \quad \textbf{(II.1)}$$

Where σ = standard deviation of z-average diameters, and d = z-average diameter.

II.2 Coating of Hematite Ellipsoids with Silica

Table II.2. Tabulated statistical descriptors for the light scattering measurements (**Figure 1.13**) of the Fe_2O_3 ellipsoids, and the nanocomposite following sol-gel coating with SiO_2, both with and without ultrasound.

Material	**Vol. weighted mean (µm)**	**d(0.1) (µm)**	**d(0.5) (µm)**	**d(0.9) (µm)**	**Uniformity**	**Weighted residual (%)**
Fe_2O_3 ellipsoids	0.62	0.36	0.58	0.94	0.31	2.71
Fe_2O_3@SiO_2 - no ultrasound	4.49	2.28	4.09	7.27	0.38	0.70
Fe_2O_3@SiO_2 - with ultrasound	0.61	0.37	0.58	0.89	0.29	1.97

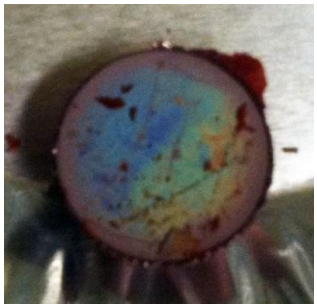

Figure II.2. Digital photograph of a colloidal crystal of Fe_2O_3@SiO_2 ellipsoids displaying opalescence.

II.3 Film Characterization of Digital Photograph Showing Multifilm Drawdown of Coatings Containing SOCAL P3, and 1st Generation Hollow Silica Particles as Pigment

Table II.3. Wet film thickness and theoretical dry film thickness, corresponding to the labelled films seen in **Figure 1.29**. [a] Labels correspond to films shown in **Figure 1.29 B**. [b] Labels correspond to films shown in **Figure 1.29 A**. [c] Theoretical dry film thickness calculated using **Equation 1.1** and assuming wet film thickness is as applied at drawdown. Volume solids is obtained by correcting the experimentally determined value (from TGA – **Table 1.8** and **1.9**), in order to account for broken hollow particles (as determined by film density measurements - **Table 1.10)**.

Film number	Sample	Wet film thickness (µm)	Dry film thickness[c] (µm)
1	SOCAL P3[a]	300	48.3
	Hollow SiO_2 (1st gen.)[b]		39.3
2	SOCAL P3	275	44.3
	Hollow SiO_2 (1st gen.)		36.0
3	SOCAL P3	250	40.3
	Hollow SiO_2 (1st gen.)		32.8
4	SOCAL P3	225	36.2
	Hollow SiO_2 (1st gen.)		29.5
5	SOCAL P3	200	32.2
	Hollow SiO_2 (1st gen.)		26.2
6	SOCAL P3	175	28.2
	Hollow SiO_2 (1st gen.)		22.9
7	SOCAL P3	150	24.2
	Hollow SiO_2 (1st gen.)		19.7
8	SOCAL P3	125	20.1
	Hollow SiO_2 (1st gen.)		16.4
9	SOCAL P3	100	16.1
	Hollow SiO_2 (1st gen.)		13.1
10	SOCAL P3	75	12.1
	Hollow SiO_2 (1st gen.)		9.8

II.4 Raw Data from Film Density Measurements

Raw data for the film density measurements are reported in **Table II.4**. All values are averages over 9 measurements.

Table II.4. Raw data for the film density as determined by the silicone oil adsorption experiment.

Sample	Mass of film in air (g)	Mass of film in DMCPS (g)	Temperature (°C)
SOCAL P3	0.09005	0.03533	22.5
Hollow SiO_2 – 1st gen. thin shell	0.0366	0.00425	22.2
Hollow SiO_2 – 2nd gen. thick shell	0.0365	0.0044	22.7

II.5 Statistical Descriptors of Laser Diffraction Measurements on $CaCO_3$@SiO_2 Particles from Section 1.2.4

Table II.5. Tabulated Mie scattering results for the data plotted in **Figure 1.31**.

Material	d(0.1) (µm)	d(0.5) (µm)	d(0.9) (µm)	Uniformity
Sample A1 nanocomposite	0.27	0.36	0.61	0.38
Sample A2 nanocomposite	0.30	0.41	0.93	0.59
Sample A3 nanocomposite	0.34	0.47	0.90	0.50
Sample A4 nanocomposite	0.40	0.51	0.85	0.40

II.6 Film Characterization of Digital Photograph Showing Multifilm Drawdown of Coating Containing 2nd Generation Hollow Silica Particles as Pigment

Table II.6. Wet film thickness and theoretical film thickness, corresponding to the labelled films seen in **Figure 1.41 B** for the dry films with 2nd generation hollow SiO_2 particles as pigment. [a] Theoretical dry film thickness calculated using **Equation 1.1** and assuming wet film thickness is as applied at drawdown. Volume solids is obtained by correcting the experimentally determined value (from TGA – **Table 1.17**), in order to account for broken hollow particles (as determined by film density measurements - **Table 1.18)**.

Film number	Wet film thickness (µm)	Dry film thickness[a] (µm)
1	300	42.3
2	275	38.8
3	250	35.3
4	225	31.7
5	200	28.2
6	175	24.7
7	150	21.2
8	125	17.6
9	100	14.1
10	75	10.6

II.7 Multifilm Drawdown Apparatus Used in Digital Photographs of Dry Coatings

Figure II.3. Multifilm thickness bar used to drawdown the wet films on Lenetta panels.

Appendix III

"Chapter 2 Supporting Information"

III.1 Zeta Potential Raw Data for Figure 2.12

Table III.1-

Table III.5 show some of the important measured values in each of the zeta-potential experiments, conducted as a function of salt concentrations, for the particles: SOCAL P3, SOCAL P3@SiO_2, SOCAL P3@SiO_2-NH_2, SOCAL P3@SiO_2-Br, and SOCAL P3@SiO_2-PVP K30.

Table III.1. Raw data for zeta-potential measurements as a function of [NaCl] for SOCAL P3 particles.

[NaCl] (M)	Zeta-potential (mV) ± S.D.	Electrophoretic mobility (µm.cm/Vs)	Conductivity (mS/cm)
0.001	7.89 ± 0.69	0.62 ± 0.05	0.08 ± 0.002
0.005	3.46 ± 0.40	0.24 ± 0.03	0.05 ± 0.002
0.01	8.45 ± 0.58	0.66 ± 0.05	0.05 ± 0.001
0.05	5.17 ± 0.34	0.41 ± 0.03	0.05 ± 0.001
0.1	5.67 ± 0.17	0.44 ± 0.01	0.05 ± 0.001
0.5	0.03 ± 0.01	0 ± 0.01	41.2 ± 0.780
1	-	-	-

Table III.2. Raw data for zeta-potential measurements as a function of [NaCl] for SOCAL P3@SiO_2 particles.

[NaCl] (M)	**Zeta-potential (mV) ± S.D.**	**Electrophoretic mobility (µm.cm/Vs)**	**Conductivity (mS/cm)**
0.001	-33.8 ± 0.76	-2.65 ± 0.06	0.04 ± 0.001
0.005	-36.1 ± 1.63	-2.83 ± 0.13	0.05 ± 0.003
0.01	-34.3 ± 0.36	-2.69 ± 0.03	0.05 ± 0.002
0.05	-35.2 ± 0.47	-2.76 ± 0.04	0.05 ± 0.002
0.1	-36.5 ± 2.83	-2.86 ± 0.22	0.05 ± 0.003
0.5	-24.3 ± 0.78	-1.90 ± 0.06	39.9 ± 0.140
1	-14.6 ± 0.92	-1.15 ± 0.08	77.8 ± 0.640

Table III.3. Raw data for zeta-potential measurements as a function of [NaCl] for SOCAL P3@SiO_2-NH_2 particles.

[NaCl] (M)	**Zeta-potential (mV) ± S.D.**	**Electrophoretic mobility (µm.cm/Vs)**	**Conductivity (mS/cm)**
0.001	16.5 ± 0.42	1.29 ± 0.03	0.05 ± 0.002
0.005	5.08 ± 0.37	0.40 ± 0.03	0.05 ± 0.004
0.01	5.89 ± 0.70	0.46 ± 0.06	0.05 ± 0.002
0.05	2.74 ± 0.27	0.21 ± 0.02	0.05 ± 0.001
0.1	0.46 ± 0.52	0.04 ± 0.04	0.05 ± 0.002
0.5	0.51 ± 0.74	0.04 ± 0.06	40.7 ± 0.945
1	-	-	-

Table III.4. Raw data for zeta-potential measurements as a function of [NaCl] for SOCAL P3@SiO_2-Br particles.

[NaCl] (M)	Zeta-potential (mV) ± S.D.	Electrophoretic mobility (µm.cm/Vs)	Conductivity (mS/cm)
0.001	-26.0 ± 0.53	-2.04 ± 0.04	0.05 ± 0.003
0.005	-31.0 ± 1.87	-2.43 ± 0.15	0.05 ± 0.004
0.01	-30.0 ± 0.45	-2.35 ± 0.03	0.05 ± 0.001
0.05	-29.7 ± 2.31	-2.33 ± 0.18	0.05 ± 0.004
0.1	-30.8 ± 2.23	-2.41 ± 0.17	0.05 ± 0.003
0.5	-9.16 ± 0.72	-0.71 ± 0.06	41.0 ± 1.060
1	-	-	-

Table III.5. Raw data for zeta-potential measurements as a function of [NaCl] for SOCAL P3@SiO_2-PVP K30 particles.

[NaCl] (M)	Zeta-potential (mV) ± S.D.	Electrophoretic mobility (µm.cm/Vs)	Conductivity (mS/cm)
0.001	-16.3 ± 0.70	-1.28 ± 0.06	0.05 ± 0.003
0.005	-19.7 ± 1.31	-1.55 ± 0.10	0.09 ± 0.003
0.01	-18.1 ± 0.45	-1.42 ± 0.03	0.05 ± 0.001
0.05	-19.1 ± 0.49	-1.50 ± 0.04	0.05 ± 0.001
0.1	-18.0 ± 1.41	-1.41 ± 0.11	0.05 ± 0.002
0.5	-5.38 ± 5.39	-0.42 ± 0.42	41.0 ± 0.92
1	-	-	-

III.2 Laser Diffraction (Mie scattering) Statistical Data for Figure 2.15

Table III.6. Statistical descriptors for the frequency distribution of particle size obtained by laser diffraction.

Sample	d(0.1) (µm)	d(0.5) (µm)	d(0.9) (µm)	Uniformity	Weighted Residual (%)
SOCAL P3 @SiO_2	0.42	0.54	0.80	0.29	4.67
SOCAL P3 @SiO_2-NH_2	0.41	0.52	0.76	0.28	1.24
SOCAL P3 @SiO_2-Br	0.41	0.53	0.82	0.46	2.72
SOCAL P3 @SiO_2-poly(NaSS)	0.46	0.60	0.94	0.30	4.85

III.3 Zeta Potential Raw Data for Figure 2.16

Table III.7. Raw data for zeta-potential measurements as a function of [NaCl] for SOCAL P3@SiO_2-poly(NaSS) particles.

[NaCl] (M)	Zeta-potential (mV) ± S.D.	Electrophoretic mobility (µm.cm/Vs)	Conductivity (mS/cm)
0.001	-26.9 ± 1.40	-2.11 ± 0.11	0.02 ± 0.008
0.005	-20.9 ± 0.44	-1.64 ± 0.03	0.02 ± 0.005
0.01	-45.3 ± 1.62	-3.55 ± 0.13	0.04 ± 0.005
0.05	-36.7 ± 0.46	-2.88 ± 0.04	0.03 ± 0.007
0.1	-30.5 ± 0.69	-2.39 ± 0.05	0.02 ± 0.006
0.5	-28.9 ± 1.22	-2.26 ± 0.10	39.8 ± 0.570
1	-26.4 ± 2.14	-2.07 ± 0.17	73.9 ± 1.360

III.4 Laser Diffraction (Mie scattering) Statistical Data for Figure 2.20

Table III.8. Statistical descriptors for the frequency distribution of particle size obtained by Mie scattering in **Figure 2.20 A** (SOCAL P3-Orotan N-4045).

Freeze-thaw cycle	d(0.1) (µm)	d(0.5) (µm)	d(0.9) (µm)	Uniformity	Weighted Residual (%)
1	0.26	0.36	0.83	0.55	6.01
2	0.24	0.34	0.75	0.53	1.42
3	0.24	0.34	0.73	0.53	1.55

Table III.9. Statistical descriptors for the frequency distribution of particle size obtained by Mie scattering in **Figure 2.20 B** (2^{nd} generation hollow SiO_2-PVP K30 from **Section 1.2.5**).

Freeze-thaw cycle	d(0.1) (µm)	d(0.5) (µm)	d(0.9) (µm)	Uniformity	Weighted Residual (%)
1	3.12	4.54	8.18	0.37	2.19
2	3.40	5.08	10.42	0.46	1.60
3	3.44	5.04	10.50	0.48	1.74

Table III.10. Statistical descriptors for the frequency distribution of particle size obtained by Mie scattering in **Figure 2.20 C** (Hollow SiO_2-poly(NaSS)).

Freeze-thaw cycle	d(0.1) (µm)	d(0.5) (µm)	d(0.9) (µm)	Uniformity	Weighted Residual (%)
1	0.44	0.56	0.86	0.30	4.13
2	0.43	0.55	0.85	0.30	1.92
3	0.44	0.56	0.86	0.30	4.03

III.5 Tabulated Film Thickness for Figure 2.24 A

Table III.11. Wet film thickness and theoretical dry film thickness for the dry films shown in Figure. [a] Theoretical dry film thickness calculated using **Equation 1.1** and assuming wet film thickness is as applied at drawdown. Volume solids is obtained by correcting the experimentally determined value (from TGA – **Table 2.3**), in order to account for broken hollow particles (as determined by film density measurements **- Table 2.4)**.

Sample Number	Wet film thickness (µm)	Dry film thickness [a] (µm)
1	300	32.4
2	275	29.7
3	250	27
4	225	24.3
5	200	21.6
6	175	18.9
7	150	16.2
8	125	13.5
9	100	10.8
10	75	8.1

III.6 Raw Data for Film Density Measurements in Table 2.4

Table III.12. Raw data for the film density of the hollow SiO_2-poly(NaSS) pigmented coating, as determined by the silicone oil absorption experiment.

Sample	Mass of film in air (g)	Mass of film in DMCPS (g)	Temperature (°C)
Hollow SiO_2-poly(NaSS) coating	0.029143	0.004343	22.4

Appendix IV

"Chapter 4 Supporting Information"

IV.1 Spatially Resolved EDAX Measurements

To verify our EDAX data we repeated the measurement on some particles that hadn't been selectively centrifuged (**Figure IV.1**/ **Table IV.1**). These results correlate well with the data in **Table 4.1**. There does however appear to be some variation in the manganese oxide content of the catalyst engine.

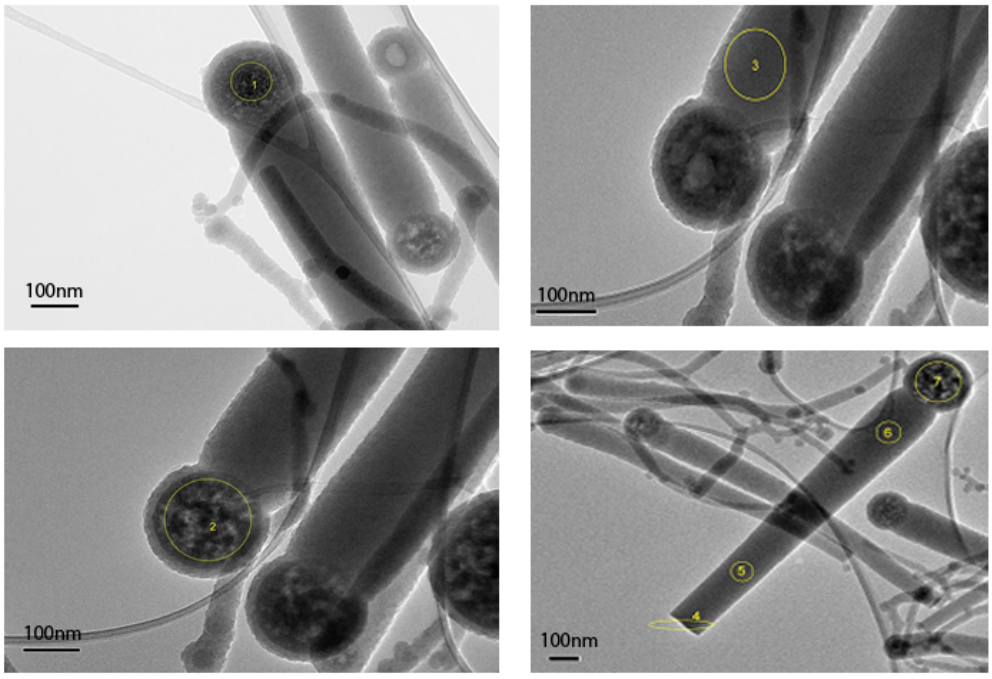

Figure IV.1. TEM images of SiO_2-Mn_xO_y matchstick particles with areas marked that correspond to regions analyzed by EDAX. Results are given in **Table IV.1**.

Table IV.1. Tabulated EDAX data for the areas marked in **Figure IV.1**.

Area	**Weight % Mn_2O_3**	**Weight % SiO_2**	**Total weight %**
1	9.8	90.2	100
2	19.5	80.5	100
3	1.9	98.1	100
4	3.3	96.7	100
5	2.0	98.0	100
6	1.0	99.0	100
7	19.4	80.6	100

IV.2 XRD Pattern Intensity of SiO_2-Mn_xO_y Particles as a Function of Temperature

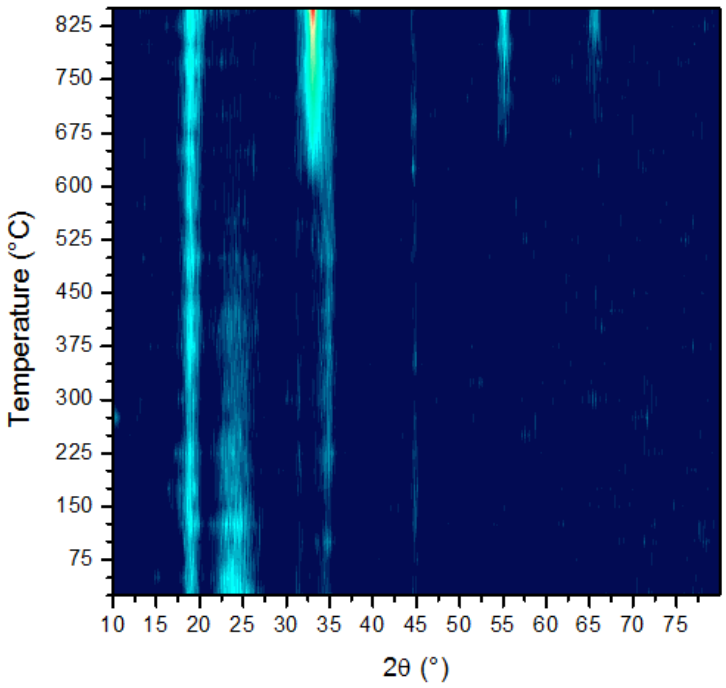

Figure IV.2. XRD plot of scattering angle intensity as function of temperature. This shows an onset of crystallinity in both the silica and manganese oxide above 800°C.

IV.3 Raw Particle Tracking Traces as a Function of $[H_2O_2]$

By looking at the particle traces at different concentrations of hydrogen peroxide we can qualitatively rule out propulsion due to convection or sedimentation as the trajectories follow a random walk type of motion (**Figure IV.3**). That is, there is no overarching directionality in the movement of the particles, which one would expect in the absence of a fuel gradient.

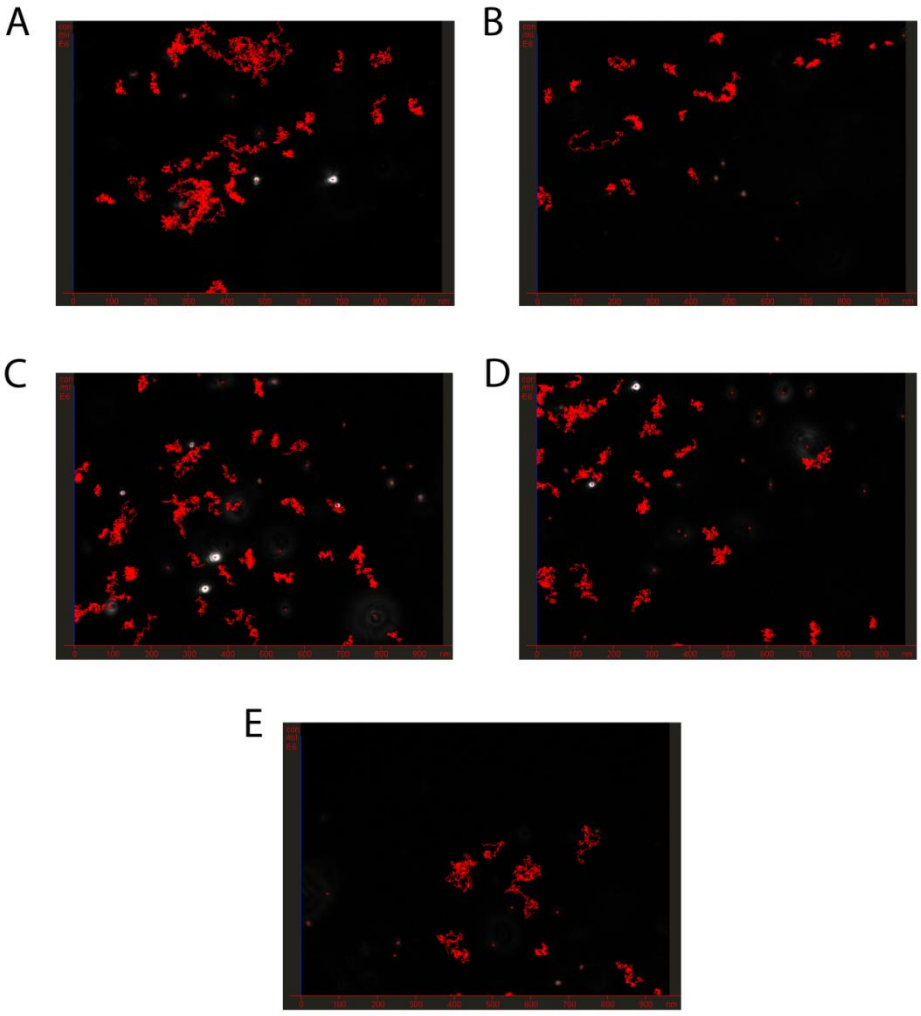

Figure IV.3. Particle traces for some of the particle trajectories analyzed by particle tracking. H_2O_2 volume percentages in the aqueous phase were (**A**) 0%, (**B**) 0.2%, (**C**) 0.4%, (**D**) 0.6%, and (**E**) 0.8%.

IV.4 Digital Photograph of a Dunn Chemotaxis Cell

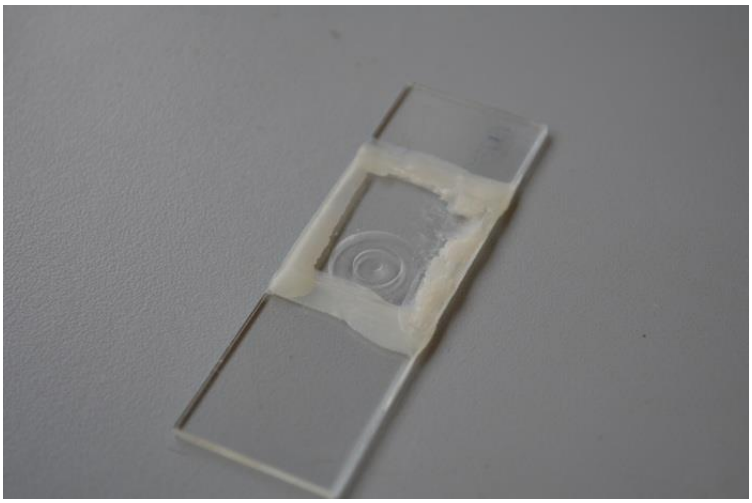

Figure IV.4. Digital photograph of a wax-sealed Dunn chemotaxis cell. Hydrogen peroxide solution is injected into the outer well, while particle solution is placed on the inside well and seeded onto the cover slip. Wax seals the coverslip in place to prevent erroneous results from convection at the edges. Imaging is then performed with an optical microscope across the bridge region in the middle of the concentric wells.